Copper-64 radiopharmaceuticals for PET imaging of copper trafficking in neurological disorders

Baguña Torres, Julia

Awarding institution:
King's College London

Copper-64 radiopharmaceuticals for PET imaging of copper trafficking in neurological disorders

A thesis submitted by

Julia Baguña Torres

In partial fulfilment of the requirements for the degree of

Doctor of Philosophy

University of London

2016

Division of Imaging Sciences and Biomedical Engineering, King's College London

ABSTRACT

Copper dyshomeostasis has been identified as a pathological feature of Alzheimer's disease (AD) and Niemann-Pick disease type C1 (NPC1), as well as other neurological disorders. However, the nature of copper dysregulation in these conditions as well as its impact on disease severity and progression remain poorly understood. The growing availability of high-resolution Positron Emission Tomography (PET) systems and copper radionuclides encourages the use of copper radiotracers to measure copper fluxes in a variety of disease states with PET imaging.

In this thesis, we investigated copper trafficking at brain and whole-body levels with ^{64}Cu-PET in preclinical models of AD and NPC1 disease. The blood-brain barrier-permeable copper-64 bis(thiosemicarbazone) complex ^{64}Cu-GTSM was used to monitor the retention, efflux and redistribution of radiocopper within the brain, while ^{64}Cu-acetate was used to visualise copper uptake into organs from blood plasma. In addition to these imaging studies, a new library of copper bis(thiosemicarbazone) complexes for potential use in molecular imaging applications, including measurement of copper trafficking, was generated.

^{64}Cu-GTSM-PET revealed significant differences in ^{64}Cu brain uptake, regional distribution and biokinetics between TASTPM transgenic AD mice and wildtype controls. Interestingly, although ^{64}Cu-GTSM was taken up by the entire brain, the regions showing the most prominent ^{64}Cu accumulation in TASTPM brain tissue did not coincide with the areas most affected by Aβ plaque pathology, suggesting that additional metabolic/pathological factors besides Aβ plaque deposition influence brain regional ^{64}Cu distribution. ^{64}Cu-acetate-PET indicated subtle but significant differences in whole-body ^{64}Cu trafficking between TASTPM transgenic mice and healthy controls. Furthermore, ^{64}Cu-GTSM-PET detected substantial differences in brain and blood ^{64}Cu concentration between symptomatic NPC1 knockout mice and wildtype controls that may have added value for the diagnosis of this disorder. Taken together, these results demonstrate the potential of ^{64}Cu-PET as a useful tool to delineate copper trafficking abnormalities associated with neurological disorders.

DECLARATION

I Julia Baguña Torres confirm that no part of this thesis has been submitted in support of any other application for a degree or qualification of King's College London, or any other university or institute of learning. I confirm that this work is my own. Where information has been derived from other sources it has been indicated in this thesis.

ACKNOWLEDGMENTS

This thesis would not have been possible without the advice, guidance and support of my supervisor, Prof Phil Blower. His commitment, dedication and generosity to students are truly inspiring and I feel very fortunate to have been given the opportunity to work under his supervision. I especially would like to thank him for his relentless encouragement and patience during my dark moments (which have been a few throughout this process). I am also deeply grateful to my second supervisor, Prof Tony Gee, for his continuous support, constructive advice and interest in my work over the years.

A big thanks goes to Dr Karen Shaw and Dr Zilin Yu for providing me with precious ^{64}Cu whenever possible, and Dr Kavitha Sunassee for valuable advice and training on preclinical imaging work. I owe a special mention to Mr David Thakor for managing the labs so efficiently and providing endless entertainment.

I would also like to thank Dr Erica Andreozzi, my partner in crime during the first half of my PhD, for sharing with me the highs and lows of the project and offering me her unconditional friendship.

I would like to express my gratitude to Julia and Dave for helping me out when I first arrived at KCL, and everybody at Imaging Sciences who contributed to my research during the first year of my PhD (Dr Putthiporn Charoenphun, Dr Levente Meszaros, Dr Krisanat Chuamsaamarkkee, Dr Lefteris Livieratos and Dr David Howlett). A special thanks goes to Dr Istvan Szanda and Dr Joel Dunn for their guidance on PET image quantification and statistical analysis throughout the project.

I am grateful to our collaborators, Dr Po-Wah So (Institute of Psychiatry, Psychology and Neuroscience, King's College London), Dr Oliver C. Brown (School of Physical Sciences, University of Kent), Prof Michael Went (School of Physical Sciences, University of Kent), Prof Frances Platt (Department of Pharmacology, University of Oxford) and Dr Katherine Holt (Department of Chemistry, University College London), for contributing their knowledge and

expertise to this study. I would also like to acknowledge the generous funding from the Alzheimer's Society, Alzheimer's Research UK and King's Health Partners.

Thanks to Enrico for being a great work husband and to Maite, Levente, Michelle, Cinzia, Alex and the rest of the Imaging Chemistry and Biology department for making these a very enjoyable four years. I will be coming back to the Crown and Cushion every now and then.

Finally, I need to thank all my good friends in London and Barcelona for putting up with my moaning and groaning all these years and providing advice and endless support.

This thesis is dedicated to my parents, whose unwavering love and encouragement have sustained me through this journey.

TABLE OF CONTENTS

LIST OF FIGURES

Chapter 1:

Chapter 2:

Chapter 3:

Chapter 4:

Chapter 5:

Chapter 6:

LIST OF TABLES

Chapter 1:

Chapter 3:

Chapter 6:

ABBREVIATIONS

^{11}C-PIB	2-(4'-[^{11}C]methylaminophenyl)-6-hydroxybenzothiazole
^{18}F-FDG	^{18}F-fluorodeoxyglucose
^{18}F-Florbetaben	trans-4-(*N*-methly-amino)-4″-(2-(2-(2-[^{18}F]Fluoro-ethoxy)ethoxy)-ethoxy) stilbene)
^{18}F-Florbetapir	trans-4-(2-(6-(2-(2-(2-[^{18}F]Fluoro-ethoxy)ethoxy)ethoxy)pyridin-3-yl)vinyl)-*N*-methyl benzeneamine)
^{18}F-Flutemetamol	2-[3-[^{18}F]Fluoro-4-(methylamino)phenyl]-1,3-benzothiazol-6-ol
^{18}F-FMISO	^{18}F-fluoromisonidazole
$^{64}CuCl_2$	copper-64 chloride
AD	Alzheimer's disease
Akt	protein kinase B
ALS	amyotrophic lateral sclerosis
AMPA	α-amino-3-hydroxy-5-methyl-4-isoxazolepropionic acid
APP	amyloid precursor protein
Aβ	amyloid-β peptide
BACE1	β-secretase 1
BBB	blood-brain barrier
BCSFB	blood-cerebrospinal fluid barrier
BOLD	blood oxygen level–dependent imaging
BTSC	bis(thiosemicarbazone)
CB-TE1A1P	11-carboxymethyl-1,4,8,11-tetraazabicyclo[6.6.2]hexadecane-4-methanephosphonic acid
CB-TE2A	4,11-bis(carboxymethyl)-1,4,8,11-tetraazabicyclo[6.6.2]hexadecane
CCO	cytochrome c oxidase
CCS	copper chaperone for superoxide dismutase-1
CHO	chinese hamster ovary cells

CNS	central nervous system
CSF	cerebrospinal fluid
Cu-(DEDTC)$_2$	copper (II) diethyldithiocarbamate
Cu-(DMDTC)$_2$	copper(II) dimethyldithiocarbamate
Cu-(DPDTC)$_2$	copper (II) diisopropyldithiocarbamate
Cu/Zn SOD-1	Cu/Zn superoxide dismutase-1
Cu-ATS	copper (II) 2,3-butanedione-bis(thiosemicarbazone)
Cu-ATSM	copper (II) diacetyl-bis(N^4-methylthiosemicarbazone)
Cu-BTSC	copper bis(thiosemicarbazone)
Cu-CTS	copper (II) 2,3-pentanedione-bis(thiosemicarbazone)
Cu-DTC	copper (II) dithiocarbamate
Cu-GTSE	copper (II) glyoxal-bis(N^4-ethyl-3-thiosemicarbazone)
Cu-GTSM	copper (II) glyoxal-bis(N^4-methyl-3-thiosemicarbazone)
Cu-GTSP	copper (II) glyoxal-bis(N^4-phenyl-3-thiosemicarbazone)
Cu-PTSM	copper (II) pyruvaldehyde-bis(N^4-methylthiosemicarbazone)
disulfiram	1,1',1'',1'''-[disulfanediylbis(carbonothioylnitrilo)]tetraethane
DMT1	divalent metal transporter 1
DOTA	1,4,7,10-tetraazacyclododecane-1,4,7,10-tetraacetic acid
D-Penicillamine	D-(−)-2-amino-3-mercapto-3-methylbutanoic acid
DTPA	diethylenetriaminepentaacetic acid
DβH	dopamine β-hydroxylase
EC-SOD	extracellular superoxide dismutase
EDTA	ethylenediaminetetraacetic acid
EPR	electron paramagnetic resonance
ERK	extracellular-signal-regulated kinase
ESI-MS	electrospray ionisation mass spectrometry
GABA	γ-aminobutyric acid
GSK3	glycogen synthase kinase 3
H_2-ATSM	diacetyl bis(N^4-methylthiosemicarbazone)
H_2-GTSM	glyoxalbis(N^4-methyl-3-thiosemicarbazone)
HD	Huntington's disease

HPLC	high-performance liquid chromatography
ICP-MS	inductively coupled plasma mass spectrometry
IEC	intestinal epithelial cell
IMS	intermembrane space
JNK	c-Jun N-terminal kinase
K_d	dissociation constant
KTS	2-keto-3-ethoxybutyraldehyde-bis(thiosemicarbazone)
LOX	lysyl oxidase
MCI	mild cognitive impairment
MD	Menkes disease
MMP	matrix metalloproteinase
MPAC	metal-protein attenuation compound
MRI	magnetic resonance imaging
MT	metallothionein
NFT	neurofibrillary tangle
NIRF	near-infrared fluorescence
NMDA	N-methyl-D-aspartate
NMR	nuclear magnetic resonance
NODAGA	1,4,7-triazacyclononane-1-glutaric acid-4,7-diacetic acid
NOTA	1,4,7-triazacyclononane-1,4,7-triacetic acid
NPC	Niemann-Pick type C disease
PAL	peptidyl-α-hydroxyglycine α-amidating lyase
PAM	peptidylglycine α-amidating monooxygenase
PCTA	3,6,9,15-tetraazabicyclo[9.3.1]pentadeca-1(15),11,13-triene-3,6,9,-triacetic acid
PD	Parkinson’s disease
PET	positron emission tomography
PHM	peptidylglycine α-hydroxylating monooxygenase
PI3K	phosphoinositol 3-kinase
pK_a	acid dissociation coefficient
PrP	prion protein

PrP^{Sc}	infectious prion protein
Riluzole	6-(trifluoromethoxy)benzothiazol-2-amine
ROI	region of interest
ROS	reactive oxygen species
sarAr	1-*N*-(4-aminobenzyl)-3,6,10,13,16,19-hexaaza-bicyclo-[6.6.6]eicosane-1,8-diamine
sar-CO_2H	(1-NH_2-8-$NHCO(CH_2)_3CO_2H$)-3,6,10,13,16,19-hexaazabicyclo[6.6.6]icosane
SPECT	single-photon emission computed tomography
SUV	standardised uptake value
TETA	1,4,8,11-tetraazacyclotetradecane-1,4,8,11-tetraacetic acid
TFA	trifluoroacetic acid
TLC	thin layer chromatography
Triethylenetetramine	*N*,*N'*-bis(2-aminoethyl)ethane-1,2-diamine
WD	Wilson's disease

Chapter 1- Copper radiopharmaceuticals in nuclear medicine: opportunities and challenges

1.1 AIMS

The essential nature of copper for most living organisms has long been established. First experimental evidence of the biological necessity for copper was provided in 1925 by J. S. McHargue in a series of studies on the role of various trace metals in the nutrition, growth and development of plants and animals (1, 2). Over the years, the participation of copper in a wide range of vital metabolic processes, such as cellular respiration, iron mobilisation, neurotransmission, oxygen transport or radical scavenging, has been demonstrated. However, many aspects of copper trafficking and metabolism in health and disease remain to be fully understood.

The aim of this review is to assess the current state of knowledge on copper biochemistry in order to identify important areas of uncertainty that need to be addressed. This is particularly critical for the characterisation of changes in the transport and metabolism of copper associated with disease. This article will then review the current uses of copper radionuclides and radiopharmaceuticals in nuclear medicine and will discuss future directions for application.

1.2 CHEMISTRY OF COPPER

The physicochemical behaviour of copper is governed by many of the characteristics of transition metals, such as a high melting point, paramagnetism in compounds with an incomplete *d* sub-shell and the formation of coloured species due to charge transfer or *d*-*d* electronic transitions. However, the coordination chemistry of this element remains relatively straightforward when compared to that of other *d*-block metals since it is mainly dominated by two oxidation states, I and II.

Copper is capable of existing in five different oxidation states (0-IV), with cuprous and cupric species predominating. Oxidation states 0 and IV are extremely rare, but the syntheses of several stabilised copper (0) and (IV) complexes have been reported (3, 4). Stable copper (III) complexes exist only with strong π-donor anionic ligands (e.g. F^-, O^{2-}, R_2N^-, RO^-) and exhibit very high Cu (III)/Cu (II) redox potentials, which may explain why the copper (III) oxidation state has not yet been assigned to any biological redox process (5).

The equilibrium between the most common oxidation states of copper is strongly influenced by the medium and may be summarised by the following equation:

$$2Cu(I) \rightleftharpoons Cu + Cu(II)$$

The presence of polarisable, "soft" bases will favour the formation of cuprous compounds, whereas the interaction of copper with weakly coordinating, "harder" donor groups will lead to the disproportionation of copper (I) into metallic copper and copper (II) species (6). The choice of solvent may also affect the relative stability of the copper (I) and (II) oxidation states. Because of the higher hydration energy of the copper (II) ion, copper (II) compounds show a greater stability in aqueous environments compared to copper (I) complexes. Conversely, copper (I) complexes exhibit a higher stability in some non-aqueous solvents (e.g. acetonitrile) than copper (II) species (7). In this manner, the nature of the chemical environment influences the stability of the copper (I) and (II) oxidation states and ultimately modulates the reducing or oxidising power of copper-dependent enzymes.

1.2.1 Copper (I)

Copper (I) ions display diamagnetic behaviour due to a completely filled *3d* sub-shell. The lack of d-d electronic transitions renders most copper (I) compounds colourless, except when colour results from charge-transfer transitions or from the ligand itself.

Copper (I) exhibits a marked class b Lewis acid behaviour, readily complexing with "soft", coordinating ligands of negligible basicity (e.g. CN^-, Cl^-, I^-, R_2S, RS^-, R_3P) (6). Due to the lack of ligand field effects, the copper (I) state is characterised by a flexible coordination geometry, with

the preferred coordination number ranging from two to four. Copper (I) complexes can adopt linear (e.g. Cu_2O, $CuCl_2$), trigonal planar (e.g. $KCu(CN)_2$, $[Cu(SPMe_3)_3]ClO_4$) and tetrahedral (e.g. CuI, $[Cu(CN)_4]^{3-}$) geometries and may even exhibit octahedral coordination (e.g. $Cu_6[S_2P(OEt)_2]_6 \bullet 2H_2O$) on rare occasions (7, 8). Since copper (I) complexes show little preference for a particular coordination geometry, ligand exchange processes are generally rapid, unless they are sterically blocked by the ligand itself.

Copper in the monovalent form is essential in all biological systems, either alone or as the copper (II)/copper (I) redox pair. However, the low kinetic stability of copper (I) complexes limits considerably their use as radiopharmaceuticals.

1.2.2 Copper (II)

Copper (II) ions have an unsaturated d^9 configuration and, consequently, behave paramagnetically, except when the magnetism is quenched by metal-metal interactions. The electronic transitions between the d sub-orbitals of the metal ion give most copper (II) compounds a blue-green colour. However, intense ligand-to-metal charge transfer transitions can cause some copper (II) complexes to appear brown coloured.

Copper (II) complexes strongly favour tetra-, penta- and hexa-coordinate geometries, and are characterised by pronounced Jahn-Teller distortion due to the unfilled *3d* sub-shell of the metal ion. In order to decrease the overall energy of the system resulting from the asymmetric distribution of electronic density, the symmetry of copper (II) complexes is reduced by elongation of the metal-ligand bonds lying along the z-axis in the case of octahedral arrangements, or by tetragonal compression in tetrahedral geometries. As a result, the most commonly encountered structures for copper (II) complexes are distorted octahedral (e.g. $CuCl_2$, $K_2[Cu(EDTA)]$) and tetrahedral (e.g. $Cs_2[CuCl_4]$), as well as square pyramidal (e.g. $[Cu(NH_3)_5]^{2+}$) and square planar (e.g. CuO) (7).

Copper (II) ions are classified as borderline Lewis acids on the Pearson scale and therefore show a preference for weakly polarisable anionic ligands, such as halides (e.g. CuF_2, $CuCl_2$),

oxoanions (e.g. $CuSO_4 \cdot 5H_2O$, $CuCO_3$) and nitrogen donor groups (e.g. $[Cu(py)_4]^{2+}$, $[Cu(NH_3)_5]^{2+}$) (6).

Despite showing higher kinetic stability than copper (I) species, copper (II) complexes are still considerably reactive when compared to kinetically inert d^3/d^6 transition metal chelates. Non-bridged and cross-bridged macrocyclic chelators as well as sarcophagine ligands have been used to enhance the stability to decomplexation of bioconjugate-based copper radiopharmaceuticals (9). However, alternatively, the accessible reduction potential and lability of some copper (II) complexes can be exploited to tailor the tissue targeting properties of copper radiopharmaceuticals and even to deposit radiocopper into cells to monitor its trafficking (10).

1.3 BIOCHEMISTRY OF COPPER

Copper is the third most abundant trace metal in the human body, after iron and zinc. Ever since the generation of an oxidising biosphere, copper has served as an essential catalytic and structural cofactor in a wide range of important enzyme-mediated biochemical processes in both aerobic and anaerobic organisms. The redox activity of copper, in the oxidation states I and II, has been exploited in catalysis by an array of metalloenzymes that play essential roles in energy metabolism, antioxidant protection, blood clotting, signal transduction, iron transport, pigmentation, cellular metabolism, oxygen transport, hormone formation and regulation and other biochemical functions (11). In proteins and enzymes, copper (I) tends to coordinate to cysteine- or methionine-rich domains, whereas copper (II) prefers to bind to aminoacids such as histidine, glutamate or aspartate, which contain harder donor groups (N, O) (12).

The importance of copper in many biological functions requires the maintenance of physiological copper levels through dietary intake. However, the ability of “free” copper ions to displace other metals from their enzymes and their involvement in the generation of reactive oxygen species (ROS) demands tight regulation of the copper homeostasis machinery (13, 14). The mechanisms that regulate the delicate balance between the essentiality and toxicity of copper have been increasingly investigated over the years but are not yet fully understood. Copper metabolism imbalance is a key pathological hallmark in a number of human diseases,

including Alzheimer's disease (AD), amyotrophic lateral sclerosis (ALS), Parkinson's disease (PD) and Wilson's (WD) and Menkes (MD) genetic disorders. Therefore, it is essential to summarise our current understanding of copper biochemistry in order to identify gaps in our knowledge that could provide critical information for detecting and treating diseases associated with copper dyshomeostasis.

Figure 1.1 illustrates the mechanisms underlying the intestinal absorption and peripheral distribution of copper ions. Dietary copper is initially taken up by intestinal epithelial cells (IECs) and incorporated into copper-dependent proteins and enzymes, or transported from the intestinal lumen into portal circulation. Copper can be then delivered to the liver for incorporation into ceruloplasmin or excreted through the kidneys. From the liver, copper can be mobilised into peripheral circulation to be transported to other organs or removed from the body through the bile. These biochemical pathways will be described in greater detail in the following sections.

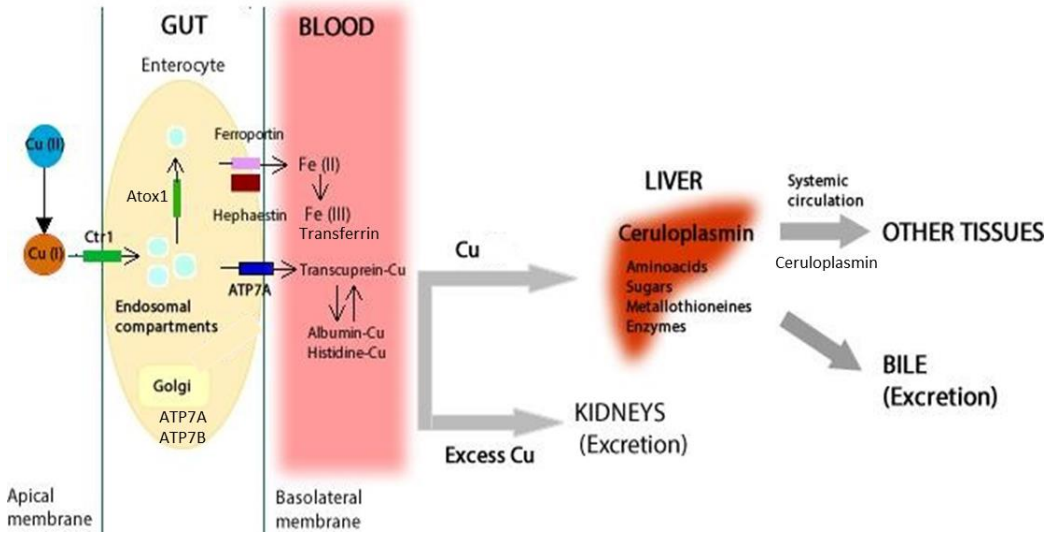

Figure 1.1: Physiological pathways followed by dietary copper. After reduction of dietary copper (II) by an unidentified metalloreductase, copper (I) is transported across the apical membrane of IECs by copper (I) transporter, Ctr1. Once inside the cell, copper (I) is pumped into the secretory compartments for incorporation into copper-dependent enzymes or mobilised across the basolateral membrane into portal circulation by copper (I) transporter ATP7A. Once in the bloodstream, excess copper is excreted in urine, whereas the rest of the absorbed copper is transported into the liver. In the liver, copper is mainly incorporated into the copper-carrier protein ceruloplasmin and mobilized to peripheral tissues. Excess hepatic copper is removed through the bile (10, 12).

1.3.1 Dietary copper and gastrointestinal absorption

Copper is acquired mainly through diet and absorbed by the small intestine after digestion. The average amount of copper in the adult human body is approximately 110 mg, most of which is found in the liver (10 mg), brain (8.8 mg), blood (6 mg), skeleton (46 mg) and skeletal muscle

(26 mg) (15). Dietary copper is mainly found in the cupric state and is tightly bound to specific proteins and, to a minor extent, small nutrient molecules. The efficiency of gastrointestinal absorption of copper in an adult human oscillates between 55 % and 75 % of the total amount ingested and is barely altered by aging (16).

The gastrointestinal absorption of dietary copper and its mobilisation across the intestinal lumen into portal circulation occur via different mechanisms. On one hand, the transfer of copper into the absorptive cells of the intestinal mucosa is a non-energy-dependent diffusive process. On the other hand, the transfer of the absorbed copper across the basolateral membrane of the IECs into the bloodstream occurs by saturable, energy-dependent mechanisms, which are influenced by dietary copper intake and cellular concentration of other transition metal ions (e.g. iron, zinc). The localisation and activity of copper transporters and chaperones varies depending on the amount of copper initially absorbed by the IECs (17).

1.3.2 Intracellular copper trafficking

In humans, dietary copper is transported into cells as copper (I) by the Ctr1 transmembrane transporter. This high-affinity copper transporter is generally located in the plasma membrane and intracellular vesicles of all cells. A second member of the Ctr family, low-affinity copper-binding protein Ctr2, has been identified both in yeast and humans but its role in copper homeostasis has not yet been defined (11, 18).

The Ctr1 transporter imports copper (I) ions across the apical membrane of intestinal cells into the cytosol in association with an unidentified metalloreductase, which is responsible for the reduction of dietary copper (II) salts. Once inside the cell, copper (I) ions are transferred from Ctr1 to different members of a family of soluble copper handling proteins called copper chaperones. The main function of these proteins is to deliver copper (I) ions to specific target proteins via direct protein-protein interactions and prevent the metal cargo from accumulating in the potentially toxic free ionic form (19).

There are four major copper trafficking pathways in mammalian cells (Figure 1.2). Firstly, the Ctr1 transporter can deliver copper (I) ions to the copper chaperone for superoxide dismutase-1

(CCS), which in turn shuttles the copper cargo to the free radical-scavenging enzyme Cu/Zn superoxide dismutase-1 (Cu/Zn SOD-1). Ctr1 can also transfer its copper payload to the Atox1 copper chaperone, which subsequently delivers copper (I) to the copper-transporting ATPases ATP7B (expressed mainly in the liver and brain) and ATP7A (expressed in all extrahepatic tissues) in the trans-Golgi network. ATP7A and ATP7B are responsible for both the incorporation of copper (I) ions into copper-dependent enzymes under normal physiological copper levels, and the efflux of copper from cells into the bloodstream (ATP7A) or bile (ATP7B) in the presence of elevated copper concentrations (20). Furthermore, copper (I) ions can also be delivered by copper chaperones into the mitochondrion for incorporation into the electron transport chain enzyme cytochrome c oxidase (CCO) and Cu/Zn SOD-1. The underlying molecular mechanism by which copper (I) is transferred from Ctr1 into the intermembrane space (IMS) of the mitochondrion has yet to be resolved. Once inside the IMS, copper (I) binds to the Cox17 metallochaperone and subsequently to the Sco1 and Cox11 proteins, which facilitate the formation of the copper centres within each structural subunit of CCO (21). Finally, copper (I) ions can be transported by Atox1 and other unknown copper chaperones to the nucleus (22). This pathway is particularly important to understand the cytotoxic mode of action of many copper-based anticancer drugs. However, very little is known about the identity of the nuclear metallochaperones and the regulatory mechanisms involved in the mobilisation of copper ions to, from and within the nucleus.

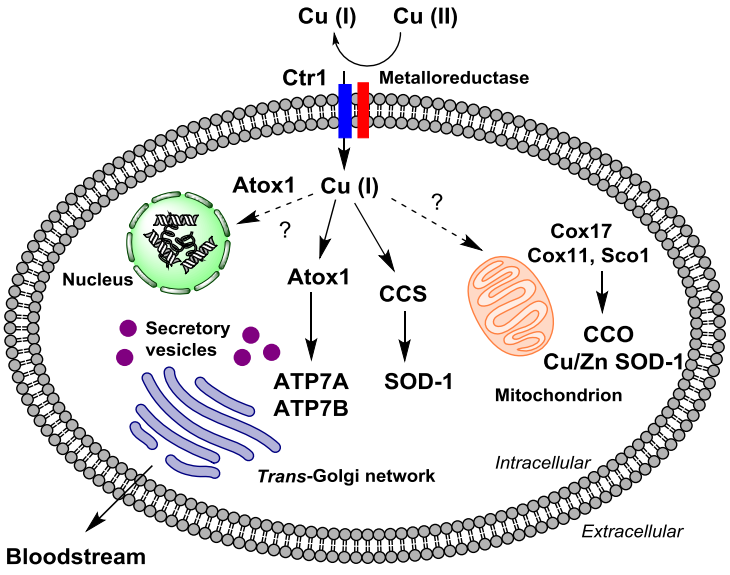

Figure 1.2: Intracellular copper trafficking pathways in mammalian cells.

In order to prevent intracellular oxidative stress, unbound copper (I) ions are typically sequestered by glutathione or metallothioneins (MTs), which serve as short-term intracellular storage sites for excess copper. Glutathione, which is present in high concentrations in the cytoplasm, has also been suggested to play a role in copper handling at the entry step since depletion of intracellular glutathione stores was found to substantially decrease the initial rate of copper uptake into cells (23).

1.3.2.1 Copper entry into cells

The Ctr1 high affinity copper transporter is the only system responsible for the entry of copper ions into eukaryotic cells that has been studied in depth. Electron crystallography studies have determined that human Ctr1 is a homotrimer with a cone-shaped pore along its central three-fold axis where the translocation of copper (I) ions occurs. Each subunit of the trimeric human Ctr1 transporter consists of three transmembrane domains (TM1, TM2 and TM3), tightly packed in a three-helix bundle. The methionine residues of the MxxxM motif on MT2 have been suggested to mediate directly the movement of copper (I) ions across the membrane by providing two neighbouring three-coordinate binding sites for the metal (24, 25).

The specificity of the Ctr1 transport system for copper (I) ions suggests the participation of a metalloreductase in the process responsible for the reduction of dietary copper (II). Lee *et al.* demonstrated that the uptake of ^{64}Cu in Hek293 mammalian cells increased by 2-fold in the presence of the reducing agent ascorbate (26). The mechanism by which the +I oxidation state of copper is maintained in the presence of oxygen before the metal ion is transferred to the Ctr1 transporter has not yet been deciphered. Copper (I) could be stabilised by a specific ligand after reduction and the complex could be then transported by Ctr1 across the cell membrane. Another mechanism to ensure the efficient delivery of copper (I) ions to the cytosol could involve the direct interaction of a cupric reductase with the Ctr1 transporter.

Despite showing a very high specificity for copper (I) ions, it has been shown that Ctr1 also mediates the uptake of the chemotherapy drug cisplatin. In a study by Ishida and co-workers, Ctr1-knockout mouse and yeast cell lines exhibited enhanced cisplatin resistance and reduced

cellular accumulation of the drug. Furthermore, copper was shown to compete with cisplatin for Ctr1 *in vitro*, resulting in reduced absorbed dose of the drug and enhanced cell survival (27).

The nature of the regulatory process that controls the entry of copper (I) ions into cells has not yet been resolved. The movement of cuprous ions across the plasma membrane could be driven by a concentration gradient, the need for maintenance of metalloenzymatic activity (CCO, Cu/Zn SOD-1) or higher copper (I)-binding affinities exhibited by specific intracellular components. Petris and co-workers reported a decrease in human Ctr1 surface levels and an increased rate of endocytosis of the transporter in HEK293 cells when these were exposed to elevated copper levels, indicating the existence of post-translational mechanisms able to modulate Ctr1-mediated copper (I) uptake (28).

Ctr1 is thought to be the major factor driving the transport of copper (I) ions across the plasma membrane into the cytoplasm but the existence of alternative copper import mechanisms has also been suggested. In a study by Nose *et al.*, copper content in IECs was found to be eight times greater in IEC-specific Ctr1-knockout mice compared to that in wildtype controls, evidencing the existence of alternative copper transport pathways activated under conditions of Ctr1 deficiency. However, the fact that significantly reduced copper-dependent enzymatic activity was also observed in the IECs of Ctr1-knockout mice seemed to indicate that Ctr1 not only mediates gastrointestinal copper absorption but also prevents the hyperaccumulation of copper in an unidentified biologically unavailable copper pool in IECs (29).

The divalent metal transporter 1 (DMT1), which plays a major role in intestinal iron uptake, is also thought to facilitate copper uptake into cells in specific organ systems (e.g. small intestine) and under certain circumstances (e.g. iron deficiency) (30, 31). For example, DMT1 was found to increase duodenal copper transport in iron-deficient rats and to enhance copper uptake into HEK-293 cells in the presence of an iron chelator (32). Lin *et al.* recently reported that Ctr1 levels decreased in umbilical vein endothelial cells in response to increasing concentrations of extracellular copper, whereas DMT1 expression increased, suggesting a compensatory role for DMT1 in the cellular uptake of copper under conditions of Ctr1 deficiency (33).

Another member of the Ctr protein family, Ctr2, has been found to mediate copper transport from vacuolar stores into the cytosol for subsequent delivery to copper chaperones in yeast cells (12). Rees and co-workers demonstrated that the S. cerevisiae Ctr2 protein functions in concert with metalloreductase Fre6 and facilitates vacuolar export of copper (I) ions into the cytosol (34). Van den Berghe *et al.* identified the mammalian Ctr2 homologue in the endosomal and lysosomal compartments of human cells and showed that the protein stimulated the delivery of copper (I) ions to the cytosol at relatively high copper concentrations. In addition to this role, it has been suggested that human Ctr2 might also facilitate copper import into cells but with a lower affinity compared to Ctr1 (35).

1.3.2.2 Copper delivery into the mitochondria

Copper is delivered to the mitochondrion primarily for incorporation into CCO, an essential metalloenzyme that acts as an electron acceptor in the last step of the respiratory electron transport chain. Cox1 and Cox2 are the two mitochondrial-encoded subunits of CCO that contain the copper centres that form the Cu_A and Cu_B enzymatic sites. Copper (I) ions are also transferred by CCS to the Cu/Zn SOD-1 enzyme, which is present in small amounts within the IMS in order to protect the mitochondrion from superoxide radicals generated from incomplete reduction of oxygen in the electron transport chain (36). However, only a small fraction of the total mitochondrial copper content is associated with these metalloenzymes. A stable and dynamic copper pool is located within the mitochondrial matrix, mostly in the form of a structurally undefined anionic complex. This mitochondrial copper fraction is responsive to changes in cytosolic copper levels and guarantees the availability of copper for the metallation of CCO and mitochondrial Cu/Zn SOD-1 (37).

The mechanism by which Ctr1-imported copper (I) is transferred from the cytosol to the IMS of the mitochondrion is not yet clear. Metallochaperone Cox17 is present both in the cytosol and mitochondrial IMS and therefore was initially suggested as a potential candidate for shuttling copper (I) ions into the IMS. Nevertheless, Wang and co-workers recently revealed that Cox17 deficiency in cultured cells significantly increased mitochondrial copper concentration, thus precluding this possibility. Interestingly, it was found that CCS-deficient cells showed a significant decrease in copper concentration in the mitochondria, suggesting a potential role for

this chaperone in the transport of copper (I) ions from the cytosol into the mitochondria. The authors additionally reported that although Cox17 appeared not to be responsible for the transfer of copper to the mitochondrion, Cox17 deficiency significantly reduced CCO activity in cultured cells, evidencing the essential role that this transporter plays in the metallation of CCO (38). Cox17 has been shown to act as a specific copper donor to accessory proteins Sco1 and Cox11 for the assembly of the Cu_A and Cu_B sites of yeast CCO (39).

1.3.2.3 Copper transfer into the trans-Golgi network

A portion of cytosolic copper (I) is also guided towards the trans-Golgi network, where the metallation of several copper-dependent proteins and enzymes occurs. These metalloproteins are subsequently directed towards other intracellular organelles for storage or cleared out from cells.

The Atx1-like family of copper chaperones plays an essential role in the delivery of Ctr1-imported copper to the secretory pathway in eukaryotic organisms. The human Atx1 homologue, Atox1, is a 68-aminoacid polypeptide that contains a conserved cysteine CXXC motif for metal binding in the N-terminus. Two Atox-1 molecules are required to coordinate a single copper (I) ion, resulting in a distorted tetrahedral metal-protein complex.

Copper (I) ions transported by Atox1 are delivered to the metal-binding domains of the N-terminus of copper-transporting ATPases ATP7A and ATP7B. In eukaryotic cells, these proteins are responsible for the delivery of copper to copper-dependent enzymes, as well as for the modulation of cellular copper levels. In elevated copper conditions, ATP7A has been found to traffic from the trans-Golgi network to the plasma membrane to mediate copper efflux (40). ATP7B has been reported to relocate to vesicular compartments under elevated copper levels and might therefore facilitate vesicular sequestration of excess intracellular copper (41).

Human copper (I) ATPases ATP7A (expressed in all extrahepatic tissues) and ATP7B (expressed mainly in the liver and brain) consist of eight transmembrane helices, a nucleotide-binding domain (N-domain), a phosphorylation domain (P-domain) and an actuator domain (A-domain), that functions to couple ATP hydrolysis with metal ion transport. The N-terminus of

human ATP7A and ATP7B is composed of six metal-binding domains, which enclose conserved cysteine CXXC sequences, to which copper (I) ions are coordinated (18). Once copper is bound to the copper-transporting ATPases, the metal can be transferred into the secretory compartment for subsequent incorporation into copper-binding proteins (e.g.lysyl oxidase, tyrosinase), transported across the basolateral membrane into portal circulation (ATP7A) or excreted into the bile (ATP7B) under elevated copper levels in the case of hepatocytes.

The MT family of proteins can also be found in the membrane of the Golgi apparatus. These low-molecular-weight, cysteine-rich proteins exhibit great heavy metal binding capacity and play an essential role in copper homeostasis by sequestering and storing copper (I) ions, especially under conditions of high intracellular copper levels. The expression of MTs is dependent on stress conditions such as heavy metal overload, oxidative stress or exposure to ionising radiation. Four MT protein types (MT-1, MT-2, MT-3 and MT-4) predominate in vertebrates, acting mainly as short-term stores for excess copper. However, MTs have not been shown to be capable of transporting excess copper out of the cell (42).

1.3.2.4 Copper incorporation into Cu/Zn superoxide dismutase-1

The main function of Cu/Zn SOD-1 is to protect the cell against ROS production, which can cause irreversible damage to DNA, lipids and proteins. In eukaryotic organisms, the transport protein CCS is responsible for the incorporation of copper (I) into Cu/Zn SOD-1. The CCS protein is mainly composed of an N-terminal Atox1-like domain containing a metal-binding site (Domain I), a middle domain structurally similar to Cu/Zn SOD-1 (Domain II) that facilitates target recognition, and a C-terminus (Domain III) that has not been structurally characterised yet (43). The Cu/Zn SOD-1 enzyme possesses a highly conserved intramolecular disulfide bond in its structure which is critical for the regulation of enzymatic activity and prevention of protein misfolding and aggregation. Furukawa *et al.* reported that the formation of this disulfide bond in yeast Cu/Zn SOD-1 was an oxygen-dependent process, catalysed by the copper-bound form of CCS (44). After the formation of the disulfide bond, it has been suggested that the Cu-CCS complex forms a heterodimeric complex with the zinc-metallated form of Cu/Zn SOD-1 via the Domain III of the CCS protein, from which copper (I) ions are shuttled from Domain I of CCS to the Cu/Zn SOD-1 active site (43).

CCS expression has been found to be strongly regulated by intracellular copper levels. Bertinato and co-workers revealed an increase in CCS levels under conditions of copper deficiency in different rodent and human cell lines, as well as a slower rate of protease-mediated degradation of CCS in copper-deficient cells compared to cells cultured in copper-rich medium (45).

The CCS transporter is thought to be predominantly responsible for the incorporation of copper into Cu/Zn SOD-1. However, a study performed on tissues from CCS-knockout mice reported residual levels of Cu/Zn SOD-1 activity, thus revealing the existence of a CCS-independent copper metallation pathway for Cu/Zn SOD-1. The identity of the metallochaperones that participate in this CCS-independent mechanism has not yet been established. Carroll *et al.* demonstrated the involvement of the reduced form of glutathione in the CCS-independent activation of human Cu/Zn SOD-1 (46). An unidentified CCS-independent metallation pathway could also be responsible for the incorporation of copper into the extracellular superoxide dismutase (EC-SOD) enzyme, which plays an essential role in the regulation of ROS levels in the extracellular space. It has been demonstrated that copper metallation of EC-SOD requires the participation of the Atox1/ATP7A pair, which is probably responsible for the transport of copper (I) ions across the trans-Golgi network. However, the identity of the chaperone that directly transfers copper into the EC-SOD enzyme remains unknown (47).

1.3.3 Copper transport into circulation

Endogenous copper metabolism is thought to involve two different phases of blood copper transport: a first wave, in which, following gastrointestinal absorption, copper binds to serum proteins (e.g. albumin, α_2-macroglobulin) and aminoacids (e.g. histidine, glutamine, threonine) and is transported through the bloodstream into the liver and kidneys; and a second phase, in which, after being incorporated into the multi-copper ferroxidase ceruloplasmin in the liver, copper re-emerges in the blood plasma to be transported into other tissues (15). A similar fate to that of dietary copper has been observed for injected radiocopper. A study conducted by Weiss *et al.* in adult rats injected with copper-67 chloride ($^{67}CuCl_2$) showed immediate localisation of ionic radiocopper in the plasma protein fractions (albumin and α_2-macroglobulin) after injection, followed by an increase in liver and kidney radioactivity at approximately 6 hours

and finally the incorporation of ^{67}Cu into ceruloplasmin at 18 hours post-injection (48). A different distribution pattern for injected radiocopper was observed in lactating rats, in which almost 60 % of a ^{64}Cu/^{67}Cu mixture was taken up by the mammary gland and incorporated into milk ceruloplasmin and the exchangeable milk copper pool (49).

The mechanism by which absorbed copper is transferred into hepatocytes is not yet fully understood. After its entry into portal circulation, copper is incorporated into an exchangeable copper pool, in which the metal is predominantly bound to plasma proteins albumin (68 kDa) and α_2-macroglobulin (270 kDa). This labile copper pool is in equilibrium with tissue copper and is characterised by rapid transfer of copper ions between serum proteins and copper delivery from proteins to cells via low molecular-weight intermediates (15). Little is known about how copper is transferred from albumin and α_2-macroglobulin into cells. Moriya and co-workers examined the uptake of albumin- and α_2-macroglobulin-bound ^{64}Cu in cultured hepatic and mammary epithelial cells and observed that uptake kinetics were different depending on the cell type. For example, the delivery of α_2-macroglobulin-bound ^{64}Cu into hepatocytes was found to involve the Ctr1 transporter, whereas a different transport system was shown to mediate the uptake of ^{64}Cu from α_2-macroglobulin into mammary epithelial cells (50).

Albumin is the most abundant protein present in the blood plasma and interstitial fluids of mammals and participates in the transport of a wide range of substances, from metal ions to fatty acids. This plasma protein has a high affinity binding site for copper (II) at the N-terminus, as well as a low affinity multi-metal binding site (51). Most of plasma copper is readily exchanged between albumin and α_2-macroglobulin, leaving a very small fraction bound to aminoacids and small peptides. This implies that copper uptake into the liver might be mediated by one or both of these proteins. Nevertheless, early research suggested that albumin might not play a central role in the delivery of copper from blood plasma to hepatocytes. A study by McArdle and co-workers on cultured rodent and human fibroblasts and hepatocytes treated with ^{64}Cu showed inhibitory effects of albumin on the cellular uptake of radiocopper in the absence and presence of histidine (52). Vargas *et al.* additionally reported that tissue uptake of ^{67}Cu was unaffected in analbuminemic rats (53). Albumin could therefore participate in the regulation of copper toxicity in blood plasma by binding copper ions and minimising the amount of ionic

copper in the “free” form.

Plasma α_2-macroglobulin is another protein with high affinity for newly absorbed copper. Despite being present in a smaller concentration, this protein exhibits a greater affinity for copper (II) than albumin and histidine-rich peptides (54). Copper ions bound to α_2-macroglobulin are delivered into hepatocytes through a number of small carriers and plasma protein receptors. However, the identity of these molecules has not yet been determined.

1.3.4 In the liver

The second phase of distribution of absorbed copper starts with the entry of the metal ion into the liver, where the multi-copper ferroxidase ceruloplasmin is primarily synthesised. After the incorporation of copper into ceruloplasmin, this enzyme is released into the bloodstream to deliver copper ions to extrahepatic tissues.

As previously mentioned the mechanism by which copper is delivered from blood plasma proteins into hepatocytes has not yet been deciphered. Ctr1 is thought to be directly involved in the transfer of copper from α_2-macroglobulin (but not from other blood proteins) into hepatocytes. Kim and co-workers evaluated the contribution of Ctr1 to hepatic copper transport using a transgenic mouse model in which Ctr1 was deleted specifically in the liver. Ctr1-deficient mice exhibited significant growth deficits and reduced hepatic copper concentration. Although the activity of copper-dependent enzymes was substantially reduced in the liver, copper levels in extrahepatic organs were found to be unaltered, indicating the existence of compensatory mechanisms that facilitate copper uptake and retention in the liver under conditions of Ctr1 deficiency (55).

The distribution of copper in hepatocytes resembles that observed in IECs. Once inside the cell, copper binds to various metallochaperones that deliver the metal to specific target molecules, such as Cu/Zn SOD-1 or CCO. The intracellular concentration of ionic copper is controlled by MTs and glutathione, which function as short-term copper storage sites under conditions of metal overload.

The ATP7B transporter plays a pivotal role in hepatic copper metabolism. A functional deficiency of this ATPase in hepatocytes is responsible for the accumulation of copper in the liver, which may lead to the development of WD, cirrhosis or other pathological conditions. Both ATP7B and Atox1 are components of the transport system that exports copper into the bile under conditions of copper overload. The COMMD1 protein is also thought to be involved in this mechanism by regulating the activity of ATP7B and its trafficking from the trans-Golgi network to vesicular compartments in the cytosol from which copper is thought to be excreted out of the cell (56).

ATP7B also facilitates copper incorporation into ceruloplasmin, which is predominantly synthesised in the liver but is also expressed in other tissues (e.g. mammary glands, lungs, brain, spleen). This enzyme was first discovered and characterised as a copper-containing protein by Holmberg and Laurell, who reported the isolation of a 151-kDa blue protein from pig serum containing 6-8 atoms of copper per molecule (57). Further research revealed that the concentration of ceruloplasmin in human blood plasma and hepatocytes oscillates in a number of diseases and hormonal states. Ceruloplasmin deficiency in serum has been observed in patients suffering from WD as a consequence of impaired ATP7B-mediated copper trafficking. Furthermore, specific mutations in the ceruloplasmin gene are the cause of an autosomal recessive disorder known as aceruloplasminemia. This genetic condition exemplifies the importance of the ferroxidase activity of ceruloplasmin, which is essential to enable the incorporation of iron into transferrin. The absence of ceruloplasmin in the bloodstream leads to the accumulation of iron in organs such as the liver, pancreas, spleen or brain (58).

Ceruloplasmin utilises the redox chemistry of copper ions to couple substrate oxidation with the complete reduction of dioxygen to water. Human ceruloplasmin has a single polypeptide chain structure composed of six compact domains separated by large loop insertions and six tightly bound copper atoms. Three copper atoms (type II and type III centres) in the form of a trinuclear cluster are coordinated at the interface between the first and the sixth domain of ceruloplasmin and constitute the oxygen-binding site of the protein. Additionally, the enzyme contains three type I copper centres located at the intra-domain sites along the polypeptide chain which confer the blue colour to the protein through ligand-to-metal charge transfer interactions (59).

A role for ceruloplasmin in copper transport from the liver to other organs was first supported by the discovery of ceruloplasmin plasma membrane receptors in chick aortic and heart tissue (60). Ceruloplasmin accounts for 95 % of blood plasma copper and has been shown to deliver copper to various cell types (61, 62) However, copper transport to extrahepatic tissues is not an exclusive function of this protein. Plasma copper can also be taken up into cells from non-ceruloplasmin sources, as evidenced by the nearly-unchanged copper levels in extrahepatic organs observed in patients suffering from aceruloplasminemia. Research conducted by Percival *et al.* on the uptake of ^{67}Cu-labeled ceruloplasmin by cultured erythroleukemic K-562 cells revealed the stimulatory effect of ascorbate on the cellular uptake of copper from ceruloplasmin. In this study, it was also observed that ^{67}Cu dissociated from ceruloplasmin before its entry into the cells since the protein fragment was not detected intracellularly. These results suggest that ceruloplasmin might bind to specific protein receptors in the plasma membrane which might in turn deliver the copper cargo into cells (63).

Copper delivery from the liver to other tissues is only one of the many biological functions of ceruloplasmin. This protein also exhibits ferroxidase activity and plays an essential role in the maintenance of iron homeostasis. Osaki *et al.* first showed that ceruloplasmin stimulated the oxidation rate of iron (II), allowing its incorporation into blood plasma transferrin for subsequent delivery to extrahepatic organs (64). The importance of ceruloplasmin in iron metabolism was also demonstrated by Ragan and co-workers, who reported the effects of injected ceruloplasmin on the levels of blood plasma iron in copper-deficient swine. In this study, the intravenous administration of ceruloplasmin resulted in a marked increase in plasma iron concentration in these animals, suggesting a role for this protein in the transfer of iron from hepatocytes to blood plasma (65). The oxidation of ferrous ions and their subsequent transfer into transferrin is thought to occur on the surface of ceruloplasmin, which is negatively charged in order to attract cationic species. The identity of the iron chaperone proteins that deliver ferrous ions to ceruloplasmin remains unknown (66). It has been suggested that iron (II) initially displaces a copper atom from a labile metal-binding site on the surface of the protein. After oxidation, ferric ions bind to an adjoining metal-binding site of ceruloplasmin for its transfer into transferrin.

In addition to the copper-binding sites on the surface of ceruloplasmin associated with its ferroxidase activity, this enzyme has another catalytic site involving a cysteine residue (Cys699) that displays copper-independent glutathione peroxidase activity. Through this site, ceruloplasmin catalyses the reduction of lipid hydroperoxides into alcohols and hydrogen peroxide into water in an effort to protect the cell against oxidative damage. Furthermore, ceruloplasmin is also capable of oxidising nitric oxide and various aromatic amines and biogenic amines, as well as regulating their concentration in blood plasma (59).

1.3.5 Copper-dependent enzymes

Copper is a key functional component of many enzymes involved in fundamental biological processes, such as energy metabolism or ROS scavenging. Some of these cuproenzymes are found in all types of cells (Cu/Zn SOD-1, CCO), whereas others are characteristic of specific cell types (dopamine β-hydroxylase). The structure and function of the most important copper-dependent enzymes will be examined in detail in the following sections.

1.3.5.1 Cu/Zn superoxide dismutase-1

In 1969, McCord *et al.* first isolated Cu/Zn SOD-1 from bovine erythrocytes and reported its inhibiting effect on superoxide-mediated cellular toxicity (67). Further research confirmed that Cu/Zn SOD-1 catalysed the dismutation of superoxide radicals into oxygen and hydrogen peroxide, which, in turn, was detoxified by the iron-dependent catalase enzyme. Superoxide radicals are generated within the cell as a result of the incomplete reduction of oxygen into water during aerobic respiration. Uncontrolled generation of ROS can cause irreversible oxidative damage to lipids, proteins and DNA, as well as the disruption of several cellular signalling mechanisms. Consequently, the superoxide radical scavenging activity of Cu/Zn SOD-1 is vital for the protection of most cellular components in aerobic organisms.

In eukaryotic cells, Cu/Zn SOD-1 is a dimeric protein whose active site consists of one catalytic copper ion and one structural zinc atom per subunit coordinated by the deprotonated imidazolate ring of a histidine residue. The remaining coordination sites for copper are occupied by three histidine residues and a water molecule, whereas zinc is coordinated to two histidines and one aspartate residue. The characterisation of bovine Cu/Zn SOD-1 purified from

erythrocytes revealed that the active copper sites of the enzyme were buried at the bottom of two narrow channels within the protein respectively. The positively charged side-chain of an arginine residue in the lining of the channel generates an electrostatic gradient that is thought to facilitate the diffusion of the superoxide anions through the channel (68, 69). Another structural characteristic of mature Cu/Zn SOD-1 is the formation of a kinetically stable disulfide bond between cysteine residues Cys-57 and Cys-146 after the incorporation of copper into the zinc-metallated form of the enzyme. This conserved intramolecular disulfide bond is essential for the stabilisation of the structure of Cu/Zn SOD-1 but is also thought to have functional significance (70).

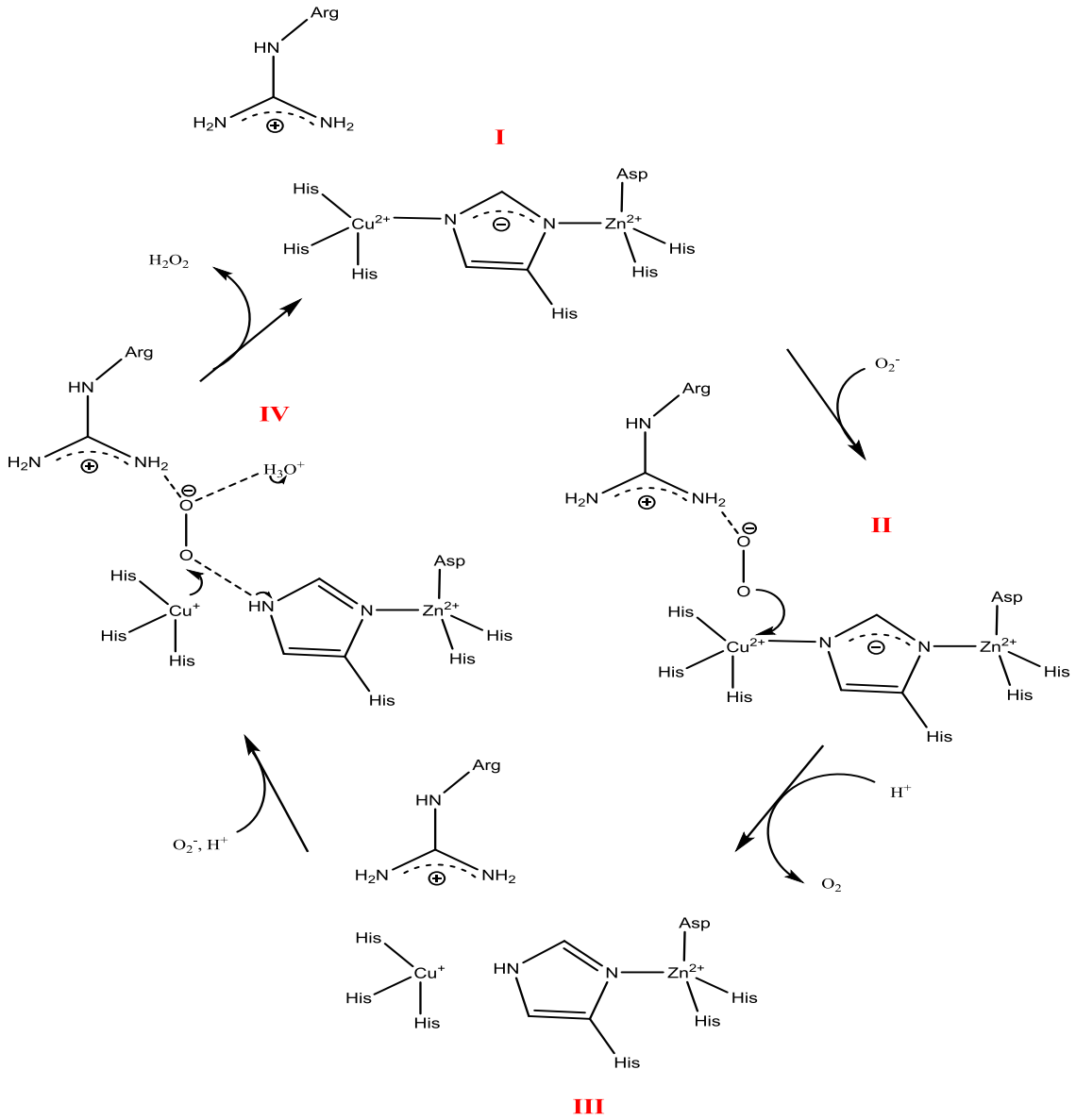

Figure 1.3: Proposed mechanism of action for Cu/Zn SOD-1 (71).

The proposed mechanism of action for Cu/Zn SOD-1 relies mainly on the redox properties of

the copper active site (Figure 1.3). The superoxide radicals are initially directed through the narrow channels of the enzyme by the guanidinium groups of the channel-lining arginine residues towards the catalytic copper (II) centre, where the radical is oxidised to molecular oxygen. The resulting copper (I) centre dissociates from the protonated imidazolate ring but remains bound to the protein. In the second part of the mechanism, the copper (I) complex is reoxidised to copper (II) by a second superoxide radical, resulting in the reassembly of the enzymatic structure and the production of hydrogen peroxide (71).

The zinc centre in Cu/Zn SOD-1 plays essentially a structural role but its absence severely affects the functionality of the enzyme. Roberts and co-workers demonstrated that the loss of zinc in Cu/Zn SOD-1 causes a series of structural changes to the enzyme that promote protein aggregation and allow better access to the catalytic copper (II) centre to intracellular reductants (e.g. glutathione, ascorbate), causing an increase in the production of free radicals.

Cu/Zn SOD-1 malfunction is associated with ineffective management of oxidative stress, which is one of the main pathological hallmarks in neurodegenerative disorders. More than 130 mutations to the Cu/Zn SOD-1 gene resulting in impaired or decreased antioxidant function of the enzyme have been linked to the pathogenesis of ALS (72). Moreover, Murakami *et al.* reported significantly increased oxidative stress-mediated Aβ peptide oligomerisation and cognitive deficits in a Cu/Zn SOD-1-deficient mouse model of AD when compared to control AD mice. In this study it was also revealed that cytoplasmic Cu/Zn SOD-1 levels were significantly reduced in brain tissue samples from patients suffering from AD compared to healthy individuals, which may indicate a role for cytosolic Cu/Zn SOD-1 in the development and course of this disorder (73).

1.3.5.2 Cytochrome c oxidase

CCO is a transmembrane cuproenzyme found in the mitochondria of eukaryotic cells. This enzyme plays an essential role in the last stage of the respiratory electron transport chain by catalysing the safe reduction of molecular oxygen to water using electrons delivered by the cytochrome c electron donor. This electron transfer process involves the translocation of four protons across the mitochondrial membrane using a proton pumping system to form a water

molecule. The exact mechanism underlying this proton pumping process driven by electron transfer still remains to be elucidated (74).

CCO is a metalloenzyme of great structural complexity, composed of thirteen different protein subunits. The metal content of CCO includes three copper atoms, two iron complexes, one magnesium ion and one zinc ion per monomer. A mixed-valence copper dimer (Cu_A), a mononuclear copper (II) centre (Cu_B) coordinated to a redox-active tyrosine residue, and two heme-iron complexes (a/a_3) consitute the active site of the enzyme. Electrons are initially transferred from the cytochrome c protein to Cu_A and subsequently delivered to the heme-iron a centre, where they are used to reduce the heme-iron a_3 complex and Cu_B. Molecular oxygen is then coordinated to the iron (II) and Cu (I) centres, which constitute the oxygen reduction site of the enzyme, leading to the formation of a [Fe^{3+}-(OOH-) Cu^{+}] complex. The cleavage of the O-O bond through electron transfer from the redox-active tyrosine residue induces the formation of [Fe^{4+}=O] and [Cu^{2+} (H_2O)] complexes and the generation of a tyrosyl radical. Finally, four reduction steps (tyrosine radical to tyrosine, Fe (IV) to Fe (III), Fe (III) to Fe(II) and Cu (II) to Cu(I)) take place coupled to the pumping of four protons across the mitochondrial membrane, yielding two water molecules (71, 75). CCO is located on the inner mitochondrial membrane and contains two aqueous-exposed surfaces facing the mitochondrial matrix and the IMS, respectively. The oxygen reduction site of the enzyme is coordinated to the IMS hydrophilic surface by a number of hydrogen bonds through which protons are delivered for the formation of water molecules (76).

Research conducted by Pan *et al.* on isolated bovine CCO revealed that zinc plays mainly a structural role since removal of the metal by mercuric chloride treatment did not alter the steady-state activity of CCO (77). Further research is required in order to determine the role of the magnesium centre in the mechanism of action of CCO.

The vital role of CCO in the last part of aerobic respiration makes this metalloenzyme indispensable for cell survival. A rare autosomal recessive disorder known as CCO deficiency characterised by degeneration of the brain stem and basal ganglia and lactic acidosis has been identified (78). Reduced CCO activity has been observed in isolated mitochondria from platelets

of AD patients when compared to healthy individuals, and this decrease has been correlated with reduced ATP levels and enhanced ROS concentration (79).

1.3.5.3 Lysyl oxidase

Cuproenzyme lysyl oxidase (LOX) plays an essential role in the biosynthesis of collagen and elastin, which are the main structural components of the extracellular matrix of connective tissue in vertebrate organisms. The main biological function of LOX is the catalysis of the post-translational oxidative deamination of peptidyl lysine to generate peptidyl aminoadipic semialdehyde, ammonia and hydrogen peroxide (Figure 1.4) (17).

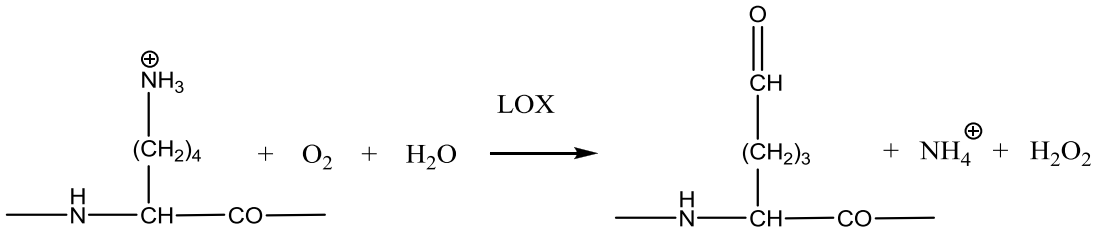

Figure 1.4: LOX-catalysed oxidative deamination of lysine ε-amino groups.

The aldehyde group of the resulting product can subsequently condense with the amino group of a neighbouring lysine residue or react with another peptidyl aminoadipic semialdehyde to form essential cross-linkages for the stabilisation of collagen fibres and the insolubilisation of elastin. The deamination of lysine ε-amino groups can also be catalysed by other amine oxidases but LOX-mediated catalysis is specific for lysine side-chains in collagen and elastin substrates. A number of studies have reported the participation of LOX in other cellular processes, such as cell signalling, proliferation or migration.

Pro-protein LOX is secreted in the extracellular space and activated upon proteolytic cleavage. The catalytic cofactors of this cuproenzyme are a copper (II) ion and a lysine tyrosylquinone prosthetic group. LOX has been principally detected in the extracellular space of different tissue cells (e.g. epithelial, cardiac, hepatic) but it has also been localised inside the nuclei of vascular smooth muscle cells and fibroblasts (80).

LOX expression has been reported to be regulated by hypoxia-inducible factors in various cancer cell lines. Research conducted by Erler *et al.* with patients affected by breast and head and neck cancer showed a significant correlation between the level of LOX expression in cancer

cells and the degree of tumour hypoxia. In the same study, it was also demonstrated that enhanced levels of LOX expression in cancer cells were associated with decreased distant metastasis-free survival and poor prognosis. Furthermore, Erler and co-workers also demonstrated that treatment of breast tumour-bearing mice with LOX inhibitor β-aminopropionitrile reduced significantly the formation of metastases (81). Nonetheless, other studies have linked LOX expression to tumour suppression. Kaneda *et al.* revealed the presence of silenced forms of LOX genes in gastric cancer cells that promoted an increase in tumour growth *in vivo* when compared with tumour-bearing mice expressing activated LOX genes (82). The role of LOX in tumorigenesis and its potential as a molecular target for cancer therapy remain to be further investigated.

1.3.5.4 Dopamine β-hydroxylase

Dopamine β-hydroxylase (DβH) is one of the most important cuproenzymes in the human brain, although little is known about its mechanism of action. This copper-dependent enzyme catalyses the monooxygenation of neurotransmitter dopamine to noradrenaline, which is the precursor of adrenaline (Figure 1.5). The synthesis of noradrenaline requires also the participation of molecular oxygen as electron acceptor and ascorbic acid as an electron donor. Secondary products of this reaction are a water molecule and dehydroascorbic acid.

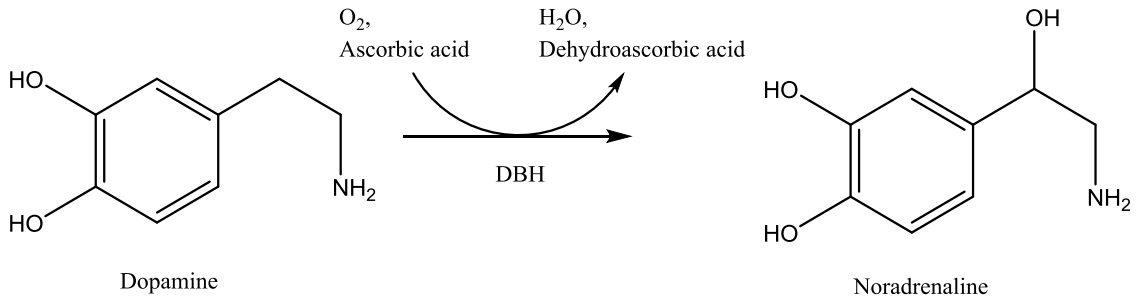

Figure 1.5: Synthesis of noradrenaline catalysed by DβH (83).

The structure of DβH consists mainly of four subunits stabilised by intermolecular disulfide linkages into two dimers. Each protein subunit contains two copper atoms, giving a total number of eight copper atoms per enzyme molecule. The enzyme is mainly found in the chromaffin granules of the adrenal medulla and the synaptic vesicles of noradrenergic neurons (84).

Noradrenaline depletion in the CNS is the main pathological feature of a rare genetic disorder known as DβH deficiency. Although DβH deficiency does not cause significant cognitive impairment, DβH-deficient patients show acute hypotension, noradrenergic failure and drooping or falling of the eyelids (85). Reduced DβH activity has also been detected in patients suffering from AD (86).

1.3.5.5 Tyrosinase

Tyrosinase is a multi-copper oxygenase that plays an essential role in the biosynthesis of the melanin pigment. Tyrosinase catalyses the hydroxylation of monophenols into o-diphenols and, subsequently the conversion of o-diphenols into o-quinones, using in both cases molecular oxygen as the electron acceptor. The catalytic domain of tyrosinase consists of two copper centres, each bound to three histidine residues. The remaining coordination sites for both copper atoms are occupied during the catalytic process by the molecular oxygen molecule and the phenolic substrate. The structure of the metalloenzyme is stabilised by a number of disulfide bonds. Mutant forms of human tyrosinase have been linked to genetic disorders, such as oculocutaneous albinism (87).

1.4 RADIOCHEMISTRY OF COPPER

1.4.1 Copper radionuclides: physical properties and production methods

The wide range of half-lives and decay modes of copper radioisotopes along with their accessible coordination chemistry offer many opportunities for the development of radiopharmaceuticals for a variety of diagnostic and therapeutic applications. Table 1.1 lists the available copper radionuclides and their physical characteristics.

Table 1.1: Physical properties of copper radioisotopes used for diagnostic imaging and therapy (10, 88, 89)

Radioisotope	Half-life	Decay mode[a]	Diagnosis *emission, energy[b], abundance*	Therapy *emission, energy[b], abundance, range[c]*	Source
^{60}Cu	23.7 min	β^+, EC	PET β^+, 0.87 MeV, 93 %	—	cyclotron
^{61}Cu	3.3 h	β^+, EC	PET β^+, 0.53 MeV, 62 %	—	cyclotron
^{62}Cu	9.8 min	β^+, EC	PET β^+, 1.32 MeV, 98 %	—	generator/ cyclotron
^{64}Cu	12.7 h	β^+, β^-, EC, internal conversion	PET β^+, 0.28 MeV, 18 %	Auger electrons, 6.84 keV, 5 µm (EC) β^-, 0.19 MeV, 39 %, 0.95 mm	reactor/ cyclotron
^{67}Cu	2.6 d	β^-	SPECT γ, 0.093 MeV, 52 %	β^-, 0.12 MeV, 100 %, 0.61 mm	reactor/ cyclotron

[a] β^+= Positron emission, EC = Electron capture, β^- = Beta decay; [b] Average energy of radiation; [c] Average range of radiation in tissue; PET = positron emission tomography; SPECT = single-photon emission computed tomography

Each of these copper radionuclides displays a unique set of physical properties (half-life, decay mode, positron range) that make it more or less suitable for a given nuclear medicine application. Long-lived ^{67}Cu ($t_{1/2}$ = 2.6 d) and ^{64}Cu ($t_{1/2}$ = 12.7 h) are attractive candidates for the radiolabelling of biomolecules with slow targeting kinetics (e.g. peptides, proteins, antibodies) for both diagnostic and therapeutic purposes, whereas the shorter half-lives of ^{60}Cu ($t_{1/2}$= 23.7 min) and ^{62}Cu ($t_{1/2}$= 9.8 min) make them more suitable as labels of smaller tracer molecules (90). The rapid physical decay of ^{60}Cu and ^{62}Cu considerably restricts the duration of the radiosynthesis process but also allows the possibility of performing repeated scans on the same individual and even dual tracer imaging. The 3.3-h half-life of ^{61}Cu provides the flexibility to image both small tracers and moderately large biological molecules, as well as native copper transport processes (91, 92).

Although physical half-life remains a major limiting factor, other decay characteristics also have an impact on the imaging performance of copper radionuclides and their use in medical imaging applications. The kinetic energy of positron particles inherently leads to a blurring in PET spatial

resolution that becomes more severe for higher-energy positron emitters. PET imaging with ^{60}Cu and ^{62}Cu radiotracers will consequently result in a poorer spatial resolution when compared to ^{64}Cu radiopharmaceuticals, which provide a positron range effect similar to that of ^{18}F. Conversely, ^{64}Cu has the lowest positron yield (18 %) among all copper radioisotopes, which contributes to a loss in image contrast due to poorer counting. However, the long half-life of this radionuclide allows for extended imaging time windows to compensate for its lower counting statistics. Short-lived radioisotopes ^{60}Cu and ^{62}Cu have positron decay fractions close to unity (0.93 and 0.98, respectively) and therefore require lower activity doses and shorter scan times than ^{64}Cu tracer molecules. From all copper PET radionuclides, ^{61}Cu achieves the best balance between spatial resolution and sensitivity, with moderate positron energy and a 62 % positron yield. The radiation burden associated with this radioisotope is comparable with that of the widely used PET radiotracer ^{18}F-fluorodeoxyglucose (^{18}F-FDG), but is considerably higher when compared to the effective dose resulting from PET imaging with shorter-lived ^{60}Cu and ^{62}Cu. ^{64}Cu provides the highest radiation dose from all copper PET radionuclides, mainly due to its prolonged half-life and beta particle emissions (93).

Of all copper radionuclides, ^{64}Cu is considered the most versatile since it combines three different types of physical decay – positron emission (18 %), beta decay (39 %) and electron capture (43 %) – and can therefore be used both for diagnostic imaging (positron emission) and targeted radiotherapy (beta particle and Auger electron emission). This singular characteristic offers the possibility of using PET imaging in the assessment of radiation dosimetry when planning targeted radionuclide therapies with ^{64}Cu radiopharmaceuticals. The decay scheme of the longest-lived copper radioisotope ^{67}Cu (beta particle and gamma emission) also allows pre-therapy diagnostic imaging (by SPECT), and was initially regarded as well suited for radioimmunotherapy applications (10). Nevertheless, despite the large number of cyclotron- and reactor-based production methods reported (94), the development and clinical use of ^{67}Cu radiopharmaceuticals is still hindered by unreliable supply, low production yields and a wide variety of radionuclide impurities (e.g. ^{62}Zn, ^{67}Ga, ^{65}Zn, ^{55}Co, ^{58}Co, ^{57}Ni) (95).

Despite the long-lasting interest of the nuclear medicine community in the development of copper radiopharmaceuticals, the clinical translation of these agents is often hampered by

limited radionuclide supply, which still relies mostly on academic institutions. The availability of the majority of copper radionuclides (^{60}Cu, ^{61}Cu, ^{64}Cu and ^{67}Cu) is principally restricted by access to cyclotron or reactor facilities and overall production cost. In this scenario, the ^{62}Zn/^{62}Cu generator has the potential to provide widespread and cost-effective clinical access to the short-lived ^{62}Cu radionuclide, thus enabling the clinical evaluation of a range of small molecule radiotracers with relatively low radiation doses to patients (96-98). The 9.3-h half-life of the ^{62}Zn parent isotope allows delivery of the generator system to clinical sites without an in-house cyclotron and the possibility of performing multiple elutions per day. Nonetheless, the rapid physical decay of ^{62}Cu makes cyclotron/reactor-based production of longer-lived copper radioisotopes a necessity.

Non-carrier added ^{60}Cu, ^{61}Cu, ^{62}Cu and ^{64}Cu can be produced in high yield and specific activity via proton (*p,n*) or deuteron (*d,2n*) bombardment of nickel-enriched solid targets (^{60}Ni, ^{61}Ni, ^{62}Ni and ^{64}Ni, respectively) (91, 99-101). In the case of ^{61}Cu and ^{64}Cu, the elevated cost of the parent radionuclide has led to the investigation of different cyclotron-based production routes, such as proton or deuteron irradiation of zinc solid targets (e.g. ^{64}Zn, ^{66}Zn, ^{68}Zn) (102-105). High specific activity ^{64}Cu can alternatively be produced by the ^{64}Zn(*n,p*)^{64}Cu reaction in a nuclear reactor. Although good yields are reported using this production method, the limited availability of nuclear reactors along with the co-production of high amounts of ^{65}Zn restrict large-scale production of ^{64}Cu via this route (106). Therapeutic quantities of ^{67}Cu can be produced on high energy accelerators by the ^{68}Zn(*p,2p*)^{67}Cu reaction or bombardment of ^{67}Zn with neutrons in high flux reactors. However, both of these routes are economically unfeasible and produce a large number of radionuclidic impurities, thus requiring long and complex purification processes. ^{67}Cu can additionally be produced in high radionuclidic purity by the ^{70}Zn(*p,α*)^{67}Cu reaction using a low energy proton beam or the photonuclear reaction ^{68}Zn(γ,p)^{67}Cu on electron accelerators. Nevertheless, the product yields of these routes need to be further validated to determine whether the proposed methods are viable production options for ^{67}Cu (90, 94, 107, 108). In addition to cost and accessibility, the extensive presence of copper in the environment remains a major challenge in the production of all copper radioisotopes since it frequently results in the reduction of the specific activity of the radiocopper.

1.4.2 Copper radiopharmaceuticals in nuclear medicine

Copper radionuclides were first used as research tools to investigate the uptake, biodistribution and trafficking of endogenous copper in living organisms (109-111). However, these radioisotopes soon became increasingly attractive to the nuclear medicine community due to their wide array of half-lives and decay schemes, amenable coordination chemistry and potential for application in the development of diagnostic, therapeutic and theranostic radiopharmaceuticals. Interest in copper radionuclides has peaked in recent years mostly due to the development of the ^{62}Zn/^{62}Cu generator system and the versatility of the copper bis(thiosemicarbazone) (Cu-BTSC) family of radiotracers, which have demonstrated great potential for delineating blood flow and tissue hypoxia. This last section of the review summarises current developments in copper radiopharmaceuticals in the field of diagnostic imaging, ranging from copper-labelled bioconjugates to small tracer molecules and plain copper salts.

1.4.2.1 Copper-labelled bioconjugates

The long-lived ^{64}Cu and ^{67}Cu radioisotopes are well suited to the slow kinetics of many molecular targeting agents (e.g. peptides, antibodies, proteins), and have been therefore extensively utilised for radiolabelling biological molecules with a variety of bifunctional chelators. The primary focus of the development of copper-labelled bioconjugates is on oncology applications, with most radiopharmaceuticals targeting somatostatin, integrin, bombesin and epidermal growth factor receptors (112).

The principal challenge in the design of copper-labelled bioconjugates is to achieve sufficient kinetic stability to prevent copper decomplexation *in vivo*, since the most common oxidation states for copper (I and II) are relatively labile and consequently the ligand may not be able to retain the metal ion in the presence of endogenous copper-binding proteins. Transchelation of copper by native proteins generally results in prolonged recirculation of the radiocopper in blood, increased non-specific uptake and retention of copper in the liver and excretion of radiocopper by the gut, which is problematic when imaging the abdomen. Moreover, copper-labelled bioconjugates should also exhibit high thermodynamic stability and form under mild reaction conditions, compatible with the biomolecule of choice. Figure 1.6 shows the chemical

structures of some of the bifunctional chelators used for the radiolabelling of biomolecules with copper radioisotopes.

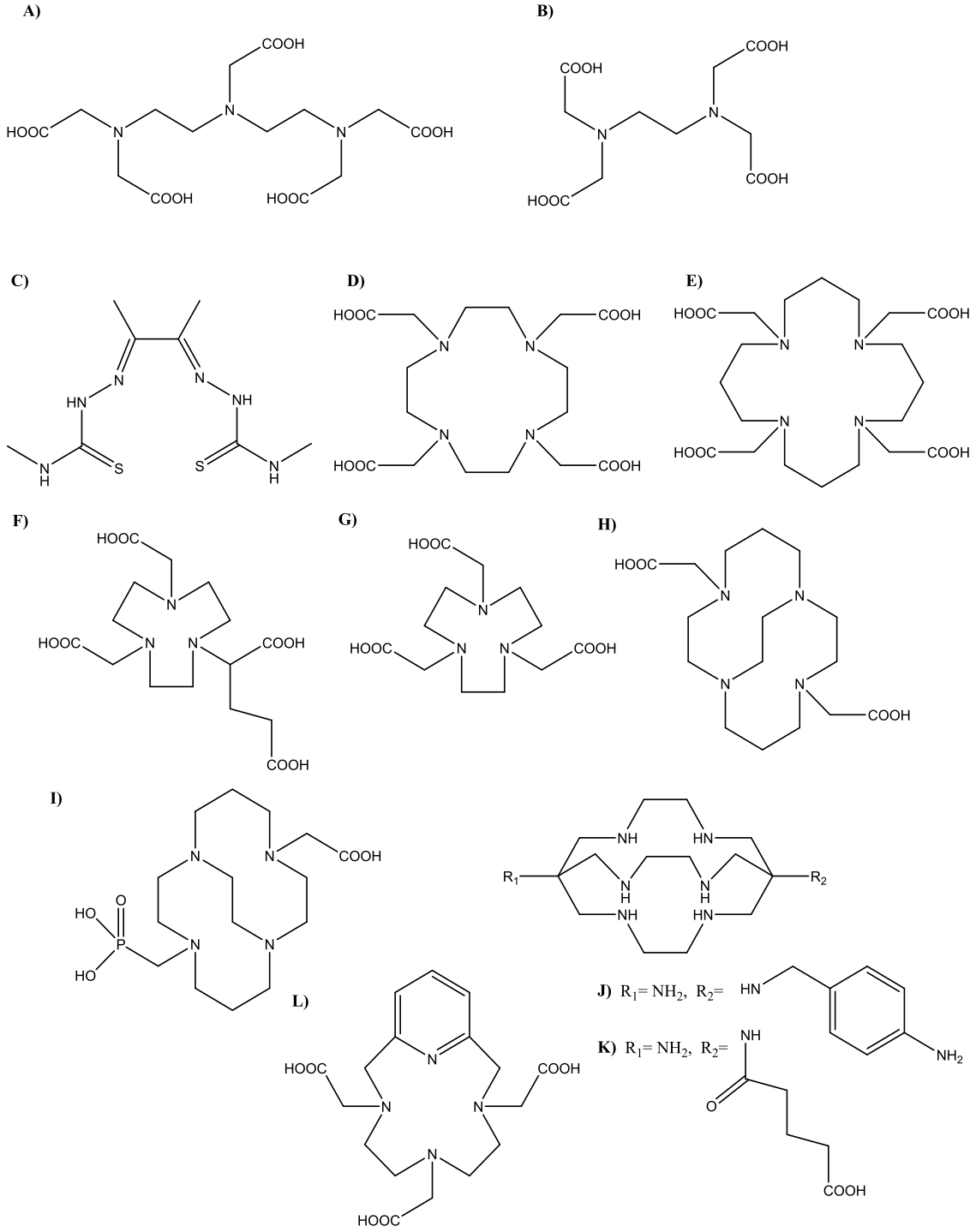

Figure 1.6: Structures of bifunctional chelators for copper radiopharmaceuticals. **A)** diethylenetriaminepentaacetic acid (DTPA); **B)** ethylenediaminetetraacetic acid (EDTA); **C)** diacetyl bis(N^4-methylthiosemicarbazone) (H_2-ATSM); **D)** 1,4,7,10-tetraazacyclododecane-1,4,7,10-tetraacetic acid (DOTA); **E)** 1,4,8,11-tetraazacyclotetradecane-1,4,8,11-tetraacetic acid (TETA); **F)** 1,4,7-triazacyclononane-1-glutaric acid-4,7-diacetic acid (NODAGA); **G)** 1,4,7-triazacyclononane-1,4,7-triacetic acid (NOTA); **H)** 4,11-bis(carboxymethyl)-1,4,8,11-tetraazabicyclo[6.6.2]hexadecane (CB-TE2A); **I)** 11-carboxymethyl-1,4,8,11-tetraazabicyclo[6.6.2]hexadecane-4-methanephosphonic acid (CB-TE1A1P); **J)** 1-*N*-(4-aminobenzyl)-3,6,10,13,16,19-hexaaza-bicyclo-[6.6.6]eicosane-1,8-diamine (sarAr); **K)** (1-NH_2-8-$NHCO(CH_2)_3CO_2H$)-3,6,10,13,16,19-hexaazabicyclo[6.6.6]icosane (sar-CO_2H); **L)** 3,6,9,15-tetraazabicyclo[9.3.1]pentadeca-1(15),11,13-triene-3,6,9,-triacetic acid (PCTA).

Acyclic polyaminocarboxylate ligands, such as DTPA (Figure 1.6.A) or EDTA (Figure 1.6.B), were initially evaluated for use in the radiolabelling of biological molecules but the resulting radiochelates demonstrated poor serum stability *in vitro* (113, 114). The potential of bis(thiosemicarbazone) (BTSC) ligands as bifunctional chelators has also been investigated, although these chelators are more frequently used for the development of copper-based small-molecule radiotracers (see section 1.2.2.4). Hueting *et al.* reported the synthesis and ^{64}Cu radiolabelling of a carboxylate functionalised BTSC ligand conjugated to a bombesin derivative with high affinity for the gastrin-releasing peptide receptor, which is overexpressed in many cancers. The radiolabelled bioconjugate exhibited good tumour uptake in nude mice with PC-3 xenografts at early imaging time points but also high kidney and liver accumulation, probably indicating some extent of demetallation *in vivo* (115). Paterson and co-workers synthesised a series of bifunctional derivatives of the H_2-ATSM ligand (Figure 1.6.C) and used these for the radiolabelling of the tumour targeting BBN(7-14)-NH_2 bombesin derivative with ^{64}Cu. Although the radiolabelled conjugates proved to be stable in the presence of excess cysteine and histidine in aqueous solution, no *in vivo* biodistribution data was reported (116).

To date, the most widely used chelators for the radiolabelling of biomolecules with copper radioisotopes are tetraazamacrocyclic ligands with functionalised pendant arms (e.g. DOTA [Figure 1.6.D], TETA [Figure 1.6.E]). Because of their ability to adopt pre-organised conformations in the free form, these chelators form kinetically and thermodynamically more stable copper (II) complexes than acyclic ligands. DOTA remains the most frequently used copper chelator, mainly due to its mild reaction conditions, commercial availability and Food and Drug administration approval (9). Although copper-labelled DOTA bioconjugates generally display good pharmacokinetics and imaging properties (117), the stability of these complexes *in vivo* has been questioned. McQuade and co-workers reported a higher degree of non-specific uptake of the ^{64}Cu-DOTA-ReCCMSH(Arg^{11}) conjugate relative to its ^{86}Y-labelled analogue in mice implanted with B16/F1 murine melanoma cells (118). When comparing the *in vivo* imaging performance of ^{64}Cu-radiolabelled DOTA and NODAGA-immunoconjugates (NODAGA: Figure 1.6.F) for the detection of epithelial cell adhesion molecule expression in a prostate cancer model, Ghosh *et al.* found lower blood retention and increased liver, prostate and pancreas accumulation of the DOTA bioconjugate, indicating some extent of ^{64}Cu transchelation (119).

Copper-radiolabelled TETA bioconjugates have also proved to be susceptible to copper (II) exchange processes *in vivo*. Bass and co-workers demonstrated the formation of [^{64}Cu] Cu/Zn SOD-1 in the liver of Sprague-Dawley rats 20 h after injection of ^{64}Cu-TETA-D-Phe^{1}-octreotide (120). Among all non-bridged macrocyclic bifunctional chelators, NOTA (Figure 1.6.G) is possibly the most promising for the radiolabelling of biological molecules with radiocopper (117). Prasanphanich *et al.* developed the ^{64}Cu-NOTA-8-Aoc-BBN(7-14)NH(2) targeting vector which showed very high affinity for the gastrin-releasing peptide receptor overexpressed in tumour-bearing PC-3 mice and excellent *in vivo* stability at 1 h post-injection (121). Liu and co-workers compared the *in vivo* stability of a ^{64}Cu-radiolabelled E. coli heat-stable enterotoxin analogue conjugated to DOTA, TETA and NOTA chelating moieties. Results from PET imaging and *ex vivo* biodistribution in SCID mice bearing T84 human colorectal cancer xenografts demonstrated significantly higher tumour/non-target tissue ratios at 1 h post-injection for the ^{64}Cu-labelled NOTA conjugate when compared to the DOTA and TETA analogues (122).

In order to improve the *in vivo* stability of copper-labelled bioconjugates, cross-bridged macrocyclic chelators have been increasingly investigated. The CB-TE2A ligand (Figure 1.6.H) is able to form copper (II) complexes of exceptional *in vivo* stability, and has been used to radiolabel bombesin, somatostatin and RGD analogues (123-126). Nevertheless, the preparation of copper-labelled CB-TE2A conjugates requires relatively harsh reaction conditions (e.g. 2 h at 95 °C) that are generally not compatible with most molecular targeting agents (127). The CB-TE1A1P chelator (I) has emerged as an effective alternative to CB-TE2A since it enables ^{64}Cu radiolabelling with high specific activity under mild reaction conditions (e.g. 1 h at 40 °C). ^{64}Cu-labeled CB-TE1A1P somatostatin and integrin $\alpha_4\beta_1$-targeting peptides demonstrated faster blood clearance, higher tumour-to-blood ratios and lower uptake in non-target tissues in tumour-bearing small animals than their corresponding CB-TE2A analogues (128, 129).

The potential of hexaaminemacrobicyclic cage amine ligands -also known as sarcophagines- as bifunctional chelators for the radiolabelling of biomolecules with copper isotopes was first explored by Bartolo and co-workers. This group reported that the sarAr chelator (Figure 1.6.J) allowed rapid ^{64}Cu radiolabelling of whole and fragmented B72.3 antibody with high specific

activity under mild reaction conditions (5 min at 20 °C). *Ex vivo* biodistribution in nude mice bearing LS174t tumours additionally demonstrated high target specificity and *in vivo* stability for all the investigated sarAr-radioimmunoconjugates (130). Moreover, Cooper *et al.* reported a good balance between mild ^{64}Cu labelling conditions (20 min at room temperature) and excellent *in vivo* stability for the sar-CO_2H-Rituximab conjugate (sar-CO_2H: Figure 1.6.K), which outperformed that of its DOTA, DTPA and PCTA (Figure 1.6.L) analogues (117). The development of sarcophagine-based chelators for the radiolabelling of molecular targeting agents with copper radioisotopes remains a highly productive research area (131-133).

1.4.2.2 Copper-labelled nanoparticles

The long half-life and suitable imaging properties of ^{64}Cu have also been exploited to develop multifunctional nanoparticles for targeted drug delivery and dual-modality imaging (e.g. PET/ magnetic resonance imaging [MRI], PET/ near-infrared fluorescence [NIRF]). The high surface area per unit volume of nanoparticulate materials allows the conjugation of a large number of targeting ligands and bifunctional chelators, thus enhancing the affinity and specific activity of the tracer (112). As with ^{64}Cu-radiolabelled bioconjugates, the choice of the bifunctional chelator is essential to reduce copper transchelation to native copper-binding proteins and ensure sufficient delivery of the probe to the target site. Size and lipophilicity are also critical for tuning the biodistribution and pharmacokinetics of nanoparticles *in vivo*, and in particular, for minimising early clearance of the agent by the mononuclear phagocyte system. The latter difficulty is exemplified by a study by Cai *et al.* who evaluated a novel ^{64}Cu-radiolabelled quantum dot probe, modified with arginine-glycine-aspartic acid peptides and DOTA ligands, targeting $\alpha_v\beta_3$ integrin receptors. Although the probe exhibited selective targeting of the vasculature of $\alpha_v\beta_3$ positive tumours, minimal extravasation into solid tumour tissue was observed and most of the tracer was taken up by the liver, spleen and bone marrow (134). Rossin and co-workers conjugated DOTA chelators to nanoparticles targeting the pulmonary endothelium with monoclonal antibodies, and observed high lung uptake of the ^{64}Cu-radiolabelled probe in wildtype mice even at late imaging time-points. However, the results of this study revealed increasing loss of the radiometal over time as well as prominent early tracer uptake in spleen and liver (135). In order to improve the *in vivo* stability of nanoparticle-based probes, de Rosales *et al.* suggested direct labelling of the inorganic surface of the particle

instead of its polymeric coating using dithiocarbamate-bisphosphonate ligands. The dual modality PET/MR agent radiolabelled with ^{64}Cu following this methodology showed excellent *in vivo* stability and targeting properties and great potential to image draining lymph nodes (136). Petersen and co-workers reported an alternative method to reduce copper transchelation *in vivo* consisting in remote ^{64}Cu loading into pre-formed DOTA-containing liposomes using 2-hydroxyquinoline chelators. The probe was evaluated in a mouse model of colon adenocarcinoma and demonstrated great kinetic inertness, prolonged blood circulation and good tumour-to-muscle ratios (137).

1.4.2.3 Copper dithiocarbamates

Although the chemistry and biological activity of copper (II) dithiocarbamate (Cu-DTC) complexes have been extensively investigated, their use as radiopharmaceuticals for medical diagnosis has been somewhat neglected when compared to other copper-based small-molecule radiotracers. The reason for this is that, although dithiocarbamate ligands are able to form neutral copper (II) chelates (2:1, ligand-metal) in high yield under mild reaction conditions, the resulting complexes exhibit relatively poor *in vivo* stability, which considerably limits their use as imaging agents (138).

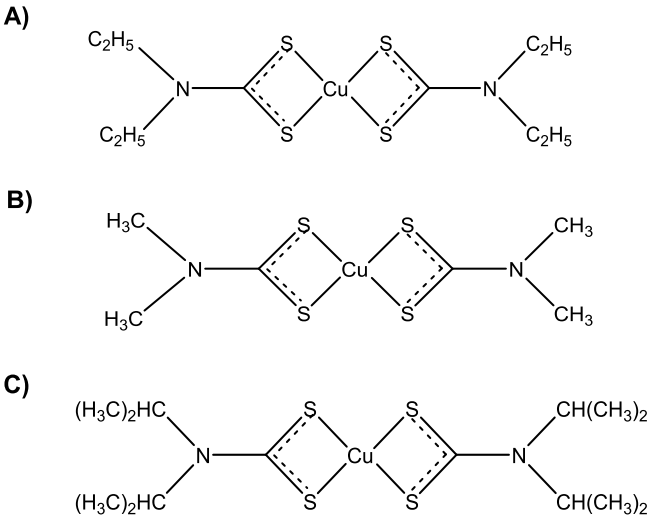

Figure 1.7: Structures of Cu-DTC complexes. **A)** copper (II) diethyldithiocarbamate (Cu-$(DEDTC)_2$); **B)** copper(II) dimethyldithiocarbamate (Cu-$(DMDTC)_2$); **C)** copper (II) diisopropyldithiocarbamate (Cu-$(DPDTC)_2$).

Because of their lipophilic nature and small size, Cu-DTCs are able to enter the cell by passive diffusion. Once inside the cell, these copper (II) complexes are thought to undergo bioreduction and metal-ligand dissociation in a similar manner as Cu-BTSC complexes (see section 1.4.2.4)

(139). Intracellular trapping of Cu-DTCs offers the possibility of using these complexes to incorporate non-selectively a ^{64}Cu label into cells for cell-tracking applications. Charoenphun *et al.* evaluated the feasibility of this approach by testing the cell labelling efficiency of a series of ^{64}Cu-DTC complexes (^{64}Cu-(DEDTC)$_2$, ^{64}Cu-(DMDTC)$_2$ and ^{64}Cu-(DPDTC)$_2$; Figure 1.7) in a J774 mouse macrophage cell line. Although the complexes exhibited different cellular uptake kinetics, the washout rate for all of them was found to be very similar, with ~65 % of ^{64}Cu radioactivity clearing out of cells over 20 h. This behaviour was also observed for several non-selective ^{64}Cu-BTSC radiotracers (e.g. ^{64}Cu-GTSM, ^{64}Cu-PTSM). The similarity of the washout profiles supports the notion that the investigated ^{64}Cu-DTC complexes underwent dissociation inside the cell and released their metal cargo, which became subject to native copper transport processes. Charoenphun and co-workers concluded that active efflux of ^{64}Cu ions from cells would only allow the use of ^{64}Cu-DTCs as cell-tracking agents on a very short time-scale, making the use of non-biological radioelements as cell labels (e.g. ^{111}In, ^{89}Zr) more preferable (140).

The rapid degradation of Cu-DTCs *in vivo* may limit the use of these complexes as cell-tracking agents but could be exploited to deliver copper into cells for other molecular imaging purposes. A preliminary biodistribution study by Matsumoto *et al.* demonstrated high brain uptake of ^{62}Cu(DEDTC)$_2$ and ^{62}Cu(DMDTC)$_2$ chelates by 15 min post-injection, unveiling the potential of these complexes as brain perfusion imaging agents (141). The utility of Cu-DTC complexes as imaging agents for the delineation of perfusion and whole-body copper fluxes remains largely unexplored.

1.4.2.4 Copper bis(thiosemicarbazone) complexes

The lability of copper (I)/(II) centres represents a major difficulty when designing bioconjugate- or nanoparticle-based probes with sufficient kinetic inertness for *in vivo* use. Nonetheless, the bioreduction of copper (II) to copper (I) and subsequent metal-ligand dissociation can also be exploited as a mechanism to selectively deposit radiocopper within cells for various imaging purposes. Cu-BTSC radiotracers have been engineered as vehicles for the selective delivery of copper isotopes into cells under varying physiological conditions.

Cu-BTSCs are a versatile family of copper (II) complexes that have been investigated as metallodrugs and PET imaging agents for many years. The main characteristic of these compounds is that their physicochemical properties can be tailored by subtle modification of the ligand structure, prompting the complex to release its copper payload intracellularly only under specific physiological conditions. For example, the number of alkyl groups attached to the diimine backbone of the ligand has been found to significantly affect the redox potential of the resulting copper (II) complex and consequently the conditions under which the latter undergoes bioreduction and metal-ligand dissociation. Meanwhile, alkylation at the terminal nitrogen atoms of the ligand is thought to alter the lipophilicity and cell permeability of the metal complex, thus affecting its tissue biodistribution, clearance rate and plasma protein binding. Controlled tuning of these two ligand sites facilitates the development of a library of Cu-BTSC complexes with distinct biological behaviours. Examples of investigated Cu-BTSC radiotracers, along with their physicochemical properties and intended application, are shown in Table 1.2.

Table 1.2: Structure, physicochemical properties and potential application of Cu-BTSC complexes (142, 143). **A)** copper (II) glyoxal-bis(N^4-methyl-3-thiosemicarbazone) (Cu-GTSM); **B)** copper (II) pyruvaldehyde-bis(N^4-methylthiosemicarbazone) (Cu-PTSM); **C)** copper (II) diacetyl-bis(N^4-methylthiosemicarbazone) (Cu-ATSM); **D)** copper (II) 2,3-butanedione-bis(thiosemicarbazone) (Cu-ATS); **E)** copper (II) 2,3-pentanedione-bis(thiosemicarbazone) (Cu-CTS).

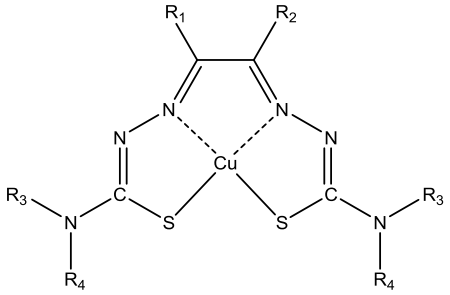

Cu-BTSC complex	R_1	R_2	R_3	R_4	Lipophilicity (logP)	$E_{1/2}$ (Cu(II)/Cu(I)) (V) [a]	Imaging application
Cu-GTSM (**A**)	H	H	CH_3	H	0.84	-0.43	Copper trafficking
Cu-PTSM (**B**)	CH_3	H	CH_3	H	1.45	-0.51	Perfusion
Cu-ATSM (**C**)	CH_3	CH_3	CH_3	H	1.48	-0.59	Tumour hypoxia
Cu-ATS (**D**)	CH_3	CH_3	H	H	0.91	-0.59	Cardiac hypoxia
Cu-CTS (**E**)	C_2H_5	CH_3	H	H	1.45	-0.59	Cardiac hypoxia

[a] Reduction potentials are vs. Ag/AgCl

The most accepted uptake mechanism for this family of radiotracers suggests that Cu-BTSCs freely diffuse into cells, where they become reduced to Cu(I)-BTSC complexes by bioavailable reducing agents (e.g. ascorbate, glutathione, NADH) and dissociate, releasing their radiocopper payload into the intracellular copper pool. Bioreduction and subsequent metal-ligand dissociation of Cu-BTSCs may occur slowly (Cu-ATSM, Cu-ATS, Cu-CTS) or rapidly (Cu-GTSM, Cu-PTSM), depending on the reduction potential and *in vivo* stability of the Cu (I) complexes. If sufficient oxygen is available, slowly-dissociating Cu-BTSC complexes are reoxidised and washed out of the cell intact, whereas that when exposed to lower physiological oxygen conditions, these become irreversibly reduced and dissociate, giving rise to a hypoxia-dependent PET signal. On the other hand, rapidly-dissociating Cu-BTSC complexes release their copper payload into cells irrespective of their redox status and are therefore good radiotracers to delineate tissue perfusion.

The effect of the backbone alkyl groups on the redox potential of Cu-BTSC complexes and the reversibility of the reduction process has been examined in some detail. Maurer and co-workers reported that the two patterns of chemical behaviour observed for Cu-BTSCs (hypoxia-selective and non-selective metal release) could be predicted by density functional theory calculations from the energy order of the lowest unoccupied molecular orbital (LUMO) and the next lowest unoccupied orbital on the electronic structure of the complexes. This group also suggested that intracellular pH might be a key factor influencing the reversibility of the copper (II) reduction process, since reduced Cu-PTSM and other non-selective Cu-BTSC complexes were shown to dissociate immediately in the presence of small amounts of weak acid by cyclic voltammetry, while hypoxia-selective analogues such as Cu-ATSM remained unaltered (144). Blower *et al.* studied the structures of eight Cu-BTSC complexes with different alkylation patterns by X-ray crystallography and found that alkylation at the diimine backbone of the ligand induced a lengthening of the C-C bond and a significant shortening of the Cu-S bonds, allowing a better metal-ligand fit and subsequently enhancing the overall stability of the hypoxia-selective complexes under normoxia (145). Although the redox potential of Cu-BTSCs is usually modified by varying the alkylation pattern of the diimine backbone of the ligand, McQuade *et al.* proposed to vary the reduction potential of the complexes by alternatively replacing sulfur with selenium as the donor atom. However, the resulting copper bis(selenosemicarbazone) complexes

showed very poor *in vitro* and *in vivo* stability which precluded their application as hypoxia imaging agents (146).

Over the years, several overlapping theories have attempted to elucidate the mechanisms underlying the cellular uptake, hypoxia selectivity, intracellular distribution and efflux of Cu-BTSC complexes, particularly focusing on the prototype hypoxia imaging agent Cu-ATSM. In 1997, Fujibayashi *et al.* first suggested that Cu(II)-ATSM was reduced to Cu(I)-ATSM only under hypoxic conditions and subsequently underwent metal-ligand dissociation and intracellular sequestration (147). An alternative mechanism proposed by Dearling and co-workers postulated that the reduction of Cu(II)-ATSM to Cu(I)ATSM occurred to some extent both in normoxic and hypoxic cellular environments, but that under sufficient oxygen concentrations Cu(I)-ATSM was reoxidised and cleared out of the cell (142). Burgman *et al.* inferred that copper (I) ions released from Cu-ATSM under hypoxia were incorporated into the intracellular copper pool by association with endogenous copper chaperones. This group also suggested that the differences observed in radiocopper retention and efflux after ^{64}Cu-ATSM dissociation between tumour cell lines might be caused by different levels of expression of copper transporters (148). In 2010, Dearling and co-workers proposed a detailed mechanism for the cellular uptake of Cu-ATSM, which they described as “biphasic”. The first phase is the bioreduction of Cu(II)-ATSM to Cu(I)-ATSM potentially by thiol groups or redox-active proteins with NADH as an enzymatic cofactor. NADH is a particularly abundant species in the mitochondria under hypoxic conditions due to the metabolic switch to anaerobic respiration. The resulting $[Cu(I)\text{-}ATSM]^-$ complex is a considerably less lipophilic species than Cu(II)-ATSM, and therefore is less likely to diffuse out of the cell. In the presence of sufficient oxygen, $[Cu(I)\text{-}ATSM]^-$ can be reoxidised back to Cu(II)-ATSM and diffuse out of the cell. In hypoxic cells, where intracellular pH is more acidic, $[Cu(I)\text{-}ATSM]^-$ might be protonated at the N3 and N6 sites of the ligand and subsequently dissociate, releasing the copper (I) ion into the endogenous copper pool. The group concluded that the bioreduction, dissociation and intracellular trapping of Cu-ATSM were mainly dependent on cellular oxygen levels, pH and NADH concentration (149).

The identity of the endogenous reducing agent responsible for the intracellular reduction of Cu-BTSCs is yet to be elucidated. Xiao *et al.* reported that in aqueous media and in the presence of

higher affinity copper-binding proteins (Atx1 and Ctr1) both glutathione and ascorbate were able to reduce the non-selective complex Cu-GTSM, but not the hypoxia-selective Cu-ATSM (150). A recently published study showed that glutathione status was not altered under hypoxia in the Langendorff-perfused rat heart model and that modulation of glutathione levels did not affect the retention and pharmacokinetics of ^{64}Cu-ATSM under either hypoxia or normoxia. However, this study did not preclude glutathione acting as a cofactor in the bioreduction of the tracer (151).

Besides the identity of the intracellular reductant, other aspects of the proposed mechanism of action of Cu-BTSCs remain unclear. Further research is needed to clarify the fate of "free" copper (I) ions and ligand molecules after dissociation, as well as the effect of pH, NADH and oxygen levels on the mechanism of hypoxia selectivity of some of these complexes. The influence of copper metabolism on the uptake, dissociation and efflux of Cu-BTSCs should also be assessed. This point is particularly relevant in the context of tumour hypoxia imaging since many cancer types exhibit altered copper trafficking and distribution (152).

The possibility of tuning the physicochemical properties of Cu-BTSCs by modification of their ligand structure allows controlled radiocopper release in different cellular environments, which can be exploited in broad range of imaging applications. Hypoxia imaging remains the main focus of Cu-BTSC radiopharmaceutical development, although the use of Cu-BTSCs for the monitoring of blood flow has also been extensively investigated. In recent years, the use of Cu-BTSC radiotracers to study disease-related changes in the transport and metabolism of copper has also been explored with promising outcomes (153-155). These three main areas of research will be discussed in further detail in the following sections.

1.4.2.4.1 Delineation of hypoxia

The antitumour activity of the family of Cu-BTSCs was first discovered by Petering *et al.* in 1964. The 2-keto-3-ethoxybutyraldehyde-bis(thiosemicarbazone) (KTS) ligand was reported to exhibit carcinostatic and carcinolytic activity against advanced rat tumours. The therapeutic capacity of the Cu-KTS complex proved to be superior to that of ligand itself and Cu-BTSCs have since been extensively investigated (156).

In 1997, Fujibayashi and co-workers reported the synthesis of the first hypoxia-selective Cu-BTSC radiotracer, ^{62}Cu-ATSM, which was successfully tested in the Langendorff-perfused rat heart model (147). Ever since it was reported that Cu-ATSM was retained selectively under hypoxic conditions, the complex became a candidate to replace the current gold standard for hypoxia imaging ^{18}F-fluoromisonidazole (^{18}F-FMISO), which suffered from slow uptake, low specificity and slow clearance from normoxic tissue (157). Lewis *et al.* conducted a comparative study between the two radiotracers in cultured EMT6 breast cancer cells and EMT6 tumour-bearing mice, in which ^{64}Cu-ATSM showed a higher retention under hypoxic conditions and a faster clearance from normoxic tissue than [^{18}F]-FMISO (158). Burgman and co-workers suggested that the hypoxia-selective accumulation of ^{64}Cu-ATSM could be cell-line dependent after observing considerable variation in the uptake, efflux and hypoxic/anoxic-to normoxic uptake ratios of ^{64}Cu among different tumour cell lines (R3327-AT, FSaII, MDA468, MCF7, DU145 and FaDu) incubated with ^{64}Cu-ATSM (148).

Despite showing promise *in vitro*, *in vivo* evaluation of Cu-ATSM has produced variable results. In a study to assess the intratumoral distribution and oxygen concentration dependence of ^{64}Cu-ATSM and [^{18}F]-FMISO *in vivo*, it was shown that the tumour distribution of the two tracers in rats bearing R3327-AT prostate tumours only correlated well at late imaging time-points (16-20 h post-injection), whereas that in rats inoculated with FaDu tumour cells ^{64}Cu-ATSM showed a good correlation with [^{18}F]-FMISO and tumour hypoxia both at early and late time-points (159). Tumour-specific dependence of ^{64}Cu-ATSM uptake was also observed by Yuan *et al.* in mice inoculated with different tumour cell lines (R3230 mammary adenocarcinomas, fibrosarcomas and 9L gliomas). This study also revealed an inconsistent correlation between ^{64}Cu-ATSM intratumoral distribution and standard hypoxia markers EF5, pimonidazole and carbonic anhydrase, indicating the influence of other factors in the retention of the tracer (160).

In 2000, Takahashi and co-workers conducted a small PET imaging study with ^{62}Cu-ATSM in 6 patients with lung cancer. The study demonstrated high tumour uptake of ^{62}Cu-ATSM in all cancer patients but did not provide any evidence of correlation between tracer distribution and tumour hypoxia (161). Dehdashti *et al.* assessed the performance of ^{60}Cu-ATSM and its relationship with treatment response in patients with cervical cancer (n = 14) and non-small-cell

lung carcinoma (n = 19). In patients with cervical cancer, ^{60}Cu-ATSM tumour uptake (expressed as tumour-to-muscle ratio) showed an inverse correlation with progression-free survival and overall survival after radiotherapy and chemotherapy (162). Tumour-to-muscle ratios of ^{60}Cu-ATSM in patients suffering from lung cancer demonstrated a similar predictive value in tumour response to treatment, although no significant difference in mean tumour ^{60}Cu-ATSM standardised uptake value (SUV) was found between responders and non-responders (163).

Although clinical evaluation of the tracer has so far shown a good correlation between Cu-ATSM tumour accumulation and prognosis, the cell-line dependence of Cu-ATSM uptake along with the inconsistent correlation between tumour tracer distribution and hypoxia-related markers suggest that there may be other factors besides tumour hypoxia governing the biodistribution and tumour uptake of Cu-ATSM. Hueting *et al.* suggested in a recent publication that copper metabolism may also play a role in the mechanism of accumulation of ^{64}Cu-ATSM in hypoxic tumour tissue. This group compared ^{64}Cu retention in cultured EMT6 and CaNT cells and tumour-bearing mice after administration of ^{64}Cu-ATSM and ^{64}Cu-acetate, and observed a very similar biodistribution of the two tracers *in vivo* and only colocalisation with the EF5 hypoxia marker at late imaging time-points (16 h post-injection). Hueting and co-workers suggested that ^{64}Cu-ATSM dissociated in blood and was subsequently taken up by the tumour as ionic copper *in vivo*. Although this study raises some valid points, it seems unlikely that the *in vivo* biodistribution of all Cu-BTSC complexes, particularly at early imaging time-points, mirrors that of ionic copper, given the wide range of biodistribution profiles of Cu-BTSC radiotracers. Nevertheless, the results of this study should be taken into consideration especially in the context of tumour hypoxia imaging, where slow clearance rates from normoxic tissue may require long imaging times and tracer distribution may be affected by altered copper metabolism in tumour tissue.

Although poor *in vivo* stability of Cu-ATSM in blood may not be a concern for cardiac imaging, where tracer kinetics are generally fast, the utility of Cu-ATSM as an imaging agent for the delineation of cardiac hypoxia has been questioned. The radiotracer was only clinically evaluated for this purpose in 7 patients with coronary artery disease with ambiguous results (164). The main disadvantage of Cu-ATSM as a cardiac hypoxia imaging agent is that the tracer

gets selectively trapped in hypoxic environments that are more severe than is experienced in hypoxically compromised but salvageable myocardium. Handley and co-workers identified two alternative Cu-BTSC agents, Cu-ATS and Cu-CTS, characterised by a lower lipophilicity than Cu-ATSM and a similar redox potential, which exhibited significantly improved hypoxic:normoxic retention ratios (14:1 and 17:1, respectively) in the Langendorff-perfused rat heart model when compared to the 8:1 contrast shown by ^{64}Cu-ATSM (143). Subsequently, Medina *et al.* performed a series of perfusion buffer oxygen titrations to identify the oxygen concentration threshold that caused a degree of low grade hypoxia in the perfused rat heart model that correlated with the moderately compromised cardiac energetics characteristic of hypoxic but salvageable myocardium. At this key threshold (30 % oxygen concentration), ^{64}Cu-CTS was the only tracer that showed hypoxia-selective retention, providing a hypoxic:normoxic contrast of >3:1, whereas that the rest of the Cu-BTSC complexes (^{64}Cu-ATS, ^{64}Cu-ATSE and ^{64}Cu-ATSM) exhibited selective trapping only below 20 % oxygen concentration (165). ^{64}Cu-CTS therefore holds great promise as an imaging agent for the delineation of pathophysiologically relevant degrees of cardiac hypoxia.

1.4.2.4.2 Perfusion imaging

Unlike Cu-ATSM, Cu-PTSM is readily reduced and intracellularly trapped in most tissues, regardless of their oxygen levels, and consequently has been extensively investigated as a marker of tissue perfusion. Cu-PTSM has one less methyl backbone substituent than Cu-ATSM, which results in an increase in redox potential, making the complex more susceptible to bioreduction and metal release (142, 166).

In the 1980s, Green *et al.* conducted a number of preclinical studies to explore the biodistribution profile of Cu-PTSM and evaluate its potential for perfusion imaging applications. An initial study revealed rapid blood clearance of the tracer (within 1 minute post-injection) and high accumulation of ^{64}Cu radioactivity in the brain (2 ± 0.4 %ID/g) and heart (4.7 ± 1.2 %ID/g) in Sprague-Dawley rats. Although the relationship between ^{64}Cu-PTSM uptake and regional blood flow could not be demonstrated, it was suggested that the uptake of Cu-PTSM in tissue was so rapid that it roughly reflected the pattern of blood distribution (167). Green and co-workers subsequently evaluated the *in vivo* distribution of ^{67}Cu-PTSM and derivatives ^{67}Cu-PTS and

^{67}Cu-PTSM$_2$ (R_3=R_4=H and R_3=R_4=CH_3, respectively) in Sprague-Dawley rats to assess their potential as cerebral and myocardial perfusion imaging agents. Lipophilic ^{67}Cu-PTSM and ^{67}Cu-PTSM$_2$ complexes exhibited rapid blood clearance and excellent brain uptake (~2 %ID/g) within 1 minute post-injection, although brain concentration of ^{67}Cu-PTSM$_2$ dropped by half after 15 min. ^{67}Cu-PTSM showed prolonged "microsphere-like" retention both in the heart and brain, where ^{67}Cu concentration remained constant over 2 h. This difference in tracer kinetics could be attributed to the considerably higher lipophilicity of Cu-PTSM$_2$ (logP = 2.35) compared to Cu-PTSM (logP = 1.45), which may prompt rapid washout of the complex from cells before bioreduction and metal-ligand dissociation take place. Contrary to its lipophilic analogues, ^{67}Cu-PTS (logP = 0.53) crossed the blood-brain barrier less efficiently (~0.3 %ID/g) but showed a similar myocardial ^{67}Cu concentration (~4.7 %ID/g). In the same study, a dual-tracer biodistribution experiment in a gerbil stroke model revealed an excellent correlation between the regional brain distribution of ^{67}Cu-PTSM and that of SPECT cerebral blood flow tracer [^{125}I]-iodoantipyrine (142, 168). Further studies by this group additionally demonstrated the utility of Cu-PTSM for measuring myocardial, renal and tumour perfusion *in vivo* (169-171).

These preclinical results encouraged the evaluation of Cu-PTSM as a blood flow imaging agent in living patients. Okazawa *et al.* first evaluated the pharmacokinetic properties and clinical applicability of ^{62}Cu-PTSM as a cerebral blood flow tracer in 10 human subjects. Arterial sampling showed rapid blood clearance of ^{62}Cu-PTSM within 3 minutes post-injection. Time-activity curves extracted from PET images revealed maximal brain uptake of the tracer within 2 minutes after injection and stable tissue activity during the following 8 minutes of scan. ^{62}Cu-PTSM brain distribution showed an excellent correlation with that of regional blood flow tracer ^{15}O-H_2O (172). Cu-PTSM also showed promising results in a pharmacological study aimed at assessing angiotensin II-induced changes in hepatic perfusion to elucidate the role of vascular manipulation applied to chemotherapy in subjects suffering from colorectal liver metastases (n = 9). ^{62}Cu-PTSM imaging before and after angiotensin II infusion revealed significant blood flow changes in the liver in 7 out of 9 patients (173). ^{62}Cu-PTSM imaging also proved effective in identifying perfusion abnormalities in 91 % of patients suffering from occlusive coronary artery disease (n = 28) (174). However, ^{62}Cu-PTSM has been shown to interact strongly with human serum albumin which may result in the attenuation of first-pass extraction of the tracer into

tissue at high flow rates (175). Further evaluation of the characteristics of ^{62}Cu-PTSM and direct comparison of the tracer with other established perfusion imaging agents will determine the extent of its clinical use.

1.4.2.4.3 Imaging of copper trafficking

Copper is an essential trace element in all living organisms but can be harmful to health if not tightly regulated. Abnormal copper metabolism has been associated with the pathophysiology of many diseases, particularly of neurological nature, and is therefore a potentially attractive diagnostic and therapeutic target (176). Radioactive copper (II) salts have traditionally been used to investigate whole-body copper metabolism in health and disease but are subject to active copper transport mechanisms, which deliver copper ions to the brain in quantities that are insufficient for meaningful imaging.

The Cu-BTSC complex Cu-GTSM has a low molecular weight and a moderate lipophilicity (logP = 0.84), both properties that enable its transfer across the blood-brain barrier (BBB), allowing *in vivo* measurement of copper trafficking within the brain. In addition, Cu-GTSM has two hydrogens instead of methyl groups on its backbone, which results in a relatively positive redox potential (-0.43 V (vs. Ag/AgCl)) that promotes rapid bioreduction of the complex and non-selective release of copper ions into cells (142). The ability of Cu-GTSM to penetrate the BBB and supply radiocopper to the intracellular copper pool offers the possibility to study changes in copper ion trafficking associated with various neurological disorders (e.g. AD, ALS, PD) and evaluate the potential of copper metabolism imbalance as a diagnostic and/or therapeutic marker. To date, this approach has only been explored in a mouse model of AD plaque pathology. Fodero-Tavoletti and co-workers showed that when ^{64}Cu-radiolabeled Cu-GTSM was administered intravenously, ^{64}Cu brain uptake as measured by *ex vivo* gamma-counting was 2-fold higher in APP/PS1 mice at 9-12 months of age (3.0 ± 0.25 %ID/g) than in age-matched controls (1.58 ± 0.14 %ID/g) at 60 min post-injection (155). Interestingly, this group found no correlation between the distribution of ^{64}Cu in human frontal cortex slices after incubation of the tissue with ^{64}Cu-GTSM and amyloid-β plaque deposition in the APP/PS1 mouse model, which contradicts the generally accepted notion of amyloid-β plaques acting as “sinks” for metal ions, at least in the acute time scale. The results of this study encourage further

evaluation of ^{64}Cu-GTSM-PET as a tool to investigate brain copper trafficking in various neurological disorders in order to determine its diagnostic potential.

1.4.2.5 Radioactive copper salts

PET imaging of ionic radiocopper provides an excellent opportunity to noninvasively measure copper trafficking *in vivo* to understand better the physiology of copper metabolism in health and disease. Radioactive copper (II) salts and copper-binding proteins labelled with radiocopper have been used to investigate the mechanisms underlying absorption, transport, distribution and excretion of endogenous copper in living organisms (16, 48, 177). However, in recent years, PET imaging of ionic radiocopper has also gained recognition as a useful tool to identify copper metabolism abnormalities, particularly in the context of the Wilson's and Menkes genetic disorders.

WD is a fatal autosomal recessive disorder characterised by excessive copper accumulation in the liver, brain, kidneys and other tissues arising from loss-of-function mutations in the gene encoding the ATP7B copper efflux transporter. Bahde *et al.* assessed the feasibility of imaging disrupted copper trafficking in WD in the ATP7B-deficient Long-Evans Cinnamon rat model using a ^{64}Cu-histidine complex. ATP7B-deficient rats exhibited increased accumulation of ^{64}Cu radioactivity in the liver and no hepatobiliary excretion compared to their wildtype counterparts as a result of the functional impairment of ATP7B. Interestingly, ATP7B-deficient rodents transplanted with healthy hepatocytes showed reduced liver uptake of ^{64}Cu and restored biliary excretion, which demonstrates the importance of ATP7B in the maintenance of copper homeostasis and the potential of this approach to monitor response to transplantation therapy (178). Subsequently, Peng and co-workers evaluated the utility of copper-64 chloride ($^{64}CuCl_2$) as a radiotracer for the non-invasive measurement of copper metabolism imbalance in WD. PET imaging of copper trafficking was performed in ATP7B knockout mice and wildtype littermates using a hybrid PET/CT scanner, which allowed real-time quantitative analysis of ^{64}Cu distribution at the whole-body level. As expected, intravenous administration of $^{64}CuCl_2$ resulted in enhanced deposition of radiocopper in the liver and impaired biliary excretion in the WD model. Moreover, ^{64}Cu concentration in extrahepatic tissues (heart, lungs, kidneys and brain) was found to be significantly lower at 24 h post-injection in ATP7B knockout mice compared to

controls, probably due to hepatic sequestration of the radiocopper (153). Peng *et al.* conducted a similar study to assess gastrointestinal absorption and whole-body distribution of dietary copper in WD in ATP7B knockout mice orally treated with $^{64}CuCl_2$. The group revealed significantly higher hepatic concentration of ^{64}Cu in the disease group compared to wildtype mice, but no significant differences in tracer uptake between the two groups were detected in the kidneys, heart, brain and blood at 24 h post-injection (179). Lutsenko and co-workers used $^{64}CuCl_2$ PET/CT imaging to investigate the mechanisms underlying urinary copper elevation at late-stages of hepatic copper accumulation in WD. The study demonstrated an age-dependent decrease in copper hepatic retention in ATP7B-knockout mice associated with the activation of a renal copper export pathway. It was additionally found that this secondary efflux pathway involves a decrease in Ctr1 transporter levels in the liver and the upregulation of small copper carrier protein in the urine (180).

$^{64}CuCl_2$ PET imaging has also been used to study copper metabolism imbalance in MD, another genetic disorder of copper trafficking caused by mutations in the gene encoding the ATP7A transporter. ATP7A dysfunction in MD causes accumulation of dietary copper in the intestines and kidneys and concomitant copper deficiency in the remaining organs. To date, the most successful treatment to correct systemic copper deficiency in MD consists of subcutaneous injections of a copper-histidine complex. However, this therapy is only effective at early stages of disease development during infancy, when the BBB is still immature and allows the complex to pass through. To ensure sufficient copper delivery to the brain in the presence of a maturing blood-brain barrier, the use of lipophilic Cu-BTSC complexes and the combination of $CuCl_2$ and brain-permeable chelators have been suggested (181, 182). In this context, Nomura and co-workers evaluated the trafficking efficacy of the copper-chelating agent 1,1',1'',1'''-[disulfanediylbis(carbonothioylnitrilo)]tetraethane (disulfiram) in a mouse model of MD by $^{64}CuCl_2$-PET. Non-treated macular mice showed increased concentration of ^{64}Cu radioactivity in the kidneys and reduced ^{64}Cu uptake in the liver and brain when compared to healthy controls. By contrast, animals pre-treated with disulfiram exhibited lower accumulation of ^{64}Cu in the kidneys and higher tracer uptake in the liver and brain than non-treated mice (154). This study demonstrated the additional potential of $^{64}CuCl_2$-PET as a tool for assessing new treatment options.

Numerous studies in the literature have reported that copper metabolism is also dysregulated in a variety of human carcinomas. Both serum and tumour copper levels have been found to be significantly increased in ovarian, breast, cervical, lung, prostate, colorectal, blood and gastric cancers, and this elevation in copper concentration has been shown to be directly correlated with disease progression (183). The discovery of abnormal copper accumulation in cancer cells has led to the development of copper-chelating strategies as potential treatment options and the use of $^{64}CuCl_2$-PET as a tool to delineate tumour tissue and investigate the role of copper metabolism in carcinogenesis. Peng and co-workers first evaluated $^{64}CuCl_2$ as an imaging agent for the visualisation of solid tumours in athymic mice transplanted with extrahepatic hepatoma cells. The group hypothesised that ^{64}Cu accumulation in hepatoma grafts might be mediated by endogenous copper transporter Ctr1, which is highly expressed in hepatocytes and whose expression might therefore be strong in hepatoma cells. Extrahepatic hepatomas were successfully visualised by $^{64}CuCl_2$-PET at 1 h post-injection of the tracer (3.68 ± 0.42 SUV), indicating the potential utility of this technique for detecting extrahepatic hepatocellular carcinoma metastasis in tissues with low uptake of $^{64}CuCl_2$ (e.g. muscle, brain). Ctr1 immunoreactivity in extrahepatic hepatoma grafts was found to be approximately 70 % of that in the liver but was significantly more intense compared to that in soft tissue and brain (184). Peng *et al.* conducted a similar imaging study in athymic mice bearing human prostate cancer xenografts and reported good tumour visualisation using $^{64}CuCl_2$ at 24 h post-injection of the tracer but not at 1h, in contrast to mice bearing extrahepatic hepatoma grafts. The authors suggested that this difference in ^{64}Cu accumulation might be due to lower expression of mouse Ctr1 and more active copper efflux mechanisms in prostate cancer cells compared to extrahepatic hepatoma cells (185). Subsequently, Jørgensen *et al.* assessed ^{64}Cu uptake in five different mouse tumour models (colorectal cancer, glioblastoma, head and neck cancer, neuroendocrine lung cancer and ovarian cancer) and compared it to gene expression of mCtr1 in tumour tissue. Tumour uptake of ^{64}Cu was found to be both time and tumour-type dependent, with ^{64}Cu accumulation in tumour tissue increasing in three out of five tumour types from 1 h to 22 h post-injection of the tracer. Surprisingly, no correlation was found between tumour ^{64}Cu concentration and mouse Ctr1 gene expression levels, which indicate the existence of a second copper influx system or the relocation of Ctr1 between intracellular vesicles and the cell membrane as a regulatory mechanism of Ctr1 activity (186). In a recent study, Qin *et al.*

evaluated the potential of $^{64}CuCl_2$ as a theranostic probe for both PET imaging and radionuclide therapy of malignant melanoma in B16F10 and A375M tumour-bearing mice. $^{64}CuCl_2$-PET showed excellent ^{64}Cu tumour uptake in the B16F10 group already at 1h post-injection of the tracer, whereas ^{64}Cu accumulation in A375M tumours was more gradual, reaching its peak value by 24 h. Additionally, the authors demonstrated that $^{64}CuCl_2$ treatment slowed down tumour growth in both melanoma models compared to the non-treated groups (187). In the first and only clinical study to date, Capasso and co-workers evaluated $^{64}CuCl_2$-PET as a tool for primary staging of patients with prostate cancer (n = 7). Preliminary results of this study demonstrated high accumulation of ^{64}Cu in tumour tissue and regional lymph nodes, demonstrating the potential of increased copper metabolism as a diagnostic and therapeutic biomarker for prostate cancer (188). Further research is needed to shed some light into the mechanisms underlying abnormal copper metabolism in neoplastic disease and its impact on disease progression and survival rates.

1.5 CONCLUDING REMARKS

Copper is an essential bioelement in the human body but can become harmful if not tightly regulated. Significant progress has been made in describing the key molecular players and pathways involved in the trafficking and regulation of copper metabolism but many aspects of these mechanisms remain elusive. Disrupted copper homeostasis has been identified as a pathological feature in a variety of inherited and acquired disorders, including WD, MD, AD and various types of cancer. There is therefore an urgent need to improve our understanding of the mechanisms governing copper transport, distribution and regulation in order to be able to identify and fully characterise abnormalities in copper metabolism associated with specific disease states and evaluate their impact on disease progression and prognosis.

Many of the early efforts to investigate copper biochemistry relied on the use of copper radioisotopes. Copper absorption, distribution and excretion were studied by administering radioactive copper salts into small animals and measuring the radioactivity present in organs and tissues. Over the last decade, the advent of proteomics has provided new insights into the study of copper metabolism, allowing the investigation of specific trafficking pathways and

protein structures, and thus the use of radiocopper has been relegated to the development of traditional radiopharmaceuticals.

Copper radionuclides have attracted considerable attention in radiopharmaceutical development due to the wide selection of half-lives and decay schemes they offer as well as their amenable radiochemistry. Over the years, this family of radioisotopes has been used in the construction of a wide array of radiopharmaceuticals, ranging from bioconjugate-based agents to small-molecule radiotracers, with various degrees of success. The choice of radiocopper as a label to monitor the distribution of bioconjugates and nanoparticles is not ideal since the resulting probes generally exhibit low stability *in vivo* due to competition with endogenous copper-binding species. The susceptibility of copper to native trafficking mechanisms also hampers the use of radiocopper complexes as cell-tracking imaging agents, making preferable the use of "non-biological" radioisotopes.

The continuous improvement in the resolution and sensitivity of PET systems along with the increasing availability of PET copper radionuclides provide the opportunity to use these isotopes to measure copper fluxes *in vivo* in a non-invasive manner, in both animals and humans. The administration of radiocopper at sub-pharmacological concentrations would allow the dynamic study of native metabolic pathways without perturbing them. This is a unique feature of PET copper radioisotopes that could be exploited not only to provide a better understanding of the physiology of copper metabolism but also to determine the potential of copper dyshomeostasis as a diagnostic and therapeutic marker in a number of diseases.

Chapter 2- Brain copper metabolism in health and disease

2.1 AIMS

The brain is one of the most copper-demanding organs in the body. In the brain, copper plays an indispensable role in normal cell physiology but is also an important contributor to brain-specific functions such as neuropeptide production or synaptic transmission. Paradoxically, the brain is also one of the most vulnerable organs to oxidative stress induced by uncontrolled redox-active metals and, as a result, copper trafficking in the central nervous system (CNS) is maintained under very tight control. Brain copper dysregulation is the main driving force for neurodegeneration in the Wilson's and Menkes genetic disorders but has also been linked to the pathophysiology of many other neurological diseases. However, despite the importance of brain copper homeostasis in neurological health and disease, very little is known about the mechanisms underlying the trafficking and distribution of copper within the CNS.

In this chapter, we aim to give an overview of our current knowledge on the metabolism and functions of copper in the CNS, as well as the mechanisms regulating brain copper homeostasis. The role of copper in a growing list of neurological disorders will also be discussed in order to identify potential opportunities for application of PET as a tool to study copper metabolism abnormalities associated with neurodegeneration and monitor the effects of copper-modulating therapies.

2.2 COPPER METABOLISM IN THE CNS

2.2.1 Copper content and distribution in the CNS

Copper is an essential bioelement for the normal development and function of the brain. The brain is one of the main sites of copper accumulation (second only to the liver) and utilises the metal for both general (e.g. antioxidative defence, energy metabolism, iron transport) and brain-specific metabolic functions (e.g. neuropeptide and neurotransmitter synthesis) (15). Due to the high rate of cerebral oxidative metabolism and relatively low abundance of brain-resident

antioxidants, brain copper trafficking is tightly regulated in order to minimise metal-catalysed production of ROS. The average concentration of copper in the human brain is approximately 80 µM, with the intracellular availability of free copper ions kept at extraordinarily low levels (189). Copper levels in the cerebrospinal fluid (CSF) are comparatively much lower (~ 0.3 µM) than those in the brain parenchyma and differ from plasma copper concentration (~ 15 µM) by 1.5 orders of magnitude (190).

The distribution of copper within the human brain is heterogeneous, as reflected by two- to three-fold higher copper levels in the grey matter compared to the white matter. Regional distribution of copper in the brain is dictated by region-specific metabolic demands but is also influenced by factors such as species or age. The area in the human brain containing the highest concentration of copper is the locus coeruleus, which is the principal site for noradrenaline production. The substantia nigra, dentate nucleus and cerebellum are other structures in the human brain with high copper levels, which reveals an enhanced metabolic requirement for copper in these regions. Interestingly, in the mouse brain, copper is most abundant along the ventricles and in the hypothalamus, which is the region responsible for the maintenance of body homeostasis (191-194).

Several studies have demonstrated that copper content in the rodent brain increases with age. Massie and co-workers first reported an increase in brain copper levels in wildtype mice from 50 to 600 days of age which was inversely correlated with cerebral Cu/Zn SOD-1 activity (195). Similarly, Wang *et al.* found increased cerebral copper content in 14-month-old wildtype mice when compared to 7-9- and 2-month-old mice, as well as significantly decreased Cu/Zn SOD-1 levels, particularly in the striatum and ventral cortex. Paradoxically, Wang and co-workers also reported an age-dependent reduction in active $^{67}CuCl_2$ brain uptake (as measured by digital autoradiography), which may depict a regulatory mechanism associated with total copper content to maintain brain copper homeostasis at a constant level (196).

2.2.2 Functions of copper in the CNS

In the CNS, copper acts as a cofactor for two essential enzymes that are ubiquitously present in all mammalian tissues, CCO and Cu/Zn SOD-1. These metalloenzymes are particularly crucial

for brain function since the brain has a high rate of oxidative metabolism which enhances its vulnerability to oxidative stress. The critical role of these proteins in the maintenance of brain homeostasis is illustrated by the Menkes genetic disorder, in which brain copper deficiency arising from mutations in the gene encoding the ATP7A copper transporter leads to a significant reduction in CCO and Cu/Zn SOD-1 activities, which in turn contributes to the neurodegenerative phenotype of the disease (197).

Copper is also a fundamental cofactor for a number of CNS-specific enzymes, including DβH, peptidylglycine α-amidating monooxygenase (PAM) and various copper amine oxidases. DβH is a component of the catecholamine biosynthetic pathway which catalyses the side-chain hydroxylation of dopamine into noradrenaline, while PAM is a bifunctional enzyme with two catalytic domains, copper-dependent peptidylglycine α-hydroxylating monooxygenase (PHM) and peptidyl-α-hydroxyglycine α-amidating lyase (PAL), responsible for the post-translational α-amidation of peptidylglycine bioactive substrates (Figure 2.1).

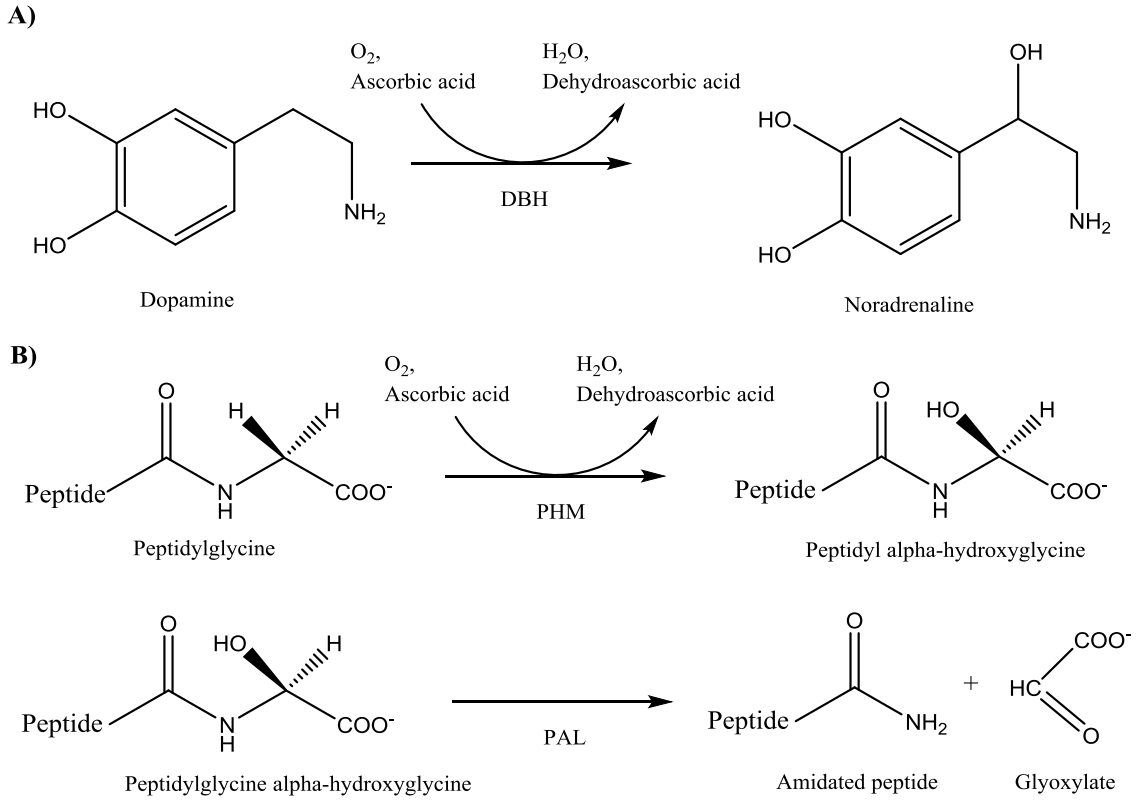

Figure 2.1: A) Synthesis of noradrenaline catalysed by DβH; **B)** Two-step α-amidation reaction catalysed by PAM consisting of stereospecific hydroxylation of peptidylglycine substrate catalysed by PHM (top), and *N*-dealkylation of peptidyl α-hydroxyglycine intermediate to produce α-amidated peptide and glyoxylate catalysed by PAL (bottom) (83, 198).

Although their substrate specificities are grossly different, these two cuproenzymes catalyse a similar type of reaction (i.e. oxygen- and ascorbate-dependent hydroxylation) and share up to 28 % structural identity throughout a common 270 aminoacid sequence (199). PAM is highly expressed in most neuronal and endocrine cells as well as glial cells and atrial myocytes, whereas DβH is found almost exclusively in chromaffin cells of the adrenal medulla and synaptic vesicles of noradrenergic neurons (200, 201). Impaired DβH activity, as observed in the rare genetic DβH deficiency disorder, has been associated with symptoms such as hypotension, hypotonia or hypoglycaemia, but surprisingly does not have severe consequences for CNS function (202). On the other hand, deletion of the PAM gene, which results in complete absence of peptide amidation activity, has been shown to induce fatal cardiovascular deficits during embryonic development in PAM null mutant mice but has not been found to alter neuroblast proliferation (203).

Copper-dependent ferroxidase ceruloplasmin is known to play a critical role in the regulation of mammalian iron homeostasis. Although this enzyme carries up to 95 % of the copper found in blood, the main physiological role of ceruloplasmin does not seem to be copper transport, as evidenced by normal copper metabolism in patients suffering from aceruloplasminemia, but plasma iron transport and efflux from mammalian cells. Despite being a systemic iron metabolism disorder, lack of ceruloplasmin activity in aceruloplasminemic patients has particularly severe manifestations for the CNS resulting from regional iron accumulation in the retina and basal ganglia (204). The presence of these neurological abnormalities suggests an essential role for ceruloplasmin in iron homeostasis in the CNS. Nonetheless, it has been shown that serum ceruloplasmin does not cross the blood-brain barrier under normal conditions, which implies the existence of local expression mechanisms of the protein within the brain (205). Klomp and co-workers first detected abundant ceruloplasmin gene expression in the epithelial cells of the choroid plexus as well as in specific subpopulations of astrocytes surrounding the brain microvasculature and retina (206). Subsequently, research by Patel *et al.* revealed that astrocytic ceruloplasmin was anchored to the cell surface via a glycosylphosphatidylinositol (GPI) motif and that this GPI-anchored form of the protein predominated in the CNS. Except for the GPI anchor, astrocyte-expressed ceruloplasmin was found to be structurally and functionally similar to the form of the protein produced by the liver

and choroid plexus (207, 208). The proximity of ceruloplasmin expression sites to blood-CNS barriers (BBB and blood-cerebrospinal fluid barrier [BCSFB]) along with the increased iron deposition observed in the brains of aceruloplasminemic patients support a role for ceruloplasmin in the efflux of ferrous ions from CNS cells, potentially through interaction with an iron transport protein.

In addition to its role as an enzymatic cofactor, copper is also thought to modulate synaptic transmission. Colburn *et al.* first reported a greater concentration of copper in synaptosomes and synaptic vesicles isolated from mouse brain tissue compared to magnesium, iron and zinc (209). In 1988, Hartter and co-workers proposed a role for copper as a neuromodulator after observing radiocopper release into the extracellular space in response to potassium-induced depolarisation in rat hypothalamic tissue incubated with a ^{67}Cu-histidine complex (210). Since then, a great number of studies have explored the effects of copper at brain synapses and its importance for synaptic plasticity. For example, it has been shown that exposure to micromolar concentrations of copper (~18-30 μM) produces an inhibitory effect on N-methyl-D-aspartate (NMDA), γ-aminobutyric acid (GABA) and α-amino-3-hydroxy-5-methyl-4-isoxazolepropionic acid (AMPA) receptors in cultured neurons, and suppresses long-term potentiation in rat hippocampal slices (211-214). Contrarily, prolonged incubation of neuronal cultures with lower concentrations of $CuCl_2$ (~10 μM) has been found to enhance AMPA receptor-mediated synaptic activity. This increase in AMPAergic neurotransmission was suggested to derive from AMPA receptor anchorage in post-synaptic membranes as a result of a copper-induced increase in the levels of scaffolding protein PSD95 (215). Although these studies are informative, they only report effects of exogenously applied copper on synaptic activity and therefore further research is required to elucidate the exact role of synaptically released endogenous copper in neurotransmission.

Copper has been reported to have an inhibitory effect on long-term potentiation but has also been suggested to play a neuroprotective role against glutamate-induced excitotoxicity. Schlief and co-workers showed that NMDA receptor activation resulted in rapid and reversible trafficking of the ATP7A copper transporter from the trans-Golgi network followed by copper efflux in cultured hippocampal neurons. ATP7A translocation was found to depend on calcium

entry through the NMDA receptor but not on intracellular copper concentration (216). Further research revealed that $CuCl_2$ addition (200 μM) decreased cell death after NMDA receptor activation in cultured neurons exposed to excitotoxic levels of glutamate/glycine, and that this protective effect was dependent on endogenous nitric oxide production (217). From this evidence, Schlief *et al.* suggested that ATP7A-related copper efflux might promote the S-nitrosylation of NMDA receptors in order to reduce excitotoxic cell death after glutamate synaptic release. Thus, ATP7A loss-of-function in MD could lead to increased neuronal excitotoxicity, which in turn could be responsible for the rapid neuronal degeneration and high seizure occurrence characteristic of this disorder (218).

2.2.3 Copper uptake into the CNS

Although many advances in the understanding of systemic copper metabolism have been made, copper processing within the CNS has not been widely investigated. Most of the current knowledge on brain copper metabolism derives from studies in yeast and extracerebral mammalian cell models. However, the importance of copper in the development and function of the CNS as well as the vulnerability of the brain to metal-induced oxidative stress imply the existence of system-specific copper handling mechanisms.

Plasma copper can enter the CNS through the BBB and/or BCSFB, which respectively separate the brain interstitial fluid and the CSF from blood. The exact role of these barrier systems in the maintenance of brain copper homeostasis is still unknown but it has been suggested that circulating copper may enter the brain mainly through the BBB, while the BCSF may act as a regulatory site of copper levels in the CSF. Choi and co-workers first provided evidence in support of this possibility in a study that evaluated the uptake kinetics of three radiocopper species ($^{64}CuCl_2$, ^{64}Cu-albumin and ^{64}Cu-ceruloplasmin) into brain vessels, parenchyma, choroid plexus and CSF using an *in situ* brain perfusion method. This study showed that the highest copper uptake in barrier tissues and brain parenchyma was achieved when the brain was perfused with ionic radiocopper, thus demonstrating that copper is transported into the brain and CSF as a free copper ion and not as a protein-bound species. Furthermore, it was found that the uptake rate of $^{64}CuCl_2$ by the choroid plexus was 3.2-fold faster compared to the transport rate for copper in cerebral capillaries but that the rate of copper entering the brain

parenchyma from brain vessels was higher than the rate of copper entering the CSF from the choroid plexus (219). Using a two-chamber *in vitro* BCSFB model system, Monnot *et al.* revealed that copper efflux from the CSF to blood across a layer of primary choroidal epithelial cells was almost 2-fold higher than copper transport in the opposite direction. Taken together, these findings suggest that copper may enter the brain primarily through the BBB and that excess copper may be transferred from the brain parenchyma into the CSF and exported back into the bloodstream via the BCSFB. The high copper sequestration capacity exhibited by choroid plexus epithelial cells and the low concentration of copper in CSF compared to copper levels in plasma may support a role for the BCSFB as a regulatory site of copper levels in the CSF (220).

Copper transporters Ctr1, DMT1, ATP7A and ATP7B are strongly expressed in brain barrier tissues and consequently are thought to mediate copper transport into and out of the CNS. The levels of gene expression of Ctr1 and ATP7A have been reported to be significantly greater (1.2- and 3.4-fold, respectively) in the choroid plexus compared to those in the BBB, whereas ATP7B has been found to be more abundant in cerebral capillaries than in the choroid plexus. Gene expression of non-specific metal transporter DMT1 at the BBB has been found to be equivalent to that at the choroid plexus but almost 3-fold higher when compared to that in the brain parenchyma (219).

The importance of Ctr1 in copper transport into the CNS is underlined by the nearly 50 % decrease in brain copper levels exhibited by Ctr1-deficient mice (221). The involvement of ATP7A in the mobilisation of copper ions from blood to brain seems also irrefutable as depicted by severe copper deficiency resulting from ATP7A loss-of-function observed in the brains of MD patients. However, ATP7A might play a dual role in copper transport since functional analysis has demonstrated that treatment with *p*-chloromercuribenzoate, a potent inhibitor of ATP7A function, markedly reduced copper efflux from mouse cerebrovascular endothelial cells (222). This possibility is further supported by the significant decrease in brain copper concentration observed in transgenic mice overexpressing ATP7A (223). Although ATP7B is also highly expressed in brain endothelial cells, its functional role in the BBB remains largely undefined. However, brain copper overload arising from ATP7B loss-of-function in WD seems to suggest

that this transporter might play a role in the export of excess copper to blood across the BBB (224).

While Ctr1, ATP7A and ATP7B are located in the cytoplasm in most brain regions, the choroid plexus epithelium (BCSFB) exhibits distinct patterns of distribution, which illustrates the unique role that this region plays in brain copper homeostasis. Immunohistochemistry of copper transport proteins showed that Ctr1 and ATP7B were primarily located along the apical membrane of the choroidal epithelium, whereas that ATP7A was mostly concentrated at the basolateral surface. This distribution pattern might indicate that Ctr1 mediates the transport of excess copper from the CSF into the choroid plexus and that ATP7A facilitates its export back into circulation across the basolateral membrane. The localisation and slow kinetics of ATP7B (with respect to ATP7A) seem to suggest that this transporter could participate in the transfer of copper ions from the choroid plexus into the CSF (225).

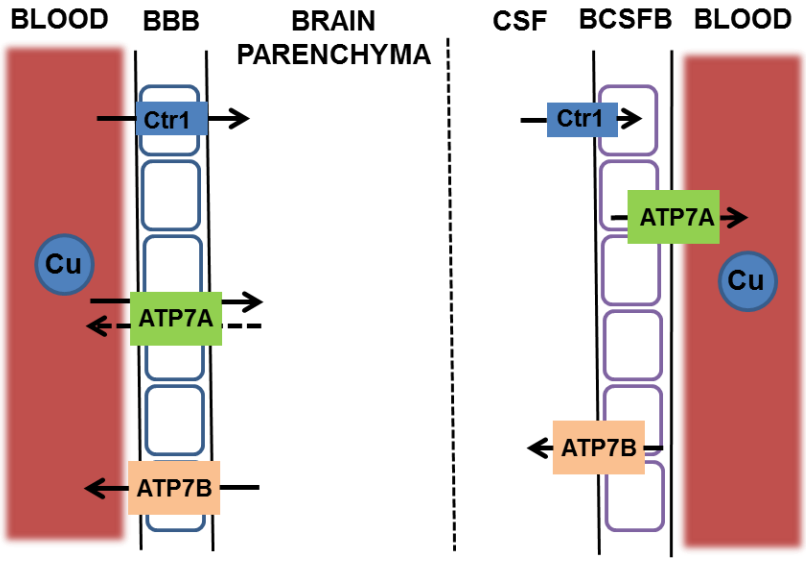

Figure 2.2: Proposed copper uptake and export mechanisms at the BBB and BCSFB. Copper transport across the BBB to the brain parenchyma is thought to be mediated by Ctr1 and ATP7A, whereas ATP7B might facilitate copper efflux back into circulation. Ctr1 has also been suggested to play a role in the transport of excess copper from the CSF into the choroid plexus. ATP7A is thought to facilitate the transfer of copper ions from the BCSFB to blood, while ATP7B has been proposed to mediate copper delivery from the choroid plexus to the CSF (221, 224, 225).

2.2.4 Astrocyte regulation of brain copper homeostasis

Astrocytes are the most abundant cell type in the CNS and perform multiple essential functions, including regulation of cerebral blood flow, glycogen storage, BBB preservation, modulation of synaptic function and maintenance of CNS homeostasis of neurotransmitters, metabolites and redox-active metal ions (226). Although this cell type is present throughout most of the CNS,

some astrocytes have been found in close association with brain endothelial cells and are thought to contribute to the development and regulation of the BBB phenotype. The strategic localisation of perivascular astrocytes between capillary endothelial cells and neuronal bodies has led to the suggestion that these cells additionally regulate the supply of metabolic substrates, oxygen and trace metals to neurons (227). It is therefore thought that astrocytes are the first brain parenchymal cells that take up copper ions after they cross the BBB.

Several studies have demonstrated that astrocytes efficiently accumulate copper ions and show a greater resistance to copper-induced toxicity when compared to other brain cells (228-231). This feature implies that astrocytes may not only supply copper to neurons but also serve as depots for copper in the brain to protect neurons and other cell types against metal-induced oxidative damage. Brown *et al.* revealed that cultured astrocytes inhibited copper toxicity in cerebellar neurons exposed to 100 μM of copper (II) sulphate. This protective effect was shown to be dependent on the expression of the copper-binding prion protein (PrP), which was released from neurons upon exposure to copper and taken up by astrocytes (230). The ability of astrocytes to sequester copper from neurons may be associated with the biological activity of PrP but is also supported by the high levels of glutathione and MTs present in these cells (229, 231-234). Scheiber and co-workers observed a concentration-dependent increase in glutathione synthesis in cultured astrocytes after copper treatment. Interestingly, this elevation of cellular glutathione content as a result of increased intracellular copper concentration does not occur in most cell types, which highlights the unique capacity of astrocytes to store and detoxify copper ions (229).

Astrocytes have been suggested to play a central role in the maintenance of brain copper homeostasis since they are involved both in the supply of copper ions to neurons, and the storage and detoxification of excess copper exported from neurons and other brain cells. Nevertheless, little is known about the molecular mechanisms that control astrocytic copper trafficking. Transport protein Ctr1 has been found to be expressed in cultured astrocytes and is thought to the primary contributor to cellular copper uptake (228). Copper export from astrocytes has been proposed to be mediated by ATP7A, although ATP7A-independent transport mechanisms are also thought to operate (235). Evidence for the involvement of

ATP7A in copper efflux from astrocytes was first provided by Kodama *et al.*, who reported increased astrocytic copper content in a mouse model of MD as a result of ATP7A dysfunction (236).

Considering the importance of astrocytes in brain copper metabolism, the mechanisms underlying astrocytic copper trafficking require further investigation in order to understand better the consequences of their malfunction for global copper homeostasis in the CNS.

2.2.5 Copper trafficking in the CNS

Despite the essential contribution of copper to the development and function of the CNS, the molecular mechanisms involved in copper trafficking within the brain and spinal cord remain poorly understood. Additionally, little is known about the differences in copper transport systems existing between the main CNS cell types. However, many cuproenzymes and copper chaperones commonly expressed in other body tissues have been also identified in the CNS (e.g. Cu/Zn SOD-1, CCO, Ctr1, Atox1, CCS, Cox17) (237-241).

Similar to copper entry into enterocytes (see Chapter I, section 1.3.2.1), copper transporter Ctr1, in conjunction with an unidentified metalloreductase, is the main transporter responsible for copper uptake into brain cells. Loss of Ctr1 function has been shown to particularly affect neural tissue, leading to abundant cell death and embryonic lethality in knockout zebra fish and mouse models (221, 242). The identity of the protein that facilitates the reduction of copper (II) to copper (I) and subsequent copper (I) uptake into brain cells is still under discussion, but it has been suggested that cupric reductase Steap2, which is highly expressed in the epithelial layers of the choroid plexus, could be a potential candidate (243). A synthetic peptide representing the copper-binding site of the amyloid precursor protein (APP) has been shown to be capable of reducing copper (II) to copper (I) *in vitro*, suggesting a potential role for this protein in the Ctr1-mediated copper uptake process (244). The non-specific DMT1 metal transporter is also thought to contribute to neuronal copper uptake, although it seems to play a more significant role in brain iron transport.

Despite the established role of Ctr1 in cellular copper uptake, Davies *et al.* surprisingly showed that the distribution of the transporter in several regions of the human brain (visual cortex, anterior cingulate cortex, caudate putamen, substantia nigra and cerebellum) was mainly cytoplasmic, except in barrier tissues where it was found closer to the apical cell surface. The authors suggested that in copper-sufficient cells Ctr1 might exist as an internalised protein pool, rather than as a membrane-bound transporter, and move back to the plasma membrane under conditions of copper deficiency. Furthermore, immunohistochemical staining of Ctr1 revealed that this transporter was mainly concentrated in neuronal cells in the cerebral cortex and caudate putamen, whereas in the cerebellum it was strongly expressed in Bergmann glia but not in Purkinje neurons (225).

Once inside brain cells, copper (I) ions are chaperoned by various copper-binding proteins and incorporated into specific cuproenzymes, or form transient complexes with glutathione or metallothioneins for storage purposes. Atox1 is a ubiquitously expressed copper chaperone whose function consists in transferring the metal to copper ATPases ATP7A and ATP7B for subsequent delivery to copper-dependent enzymes or efflux from cells. In the rat brain, the highest concentrations of Atox1 have been detected in the pyramidal neurons of the cerebral cortex and hippocampus as well as in the neuronal cells of the locus coeruleus, which might indicate a higher need for copper in these regions in the rodent brain (225, 245).

Copper ATPases ATP7A/B are crucial components of the copper homeostasis machinery since they facilitate the incorporation of copper into essential copper-dependent enzymes and also exert a tight control over intracellular copper levels, which is of particular importance for the CNS. The faster kinetics of copper transport by ATP7A compared to ATP7B seem to suggest that ATP7B might be mainly responsible for the delivery of copper ions to cuproenzymes (e.g. ceruloplasmin), while ATP7A might be more inclined to play a regulatory role in the maintenance of cellular copper content. Both transporters are ubiquitously expressed in the brain but are especially abundant in barrier tissues, cerebellum, olfactory bulb, hippocampus and cerebral cortex (246, 247). In the CNS, the levels of expression of ATP7A/B seem to be inversely correlated to those of Ctr1, although the significance of this difference in expression patterns still needs to be fully elucidated. It has been proposed that cells that express high

levels of Ctr1 and relatively low levels of ATP7A/B might have greater metabolic requirements than other cell types, whereas that cells that exhibit greater levels of expression of copper ATPases relative to Ctr1 might be more sensitive to copper-induced cellular toxicity. For example, in the human brain, abundant expression of ATP7A/B was observed in Purkinje neurons in the cerebellum but not in Bergmann glia, while Ctr1 showed the inverse pattern of expression. Copper-transporting ATPases were also present at high levels in the proximal fibers of the anterior cingulate cortex and in the striosomes of the caudate putamen complex, while Ctr1 expression was reported to be low in these regions (225).

ATP7A has been reported to release copper ions into the synaptic cleft in order to reduce neuronal excitotoxicity after NMDA receptor-mediated neurotransmission in hippocampal neurons (216, 217). In view of this, the lack of ATP7A expression observed in the axons of neurons of the substantia nigra, the brain region with the highest concentration of dopaminergic neurons, seems rather surprising (225). However, it has been suggested that copper might be released into the synaptic cleft by ATP7A-mediated vesicle exocytosis and not necessarily pumped out of the cell across the plasma membrane directly by ATP7A (235).

The copper transporter CCS is the main transporter responsible for activating the copper-dependent antioxidant enzyme Cu/Zn SOD-1 through the insertion of copper, although the existence of CCS-independent Cu/Zn SOD-1 metalation mechanisms has also been reported (46). The distribution of CCS within the brain mirrors that of Cu/Zn SOD-1, which implies that CCS might have a role in CNS disorders characterised by Cu/Zn SOD-1 dysfunction, such as ALS. In the CNS, CCS expression was reported to be similar across all brain and spinal cord regions and was detected throughout the neuropil, primarily in neurons and some astrocytes. Although CCS was found to be present in most brain regions (e.g. cerebellum, cerebral cortex, hippocampus), it was reported to be largely absent from white matter tracts in both mouse and human brain (239). Angeletti *et al.* revealed that CCS was able to interact with the cytoplasmic domain of β-secretase 1 (BACE1), one of the enzymes involved in the production of the AD-associated amyloid-β peptide (Aβ). This group demonstrated that overexpression of BACE1 led to a significant decrease in Cu/Zn SOD-1 activity in cultured rat cortical neurons, thus revealing

a competitive copper (I)-binding mechanism between CCS and BACE1 that might contribute to increased vulnerability to oxidative stress in AD (248).

Another essential copper chaperone is Cox17, which mediates the incorporation of copper into the cellular respiration enzyme CCO along with accessory proteins Sco1 and Cox11. Little is known about the cellular functions of this copper transporter in the CNS. Detailed examination of the expression pattern of Cox17 in the mouse brain revealed that this chaperone was ubiquitously expressed in all brain regions, with highest levels of expression observed in the pituitary gland. Abundant expression of Cox17 was also detected in the cerebral cortex, brain stem and cerebellum, while the lowest expression levels were measured in the hippocampus and hypothalamus. High expression of Cox17 in pituitary tissue strongly suggests that this transporter might not only be involved in cellular respiration but might also play a role in neuroendocrine function (240).

The APP and PrP, which are commonly associated with the pathogenesis of AD and prion diseases, have been reported to bind copper ions and are therefore thought to play a role in normal copper metabolism (249, 250). It was initially suggested that PrP could play a role in the uptake of copper into brain cells since PrP-knockout mice were found to exhibit severely reduced copper levels in the brain as well as decreased Cu/Zn SOD-1 activity (251). Pauly and co-workers later observed that exposure to copper (II) sulphate (> 200 μM) reversibly stimulated the endocytosis of PrP in cultured neuroblastoma cells, suggesting the possibility of PrP-mediated copper uptake by endocytosis (252). PrP has also been proposed to act as a buffer for copper (II) ions at the presynaptic terminal, mediating both the release of copper into the synaptic cleft after neurotransmission and the redistribution of copper into the presynaptic cytosol (253). Moreover, Brown and co-workers reported that copper-bound PrP had Cu/Zn SOD-1-like activity, suggesting a potential neuroprotective role for PrP against oxidative stress (254).

The physiological function of APP in copper metabolism remains equally unresolved. Multhaup and co-workers reported that a synthetic peptide representing the copper-binding site of APP was capable of reducing copper (II) to copper (I) *in vitro* (244). Suazo *et al.* demonstrated that

APP overexpression induced an increase in copper (II) reduction capacity and intracellular copper levels in HEK293 cell cultures exposed to 10 μM of copper, suggesting that APP could act as a metalloreductase in the Ctr1-mediated copper uptake mechanism (255). Nevertheless, an earlier study by Treiber *et al.* provided conflicting evidence that showed that expression of human APP in cultured yeast cells incubated in media supplemented with 0.5 μM and 1 mM of copper resulted in a significant reductions in intracellular copper levels compared to control cells (256). These findings were consistent with previous transgenic mouse studies that demonstrated that APP overexpression also resulted in a decrease in brain copper content *in vivo* (257, 258), suggesting a potential role for this protein as a copper efflux transporter.

Copper trafficking in the CSF differs considerably from that in blood plasma. In the CSF, copper is not predominantly bound to ceruloplasmin but to a low-molecular-weight protein or ligand not yet identified (259). The concentration of copper in the CSF may be indicative of BCSFB integrity or abnormal copper metabolism. For example, elevated copper concentration in the CSF in patients suffering from WD results from the accumulation of copper in the brain due to ATP7B loss-of-function (260).

2.2.6 Copper buffering in the CNS

Due to its elevated copper content and high oxygen demand, the brain is particularly vulnerable to copper-induced oxidative stress. It is therefore crucial that the intracellular concentration of free copper ions in all brain cells is maintained at very low levels.

MT proteins are an essential component of the metal homeostasis machinery since they are able to buffer several heavy metals (e.g. Cd, Pb, Zn, Co, Hg, Cu), thus minimising metal-induced cellular toxicity. MTs bind excess copper (I) ions for detoxification purposes but also serve as a copper depot in the event of intracellular copper deficiency (261). The role of MTs in the maintenance of copper homeostasis is supported by reported increases in MT content in response to cellular copper overload. Wake *et al.* observed 16- and 6-fold increases in hepatic and renal MT mRNA in rats intraperitoneally injected with $CuCl_2$ (1.5 mg/kg) (262). In the CNS, elevation of intracellular MT levels upon exposure to copper was also reported. Hidalgo and co-workers demonstrated that MT expression levels increased up to 5-fold in neurons and up to

15-fold in astrocytes in response to exposure to a range of copper concentrations (0-50 µM) (263). The difference in MT content observed between neurons and astrocytes might illustrate the greater resistance of astrocytes against copper toxicity compared to other cell types.

The localisation of MT expression within the CNS remains unclear, probably due to the different specificities and sensitivities of the antibodies used in immunohistochemical studies. For example, Hidalgo *et al.* reported elevated MT immunoreactivity in glial cells in most regions of the rat brain as well as in neuronal cell subsets of the cerebral cortex, hippocampus, hypothalamus, brain stem and cerebellum. However, in an earlier study, Nishimura and co-workers detected almost no MT expression in the adult rat brain and intense MT immunostaining in glial cells, arachnoid and pia mater of the mouse brain but not in neurons. Both studies revealed strong MT expression in the ependymal cells of the ventricular system and choroid plexus, underlining the potential role of the BCSFB as a site for copper homeostatic regulation (263, 264).

MT-I and -II are protein isoforms ubiquitously expressed in most organ systems, while MT-III is predominantly expressed in the CNS. In addition to its role in heavy metal detoxification and intracellular copper storage, MT-III is thought to be involved in the utilisation of zinc as a neuromodulator since a direct correlation has been established between neurons with high expression levels of MT-III and neurons that store zinc at their presynaptic terminals (265). This possibility is further supported by the increased susceptibility to seizures and hippocampal neuron injury observed in MT-III-deficient mice (266).

The cellular antioxidant glutathione has also been shown to form stable complexes with copper (I) ions. This tripeptide is present intracellularly at millimolar concentrations and is therefore considered the primary contributor to the exchangeable cytosolic copper pool (267). Freedman and co-workers reported that over 60 % of the cytoplasmic copper isolated from wildtype hepatoma and copper resistant cell lines was in the form of copper (I)-glutathione complex (268). Glutathione plays a crucial role in copper storage and detoxification but is also thought to be involved in intracellular copper trafficking. Carroll *et al.* demonstrated that the reduced form of glutathione mediates the CCS-independent incorporation of copper into mammalian Cu/Zn

SOD-1 in both yeast and murine cells deficient for CCS (46). Moreover, glutathione is also thought to transfer copper (I) ions to MT proteins after they enter the cell. Freedman *et al.* revealed that inhibition of glutathione synthesis led to a 55 % decrease in ^{67}Cu-MT concentration in cultured wildtype hepatoma cells (268). A role for glutathione in the early steps of cellular copper uptake was further corroborated by Maryon and co-workers, who reported a significant reduction in the initial rate of copper uptake as a result of glutathione depletion in HEK293 cells (23). Whether glutathione exerts this function also within the CNS remains unknown.

2.3 COPPER IN NEUROLOGICAL DISORDERS

Copper is an essential nutrient for CNS development and function but has also been shown to promote molecular processes associated with aging and age-related diseases, such as ROS production and the formation of protein aggregates. Hence, copper homeostasis in the CNS needs to be tightly regulated, as even a slight imbalance may have deleterious consequences. Copper (I) can react with molecular oxygen to produce superoxide radicals and subsequently hydrogen peroxide (Figure 2.3.a). Copper (II) ions can be then reduced by superoxide radicals to copper (I), which in turn can react with hydrogen peroxide to produce hydroxyl radicals via the Fenton mechanism (Figure 2.3.b). The formation of these ROS species may lead to lipid and protein oxidation, oxidative inactivation of specific enzymes and irreversible DNA damage, and is a common pathological hallmark in most neurodegenerative disorders (269).

a) $Cu^{+} + O_2 \longrightarrow Cu^{2+} + O_2^{-}$

$2O_2^{-} + 2H^{+} \longrightarrow H_2O_2 + O_2$

b) $Cu^{+2} + O_2^{-} \longrightarrow Cu^{+} + O_2$

$Cu^{+} + H_2O_2 \longrightarrow Cu^{+2} + OH^{\cdot} + OH^{-}$

Figure 2.3: Copper-catalysed production of ROS.

Copper has also been reported to bind to a number of proteins associated with neurodegenerative diseases (e.g. Aβ, APP, PrP, α-synuclein) and subsequently promote their aggregation process. In addition to the accumulation of neurotoxic aggregates in the brain, copper binding to these molecular entities may lead to the disruption of normal copper metabolism pathways and to a further increase in the level of oxidative stress.

Copper dyshomeostasis in the CNS is thought to contribute either directly or indirectly to the pathophysiology of various neurological diseases, including AD, WD, ALS, MD, prion disease, Huntington's disease (HD) and PD. Although multiple reports have evidenced a role for copper in these disorders, the causes and consequences of copper dysregulation as well as its significance in disease severity and progression are not fully understood. The following sections of this review will evaluate the current state of knowledge on copper dyshomeostasis in the above mentioned neurological diseases and discuss its potential as a diagnostic and therapeutic biomarker.

2.3.1 Menkes disease

Mutations in the gene encoding the copper transporter ATP7A are the main cause of the X-linked recessive Menkes syndrome. Symptoms manifested by patients suffering from MD include sparse and fragile hair, progressive neurodegeneration and connective tissue abnormalities (270). ATP7A loss-of-function results in altered copper gastrointestinal absorption and hyperaccumulation in intestinal and renal tissues, which in turn leads to severe copper deficiency in peripheral organs, including brain. Due to decreased brain copper bioavailability, the activities of essential cuproenzymes (e.g. Cu/Zn SOD-1, ceruloplasmin, CCO, LOX, DβH) are significantly reduced in MD, resulting in impaired antioxidant activity, decreased neurotransmitter synthesis, enhanced sensitivity to glutamate-mediated NMDA receptor-dependent excitotoxicity and reduced axon outgrowth. Brain copper deficiency is therefore the primary contributor to the neurodegenerative phenotype of MD, which is characterised by profound developmental delay and mental retardation (271).

Among the available therapeutic strategies for the treatment of MD, intravenous administration of copper complexes (e.g. copper-histidine) has shown some degree of success in restoring physiological copper levels and improving neurodevelopmental outcomes. However, the efficacy of this treatment has been found to be highly dependent on early diagnosis, residual ATP7A activity and ATP7A mutation type (272, 273). Copper replacement treatment is thought to be less effective if initiated after two months of age since the injected copper is sequestered by mature BBB endothelial cells and is not transported to neurons. In order to improve copper delivery to neuronal cells, the combination of intravenous copper injections and oral

administration of lipophilic chelator disulfiram was evaluated in a mouse model of MD. Combination therapy resulted in increased copper concentration (as measured by atomic absorption spectroscopy) in the cerebellum, liver and serum of macular mice and improved CCO and DBH activities, thus suggesting that the administration of disulfiram facilitated copper transfer across the BBB (274). Nomura *et al.* also investigated the effects of disulfiram pre-treatment on copper biodistribution in MD mice injected with $^{64}CuCl_2$ by PET imaging. PET imaging showed significantly reduced renal ^{64}Cu concentration and enhanced liver and brain ^{64}Cu uptake in macular mice pretreated with disulfiram compared to untreated controls at 4 h post-injection of $^{64}CuCl_2$ (kidneys: 14.54 vs. 25.56 %ID/g; liver: 29.42 vs. 13.83 %ID/g; brain: 5.12 vs. 0.96 %ID/g). Moreover, *ex vivo* brain autoradiography demonstrated that disulfiram pretreatment in macular mice led to increased ^{64}Cu accumulation in the cerebral cortex and thalamus and decreased ventricular uptake (154). Despite promising preclinical outcomes, combination therapy has produced mixed results in patients with MD and is still under investigation (275).

ATP7A gene addition has emerged as a very promising treatment option for MD sufferers since it is likely to improve the outcome of patients that remain unresponsive to conventional therapies. Combined injection of human ATP7A complementary DNA and $CuCl_2$ into the lateral cerebral ventricles of neonatal MD mice was reported to significantly enhance survival rates and brain copper content as well as CCO and DβH activities. Nevertheless, although the combination of ATP7A gene addition and copper treatment restored myelination to normal levels and prevented cortical ultrastructural abnormalities, this type of treatment was not able to decrease the loss of Purkinje neurons in MD mice, which is thought to impact significantly upon motor coordination function (276).

2.3.2 Wilson's disease

WD is an autosomal recessive disorder caused by mutations in the gene encoding the ATP7B transporter. Copper-transporting ATP7B is predominantly expressed in the liver but can also be found in the kidneys, intestines, mammary glands, eyes and brain (277). The main biological function of ATP7B is the incorporation of copper into ceruloplasmin, a copper-dependent ferroxidase that mediates the transfer of iron into transferrin. In addition to its role in the copper

metalation of ceruloplasmin, ATP7B is also involved in the excretion of excess hepatic copper into the biliary tract and the efflux of copper ions from the brain. Defective ATP7B activity in WD therefore results in copper and iron hyperaccumulation in the liver, kidneys and brain, which in turn leads to liver disease, oxidative damage and neuronal degeneration. Brain copper overload in WD may give rise to several neuropsychiatric symptoms, including body tremors, dystonia, depression or psychosis (278).

Unlike MD, WD is a relatively treatable condition. The use of copper chelating agents (e.g. D-(−)-2-amino-3-mercapto-3-methylbutanoic acid [D-Penicillamine], *N*,*N′*-bis(2-aminoethyl)ethane-1,2-diamine [Triethylenetetramine]) has been shown to be effective in promoting urinary copper excretion, thus reducing excess copper in specific organs. D-Penicillamine is most commonly used for this purpose but its clinical application is somewhat limited by high incidence of side effects. An alternative option for the treatment of WD is the administration of zinc salts. Ingestion of zinc salts has been found to block gastrointestinal copper absorption and to enhance the expression of MT proteins in intestinal epithelial cells, which in turn leads to the trapping of copper in the intestinal mucosa and its subsequent excretion. In addition, zinc therapy is also thought to increase MT levels in hepatocytes, thus decreasing copper-induced toxicity in the liver. The combination of zinc and chelation therapies for the treatment of WD has been proposed but so far no significant improvements compared to the individual treatments have been reported (279, 280).

The most common pathological hallmark found among WD patients is the formation of Kayser-Fleischer rings due to copper deposition in the periphery of the cornea. The presence of the latter together with lower-than-normal ceruloplasmin levels in blood plasma and elevated urinary copper is typically sufficient for a positive diagnosis. Nonetheless, additional diagnostic approaches are required for cases in which these symptoms are absent. MRI has been used with some success to examine brain abnormalities in WD sufferers (281). Another non-invasive diagnostic method that has shown great promise for clinical application is $^{64}CuCl_2$-PET. Peng *et al.* demonstrated the feasibility and utility of imaging the trafficking of both intravenously and orally administered $^{64}CuCl_2$ with PET in an ATP7B knockout mouse model of WD. This group revealed significantly increased hepatic ^{64}Cu accumulation in ATP7B knockout mice orally

treated with $^{64}CuCl_2$ compared to healthy controls at 24 h post-ingestion of the tracer (179). Peng and co-workers also reported significantly increased hepatic ^{64}Cu concentration in ATP7B knockout mice intravenously injected with $^{64}CuCl_2$ relative to controls at 24 h post-injection of the tracer, as well as significantly reduced ^{64}Cu uptake in the kidneys, heart and brain of the transgenic mice compared to wildtype controls (153). Alternatively, Gray *et al.* used $^{64}CuCl_2$-PET to characterise the mechanism underlying urinary copper elevation in WD. This group revealed an age-dependent decrease in the capacity of ATP7B-knockout livers to accumulate copper, resulting in increased renal copper excretion. This decrease in hepatic ^{64}Cu accumulation was found to occur due to age-dependent downregulation of the Ctr1 copper transporter in the liver of ATP7B-knockout mice (180). Taken together, these preclinical findings demonstrate the potential of $^{64}CuCl_2$-PET as a tool to detect and monitor WD as well as to understand better its pathophysiology *in vivo*.

2.3.3 Amyotrophic Lateral Sclerosis

ALS or Lou Gehrig disease is a fatal neurodegenerative disorder that affects primarily the motor neuron system. The main pathological hallmarks of the disease include degeneration and death of motor neurons and gliosis. Most ALS cases are sporadic, while 5-10 % are due to genetic causes. 20-25 % of familial ALS cases derive from mutations in the gene encoding the copper-dependent enzyme Cu/Zn SOD-1. Over 155 mutations in this gene have been identified so far, although only some of these have been described as pathogenic (282, 283).

The mechanism by which mutant Cu/Zn SOD-1 induces motor neuron death remains unclear. It has been proposed that mutations in the Cu/Zn SOD-1 gene could enhance the pro-oxidative capacity of the enzyme, thus leading to oxidative damage and motor neuron degeneration. Conversely, it has been suggested that mutations near the metal-binding sites of Cu/Zn SOD-1 could result in loss of function of the enzyme, deeply affecting the antioxidant defence system of motor neurons. Finally, it has also been proposed that the deleterious effects of mutant Cu/Zn SOD-1 could be due to the formation of intracellular mutant Cu/Zn SOD-1 aggregates. This is supported by the detection of protein inclusions rich in mutant Cu/Zn SOD-1 in the spinal cord of familial ALS sufferers (284). However, the formation of these insoluble protein aggregates has been found to occur in advanced stages of the disorder and is therefore unlikely to be

responsible for progressive motor neuron loss. Instead, mutant Cu/Zn SOD-1 oligomers, which have been shown to stimulate ROS production, have been postulated to be the main neurotoxic species involved in familial ALS pathology (285).

Symptoms displayed by ALS patients reflect neuronal cell death at all levels of the motor system. Upper motor neuron degeneration causes bulbar symptoms such as slurred speech, emotional lability, muscular atrophy or respiratory dysfunction, while motor neuron loss in the cervical and lumbar regions of the spinal cord results in muscle weakness and spasms in upper and lower extremities. To date, there are no effective treatments to halt and reverse the course of ALS and most therapeutic approaches are focused on slowing the progression of the disease and improving the quality of life of patients. The only approved treatment for ALS is the oral administration of 6-(trifluoromethoxy)benzothiazol-2-amine (Riluzole). This drug is thought to exert a neuroprotective effect in some ALS patients by preventing excessive glutamate release into the synaptic cleft through the inactivation of voltage-dependent sodium channels. Although Riluzole has been shown to attenuate glutamate-mediated excitotoxicity in motor neurons, the treatment results in only a modest increase in patient survival and does not significantly improve muscle deterioration. Other therapeutic substances, including vitamin E, creatine and various antioxidant, antiapoptotic and antiexcitotoxic agents, have been evaluated but none has demonstrated substantial efficacy in human clinical trials (286, 287).

In recent years, the potential of the Cu-ATSM complex (see Chapter I, section 1.4.2.4) as a therapeutic agent for the treatment of ALS has been extensively investigated. Soon *et al.* first reported that Cu-ATSM behaved as an effective scavenger for peroxynitrite, a powerful antioxidant resulting from the reaction of nitric oxide and superoxide radicals (288). Peroxynitrite has been shown to form a neurotoxic intermediate with Cu/Zn SOD-1 that is capable of nitrating tyrosine residues in critical cellular targets, profoundly altering their structure and function (289). Soon and co-workers also demonstrated that oral treatment of transgenic mice expressing low levels of mutant Cu/Zn SOD-1 with Cu-ATSM at presymptomatic and symptomatic stages of the disease significantly delayed onset of paralysis and increased survival rate. Cu-ATSM treatment was found to reduce protein nitration and motor neuron loss and enhance the antioxidant activity of Cu/Zn SOD-1 in the spinal cord (288). McCallum *et al.* subsequently showed that Cu-

ATSM administration prolonged lifespan and improved locomotor function in transgenic mice expressing elevated levels of mutant Cu/Zn SOD-1 at early stages of the disease compared to Riluzole treatment (290). Roberts *et al.* used the same mouse model of ALS to examine the therapeutic effects of Cu-ATSM in further detail and found that Cu-ATSM treatment surprisingly increased the levels of mutant Cu/Zn SOD-1 in the spinal cord of transgenic mice. Mass spectrometry analysis revealed that most mutant Cu/Zn SOD-1 present in the spine of ALS mice was copper deficient and that Cu-ATSM was capable of improving its metal content *in vivo*, resulting in a decrease of its cellular toxicity (291). Treatment of transgenic mice overexpressing mutant Cu/Zn SOD-1 with Zn-ATSM also improved the phenotype of the disease potentially through the transmetallation of Zn-ATSM to Cu-ATSM and subsequent delivery of copper ions from the complex to Cu/Zn SOD-1 (292).

Due to the high variability in disease phenotype and the overlap between ALS and other neurodegenerative disorders, no definitive diagnostic methods currently exist for ALS. For patients with a clear-cut family history of ALS, genetic testing is applied. Routine evaluation of patients with suspected sporadic ALS includes serum, urine and CSF analysis, and electromyography to detect loss of lower motor neurons. However, these diagnostic techniques mainly serve to exclude other conditions that mimic ALS features and cannot be used to monitor disease progression and response to treatment. MRI of the brain and spinal cord has the potential to become a more specific diagnostic tool for ALS. A variety of MRI techniques aimed at detecting structural (e.g. grey/white matter volumetric changes, motor cortex atrophy) and functional (e.g. cortical activation, neuronal connectivity) abnormalities associated with ALS are currently under development (293).

The encouraging results obtained from the preclinical assessment of Cu-ATSM as a therapeutic agent along with the hypoxia selectivity exhibited by this complex recently prompted its evaluation as a diagnostic tool to delineate cerebral oxidative stress based on an over-reductive state caused by mitochondrial dysfunction in ALS. In a relatively small PET clinical study (12 ALS patients vs. 9 age-matched healthy individuals), Ikawa *et al.* reported significantly greater ^{62}Cu concentration in the motor cortex of ALS patients compared to controls at 20 min post-injection of ^{62}Cu-ATSM. ^{62}Cu accumulation in the motor cortex correlated well with the severity

of the disease, which suggests that ^{62}Cu-ATSM-PET could be a useful tool to monitor ALS progression (294).

2.3.4 Parkinson's disease

PD is another progressive neurodegenerative disorder characterised by the disruption of motor function. Patients suffering from PD generally experience slowness of movements, muscle rigidity, resting tremors, problems with balance and sensorial alterations. The key pathophysiological characteristics of this disorder are dopaminergic neuron loss, particularly in the substantia nigra, and the formation of intracellular protein inclusions known as Lewy bodies whose main component is the presynaptic protein α-synuclein. In some patients the development of PD has been linked to mutations in the gene encoding α-synuclein but in the majority of cases the causes of PD remain unknown. It has been suggested that the dysfunction of the mitochondrial complex I of the electron transport chain could play a key role in the pathogenesis of PD. Impaired mitochondrial metabolism has been evidenced in some PD patients through autopsy and *in vitro* studies. Impaired functioning of complex I has been shown to enhance the production of ROS, which in turn promotes oxidative damage to proteins, neuronal excitotoxicity and aggregation of α-synuclein into fibrils, eventually leading to neuronal death (285, 295).

The mechanism by which the formation of α-synuclein aggregates induces the death of dopaminergic neurons still needs to be elucidated. However, it has been shown that exposure to specific metals, in particular copper, might affect the aggregation behaviour of the protein. Paik *et al.* first demonstrated that copper was an effective enhancer of the self-oligomerisation of α-synuclein. The self-oligomers of this protein are thought to subsequently aggregate and form Lewy Body fibrils, although whether the fibrillar or the oligomeric forms of α-synuclein are the primary cause of toxicity in PD is still unknown (296). Copper has been shown to accelerate the formation of α-synuclein fibrils at physiological concentrations without modifying the structure of the protein aggregates. The α-synuclein protein is known to contain a high affinity copper (II)-binding site at the N-terminus and a low-affinity copper (II)-binding site at the C-terminal domain (297). Copper (II)-α-synuclein complexes have been found to oxidise ascorbic

acid, dopamine and glutathione *in vitro*, leading to the generation of ROS and to the depletion of these cellular species (298).

In addition to the ability of copper to accelerate α-synuclein aggregation and promote oxidative stress, several copper metabolism abnormalities have been detected in PD pathology. Whether these abnormalities are a consequence of the interaction of copper ions with α-synuclein is not known. Interestingly, it has recently been reported that brain areas most affected by α-synuclein pathology in PD (substantia nigra and locus coeruleum) display significantly reduced levels of copper and copper transporter Ctr1 (299). This is consistent with the marked increases in total iron content observed in these regions, probably due to decreased ceruloplasmin ferroxidase activity (194). Defective ceruloplasmin function might result from intracellular copper deficiency but might also arise from the oxidation of the enzyme leading to an enzymatic form that lacks ferroxidase activity. Olivieri and co-workers first suggested this possibility after detecting the presence of acidic isoforms of ceruloplasmin in the CSF of PD patients, resulting from the oxidation of the enzyme (300). Copper levels in the CSF have been found to be significantly higher in PD patients compared to healthy controls and this increase has been shown to correlate with disease severity and progression (301). On the other hand, plasma copper concentration is not considered a relevant marker of the pathology since only a modest decrease in plasma copper levels has been detected in PD patients (302).

A great number of therapeutic strategies have been developed in order to improve the quality of life of individuals affected by PD, including the administration of dopamine precursors, dopamine agonists and even inhibitors that block the breakdown of dopamine. Although some of these therapies are effective at controlling PD symptoms, none of them are able to halt or reverse the progression of the disease (303). The copper (II) complex Cu-ATSM, which is currently under investigation as a potential treatment for ALS, is also being evaluated as an inhibitor of peroxynitrite-mediated nitrosative stress in PD. PD patients are particularly vulnerable to nitrosative stress since their levels of uric acid, a natural scavenger of peroxynitrite, have been found to be markedly reduced. Oral administration of Cu-ATSM has been shown to increase the degradation rate of peroxynitrite, reduce peroxynitrite-mediated nitrosative stress and α-synuclein aggregation and improve motor and cognitive performance in

hA53T α-synuclein-overexpressing transgenic mice and several MPTP and 6-OHDA lesion murine models of PD (304). Whether these promising preclinical results will translate into the clinical setting remains to be seen.

Except for those cases with a clear-cut family history of genetic disease, the diagnosis of PD is still largely based on the identification of its clinical symptoms and the exclusion of other diagnoses. MRI can be used to identify structural abnormalities in the basal ganglia or the presence of iron deposits in the substantia nigra and is therefore able to exclude symptomatic parkinsonism caused by other pathologies. PET imaging of dopamine production and metabolism with ^{18}F-DOPA and SPECT imaging of dopamine transporter density with ^{123}I-FP-CIT are useful tools to visualise dopaminergic neuron degeneration and monitor disease progression (305). The Cu-ATSM complex has also been evaluated as an imaging agent to delineate regionalised oxidative stress in PD, as with ALS. In a small clinical study, Ikawa *et al.* reported significantly higher ^{62}Cu-ATSM striatum-to-cerebellum SUV ratios in PD patients compared to controls, which correlated moderately with disease progression (306). Donnelly and co-workers further examined the mechanism of cellular retention of Cu-ATSM in cultured cell models of PD-like electron transport chain impairment. This *in vitro* study demonstrated that the accumulation and dissociation of the copper complex was driven by the buildup of NADH resulting from impaired activity of the electron transport chain, thus suggesting that Cu-ATSM retention may be more indicative of mitochondrial dysfunction than oxidative stress (307).

2.3.5 Prion diseases

Prion diseases are a diverse group of transmissible neurodegenerative disorders which are thought to originate from changes in the conformation of endogenous PrP resulting in the formation of an infectious conformer of the protein (PrP^{Sc}). These conditions are very rare among humans and are mainly characterised by spongiform degeneration of the brain and spinal cord, formation of amyloid-like fibrils, neuronal loss and gliosis (285).

PrP is a membrane-anchored protein predominantly expressed in the CNS with a high affinity for copper (II) ions. The mechanism underlying the conversion of PrP into its infectious form and the pathological effects of this transformation are poorly understood. The infectious form of PrP

is characterised by its insolubility, resistance to protease activity and lack of nucleic acid content, which makes its mode of transmission very intriguing. Once formed, PrP^{Sc} acts as a template for PrP conversion into additional PrP^{Sc}, thus promoting the accumulation of the PrP^{Sc} isoform in the CNS and its aggregation into amyloid-like fibrils. Much like in other neurodegenerative diseases associated with abnormal protein aggregation, the buildup of misfolded PrP^{Sc} in prion disease is thought to lead to enhanced production of ROS and neuronal degeneration (250).

In addition to the neurotoxic effects associated with the misfolded form of PrP, the conversion of PrP into PrP^{Sc} also entails the loss of function of the native protein, although the exact physiological role of the latter still remains undefined. Several reports have linked PrP to normal brain copper metabolism and have suggested potential roles for the protein in the cellular uptake and buffering of copper ions and even as a copper-dependent antioxidant species (see section 2.2.5). The impact of the conversion of PrP into PrP^{Sc} on brain copper metabolism is poorly understood but abnormal brain copper levels have been observed in patients with prion disease. Wong and co-workers reported a 50 % decrease in copper content and a 10-fold increase in manganese levels in brain homogenate samples of patients suffering from sporadic Creutzfeldt-Jakob disease, the most prevalent form of prion disease in humans. These changes in trace metal concentrations in the brain were supported by increased manganese binding to PrP accompanied by severely reduced levels of copper-bound PrP. Furthermore, the SOD-like activity of the PrP fraction extracted from brain homogenates of prion disease patients was found to be markedly decreased, potentially due to reduced copper binding to PrP (308). Brown and co-workers examined the inverse correlation between brain levels of manganese and copper in prion disease in cultured neurons and demonstrated that manganese ions were able to displace copper from PrP, thus reducing its antioxidant activity and increasing its protease resistance (309).

Although the previous studies seem to indicate that copper binding to PrP is associated with neuroprotective properties of the protein, some deleterious effects of the copper-PrP connection have also been reported. For example, incubation of PrP with copper *in vitro* has been found to produce an increase in the hydrophobicity and proteinase K resistance of the protein, which are

properties reminiscent of PrP^{Sc} (310). Copper is also thought to contribute to the aggregation of PrP, although a specific copper-induced proaggregatory effect has not been proved yet. Jobling and co-workers demonstrated that removal of copper (II) and zinc (II) ions from aqueous media inhibited the aggregation of human PrP *in vitro* (311). Copper chelation therapy with D-Penicillamine has been shown to significantly delay the onset of prion disease in infected mice by specifically decreasing copper concentration in the brain and blood (312). Paradoxically, Hijazi *et al.* observed a significant delay in prion disease onset in hamsters infected with PrP^{Sc} after copper supplementation, and suggested that copper might promote the cellular internalisation of PrP, thus hindering the interaction of PrP with infectious PrP^{Sc} molecules (313). The latter contradiction exemplifies the complexity of the relationship between copper, PrP and prion disease, and highlights the importance of defining the physiological role of PrP in brain copper metabolism in order to better understand the role of copper in the pathophysiology of prion diseases.

2.3.6 Huntington's disease

HD is another neurological disorder characterised by abnormal protein aggregation. This neurodegenerative disease of genetic origin is caused by the expansion of glutamine repeats within the N-terminus of the huntingtin protein, whose physiological function has not yet been determined. The misfolding and aggregation of the huntingtin protein is thought to promote oxidative stress, mitochondrial dysfunction and neuronal loss, particularly in the striatum and cerebral cortex. Patients suffering from this condition experience movement abnormalities, psychiatric symptoms and progressive cognitive impairment (314).

Much like other neurodegenerative disorders, HD is also characterised by brain metal dyshomeostasis. High levels of iron and copper have been detected by inductively coupled plasma mass spectrometry (ICP-MS) in the basal ganglia of patients with HD (315). Fox and co-workers suggested that elevated brain copper content might substantially contribute to pro-oxidative and neurodegenerative processes in HD by modulating the structure of the huntingtin protein and inhibiting the activity of the copper-sensitive enzyme lactate dehydrogenase. This group demonstrated that copper (II) was able to interact with human huntingtin protein fragments *in vitro* and stimulate their aggregation. Moreover, it was found that lactate

dehydrogenase activity was severely reduced in the brains of HD mice although expression levels of the enzyme remained unchanged. Fox *et al.* suggested that excess copper, which has an inhibitory effect on lactate dehydrogenase *in vitro*, might also be responsible for the decreased activity of the enzyme *in vivo*, thus triggering progressive striatal degeneration (316). Xiao and co-workers further examined the influence of copper in HD severity by manipulating the levels of expression of several copper transporters in a *Drosophila* model of HD. Reduced expression levels of copper uptake transporters and dietary copper restriction were found to rescue the survival rate of HD flies and remarkably decrease the levels of oligomerised and aggregated huntingtin protein (314).

These observations first supported the idea that the reduction of brain copper levels might substantially mitigate HD pathology. Nguyen *et al.* evaluated the effects of copper chelation therapy in a mouse model of HD with 5-chloro-7-iodo-8-hydroxyquinoline (Clioquinol, CQ; Figure 2.4.A), a copper (II)/ zinc (II) chelating agent designed to interrupt neurotoxic interactions between these metals and target proteins in the brain. CQ treatment was shown to inhibit brain accumulation of aggregated huntingtin *in vivo* and improve motor function, survival rate and overall health in HD mice (317). Another 8-hydroxyquinoline metal chelator, 5,7-dichloro-2-[(dimethylamino)methyl]quinolin-8-ol (PBT2, Figure 2.4.B), demonstrated similar neuroprotective effects in both *Drosophila* and mouse models of HD (318). However, the clinical evaluation of PBT2 treatment only revealed a modest improvement in executive function but not in cognition in early-stage to mid-stage HD patients, and therefore this chelation approach is not likely to progress clinically (189).

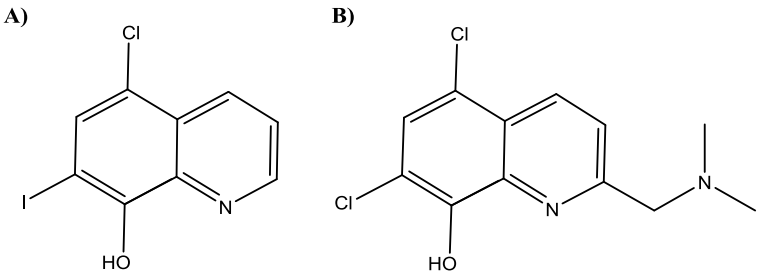

Figure 2.4: Structures of CQ (**A**) and PBT2 (**B**).

2.3.7 Niemann-Pick disease type C

Niemann-Pick type C disease (NPC) is a genetically inherited neurodegenerative disorder characterised by disrupted intracellular trafficking of endocytosed cholesterol and subsequent accumulation of the latter and other lipids in lysosomes and late endosomal compartments. The majority of NPC cases arise from mutations in the gene encoding the NPC1 protein, while only a few cases involve mutations in the NPC2 gene. Little is known about the exact physiological roles of NPC1 and NPC2 but it is thought that these two proteins are crucial players in the intracellular transport and processing of cholesterol and other lipids. Loss of function of NPC1 and/or NPC2 results in the accumulation of ganglioside lipids in the brain and lysosomal/late endosomal buildup of cholesterol and other lipid molecules (sphingomyelin, glycosphingolipids, sphingosine) in extraneural tissues, resulting in profound abnormalities in lipid metabolism. The clinical manifestations of NPC disease are extremely variable and range from systemic disease involving liver, spleen and/or lungs, to psychiatric symptoms. The main pathological hallmarks of the neurodegenerative component of NPC disease are distortion of neuron shape, formation of neurofibrillary tangles (NFTs), neuroinflammation, neuroaxonal dystrophy and death of cerebellar Purkinje cells. Nevertheless, how lipid storage abnormalities lead to these processes is not understood (319).

In recent years, some preclinical and clinical studies have suggested that impaired lipid metabolism in NPC disease may be accompanied by disrupted metal homeostasis. Among other transition metal imbalances, copper levels in the liver, blood and CNS have been found to be altered in both NPC1 knockout mice and patients, despite occasional inconsistencies in the direction of these metal changes between species. Hepatic copper content has been shown to be increased in NPC1 knockout mice and human subjects (320-323). Elevated copper levels in the liver of NPC1 knockout mice have been linked to reduced hepatic iron content and enhanced gene expression of ceruloplasmin, MT-1 and transferrin, suggesting an increased efflux rate of iron from liver stores in NPC1 disease. Dietary copper restriction and copper chelation therapy have been found to minimise the symptoms of liver disease in this preclinical NPC1 model but have not been shown to improve significantly cognitive decline, suggesting that hepatic copper overload might only be a regional effect of NPC1 loss-of-function (322). High copper and low iron content in the liver of NPC1 knockout mice are consistent with

significantly increased copper levels as well as enhanced ceruloplasmin concentration in blood plasma (321, 324). Although plasma copper levels have not been found to be increased in NPC1 patients, the concentration of copper-metallated ceruloplasmin in blood has been shown to be higher compared to apoceruloplasmin levels. While no significant abnormalities in brain copper homeostasis have been detected so far in human NPC1 subjects, levels of transition metals in the CSF have been found to be remarkably reduced compared to those of healthy subjects. Paradoxically, holoceruloplasmin concentration in the CSF has been reported to be increased in NPC1 patients and to positively correlate with disease severity (321).

The origin of these copper metabolism abnormalities as well as their impact on the severity and progression of NPC disease is poorly understood. It has been demonstrated through dietary manipulation in animal studies that abnormal cholesterol metabolism has an effect on copper homeostasis, although the precise mechanisms that interlink these pathways have yet to be elucidated (325). Alternatively, a direct role for NPC1 in normal copper metabolism could explain the impact of NPC1 loss-of-function on copper homeostasis in NPC disease. Yanagimoto *et al.* revealed that cholesterol transport inhibition and NPC1 knockdown in hepatocytes resulted in reduced holoceruloplasmin secretion to culture medium, suggesting a potential role for the NPC1 protein in the incorporation of late endosomal copper into ceruloplasmin (326, 327).

2.3.8 Alzheimer's disease

AD is a progressive, fatal neurodegenerative disorder and the most widespread form of dementia in the elderly. AD patients initially exhibit symptoms such as short-term memory loss, communication problems, disorientation or mood swings, which in later stages of the disease degenerate into profound cognitive impairment and ultimately lead to death. The main pathological hallmarks of AD are neuroinflammation, neurotransmitter imbalance and the accumulation of Aβ plaques and NFTs in the CNS (328).

The progressive formation and deposition of Aβ plaques in the brain is considered a key pathological event in the onset and progression of AD. These plaques are mainly composed of insoluble aggregated forms of Aβ, a 39-43-aminoacid peptide that results from the sequential

cleavage of endogenous APP, whose biological role remains to be established. APP can be proteolytically processed through the non-amyloidogenic α-/γ-secretase pathway, or sequentially cleaved by BACE1 and γ-secretase, resulting into the production of neurotoxic Aβ species (329). The molecular mechanisms that regulate the activity and access of these proteolytic enzymes to APP have not been deciphered yet, although risk factors such as cholesterol or apolipoprotein E e4 allele have been associated with the amyloidogenic processing of the protein (330). The most abundant Aβ species in human plasma and CSF is Aβ-40, whereas Aβ-42 is the primary component of the Aβ plaque deposits. In familial AD, mutations in the genes encoding APP and the presenilin 1 and 2 proteins, which are components of the γ-secretase enzymatic complex, trigger an increase in the production ratio of Aβ-42 to less aggregation-prone Aβ-40 (331).

Insoluble Aβ deposits are easily identifiable structures in the AD brain but their contribution to neuronal degeneration and cognitive decline is still unclear. Soluble Aβ oligomers have alternatively been proposed as the primary molecular culprits behind AD since a direct correlation has been demonstrated between Aβ oligomer levels and several markers of disease severity in AD patients (332). In addition to the deposition of extracellular Aβ plaques and the presence of oligomeric Aβ pools in both intracellular and extracellular compartments, Aβ-42 aggregates have also been reported to accumulate intraneuronally, prior to the formation of NFTs (333). In most AD cases, Aβ plaque deposits also form in the perivascular space of blood vessels in the brain and are considered a risk factor for cerebral infarction and white matter ischemic lesions (334).

For many years, the accumulation of Aβ plaques in the brain has been regarded as the main contributor to AD pathology, and neuronal cell death, vascular damage, NFT formation and cognitive impairment have been considered direct effects of this deposition (335). However, further research is needed to elucidate the mode of action of these Aβ species, identify their cellular targets and link their molecular pathways to the prodromal stages of AD. Aβ plaque deposits are thought to first develop in the synaptic clefts of glutamatergic synapses of the hippocampus and cerebral cortex and have therefore been associated with the inhibition of long-term potentiation, a synaptic enhancement process that contributes to memory formation

(269). Snyder *et al.* suggested that the accumulation of Aβ species might contribute to synaptic dysfunction by inhibiting the expression of NMDA glutamate receptors and even promoting their endocytosis (336). Aβ plaque deposition has also been linked to the hyperphosphorylation of the microtubule-associated tau protein and subsequent formation of the so-called NFTs, another key pathological hallmark of AD. However, the nature of this connection remains unclear. By crossing different transgenic AD mouse strains it has been found that Aβ promotes tau hyperphosphorylation and aggregation but also that tau aggregates contribute to Aβ neurotoxicity (337, 338).

The neurotoxic effects of Aβ constitute the basis for the most widespread theory to explain the pathogenesis of AD, "The Aβ Cascade Hypothesis", which posits that Aβ plaque deposition is the event that triggers the onset of AD. Nevertheless, the validity of this hypothesis has been questioned in recent years and is presently a matter of debate. It has been widely argued that the self-aggregating properties of Aβ might not be enough to justify the deposition of Aβ plaques in certain areas of the brain. Aβ species are generally found at nanomolar concentrations in the brain parenchyma, CSF, brain interstitial fluid and blood plasma of healthy subjects. Considering that the distribution of Aβ as well as APP in the CNS is homogenous, it is not yet clear how focal deposits of Aβ plaques form in AD. Furthermore, it has been reported that, while the deposition of Aβ plaques in the brain is an age-dependent process, the production rate of Aβ by proteolytic cleavage of APP does not increase with age. This evidence, together with the lack of effective anti-Aβ therapies, supports the notion that additional biochemical processes might contribute to the toxicity associated with Aβ buildup in AD (339).

Bush *et al.* first reported that exposure to zinc accelerated synthetic Aβ-40 aggregation and precipitation and increased the resistance of the peptide to proteolytic degradation (340). Post-mortem analysis of human AD brain tissue revealed elevated concentrations of zinc (~1 mM), copper (~400 µM) and iron (~1 mM) associated with extracellular Aβ plaque deposits. Copper and zinc were found to be directly bound to Aβ plaques, whereas iron was found in the form of ferritin complexes, which are thought to participate in inflammatory processes associated with senile plaques (269, 341, 342). This abnormally high transition metal content in Aβ plaque deposits has been repeatedly linked in recent years to key pathological processes in AD, such

as protein aggregation, ROS production, impaired neurotransmission and even brain metal dyshomeostasis. Collectively, this evidence has been used to support the so-called “Metal hypothesis of AD”, which suggests that AD pathogenesis is driven primarily by the interaction of Aβ and other AD-related proteins (e.g. APP, BACE1) with specific biometals (339).

2.3.8.1 Copper homeostasis in AD

Reports on endogenous copper content in the human AD brain are variable and often contradictory. For example, Lovell *et al.* detected by micro particle-induced X-ray emission elevated concentrations of copper in the rim of Aβ plaques and plaque-free neuropil of the amygdala of AD patients (341). Nevertheless, copper levels in the amygdala and hippocampus of AD subjects as measured by ICP-MS were found to be significantly decreased (~ 50 %) when compared to non-dementia controls (343). Controversy also exists regarding the concentration of copper in biological fluids in AD. Pajonk and Kessler reported reduced levels of copper and copper carrier ceruloplasmin in blood plasma of mild-to-moderate AD patients compared to healthy individuals, which correlated with cognitive decline (344, 345). However, in other studies, the concentration of copper and ceruloplasmin in the serum of AD subjects was found to be significantly higher relative to control subjects (346, 347). On the other hand, copper levels in the CSF have been reported to be similar between AD patients and control subjects (348, 349).

Copper status in AD is also reflected by reported alterations in the activities of essential copper-dependent enzymes. Decreased Cu/Zn SOD-1 activity was measured in the brains of APP-overexpressing mice. Normal antioxidant activity in this preclinical model was restored via copper supplementation, which implies a putative intracellular copper deficiency associated with Aβ plaque pathology (257). In support of this notion, the activities of cuproenzymes CCO and DβH were also found to be significantly reduced in brain regions affected by Aβ plaque deposition (e.g. cerebral cortex, hippocampus) in AD subjects, probably leading to impaired energy metabolism and neurotransmitter synthesis in those regions (86, 350).

Aβ plaques have been frequently described as *metal sinks* due to their remarkable ability to sequester metal ions. It has been shown that iron, copper and zinc are enriched in extracellular

Aβ plaque deposits and that the Aβ peptide has high and low affinity copper and zinc binding sites on its structure (351). Considering that the mobilisation of metal ions across the BBB is tightly regulated, it has been suggested that the interactions of copper and zinc ions with Aβ could be responsible for the disruption of brain metal homeostasis in AD.

The coordination chemistry of copper (II) ions to truncated Aβ peptides (Aβ-16, Aβ-28) and native Aβ oligomers (Aβ-40, Aβ-42) has been extensively investigated via nuclear magnetic resonance (NMR) and electron paramagnetic resonance (EPR). The coordination environment for copper (II) when bound to Aβ is still unclear but a distorted square planar geometry with a 3N1O coordination mode has been proposed for the copper (II) coordination site on Aβ in solution (Figure 2.5.A) and a binuclear model involving a bridging histidyl ligand has been suggested as the copper (II) coordination mode in Aβ aggregates (Figure 2.5.B) (352). It has not yet been determined whether Aβ is also capable of binding copper (I) ions. Considering that the redox behaviour of copper when bound to Aβ aggregates has been linked to ROS generation, the coordination of copper (I) to Aβ plaques seems quite probable (351).

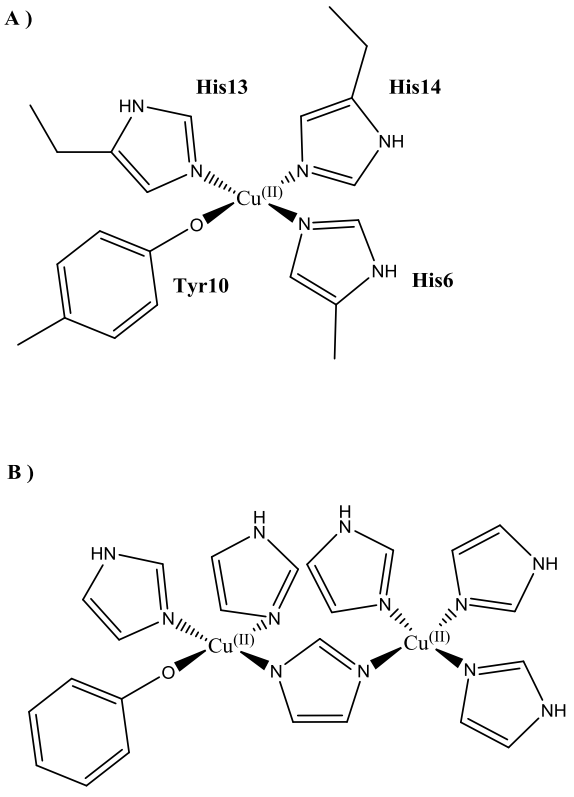

Figure 2.5: Proposed models for the coordination of copper (II) on Aβ species. Copper (II) coordination mode in soluble Aβ **(A);** Binuclear histidine-bridged copper (II) coordination site on Aβ aggregates **(B)** (352).

APP is also capable of binding copper ions with high affinity. This protein possesses a copper (I) binding site in its N-terminus and a second coordination site for copper (II) acquired after proteolytic cleavage by BACE1 (353). Growing evidence indicates that APP is not only capable of binding copper ions but that it also plays a critical role in brain copper homeostasis. Research conducted on APP-knockout transgenic mice revealed high concentrations of copper in the cerebral cortex and liver, while APP overexpression in transgenic mouse models of AD resulted in significantly decreased brain copper levels (257, 258, 354). This evidence seems to indicate that APP might function as an efflux transporter for copper in the CNS.

Another key player in AD pathology capable of binding copper is BACE1. The cytoplasmic domain of this enzyme has been shown to bind a single copper (I) ion with high affinity. Additionally, BACE1 has been reported to be able to interact with CCS, thus interfering with the delivery of copper from CCS to apo-Cu/Zn SOD-1. Angeletti *et al.* demonstrated that overexpression of BACE1 in cultured cells led to the downregulation of Cu/Zn SOD-1 activity due to direct competition between BACE1 and apo-Cu/Zn SOD-1 for CCS. This competitive effect could further weaken the antioxidant defences of brain cells in AD, leading to enhanced vulnerability of the brain to oxidative stress (248).

Copper has also been reported to interact with the tau protein *in vitro*, resulting in the formation of redox-active complexes capable of pro-oxidant or antioxidant behaviour depending on the redox status of the cell (355). Despite the ability of copper to increase the aggregation rate of tau *in vitro*, the presence of copper in NFTs has not yet been confirmed, and therefore its potential contribution to the aggregation behaviour and neurotoxicity of hyperphosphorylated tau is still under investigation (356).

2.3.8.2 Copper-induced synaptic toxicity in AD

As previously mentioned, the formation of Aβ plaque deposits in AD initially occurs at the synaptic clefts of glutamatergic synapses in the cerebral cortex and hippocampus, where elevated concentrations of both copper and zinc ions have been detected. Zinc (II) ions are transferred by transporter ZnT3 into synaptic vesicles, from where they are released along with glutamate into the synaptic cleft during neurotransmission. The role of zinc in neurotransmission

still has to be defined but it has been suggested that this transition metal could act as a neurotransmitter and/or modulator of the activity of glutamate receptors (269). Schlief *et al.* demonstrated the existence of a correlation between the activation of NMDA receptors and increased post-synaptic trafficking of copper transporter ATP7A towards the synaptic cleft and subsequent copper release in cultured hippocampal neurons. It has been suggested that copper may act as an electron acceptor in the S-nitrosylation of NMDA receptors in the presence of nitric oxide, thus modulating the activity of NMDA receptors and minimising neuronal excitotoxicity (216).

Considering that Aβ is also released into the synaptic cleft of glutamatergic synapses during neurotransmission, it has been suggested that potential interactions of the peptide with copper and zinc ions could be responsible for abnormal Aβ aggregation and ROS production in those brain regions (Figure 2.6). The binding of copper and zinc ions to the brain-specific MT-3 protein, which is released into the synaptic cleft by neighbouring astrocytes, is thought to reduce Aβ aggregation and cross-linking and oxidative stress. However, this protein has been found to be downregulated in the AD brain (357).

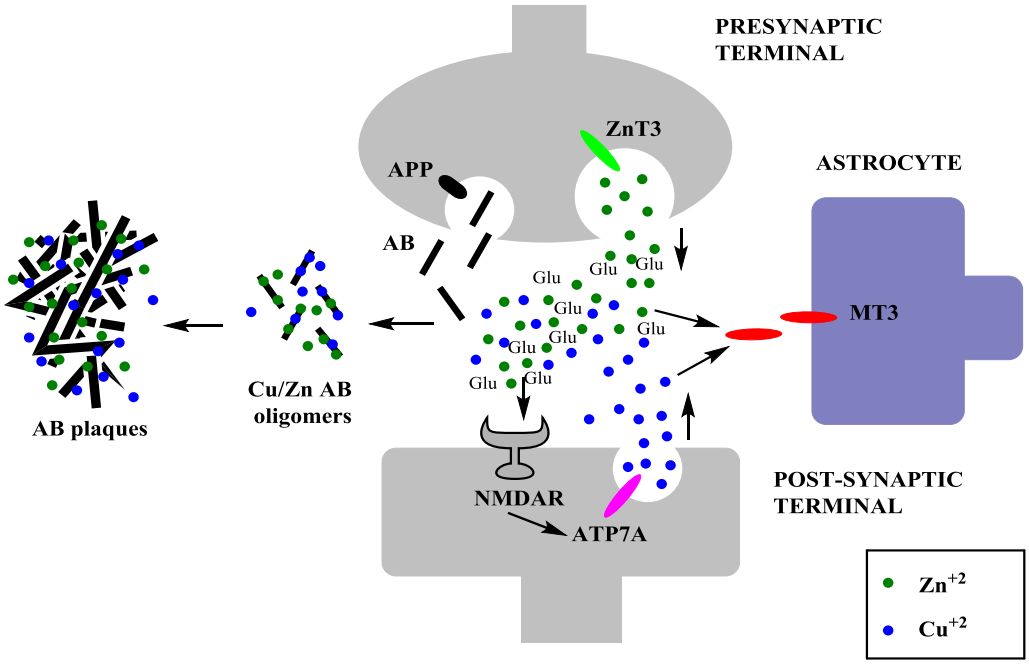

Figure 2.6: Copper/zinc-induced synaptic toxicity. During neurotransmission, zinc (II) ions are released along with glutamate from the presynaptic terminal of glutamatergic synapses into the synaptic cleft by transporter ZnT3. Aβ is also released during glutamatergic excitation into the synaptic cleft. Copper (II) ions are released from the post-synaptic terminal into the synaptic space by ATP7A as a response to the activation of NMDA receptors. The interaction of Aβ with copper (II) and zinc (II) ions leads to increased Aβ aggregation and oxidative stress. Metallothionein-3 is capable of minimising Aβ-metal interactions at the synaptic cleft but is downregulated in AD (339).

2.3.8.3 Copper-induced oxidative stress in AD

Copper-induced oxidative stress is a characteristic pathological process occurring in many neurodegenerative diseases, including AD, as a result of brain copper dyshomeostasis. The Aβ peptide has been shown to be capable of binding copper (II) ions with high affinity and to utilise their redox cycling properties to produce ROS *in vitro*. Copper (II)-Aβ complexes are able to produce hydrogen peroxide via reduction of copper (II) to copper (I) and double electron transfer to molecular oxygen. The electron source responsible for the initial reduction of Aβ-bound copper (II) has not been identified yet but it has been suggested that electrons could be generated from Aβ side-chain oxidation, which in turn might enhance Aβ aggregation. Opazo *et al.* suggested that cholesterol, catecholamines (e.g. dopamine, noradrenaline, adrenaline) and vitamin C could act as electron donors to reconstitute the copper (II)-Aβ complex. Hydrogen peroxide is able to diffuse across cell membranes and oxidise different cellular components but can also react with copper (I)-Aβ complexes and form hydroxyl radicals, which can cause further oxidative damage (269, 358). Moreover, it has been shown that the presence of Aβ can modulate the concentration of glutathione, an essential component of the antioxidant defence machinery of the cell. White and co-workers demonstrated that pretreatment of cultured neurons with fibrillary Aβ fragments depleted cellular glutathione, resulting in increased copper toxicity and oxidative stress (359).

2.3.8.4 Therapeutic approaches based on copper supplementation

Multiple lines of evidence support the idea that brain copper homeostasis is disrupted in AD as a result of the interaction of copper ions with key molecular players in AD pathology (e.g. Aβ, APP, BACE1, tau). In particular, the accumulation of copper in extracellular Aβ plaque deposits has been proposed to result in a marked decrease in intracellular copper bioavailability leading to reduced activity of essential copper-dependent enzymes (339, 360, 361).

In recent years, a great number of therapeutic approaches that seek to restore this putative brain copper deficit in AD have been developed. Bayer *et al.* examined the effects of increasing copper bioavailability in APP23 transgenic mice treated with copper-supplemented drinking water. Dietary copper treatment was shown to restore intracellular copper levels and Cu/Zn SOD-1 enzymatic activity in the brains of APP23 mice, as well as significantly decrease soluble

Aβ-40 and Aβ-42 levels, although this effect was only observed in male mice (257). Manso and co-workers treated three different groups of APP/PS1 transgenic AD mice with copper-supplemented water, cholesterol-rich food or a combination of both in order to assess the effect of these parameters on Aβ burden and cognitive decline. All three different treatments caused a significant decrease in Aβ plaque burden in transgenic mice when compared to controls, but the combination of copper and cholesterol supplementation had the most dramatic impact (362). However, these findings are inconsistent with those reported by Sparks *et al.*, who revealed that treatment of cholesterol-fed rabbits with copper-supplemented water promoted Aβ plaque accumulation in the hippocampus and temporal lobe and induced learning deficits relative to untreated controls (363). This discrepancy in the effects of copper supplementation may arise from differences in the administered copper doses but may also be due to the phenotypic variability existing between the different AD models.

White and co-workers revealed that treatment with copper (II)/zinc (II)-CQ complexes induced a dramatic decrease in secreted levels of Aβ-40 and Aβ-42 in APP-overexpressing chinese hamster ovary cells (CHO) and neuroblastoma cells compared to non-treated controls. This group demonstrated that this reduction of Aβ burden resulted from copper (II) and zinc (II)-mediated upregulation of matrix metalloproteinase (MMP) enzymatic activity. Copper (II)/zinc (II)-CQ complexes were found to induce the activation of the phosphoinositol 3-kinase (PI3K) enzyme as well as the phosphorylation of protein kinase B (Akt) and glycogen synthase kinase 3 (GSK3). Treatment of cultured APP-overexpressing cells with these metal complexes was shown to also trigger the activation of c-Jun N-terminal kinases (JNKs) and extracellular-signal-regulated kinases (ERKs). The activation of all these molecular pathways ultimately led to the upregulation of MMPs and the subsequent degradation of Aβ aggregates (364).

Despite these promising initial results, CQ shows only moderate copper (II) binding affinities (K_d= 10^{-10} M) and consequently the resulting complexes might offer moderate control over cellular uptake and intracellular metal release. In addition to this, White *et al.* failed to clarify some key aspects of the mechanism of action of CQ complexes since it remained uncertain whether copper-mediated upregulation of MMP activity required the release of the metal ion from the complex or whether the complex remained intact instead.

In an attempt to find suitable alternatives to CQ, Donnelly and co-workers investigated the effects of a series of Cu-BTSC complexes on Aβ burden in cultured APP-overexpressing CHO cells (Figure 2.7). The structural tunability of these metal complexes, which enables the modification of some of their physicochemical properties (e.g. redox potential, lipophilicity), allows subtle control over their uptake and metal release within specific cell microenvironments (see Chapter I, section 1.4.2.4). Treatment of APP-CHO cells with Cu-GTSM (Fig. 2.7.A) and Cu-ATSM (Figure 2.7.B) resulted in 216- and 177-fold increases in cellular copper levels respectively compared with untreated controls. Moreover, Cu-GTSM and its derivatives copper (II) glyoxal-bis(N^4-ethyl-3-thiosemicarbazone) (Cu-GTSE, Figure 2.7.C) and copper (II) glyoxal-bis(N^4-phenyl-3-thiosemicarbazone) (Cu-GTSP, Figure 2.7.D) induced 15, 16 and 38 % decreases in secreted monomeric Aβ-40 levels respectively, while treatment of APP-CHO cells with Cu-ATSM had no effect on Aβ burden. Donnelly *et al.* suggested that the lack of impact of Cu-ATSM on Aβ turnover could be due to the higher thermodynamic stability and resistance to bioreduction and dissociation of the complex compared to Cu-GTSM and its derivatives, thus supporting the idea that copper-mediated Aβ proteolytic degradation requires the intracellular dissociation of the complex (142). This group also demonstrated that treatment of APP-CHO cells with Cu-GTSM triggered the phosphorylation of the Akt, JNK and GSK3 kinases and subsequent upregulation of MMP activity, resulting in dose-dependent reduction in the levels of extracellular monomeric Aβ (365).

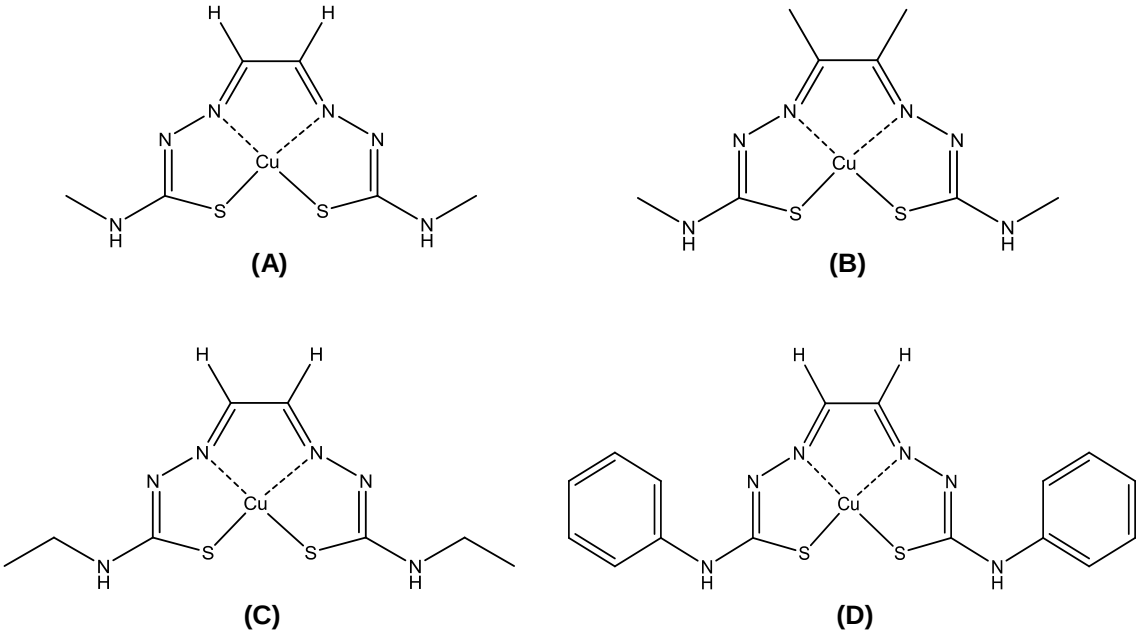

Figure 2.7: Structures of Cu-GTSM (**A**), Cu-ATSM (**B**), Cu-GTSE (**C**) and Cu-GTSP (**D**).

Crouch *et al.* investigated further the effect of increasing copper bioavailability in the brain by treatment with Cu-GTSM and Cu-ATSM *in vivo*. Oral supplementation of Cu-GTSM resulted in a reduction of the levels of neurotoxic Aβ trimers and inhibition of GSK3β and tau hyperphosphorylation in 6-month-old APP/PS1 transgenic mice when compared to sham-treated controls. Moreover, Cu-GTSM-supplemented AD mice also showed restored cognitive performance in the Y-maze test to the level of healthy animals. Conversely, Cu-ATSM supplementation in APP/PS1 transgenic mice produced no significant effect on Aβ burden, GSK3β activity or cognitive performance (366).

Despite these promising preclinical results, the restoration of brain copper levels via copper (II)-orotate-dihydrate supplementation had no effect on cognition in patients with mild AD (367). This discrepancy in the effects of copper supplementation may be due to different copper (II) complexes used or differences in copper metabolism between species, but may also be the result of the disconnection between AD animal models and human AD.

2.3.8.5 Therapeutic approaches based on copper redistribution

With the purpose of preventing neurotoxic copper-Aβ interactions and restoring brain copper homeostasis in AD, the ability of several copper (II)-chelating agents (e.g. EDTA, DTPA) to sequester copper ions from plaques and redistribute them into cells has been investigated. However, despite the ability of some of these chelators to extract copper from cerebral Aβ plaque deposits, their clinical application presents major drawbacks, such as limited BBB permeability and cell permeability or poor metal ion specificity, which may lead to excessive removal of essential biometals (368).

The efficacy of several clinically approved metal-chelating drugs (e.g. Desferrioxiamine B, Deferiprone, D-Penicillamine) in attenuating neurotoxic copper-Aβ interactions has also been investigated. Clinical evaluation of these traditional chelators as therapeutic agents for AD treatment has produced mixed results so far. Treatment of AD patients with D-Penicillamine for 6 months produced no effects on cognition but led to a moderate decrease in the levels of oxidative stress markers in serum (369). Conversely, daily intramuscular administration of Desferrioxiamine for 2 years resulted in a reduction in the rate of decline of daily living skills in

AD patients, demonstrating the potential of this drug to modestly delay the clinical progression of dementia (370). However, Desferrioxiamine is a non-specific metal chelator capable of binding copper, zinc, iron and aluminium and, as a result, this type of treatment could progressively lead to systemic metal depletion (339).

The failure of traditional copper chelators to halt AD progression led to the notion that more sophisticated copper chelators were required to prevent copper-induced neurotoxicity in AD. In 1997, Bush and co-workers first introduced the concept of metal-protein attenuation compounds (MPACs). These “smart” chelating agents are characterised by BBB-permeability, low molecular weight and nanomolar affinity for copper (II) and zinc (II) ions, which facilitates the sequestration of these metals from the low-affinity metal binding sites of Aβ (339).

The copper (II)/zinc (II) chelator CQ was initially established as the gold-standard of this generation of “smart” chelating agents. Cherny *et al.* reported a 49 % reduction in brain Aβ accumulation in 21-month-old APP2576 transgenic mice orally treated with CQ (30 mg/kg/day) for a 9-week period when compared with sham-fed transgenic controls. Furthermore, a significant improvement in general health, body weight parameters and behaviour in CQ-treated APP2576 mice was observed, highlighting the therapeutic potential of CQ-like drugs for the treatment of AD. Interestingly, a significant increase in copper (19 %) and zinc (13 %) levels in brain homogenate samples of CQ-treated transgenic AD mice was also detected. Cherny and co-workers suggested that this increment in brain copper and zinc content could result from CQ-mediated redistribution of the metals from Aβ plaque deposits to copper/zinc-deficient brain regions (371).

These results supported the idea that the mechanism of action of CQ was much more complex than originally estimated (Figure 2.8). Treiber *et al.* subsequently reported that addition of CQ to cultured yeast cells dramatically increased intracellular copper levels, thus revealing the ability of CQ to alter copper distribution and stimulate intracellular copper uptake (256). Furthermore, treatment with copper/zinc-CQ complexes was shown to activate specific cell signalling pathways that in turn triggered the proteolytic degradation of Aβ plaques as well as the downregulation of GSK3 activity and tau phosphorylation rate in AD transgenic mice (364).

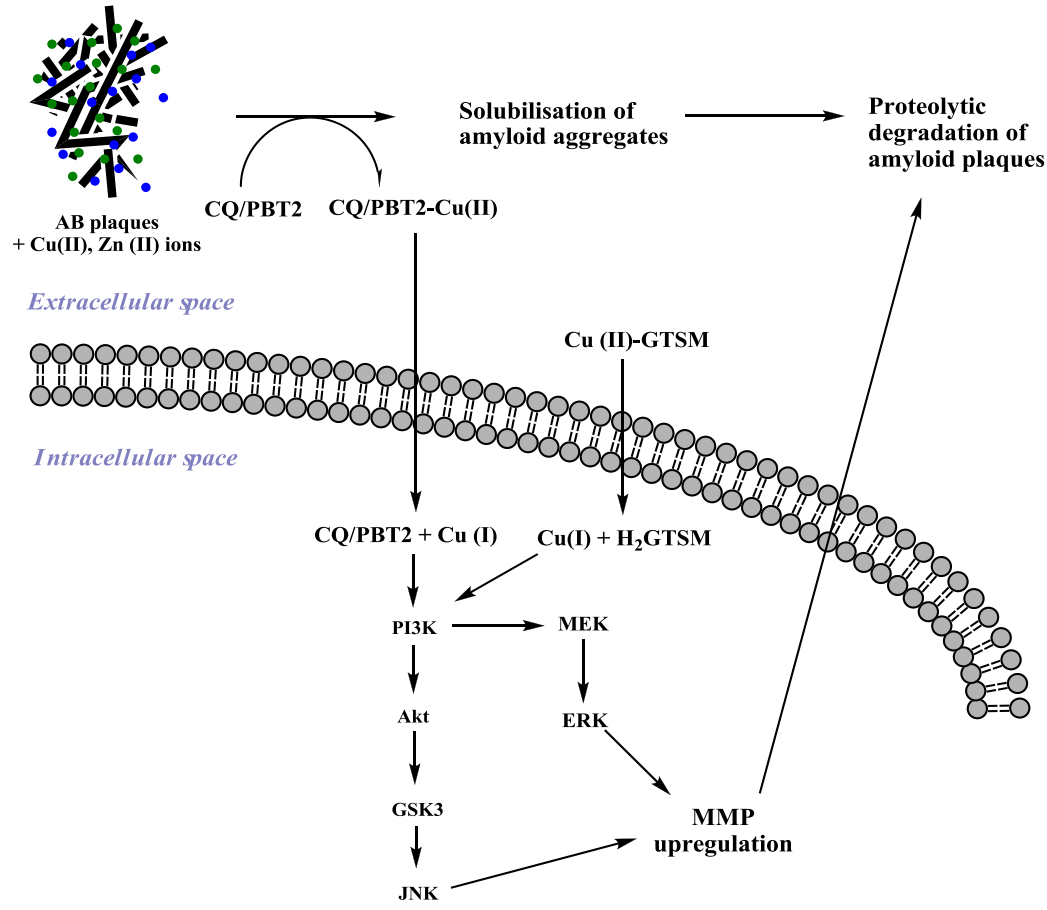

Figure 2.8: Proposed mechanisms of action for CQ and Cu-GTSM (364, 365).

Despite these encouraging preclinical results, CQ treatment was found to produce significant clinical impact only on advanced AD cases. Reduced Aβ-42 plasma levels and enhanced plasma zinc concentration were observed in CQ-treated severe AD patients when compared with placebo-treated controls (372). Additional clinical studies on CQ treatment have not been performed due to the production of a carcinogenic impurity during drug manufacture (339).

In recent years, PBT2 has become the leading MPAC alternative to CQ for the treatment of AD and other neurodegenerative disorders associated with brain copper dyshomeostasis. This 8-hydroxyquinoline derivative presents several advantages over CQ, such as greater solubility and BBB penetration as well as straight-forward synthesis and purification. Moreover, Adlard *et al.* demonstrated that PBT2 also outperforms CQ as a copper (II)/zinc (II) ionophore. PBT2 was found to be able to promote copper and zinc intracellular uptake, thus reducing copper-induced hydrogen peroxide production and increasing the solubilisation of insoluble Aβ aggregates *in vitro*. In addition, PBT2 treatment resulted in marked decreases in soluble Aβ concentration,

plaque burden, synaptotoxicity marker levels and tau phosphorylation in two different mouse models of AD (APP/PS1 and Tg2576), resulting in marked behavioural improvement and rapid restoration of cognitive deficits (373).

Nevertheless, clinical assessment of PBT2 as a therapeutic agent for the treatment of AD has failed to yield satisfactory results. Drug safety evaluation initially revealed that 12-week PBT2 treatment (250 mg) induced a significant decrease in the levels of Aβ-42 in the CSF of patients with prodromal AD and produced significant improvements in two measures of executive function (374, 375). Despite these promising results, larger-scale testing of PBT2 in patients with mild AD did not show a significant reduction in brain levels of Aβ plaques or lead to a significant improvement in brain metabolic activity, cognition or function (376). The failure of MPAC therapies to improve the symptoms of human AD and halt disease progression reflects the discrepancies between current AD animal models and human AD as well as the critical gaps in knowledge of the pathophysiology of the disease and the role of copper in neurodegeneration.

2.3.8.6 Cu-BTSCs for the delineation of brain copper trafficking in AD

The complexity of AD pathology and the common symptoms existing between AD and other neurodegenerative diseases (e.g. frontotemporal dementia, vascular dementia, PD) complicate considerably the accurate diagnosis of this disorder. At present, absolute diagnosis of AD relies only on histological staining of Aβ plaque deposits and NFTs in post-mortem brain tissue. There are currently no reliable diagnostic biomarkers or techniques that can be used to detect AD before the onset of full dementia and monitor disease progression and response to treatment. Neuropsychological testing remains the most frequently used tool in AD diagnosis since it allows the assessment of multiple cognitive domains (memory, language, perceptual skills, attention, orientation, problem-solving and functional and constructive abilities) (377). However, the interpretation of these tests is considered rather subjective and does not differentiate between AD and other forms of dementia nor detect early onset AD. In recent years, the use of imaging in various modalities (MRI, PET and SPECT) has provided the possibility of measuring in an objective and reliable manner disease markers that are indicative of specific pathological processes associated with AD. In particular, over the last decade, efforts have been focused on

the development of imaging agents capable of targeting Aβ plaque deposits *in vivo*. Although these agents can be used to effectively map Aβ plaque deposits in the brain, they only provide information on a particular feature of AD pathology, whose predictive value as a marker of disease progression and severity still remains unclear.

Given the multifactorial nature of AD pathophysiology, the delineation of a biomarker that is affected by multiple pathological features of the disease could provide useful insight into the severity and progression of AD as well as valuable information for assessing prognosis and response to therapy. In this regard, brain copper trafficking is considered an attractive target since copper has been shown to interact with multiple molecular entities involved in AD pathology (e.g. Aβ, APP, BACE1, tau) and is known to contribute to several pathological processes that enhance AD severity (e.g. oxidative stress, abnormal protein aggregation, synaptic toxicity).

The use of Cu-BTSC complexes as therapeutic agents for the treatment of AD illustrates the ability of these compounds to release their copper payload into cells selectively or non-selectively, depending on their physicochemical properties. Cu-BTSC complexes Cu-ATSM and Cu-GTSM have both been shown to be capable of crossing the BBB *in vivo* and increasing intracellular copper bioavailability, but the higher susceptibility of Cu-GTSM to intracellular bioreduction and metal release has been found to enable the delivery of higher quantities of copper into the brain when compared with Cu-ATSM (366). Fodero-Tavoletti and co-workers first assessed the ability of these complexes to delineate brain copper trafficking in AD by PET in APP/PS1 transgenic mice. *Ex vivo* biodistribution data revealed almost a 2-fold greater uptake of ^{64}Cu-GTSM in the brains of 9-12-month-old APP/PS1 mice (3.0 ± 0.25 %ID/g) when compared to age-matched controls (1.58 ± 0.14 %ID/g) at 1 h post-injection of the tracer. Conversely, no significant differences in brain ^{64}Cu-ATSM concentration were observed between APP/PS1 and controls, which is consistent with the lower susceptibility of the complex to intracellular bioreduction and metal release. Furthermore, immunohistochemistry and *in vitro* autoradiography showed that ^{64}Cu-GTSM accumulation in post-mortem human AD brain tissue did not co-localise with Aβ plaque deposits, demonstrating that ^{64}Cu signal in brain tissue was not the consequence of ^{64}Cu-GTSM or ^{64}Cu binding to Aβ plaques (155). Although preliminary,

these results warrant further investigation and demonstrate the potential of ^{64}Cu-GTSM-PET as a tool to investigate the role of copper in AD and other neurological disorders linked to brain copper dyshomeostasis.

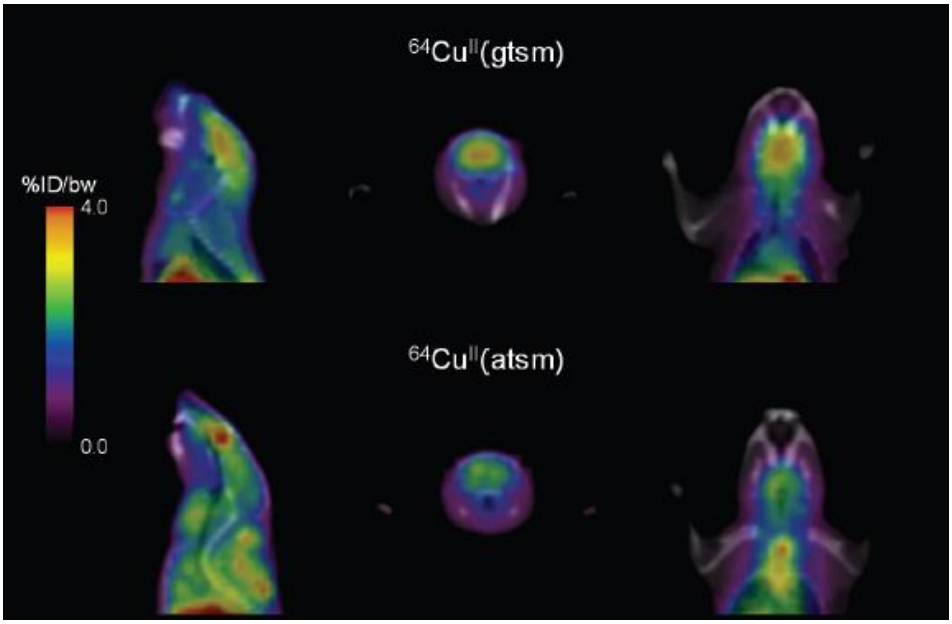

Figure 2.9: MicroPET/CT images (sagittal, axial and coronal planes) of APP/PS1 trangenic mice injected with ^{64}Cu-GTSM and ^{64}Cu-ATSM at 30 min post-injection of the tracer. Reproduced with permission from (155).

2.4 CONCLUDING REMARKS

Copper is a fundamental bioelement for the normal development and function of the CNS. As a cofactor of both systemic and brain-specific enzymes and modulator of synaptic transmission and other cell signalling pathways, copper participates in many physiological processes that are essential for the maintenance of neurological health and function. However, due to the low antioxidant capacity of the brain, copper content in the CNS needs to be tightly regulated in order to minimise copper-induced production of ROS. Although significant progress has been made in identifying the molecular entities that regulate brain copper trafficking and distribution, many aspects of these homeostatic mechanisms remain to be elucidated. Little is known about the specific copper transport mechanisms of the different types of brain cells as well as the function and interactions of these cell types in brain copper homeostasis. The role of several copper-binding proteins associated with neurodegenerative diseases (e.g. PrP, NPC1, APP) in

normal copper metabolism also needs to be defined in order to better understand the origin and effect of copper imbalance in these disorders.

The deleterious effects of brain copper deficiency and overload on CNS function are illustrated by the inherited Menkes and Wilson's disorders, which result from mutations in the genes encoding copper transporters ATP7A and ATP7B, respectively. In recent years, brain copper imbalance has also been associated with other neurological diseases, including ALS, PD and AD. In addition to the dysregulation of copper-dependent signalling and enzymatic activity, brain copper dyshomeostasis is thought to contribute to common pathological features of these neurodegenerative conditions, such as abnormal protein aggregation and oxidative stress. However, it should be pointed out that the enhancement of these pathological processes is not an exclusive effect of brain copper imbalance since other trace metal abnormalities have also been reported in most of these disorders. A better knowledge of the interrelationships between copper and other transition metals in the brain, particularly iron and zinc, is required in order to understand the consequences of their dysregulation to CNS function as well as their specific contribution to neurodegeneration.

Whether abnormal copper homeostasis is a cause or a consequence of neurological disease or merely a result of aging that enhances the severity of neurodegeneration is currently not known. The potential of trace metal abnormalities as disease markers needs to be investigated in order to determine whether they could provide meaningful information on disease severity and progression. The use of brain copper dyshomeostasis as a disease marker could be particularly informative for multifaceted neurodegenerative diseases such as AD, which ideally require biomarkers that are perturbed by several pathological factors. In AD, copper has been shown to interact with various molecular players of the pathology (e.g. Aβ, APP, BACE1, tau) and is thought to contribute to pathological processes such as Aβ and tau peptide aggregation, oxidative stress or synaptic toxicity. Brain copper dyshomeostasis could therefore be a much more useful marker to characterise the status and progression of AD than single molecular targets such as Aβ plaque deposition, which only provide information about one aspect of the disease.

The growing availability of high-resolution PET systems and copper radionuclides encourages the use of copper radiotracers, in particular the BBB-permeable ^{64}Cu-GTSM complex, to measure brain copper fluxes *in vivo* in real-time with PET. ^{64}Cu-PET offers the unique opportunity to study brain copper trafficking in disease models and humans to determine its predictive value as a disease marker in several neurological disorders and further characterise the role of copper in neurodegeneration. ^{64}Cu-PET imaging of copper trafficking could additionally be used as a tool to monitor the effect of copper-modulating therapies on copper biodistribution in diseases associated with copper dyshomeostasis, and even elucidate the mechanism of action of new copper-chelating agents.

Chapter 3- PET imaging of brain copper trafficking in a mouse model of Alzheimer's disease: potential new diagnostics

3.1 AIMS

The aim of this chapter is to investigate brain copper trafficking in a mouse model of AD by ^{64}Cu-GTSM-PET in order to detect and characterise potential metabolic abnormalities that might have added value in the diagnosis of the disorder.

3.2 INTRODUCTION

3.2.1 Diagnosis of AD

AD is the most common form of dementia in the elderly. Its prevalence in an ageing global population is rapidly increasing, creating a major socio-economic burden. There is no satisfactory method for its early diagnosis and no effective treatment to halt or delay cognitive decline experienced by patients. The disease is mainly characterised by neuronal cell death, neurotransmitter imbalance, neuroinflammation and the deposition in the brain of two types of abnormal protein aggregates, namely NFTs and Aβ plaques (see section 2.3.8, Chapter II). At present, absolute diagnosis of AD is only possible via post-mortem histological identification of characteristic hallmarks of the pathology (e.g. Aβ plaque deposits, NFTs, microglia activation), while clinical diagnosis relies mostly on the neuropsychological assessment of the subject.

Complementary diagnostic techniques to cognitive testing that have potential for routine clinical use include PET imaging of reduced regional brain glucose metabolism with ^{18}F-FDG, CSF analysis, structural MRI, blood oxygen level–dependent (BOLD) functional MRI and PET imaging of Aβ plaques (378). Among these tests, ^{18}F-FDG-PET has been shown to detect AD in human subjects with the highest sensitivity (~93 %) and specificity (~ 76 %) (379). Furthermore, ^{18}F-FDG-PET has been reported to be able to differentiate accurately AD from frontotemporal

dementia, and even mild cognitive impairment (MCI) cases from healthy elderly subjects when combined with executive function tests (380, 381). However, brain ^{18}F-FDG uptake is a non-specific indicator of cerebral glucose metabolism, which may be altered due to non-AD pathological processes, and consequently cannot be used as an independent diagnostic marker of AD pathology (378).

The CSF is a valuable source of disease markers for several CNS disorders since its composition reflects the biochemical changes occurring in the brain. AD subjects have been reported to exhibit markedly increased CSF levels of total and phosphorylated tau, and significantly reduced levels of Aβ-42 when compared to controls (382). The combined analysis of CSF total and phosphorylated tau, and Aβ-42 has been found to differentiate AD sufferers from healthy individuals with high sensitivity and specificity (~80-90 %), particularly at early stages of the disorder. Nevertheless, the large overlap in pathology between AD and other types of dementia (e.g. vascular dementia, dementia with Lewy bodies) along with the presence of the latter AD biomarkers in the CSF of cognitively normal elderly individuals, limit the accuracy of CSF analysis as a diagnostic test. Moreover, CSF analysis involves invasive lumbar puncture procedures, which often cause discomfort to patients (383).

Structural MRI is an effective imaging methodology to measure the degree of cerebral atrophy in AD, particularly in regions such as the hippocampus or the entorhinal cortex, in which tissue loss occurs before cognitive symptoms begin. Cerebral atrophy has been shown to correlate very closely with cognitive decline and therefore shows promise as a diagnostic marker of AD progression. However, brain structural measures on their own are not capable of detecting AD at the MCI stage and do not produce sufficiently specific spatial patterns to distinguish between AD and other types of dementia (384).

The clinical utility of BOLD functional MRI methods has also been increasingly investigated in recent years. These diagnostic tests offer an indirect measure of neuronal activity inferred from changes in MRI signal caused by variations in blood flow, blood volume and blood oxyhemoglobin/deoxyhemoglobin ratio. Aberrant task-related BOLD MRI signal has been detected in regions exhibiting high Aβ plaque deposition and is therefore considered a

promising marker to assess the effects of anti-Aβ therapies in clinical trials. Nonetheless, BOLD functional MRI is logistically challenging when testing cognitively impaired subjects and has been reported to yield variable results across individuals, which hampers its clinical application (378). A wide range of MRI techniques capable of characterising other functional markers of AD (e.g. cerebral perfusion, axonal transportation, integrity of fibre tracts, N-acetylaspartate and glutamate levels) are currently in preclinical development (385).

Molecular imaging offers unique potential to characterise and measure disease-specific molecular markers capable of accurately monitoring disease progression and response to treatment *in vivo* and in a non-invasive manner. To date, the most popular application of molecular imaging in AD is the delineation of Aβ plaque burden by PET or MRI. The majority of PET-based diagnostic approaches in AD are based on the development of radioligands capable of crossing the BBB and binding specifically to Aβ plaques. In 2004, Klunk and co-workers developed 2-(4'-[^{11}C]methylaminophenyl)-6-hydroxybenzothiazole (Pittsburgh Compound B [^{11}C-PIB]; Figure 3.1.A), a ^{11}C-radiolabelled derivative of the fluorescent Aβ dye thioflavin T capable of binding to fibrillar Aβ with high affinity and specificity (386). Brain uptake of ^{11}C-PIB in AD subjects was found to be greater compared to healthy elderly individuals and to correlate with regional glucose hypometabolism, reduced levels of Aβ-42 in the CSF and degree of cerebral atrophy (as measured by structural MRI) (387-389). However, although brain accumulation of ^{11}C-PIB showed a positive correlation with the rate of memory decline in MCI and prodromal AD subjects, it did not correlate with the rate of memory impairment at later stages of the disease. Another drawback of brain amyloid imaging using ^{11}C-PIB is the fact that the tracer shows moderate non-specific white matter binding, which together with age-dependent accumulation of Aβ plaques in the brains of some healthy individuals might contribute to false-positive results (390).

The ability of ^{11}C-PIB to delineate Aβ plaque deposition encouraged the development of other Aβ-targeting agents using longer lived PET radioisotopes, such as fluorine-18 ($t_{1/2}$= 109.8 min). Among these, the ^{18}F-labelled radioligands 2-[3-[^{18}F]Fluoro-4-(methylamino)phenyl]-1,3-benzothiazol-6-ol (^{18}F-Flutemetamol), trans-4-(*N*-methly-amino)-4″-(2-(2-(2-[^{18}F]Fluoro-ethoxy)ethoxy)-ethoxy) stilbene) (^{18}F-Florbetaben) and trans-4-(2-(6-(2-(2-(2-[^{18}F]Fluoro-

ethoxy)ethoxy)ethoxy)pyridin-3-yl)vinyl)-*N*-methyl benzeneamine) (^{18}F-Florbetapir) (Figure 3.1.B/C/D) are currently the most promising candidates for clinical use. Although these probes have been shown to be able to accurately map cerebral Aβ plaque load, they exhibit greater non-specific white matter binding and lower average cortical uptake than ^{11}C-PIB, which hinders the interpretation of their PET scans (390).

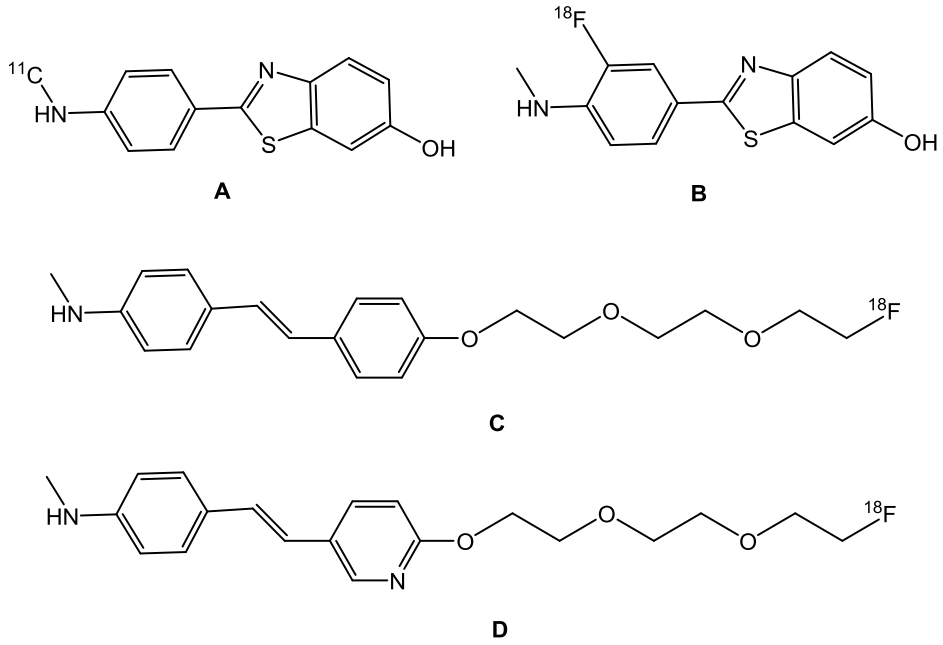

Figure 3.1: Chemical structures of ^{11}C-PIB (**A**), ^{18}F-Flutemetamol (**B**), ^{18}F-Florbetaben (**C**) and ^{18}F-Florbetapir (**D**).

Because of its superior spatial resolution compared to PET, MRI has also been applied to delineate cerebral Aβ plaque load in AD. Several non-contrast MRI protocols have been shown to be capable of detecting thalamic, cortical and hippocampal plaques in different transgenic mouse models of AD. However, MRI detection of Aβ plaques without contrast agents has been found to be subject to the accumulation of iron and calcium within plaques, which is a feature of Aβ plaque deposits at late stages of the disease but not at the prodromal phase. In order to overcome this limitation, a large number of targeted contrast agents aimed at enhancing MRI image contrast and improving the detection of Aβ plaque deposits have been developed and are currently under preclinical evaluation (385).

Although most of these molecular imaging approaches provide a reliable assessment of cerebral Aβ plaque burden, clinical data indicate that imageable Aβ plaque load alone is not an adequate diagnostic marker for AD. Cerebral Aβ plaque load displays only a weak correlation

with cognitive impairment, suggesting that other pathological factors influence disease progression (391). Moreover, many cognitively normal subjects with high Aβ burden (as detected by PET) did not subsequently develop AD, and there is much interest in developing PET radiotracers for a wider range of molecular features of the disorder (328, 392, 393). Several PET radiotracers targeting tau pathology and neuroinflammatory processes have been recently developed but the relevance of these markers for the diagnosis and assessment of AD still remains to be determined (394).

In recent years, there has been growing evidence associating changes in trafficking and distribution of trace metals within the brain, including copper, with the onset and progression of AD (see section 2.3.8.1, Chapter II) (269, 271). Whether this association is a cause or consequence of the pathology is unknown and the nature of the changes is poorly understood. Copper has been found to interact with key components of AD pathology (e.g. Aβ, APP, BACE1, tau) and, as a result, is thought to contribute to abnormal protein aggregation, synaptic toxicity and oxidative stress (248, 353, 395-397). Aβ plaques have been described as “sinks” of iron, zinc and copper ions, which have been shown to enhance Aβ aggregation and neurotoxicity (341, 351, 398, 399). It has been suggested that the association of copper with Aβ aggregates and other molecular entities involved in AD might also lead to decreased intracellular copper bioavailability and reduced activity of copper-dependent enzymes in the brain (86, 400, 401).

This “metal hypothesis of AD” is the basis of the development of treatments aimed at minimising copper-induced neurotoxicity and restoring brain copper homeostasis (339, 361). Studies in AD animal models demonstrated reduced Aβ burden, increased intracellular copper levels and improved cognitive function following administration of copper (II) chelators (e.g. CQ, PBT2) capable of stripping away copper ions from Aβ plaque deposits and redistributing them into cells (256, 364, 372, 375). A recent investigation showed that treatment with Cu-GTSM - a Cu-BTSC complex that delivers copper into cells and releases it bioreductively - enhanced cognitive performance in APP/PS1 transgenic AD mice by triggering neuroprotective mechanisms that inhibited GSK3β and decreased phosphorylated tau and Aβ trimer levels (365, 366). Hence,

understanding the role of copper homeostasis in AD pathology may be critical to develop both novel diagnostics and therapeutics.

A PET radiotracer able to measure brain copper trafficking *in vivo* could be a valuable tool to investigate changes in copper metabolism in brain and determine the potential of copper dyshomeostasis as an early diagnostic marker for AD and a useful complement to other imaging biomarkers. The availability of positron-emitting copper isotopes (^{60}Cu, ^{61}Cu, ^{62}Cu, ^{64}Cu) raises the possibility to study the trafficking of copper to, from and within brain, not only in animal models but also in humans, by imaging with PET over a period of hours and repeatedly during the lifetime of the subject. Intravenous injection of ^{64}Cu in the form of ionic copper (II) salts leads to delivery of radiotracer to the brain via native copper transport processes in quantities that are insufficient for meaningful imaging (153, 154). However, by exploiting the ability of uncharged lipophilic copper (II) complexes, such as Cu-GTSM, to penetrate the BBB and release their copper payload non-selectively into cells, the intracellular copper pool can be supplemented with tracer quantities of ^{64}Cu sufficient to allow imaging of its subsequent trafficking (Figure 3.2) (144, 149, 166). A preliminary study by Fodero-Tavoletti and co-workers showed that when ^{64}Cu-labelled Cu-GTSM was administered intravenously, brain uptake of ^{64}Cu as measured by *ex vivo* gamma-counting was found to be significantly greater in APP/PS1 mice than in their age-matched wild-type counterparts at 60 min post-injection of the tracer (155).

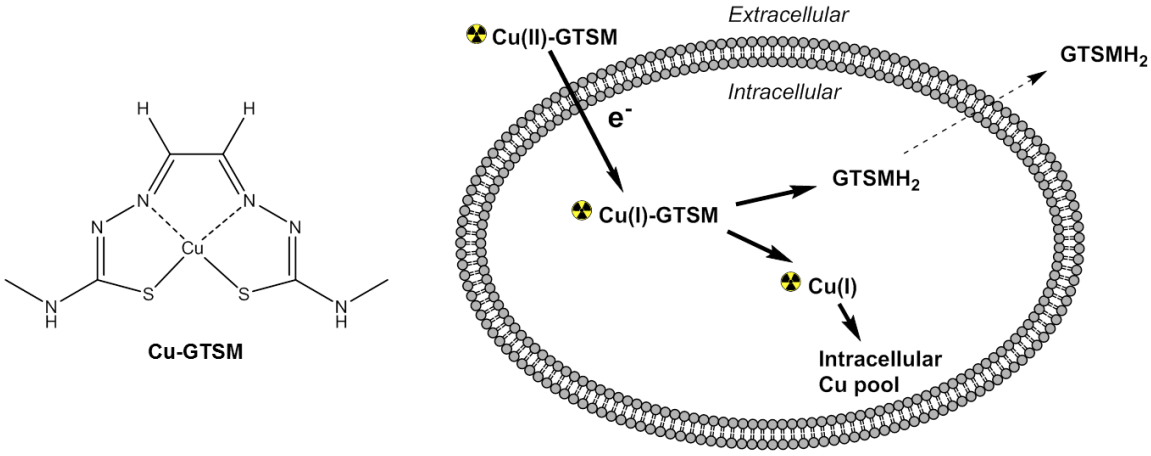

Figure 3.2: Chemical structure of Cu-GTSM and proposed uptake mechanism.

Following up on the work by Fodero-Tavoletti *et al.*, in this chapter we explore brain copper trafficking in AD by ^{64}Cu-GTSM-PET in the TAS10 x TPM (TASTPM) transgenic mouse model

of AD-like pathology. The visualisation, mapping and monitoring of ^{64}Cu trafficking in this model of AD will provide valuable information to determine the potential of imaging brain copper trafficking as a diagnostic marker for AD.

3.2.2 The TASTPM mouse model of AD

Animal models have played a crucial role over the years in improving our understanding of AD pathology. The use of AD animal models has allowed the dissection of disease-related pathways, the study of interactions between pathological markers (e.g. Aβ and tau) and the *in vivo* evaluation of new treatment options. Since the etiology of sporadic AD remains unknown, the generation of most AD animal models has been based on the use of genetic mutations associated with familial AD (e.g. APP, Presenilin-1, BACE1, tau). Although these transgenic models are capable of mimicking certain features of AD, an animal model that recapitulates all aspects of the human condition has not been developed yet. The lack of concordance between AD-like pathology in preclinical models and human disease, along with the metabolic differences between humans and preclinical species, contribute to discrepancies between the results obtained in the preclinical evaluation of potential therapeutic agents and the outcome of clinical trials. More sophisticated transgenic models are therefore necessary in order to improve the translation of new treatment options from animal models to clinical practice. Regardless, the existing animal models of AD remain useful tools for studying specific pathological features of the disorder (402, 403).

Since copper has been reported to interact with several components of the Aβ cascade (e.g. APP, BACE1, Aβ), we have chosen to investigate ^{64}Cu trafficking in a transgenic mouse model of AD-like Aβ plaque pathology. Double-transgenic TASTPM mice overexpress the hAPP695swe (TAS10) and presenilin-1 M146V (TPM) mutations, which lead to early-onset cerebral Aβ plaque deposition and cognitive deficits. Both transgenes are driven by the murine Thy-1 promoter. Howlett *et al.* reported that Aβ plaque deposition in the brains of TASTPM mice was first apparent by 3 months, preceding the onset of cognitive impairment at 6 months of age. Cerebral Aβ plaque load was found to increase with age and to be greater in females than males. In addition to cerebral Aβ plaque deposition, TASTPM mice have been shown to exhibit neuronal loss and inflammatory pathology, although not to the same level as human AD. Like

other APP transgenic lines, the TASTPM mouse model does not develop NFTs, even though hyperphosphorylated tau immunoreactivity can be observed by 4 months of age (404, 405).

In the present study, TASTPM mice have been imaged at 6-8 and 13-15 months of age. We have chosen the 6-8-month range as an early clinical disease phase, since cognitive impairment in TASTPM mice becomes apparent at that age, while the 13-15-month-old group represents a moderate-to-severe stage of the disorder. Imaging experiments were initially conducted in female TASTPM mice since these have been shown to develop more severe Aβ plaque pathology than males. However, female TASTPM mice were soon replaced by their male counterparts due to high mortality rates.

3.3 MATERIALS AND METHODS

3.3.1 Chemistry

All reagents were purchased from Sigma-Aldrich, Alfa Aesar, Interlink Scientific Services and VWR International Ltd. and were used without further purification, unless otherwise stated. NMR spectra were recorded on a Bruker Ultrashield 400WB PLUS 9.4 T spectrometer (^{1}H NMR at 400 MHz). All chemical shifts were referenced to residual solvent peaks and are quoted in ppm relative to tetramethylsilane. High-performance liquid chromatography (HPLC) was performed using an Agilent Technologies 1200 series unit with an Eclipse XDB-C_{18} column (4.6 x 150 mm, 5 µm) and UV/VIS detection at 254 nm and water + 0.1 % (v/v) trifluoroacetic acid (TFA) (A) / acetonitrile + 0.1 % (v/v) TFA (B) gradient system (0 min: 95 % A / 5 % B; 15 min: 5 % A / 95 % B; 20 min: 5 % A / 95 % B; 25 min: 95 % A / 5 % B; 30 min: 95 % A / 5 % B). Mass spectra were recorded on an Agilent Technologies 6520 Accurate-Mass Q-TOF LC-MS mass spectrometer using the positive ion electrospray technique (ESI$^+$-MS). Thin layer chromatography (TLC) was performed using MERCK 60 F_{254} silica gel TLC plates as the stationary phase and ethyl acetate as the mobile phase.

Glyoxalbis(*N*^{4}-methyl-3-thiosemicarbazone) (H_2-GTSM) was synthesised following a previously reported procedure (142, 406). 4-Methyl-3-thiosemicarbazide (2.49 g, 23 mmol, **1**) was dissolved at 50 °C in 50 mL of distilled water containing 5 % acetic acid (v/v). To this, 1.31 mL

of glyoxal solution (11.4 mmol, **2**) were added dropwise. The reaction mixture was left to stir overnight at room temperature. The resulting white precipitate was collected by filtration and washed with distilled water (3 x 50 mL), ethanol (2 x 25 mL) and diethyl ether (25 mL) to yield the final product (2.5 g, 94 %, **3**). IR ν_{max}/cm^{-1}: 3317, 3148, 3000, 2328, 1512, 1248, 1083, 914; ^1H NMR (400MHz, DMSO-d_6) δ 2.965 (6H, d, 2 x NHCH_3, $^3J_{H-H}$ = 4 Hz), 7.728 (2H, s, 2 x *H*C(=N)NHC(=S)), 8.505 (2H, q, 2 x C(=S)N*H*CH_3 $^3J_{H-H}$ = 4 Hz), 11.770 (2H, s, 2 x HC(=N)N*H*C(=S)); HPLC: R_t = 6.15 min. ESI^+ MS: m/z for $[C_6H_{12}N_6S_2 + H]^+$ = 233.0638 (calc.), 233.0671 (found). TLC: R_f = 0.75.

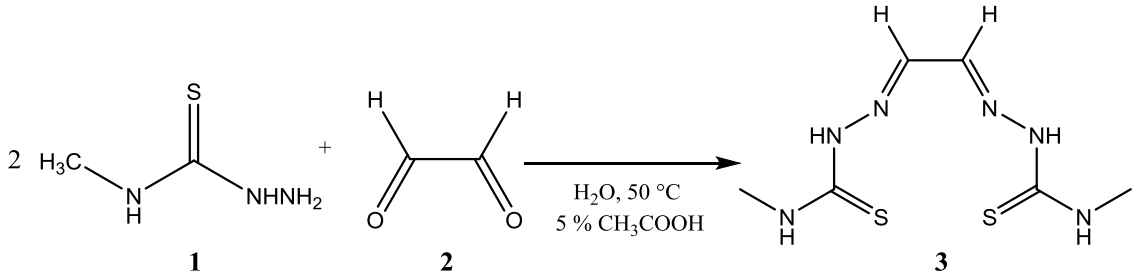

Figure 3.3: Synthesis of H_2-GTSM (**3**) from 4-Methyl-3-thiosemicarbazide (**1**) and glyoxal (**2**).

The Cu-GTSM complex was prepared following a previously reported protocol (142). The H_2-GTSM ligand (0.33 g, 1.4 mmol, **3**) was dissolved in 1 M sodium hydroxide solution (25 mL). To this, an aqueous solution of copper (II) acetate (0.25 g, 1.4 mmol, **4**) was slowly added, resulting in the formation of a brown precipitate. The reaction was left to stir overnight at room temperature. The solid was then retrieved by filtration and washed with distilled water (3 x 50 mL) and cold methanol (50 mL) (0.28 g, yield= 68 %, **5**). IR ν_{max}/cm^{-1}: 3307, 3000, 1747, 1533, 1452, 1384, 1201, 863. HPLC: R_t = 5.57 min. ESI^+ MS: m/z for $[CuC_6H_{10}N_6S_2 + H]^+$= 293.9777 (calc.), 293.9805 (found).

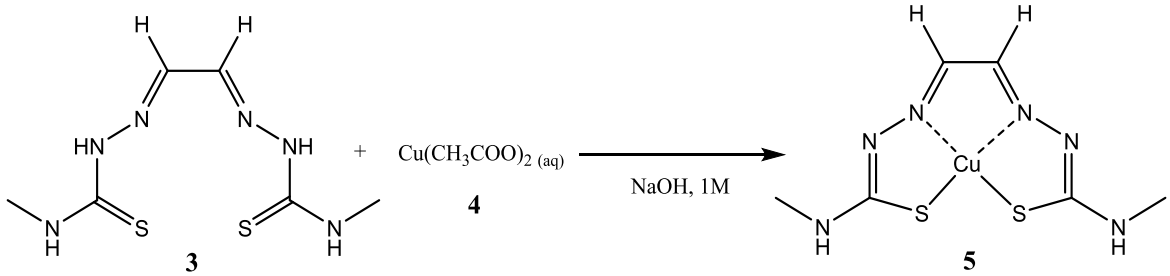

Figure 3.4: Synthesis of Cu-GTSM (**5**).

3.3.2 Radiochemistry

^{64}Cu was produced as previously reported on a CTI RDS 112 biomedical cyclotron at the Clinical PET Centre of St Thomas' Hospital in the form of $^{64}CuCl_2$ in 0.1 N HCl solution (4.8 GBq/µg) (99). Radioactivity was measured using a Capintec CRC-25R dose calibrator. Radio-TLC was performed on a LabLogic Flow-Count scanner (scan speed: 0.25 mm/s), using MERCK 60 F_{254} silica gel TLC plates as the stationary phase and ethyl acetate as the mobile phase.

$^{64}CuCl_2$ (~300 MBq, pH 1) was neutralised to pH 6 with a 3 M solution of sodium acetate (R_f = 0, 100 % radiochemical purity). ^{64}Cu-GTSM (~90 % isolated radiochemical yield, ≥ 95 % radiochemical purity) was synthesised by reaction of the GTSM ligand with ^{64}Cu-acetate (~300 MBq) using a previously reported radiolabelling protocol (142). $^{64}CuCl_2$ was initially buffered with 3 M sodium acetate to pH 6. To this solution, 10 µL of a 1 mg/mL solution of GTSM in dimethyl sulfoxide (DMSO) were added. The reaction mixture was vortexed for 1 minute and allowed to stand at room temperature for 5-10 minutes. The resulting ^{64}Cu-GTSM solution was then loaded onto a C_{18} cartridge (Sep-Pak C_{18} Plus Short Cartridge, 360 mg Sorbent, 55-105 µm particle size, Waters Ltd.), previously conditioned with ethanol and water. The sample was washed through with water (5 mL) and finally eluted in ethanol (2 mL). The initial 0.3 mL of ethanol was discarded, the following 1 mL fraction containing the purified ^{64}Cu-GTSM complex, was collected and the remaining portion was discarded. Radio-TLC analysis of the radiolabelled complex was performed before and after purification (R_f = 0.37; RCP≥ 95 %). For intravenous administration, ^{64}Cu-GTSM was diluted in sterile 0.9 % saline solution (w/v) to <10 % of total injected volume (< 200 µL).

3.3.3 Animals

All animal experiments were performed in accordance with the Animals (Scientific Procedures) Act, 1986 and approved by the local ethics committee. Mice were fed *ad libitum* with regular animal feed (Rat and Mouse No.1 Maintenance, SDS, UK).

Double-mutant TASTPM mice on a C57BL/6J background were bred in-house from mice provided by GlaxoSmithKline (GSK), and genotyped to confirm the presence of the TAS and

TPM mutant transgenes. C57BL/6J wild-type mice were obtained from Charles River Laboratories International, Inc. Both TASTPM and C57BL/6J mice were kept under the same housing conditions (21°C, 50 % humidity).

3.3.4 Genotyping

DNA was extracted from ear tissue samples from TASTPM mice in the following manner. Ear tissue samples were initially incubated in 30 µL of polymerase chain reaction (PCR) lysis buffer, consisting of 2 µL of a 20 mg/mL proteinase K aqueous solution and 950 µL of lysis buffer (3.60 mL of 10x GB buffer, 0.72 mL of 25 % [v/v] Triton X-100, 0.36 mL of β-mercaptoethanol and 31.32 mL of water; 10x GB buffer: 4.47 mL of 1.5 M Tris-HCl pH 8.8, 1.66 mL of 1 M $(NH_4)_2SO_4$, 0.67 mL of 1 M $MgSO_4$ and 3.20 mL of water). The mixture was subsequently incubated in a thermo-shaker (PHMT Grant-bio) at 55 °C for 1 h and at 95 °C for 5 minutes. The resulting sample was then vortexed for 1 minute at 2500 g (Eppendorf centrifuge 5424R) and stored at -20°C.

Multiplex PCR was performed using an Agilent Technologies SureCycler 8800 unit. Each PCR reaction mixture contained 2 µL of DNA template, 12.5 µL of QIAGEN multiplex PCR mastermix (*Taq* DNA polymerase, deoxynucleotide triphosphates and $MgCl_2$ in a $KCl/(NH_4)_2SO_4$ buffer), 10.4 µL of water, 0.05 µL of TAS or TPM 5'→3' primer and 0.05 µL of TAS or TPM 3'→5' primer (TAS 5'→3': CAG CTG GTT GAC CTG TAG CTT T; TPM 5'→3': CAG CTG GTT GAC CTG TAG CTT T; TAS 3'→5': GTG TGC CAG TGA AGA TGA; TPM 3'→5': ATG CTT GGC GCC ATA TTT CAA TG). Amplification reactions consisted of an initial denaturation period (10 minutes at 95 °C), followed by 9 cycles (95 °C for 15 seconds, 68 °C for 15 seconds and 72 °C for 30 seconds) and 25 cycles (95 °C for 15 seconds, 58 °C for 15 seconds and 72 °C for 30 seconds). 5 µL of 6 X orange DNA loading dye (Thermo Fisher Scientific Inc.) were subsequently added to each PCR reaction mixture. The samples were then subjected to electrophoresis in 1.2 % agarose gel in TAE buffer (Tris, CH_3COOH and EDTA) containing 0.01 % (v/v) of SYBR safe DNA stain (Life Technologies-Invitrogen). Quick-Load 2-Log DNA ladder (0.1-10.0 kb, New England Biolabs Inc.) was used as a molecular weight marker. Amplified PCR products were photographed under UV light using a UVP GelDoc-It^{TS2} gel imaging system.

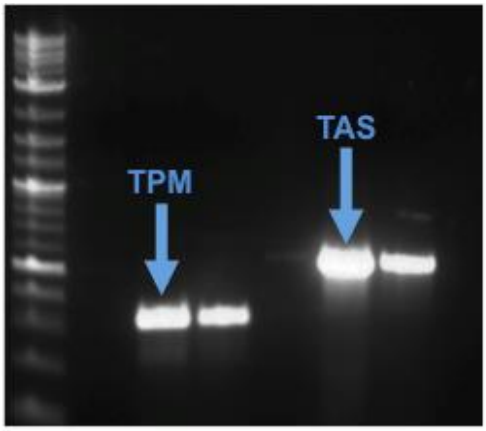

Figure 3.5: Gel electrophoresis illustrating the presence of the TAS and TPM mutant transgenes.

3.3.5 Immunohistochemistry

The extent of Aβ plaque deposition in the TASTPM mouse model was characterised following a previously reported immunohistochemistry protocol (404). Brain hemispheres of male and female TASTPM mice (6-8 and 13-15 months old) were immersed in 4 % (w/v) paraformaldehyde in 0.1 M phosphate buffered saline (pH 7.4) for 72 h. Brain tissue was then processed into paraffin wax (through sequential immersion in ethanol and xylene) and sectioned in the sagittal plane (6 μM). For Aβ-40 and Aβ-42 immunostaining, sections were dewaxed in xylene, rehydrated through a series of graded alcohols (100 %, 90 %, 70 % industrial methylated spirits, v/v), washed with distilled water, treated with 98 % (v/v) formic acid for 15 min to increase Aβ antigenicity and incubated in 0.3 % (v/v) hydrogen peroxide in phosphate-buffered saline (PBS) for 30 min to quench endogenous peroxidase activity. Brain slices were then incubated overnight at 4°C with monoclonal mouse antibodies to Aβ-42 (20G10, 1:10000, GlaxoSmithKline Pharmaceuticals R&D, UK) and Aβ-40 (11C5, 1:1000, GlaxoSmithKline Pharmaceuticals R&D, UK) in primary buffer (0.3 % [v/v] Triton X-100, 2 % [v/v] bovine serum albumin and 0.01 % [v/v] sodium azide in PBS). After incubation, brain sections were washed and incubated with biotinylated anti-mouse IgG (1:500, Vector Laboratories) in secondary buffer (0.3 % [v/v] Triton X-100 in PBS) for 45 min at 4°C. Tissue slices were then washed and incubated with the avidin-biotin complex (ABC Peroxidase Standard Staining Kit, Thermo Fisher Scientific Inc.) for 1 h at room temperature. For colour development, brain slices were incubated with the 3,3'-diaminobenzidine (DAB) reagent (DAB Substrate kit, Vector Laboratories) and counterstained with Mayer's hematoxylin (Sigma Aldrich). Finally, tissue sections were dehydrated and mounted with DPX new mounting medium (Merck Millipore). Images of

immunostained slices were acquired using a light microscope (DM6000B; Leica Microsystems Ltd., Bucks, UK).

3.3.6 Serum stability

The stability of ^{64}Cu-GTSM in serum was assessed following a previously reported method (146). ^{64}Cu-GTSM (0.5 MBq in saline) was incubated in 500 µL of fresh human serum at 37°C and 250 rpm. At selected time-points (1, 15, 30, 45, 60, 90, 120 min and 24 h), the amount of intact complex was determined in triplicate by radio-TLC.

3.3.7 Solvent extraction

6-8-month-old TASTPM mice and age-matched controls were injected with ^{64}Cu-GTSM (~20 MBq) and sacrificed at 30 min and 24 h post-injection (n = 2/group/time point). Brains were explanted and homogenised in 500 µL of ice-cold PBS. 1 mL of n-octanol was subsequently added to the brain homogenate and the mixture was incubated at 0°C for 30 min under stirring. Samples were then centrifuged at 14000 g for 15 min at 4°C. The organic layer was separated from the aqueous phase (which contained denatured proteins and cell debris) and the two fractions were subsequently gamma-counted. The octanol-extractable fraction was analysed via radio-TLC to determine the presence of intact ^{64}Cu-GTSM complex.

3.3.8 *In vivo* blood sampling

Following intravenous ^{64}Cu-GTSM administration to wildtype mice (6-8 months old, n=4), blood samples (~10 µL) were withdrawn from the jugular vein at 1, 2, 5, 10, 15, 20, 30, and 60 min post-injection. Blood aliquots were subsequently weighed and gamma-counted. Time-activity curves were constructed to determine the blood half-life of the tracer.

3.3.9 PET/CT imaging

Imaging experiments were conducted using a nanoScan® PET/CT (Mediso Medical Imaging Systems, Budapest, Hungary) (407). Dynamic PET/CT imaging was conducted in female TASTPM mice and C57BL/6J wild-type controls at 6-8 months of age (n=3). Mice were anaesthetised by isoflurane inhalation (3 % [v/v], Vet Tech Solutions Ltd.), cannulated via lateral tail vein on the scanning bed, injected with ^{64}Cu-GTSM (10 MBq, ≤200 µL) and imaged by PET

for 4 h (400-600 keV energy window; 5 ns coincidence window, 0.30 x 0.30 x 0.30 mm^3 voxel size), followed by a CT scan (180 projections, 45 KVp, 0.25 x 0.25 x 0.21 mm^3 voxel size). Longitudinal ^{64}Cu-GTSM PET experiments were performed in 6-8- (n=4) and 13-15-month-old (n=3) male TASTPM mice and age-matched controls (n=6 and n=3, respectively). Animals were anaesthetised by isoflurane inhalation (3 %), injected with ^{64}Cu-GTSM (35 MBq, ≤200 µL) via lateral tail vein and immediately placed on the scanning bed in a prone position. PET acquisition (400-600 keV energy window; 5 ns coincidence window, 0.30 x 0.30 x 0.30 mm^3 voxel size) was started 1 min after tracer injection and continued for 30 min, followed by a CT scan (180 projections, 45 KVp, 0.25 x 0.25 x 0.21 mm^3 voxel size) for anatomical reference and attenuation correction. Anaesthesia was maintained at 2 % isoflurane throughout the duration of the scan. Animals were allowed to recover from anaesthesia and housed for 24 h. Urine and faeces were collected overnight. At 24 h post-injection of the tracer, mice were anaesthetised (3 % isoflurane) and re-scanned for 1 h. Respiration rate and bed temperature were monitored throughout all scans.

3.3.9.1 PET image analysis

All PET/CT datasets were reconstructed using a novel Monte Carlo-based full 3D iterative algorithm called Tera-Tomo (Mediso Medical Imaging Systems, Budapest, Hungary) (408). To visualise small structures within the mouse brain, ‘fine’ reconstruction settings were used (8 iterations, 6 subsets, 0.25 x 0.25 x 0.25 mm^3 voxel size) for all PET datasets. Decay, dead-time, and intercrystal scatter corrections were applied as part of the reconstruction. Reconstructed CT images were used to derive an attenuation map for PET attenuation correction. Dynamic 0-4 h PET scans were reconstructed into 5-min (0-30 min) and 30-min (30-240 min) time bins. The 0-30 min PET datasets were reconstructed into 5-min bins and binned images corresponding to 25–30 min post-injection were used for ROI analysis. Static 24-25 h PET datasets were reconstructed into single bins representing the average radiotracer biodistribution during this time frame. All reconstructed datasets were analysed using VivoQuant 1.21 software (inviCRO, LLC, Boston, USA), which enables automatic co-registration of PET and CT images and delineation of regions of interest (ROIs) for quantification of activity in specific organs. When the initial automatic co-registration of PET and CT images was unsatisfactory, manual co-registration functions were used to ensure accurate alignment of CT and PET images in all

planes. ROIs for different organs (e.g. brain) were defined in order to express ^{64}Cu uptake in each organ as percentage of injected dose per milliliter (%ID/mL)**.** The sum of activity (MBq) in the organ ROI was divided by the sum of activity (MBq) in the whole-body ROI (excluding tail) at the time of injection and the resulting percentage (%ID) was normalised by the volume of the organ ROI (%ID/mL). A mouse brain atlas NM/CT module (inviCRO, LLC) with 14 pre-defined regions was automatically co-registered to all PET datasets to enable measurement of global and regional brain uptake of ^{64}Cu as %ID/mL.

3.3.9.2 Texture analysis

All PET/CT datasets were initially co-registered using VivoQuant 1.21 (InviCRO, LLC) and exported to in-house software implemented in MATLAB 2013b (The MathWorks, Inc.) capable of measuring first, second and high order heterogeneity parameters (409, 410). PET and CT image files were simultaneously imported in DICOM format and aligned. 3D ROIs were then manually drawn on the CT image file to separate the object of interest from the background. The same ROI was automatically overlaid on the PET scan in order to compute the properties of both modalities for the same region. First order parameters (mean, minimum/ maximum intensity, standard deviation, skewness, kurtosis, coefficient of variation, median, energy and entropy) measuring the distribution of voxel intensities were measured and statistically analysed.

3.3.10 *Ex vivo* biodistribution

Mice were sacrificed by cervical dislocation immediately after imaging (25 h post-injection of ^{64}Cu-GTSM) and all major organs were explanted, weighed and gamma-counted (LKB Wallac 1282). ^{64}Cu uptake in each organ was expressed as %ID/g. The total injected dose was defined as the sum of all whole-body counts (excluding tail) and excreted activity (urine and faeces).

3.3.11 *Ex vivo* brain autoradiography

Brain tissue explanted from imaged mice was immersed in a 30 % (w/v) sucrose solution for ~6 h and stored at -80°C overnight. Cryopreserved brains were then sectioned (10 µm) in the sagittal plane using a Bright 5040 cryotome. Tissue sections were thaw-mounted onto Superfrost PLUS glass microscope slides (Menzel-Glaser, Thermo Scientific) and allowed to dry

at room temperature. The slides were then exposed to a storage phosphor screen (PerkinElmer, Super Resolution, 12.5 x 25.2 cm) in a standard X-ray cassette for 15 h. The phosphor screen was then imaged using a Typhoon 8600 scanner (Molecular Dynamics) and images were analysed with OptiQuant 5.0 (PerkinElmer) and ImageJ (NIH).

3.3.12 Congo red staining

Following autoradiography, brain slices were stored at -80°C until decayed. For Congo red staining, frozen brain slices were fixed in 4 % (w/v) PFA for 45 min and subsequently washed with distilled water. Brain slices were then incubated in Congo red solution (0.5 % [w/v] Congo red dye [Sigma Aldrich] in 50 % [v/v] EtOH) for 15-20 min, rinsed with distilled water, and dipped (5-10 times) in alkaline alcohol solution (1 % [w/v] NaOH, 50 % [v/v] EtOH). Tissue slices were subsequently rinsed in tap water for 1 min and counterstained with Harris' hematoxylin solution (Sigma Aldrich) for 10 s. Brain sections were then rinsed in tap water for 2 min and incubated in acid alcohol solution (1 mL 3M HCl in 200 mL 70 % [v/v] IMS) for 1 min. Finally, brain slices were incubated in 95 % (v/v) alcohol (3 min, 2 changes), 100 % alcohol (3 min, 2 changes) and Histo-Clear II solution (National Diagnostics, 1 min, 2 changes), and mounted with DPX new mounting medium (Merck Millipore). All cover-slipped slides were then evaluated under bright-field microscopy using a light microscope (DM6000 B; Leica Microsystems Ltd., Bucks, UK).

3.3.13 Statistical analysis

All data are reported as mean ± SD. Statistical analysis was performed using GraphPad Prism 5 (GraphPad Software Inc.). Two-way repeated measures ANOVA with post-hoc analyses using the Bonferroni multiple comparison correction was used to determine statistically significant differences between TASTPM mice and controls at different imaging time-points. A Student t-test (2-tailed, unpaired) was used to compare individual datasets.

3.4 RESULTS

3.4.1 Immunohistochemistry

In order to determine the extent of cerebral Aβ plaque deposition in male and female TASTPM mice at early (6-8 months old) and middle stages of the disease (13-15 months old), we stained

serial sections of TASTPM brain tissue with Aβ-40- and Aβ-42-specific antibodies. The Aβ-40 and Aβ-42 isoforms are believed to be the primary components of Aβ plaque deposits, with Aβ-42 being the most aggregation-prone of all Aβ species (411). As depicted in Figure 3.6, Aβ immunolabelling was associated with both dense-core plaques and the halo of diffuse Aβ species surrounding their cores.

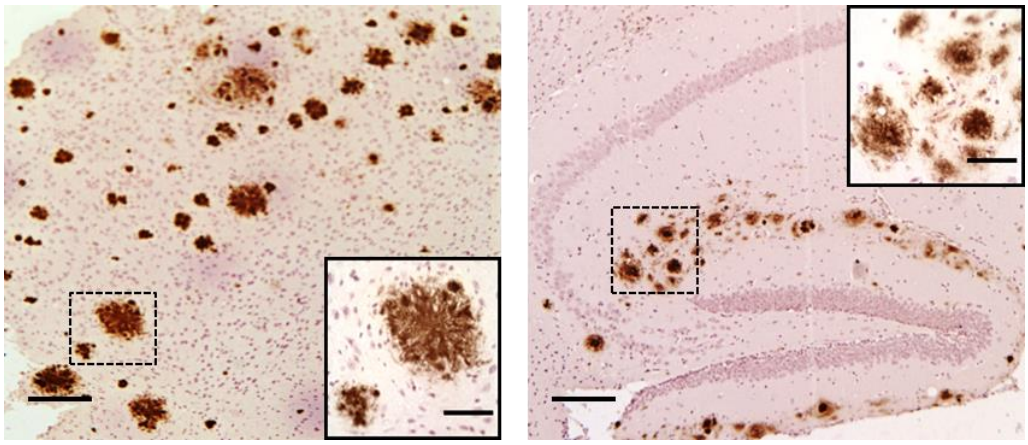

Figure 3.6: Photomicrographs of a sagittal section through the cerebral cortex (left) and hippocampus (right) of a 13-month-old female TASTPM mouse immunostained with an Aβ-42-specific antibody. The scale bars represent 100 μm on the main figures and 10 μm on the insets.

As expected, both male and female TASTPM mice showed extensive Aβ-40 and Aβ-42 immunoreactivity in the cerebral cortex, hippocampus and thalamus at 6 months of age (Figures 3.7 and 3.8). In contrast, the cerebellum, caudate putamen and medulla exhibited the lowest concentrations of Aβ species. Aβ-40 load was found to be greater than that of Aβ-42 in both male and female TASTPM mice. Cerebral Aβ-40 and Aβ-42 levels were found to increase considerably between 6 and 13 months of age in both males and females. At both ages, female TASTPM mice exhibited higher Aβ-40 and Aβ-42 immunoreactivity than their male counterparts. These observations are consistent with those of Howlett *et al.*, who reported a significant effect of age and gender on cerebral Aβ load in this model (404).

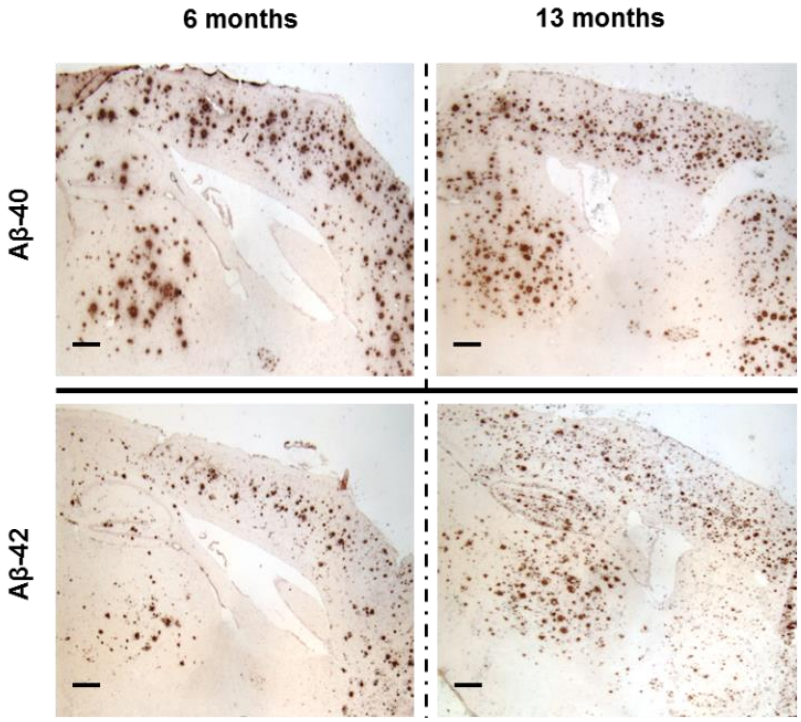

Figure 3.7: Immunohistochemical characterisation of cerebral Aβ-40/ Aβ-42 deposition in female TASTPM mice at 6 (left) and 13 (right) months of age. Photomicrographs depict areas of high Aβ plaque burden, namely the hippocampus, thalamus and cerebral cortex. The scale bars represent 200 μm.

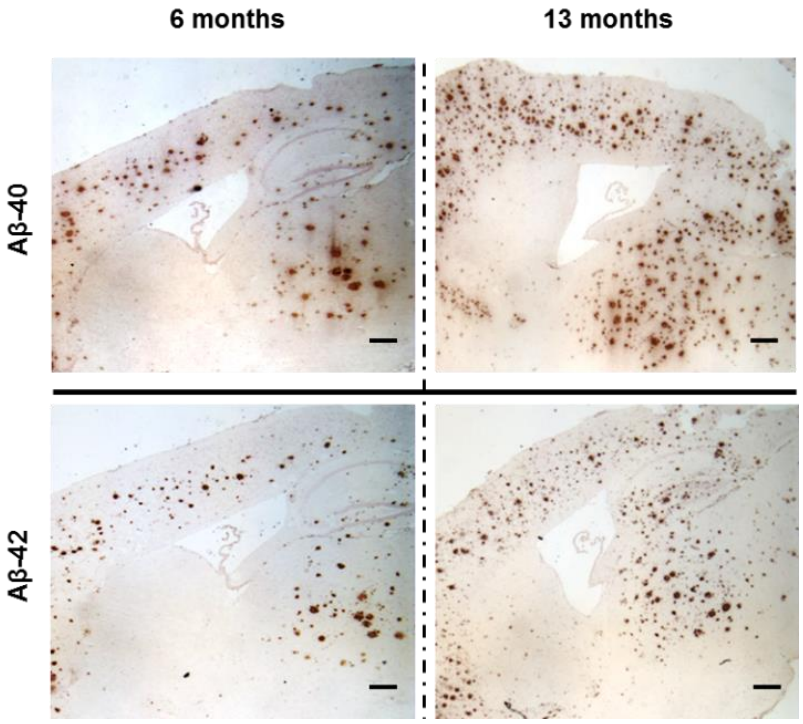

Figure 3.8: Immunohistochemical characterisation of cerebral Aβ-40/ Aβ-42 deposition in male TASTPM mice at 6 (left) and 13 (right) months of age. Photomicrographs show Aβ plaque deposition in the hippocampus, thalamus and cerebral cortex. The scale bars represent 200 μm.

3.4.2 Serum stability

To evaluate the stability of ^{64}Cu-GTSM in a biological milieu, the complex was incubated in fresh human plasma and monitored by radio-TLC at different time-points. Radio-TLC revealed that ^{64}Cu-GTSM remained intact after 2 h of incubation in serum (Figure 3.9.C). At 24 h, over 90 % of ^{64}Cu radioactivity was still in the form of the complex, demonstrating the excellent serum stability of this tracer *in vitro* (Figure 3.9.D).

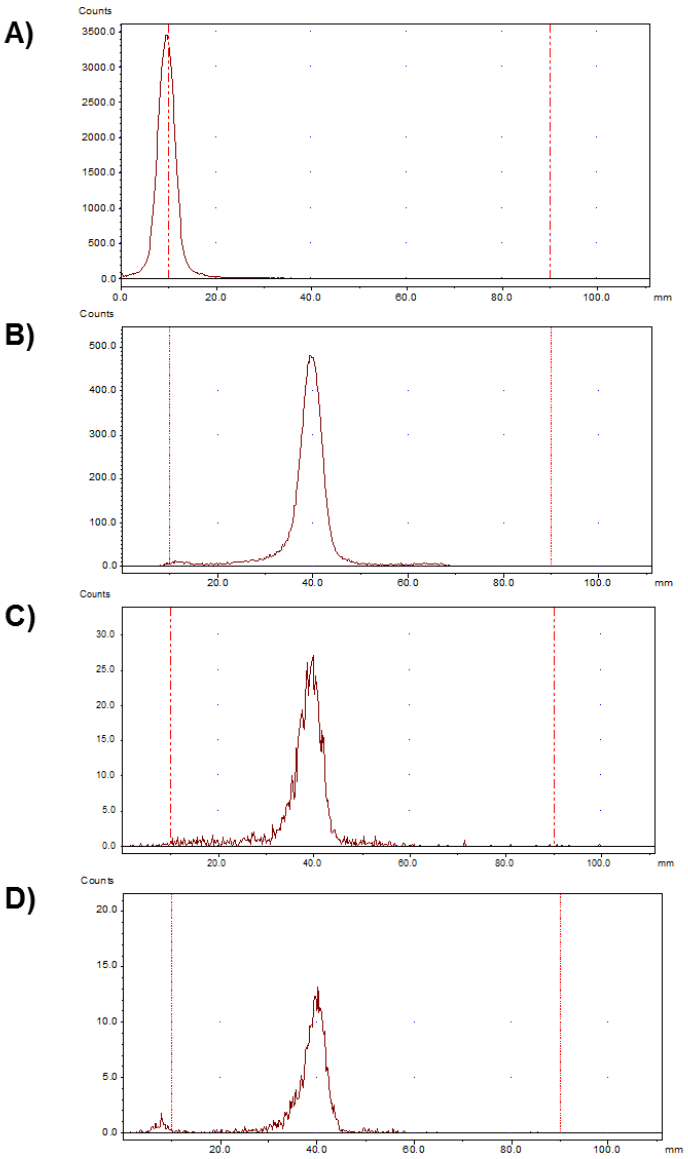

Figure 3.9: Radio-TLC chromatograms of free ^{64}Cu (**A**), ^{64}Cu-GTSM (**B**), ^{64}Cu-GTSM after 2 h of incubation in human serum (**C**) and ^{64}Cu-GTSM after 24 h of incubation in serum (**D**). Ethyl acetate was used as the mobile phase.

3.4.3 Solvent extraction

In order to assess the ability of ^{64}Cu-GTSM to release ^{64}Cu intracellularly within the brain, we determined the amount of intact complex in brain homogenates of TASTPM and wild-type mice (n = 2/group/time-point) injected with ^{64}Cu-GTSM using a previously reported octanol-extraction

method (412). Gamma-counting of aqueous/protein-bound and octanol-extractable fractions revealed high water solubility and protein/cell debris binding of ^{64}Cu activity, and little octanol extractable activity, at all time-points after tracer injection for both groups of mice. At 30 min post-administration of ^{64}Cu-GTSM, less than 4 % of brain ^{64}Cu radioactivity was associated with the octanol fraction. The partitioning of ^{64}Cu activity did not change significantly with time, with less than 3 % of the radiocopper remaining in the octanol fraction at 24 h after injection (Table 3.1). Radio-TLC of the octanol-extractable fractions showed that ^{64}Cu radioactivity was no longer in the form of ^{64}Cu-GTSM but instead behaved like ionic ^{64}Cu.

Table 3.1: Distribution of ^{64}Cu radioactivity in brain homogenates of mice injected with ^{64}Cu-GTSM.

Time post-injection (h)	Percentage of ^{64}Cu in aqueous/protein-bound fraction
0.5	96.19 ± 2.98
24	97.18 ± 0.14

Data are mean (n = 4 mice per time point) ± SD.

3.4.4 *In vivo* blood sampling

After testing the ability of ^{64}Cu-GTSM to deliver ^{64}Cu into the brain, we evaluated the clearance rate of this tracer from blood by jugular vein blood sampling in wildtype mice. ^{64}Cu-GTSM cleared rapidly from blood, following a monoexponential decay pattern with a half-life of 5.31 ± 2.03 min.

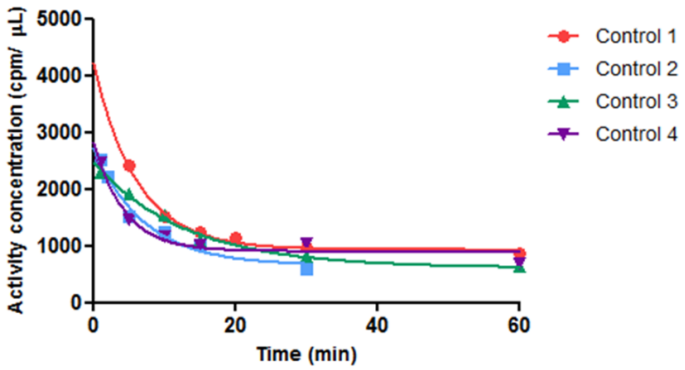

Figure 3.10: Blood time-activity curves resulting from *in vivo* blood sampling in wildtype mice injected with ^{64}Cu-GTSM. Blood clearance of the tracer showed a monoexponential decay behaviour with an elimination half-time of 5.31 ± 2.03 min.

3.4.5 PET/CT imaging

PET/CT imaging of ^{64}Cu trafficking with ^{64}Cu-GTSM was initially performed in female TASTPM mice since these displayed a more severe Aβ plaque pathology than their male counterparts, as revealed by immunohistochemistry. Dynamic PET/CT imaging (0-4 h) of 6-8-month-old female TASTPM mice and age-matched controls revealed high ^{64}Cu accumulation in the heart, lungs, liver, intestines, kidneys, spine and brain in both groups of animals. Time-activity curves showed that ^{64}Cu-GTSM uptake in the brain was rapid, reaching a plateau within the first 10 minutes after injection (Figure 3.11). Brain concentration of ^{64}Cu was found to be significantly greater in female TASTPM mice when compared to healthy controls at 30 min post-injection of ^{64}Cu-GTSM (7.51 ± 0.29 %ID/mL vs. 5.11 ± 0.01 %ID/mL, $p<0.01$, n=3/group).

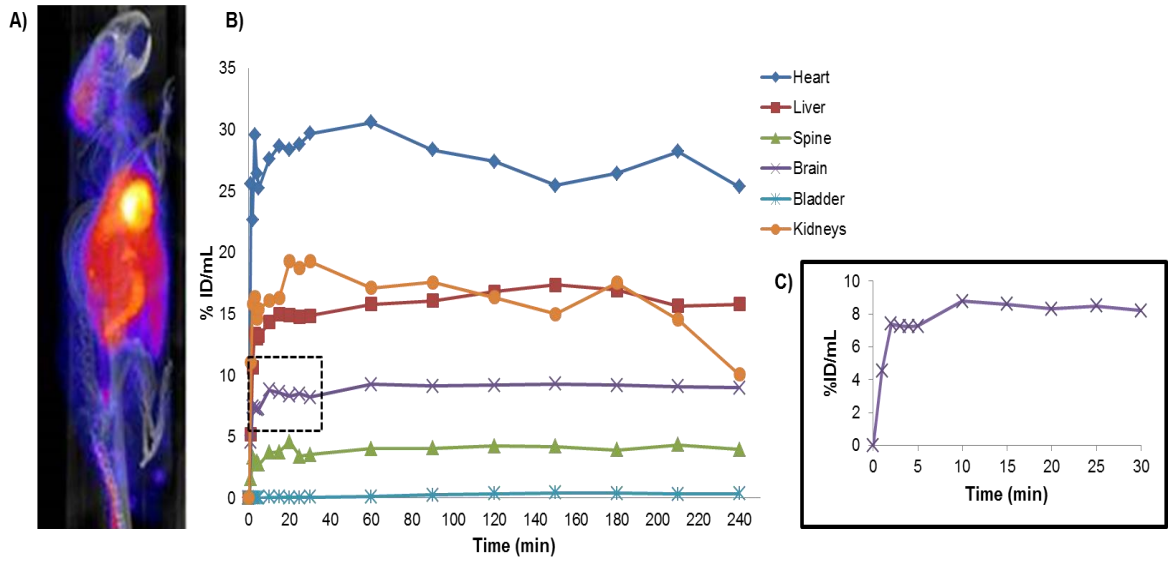

Figure 3.11: PET/CT imaging of ^{64}Cu trafficking in a female TASTPM mouse (6-8 months old) with ^{64}Cu-GTSM showing high ^{64}Cu accumulation in the heart, lungs, liver, intestines, kidneys, spine and brain (**A**). Time-activity curves generated from dynamic PET images illustrating ^{64}Cu concentration in organs of interest (**B**). Tracer uptake in the brain was rapid, peaking within 10 min after injection (**C**).

Due to high mortality rates during experimental procedures and increased seizure incidence, female TASTPM mice were replaced by males in longitudinal PET/CT imaging experiments. In order to investigate whole-body copper fluxes *in vivo* in AD-like pathology at early and middle stages of the disease, 6-8- and 13-15-month-old male TASTPM mice (n=4 and n=3) were imaged with ^{64}Cu-GTSM from 0-30 min and from 24-25 h after injection and compared to age-matched controls (n=6 and n=3, respectively) (Figures 3.12 and 3.13).

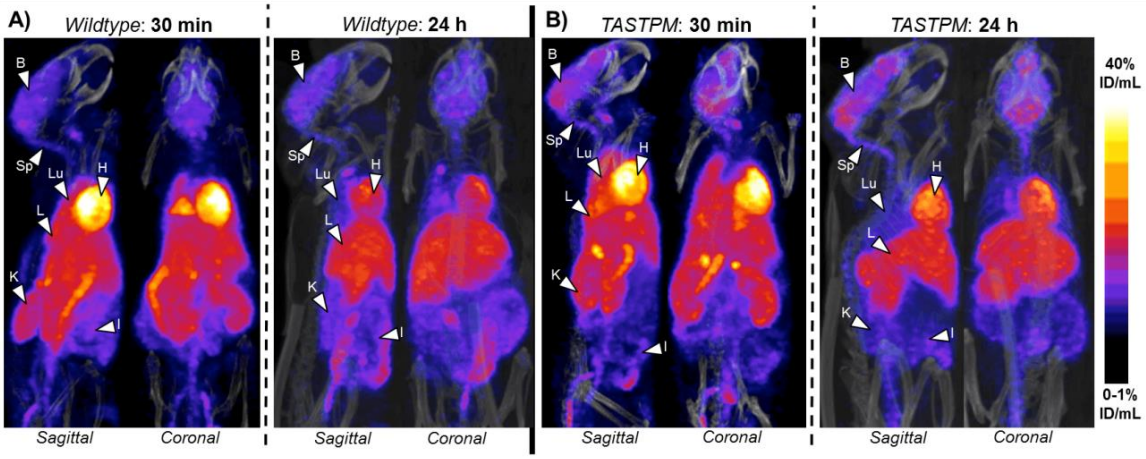

Figure 3.12: Exemplar sagittal and coronal views of PET/CT MIPs of 6-8-month-old male wild-type controls (**A**) and age-matched TASTPM transgenic mice (**B**) at 30 min and 24 h post-administration of ^{64}Cu-GTSM. ^{64}Cu-GTSM PET/CT scans showed high accumulation of ^{64}Cu in the liver, lungs, heart, kidneys, intestines, spine and brain of both TASTPM mice and age-matched controls at 30 min post-injection of the tracer. Kidney, lung and heart concentrations of ^{64}Cu decreased substantially from 30 min to 24 h post-injection, whereas tracer uptake in the brain remained relatively constant over time in both groups. Concentration of ^{64}Cu in brain appeared higher in TASTPM mice than in controls at both 30 min and 24 h post-injection of ^{64}Cu-GTSM. Organs are indicated by arrows: B = brain; Sp = spine; H = heart; Lu = lungs; L = liver; K = kidneys; I = intestines. All MIPs were scaled to 0-1 %ID/mL (min) and 40 %ID/mL (max).

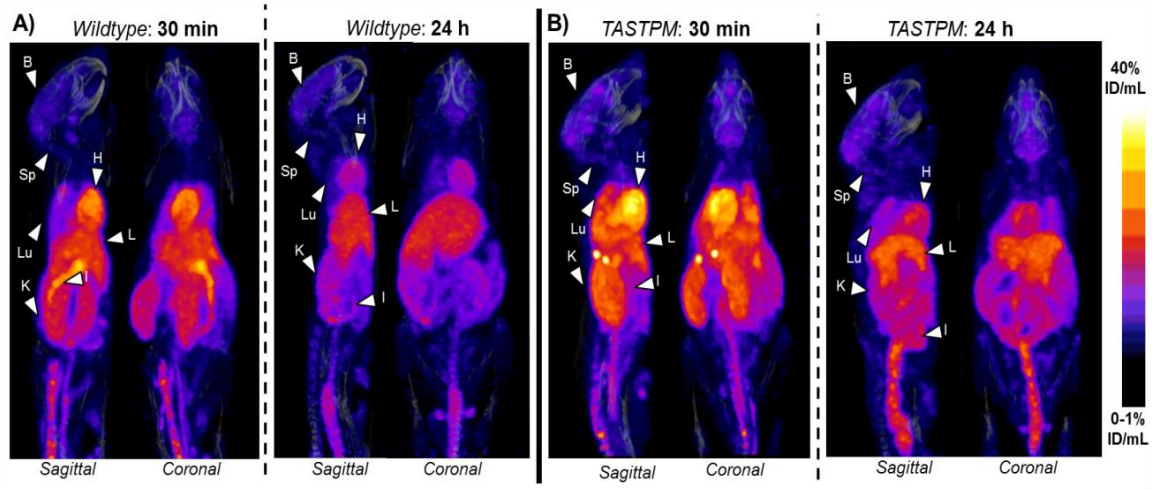

Figure 3.13: Exemplar sagittal and coronal views of PET/CT MIPs of 13-15-month-old male wild-type controls (**A**) and age-matched TASTPM transgenic mice (**B**) at 30 min and 24 h post-administration of ^{64}Cu-GTSM. ^{64}Cu radioactivity accumulated primarily in the liver, lungs, heart, kidneys, intestines, spine and brain of both TASTPM mice and age-matched controls at 30 min post-injection of the tracer. As previously observed in the 6-8-month-old mouse groups, ^{64}Cu concentration decreased in kidney, lung and heart over time but remained relatively constant in the brain. The concentration of ^{64}Cu in brain was found to be higher in TASTPM mice compared to controls at both imaging-time-points, although the difference between groups seemed less pronounced than in the case of 6-8-month-old mice. Organs are indicated by arrows: B = brain; Sp = spine; H = heart; Lu = lungs; L = liver; K = kidneys; I = intestines. All MIPs were scaled to 0-1 %ID/mL (min) and 40 %ID/mL (max).

The general biodistribution of the tracer was similar for all animal groups. At 30 min after injection, ^{64}Cu radioactivity accumulated primarily in the heart, lungs, liver, intestines, kidneys, spine and brain in both TASTPM and wild-type mice. After 24 h, a notable decrease in ^{64}Cu activity was observed in the lungs, kidneys and heart, whereas ^{64}Cu concentration in the brain

declined much more slowly, demonstrating greater ^{64}Cu retention in brain tissue compared to other organs (2.04 ± 3.57 % decrease in brain %ID/mL vs. 67.51 ± 9.48, 47.25 ± 10.34 and 50.76 ± 9.90 % decrease in lungs, kidneys and heart %ID/mL, in 6-8-month-old wildtypes). Hepatic ^{64}Cu concentration remained relatively constant over time in all groups of animals, with a slight tendency to increase (Figure 3.14). Radioactivity concentration (expressed as %ID/mL) in brain decreased with age but was higher in TASTPM mice than in wildtype controls in both age groups.

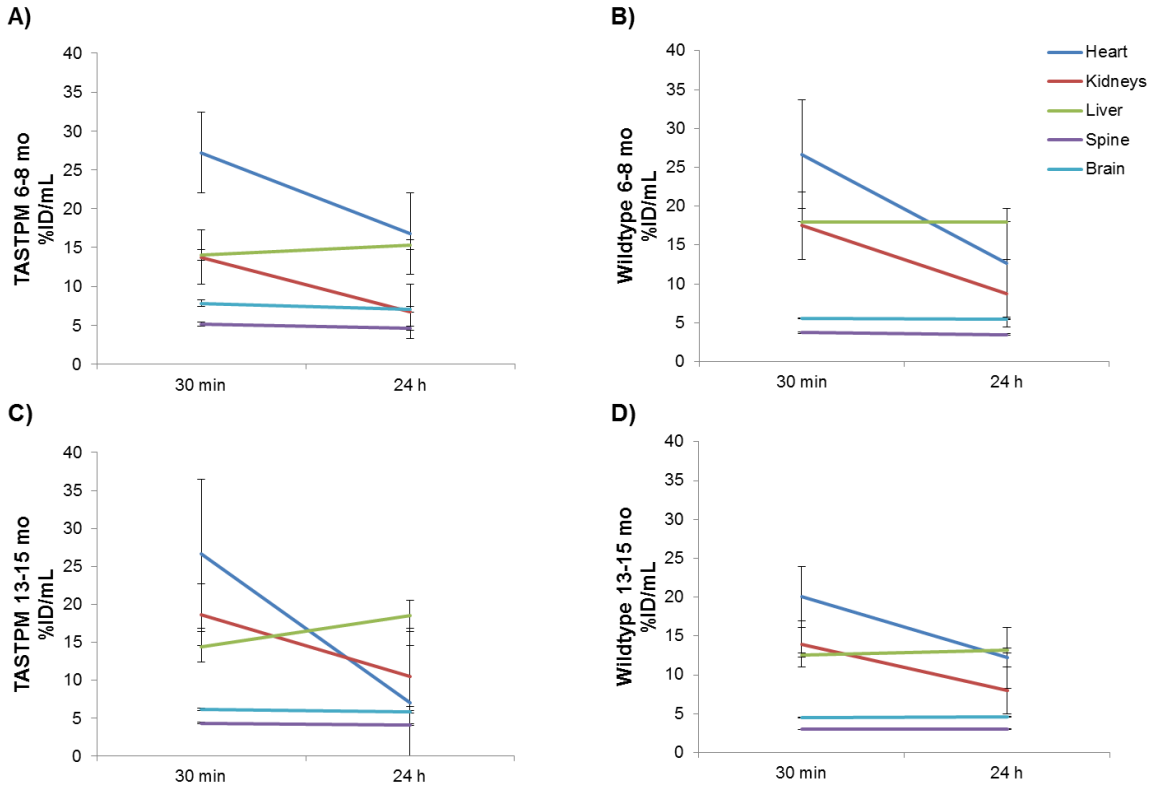

Figure 3.14: Time-activity curves extracted from PET image analysis showing ^{64}Cu concentration (expressed as % ID/mL) over time in the heart, kidneys, liver, spine and brain of 6-8- (**A**) and 13-15-month-old (**C**) male TASTPM mice and their respective age-matched controls (**B** and **D**, respectively).

^{64}Cu biokinetics within the CNS (brain and spine) were assessed using PET ROI analysis and compared between AD mice and healthy controls at both ages. Repeated measures ANOVA indicated significant effects of group ($F_{1,8}$ = 10.41, p = 0.012), time ($F_{1,8}$ = 36.04, p = 0.0003) and group by time interaction ($F_{1,8}$ = 19.84, p = 0.0021) on brain ^{64}Cu concentration in 6-8-month-old TASTPM mice and age-matched controls. Post-hoc evaluation revealed that global average brain concentration of ^{64}Cu was significantly higher in TASTPM transgenic mice than in wild-type controls at 30 min (7.83 ± 1.08 %ID/mL vs. 5.57 ± 0.70 %ID/mL, p<0.01) and 24 h (7.04 ± 0.94 %ID/mL vs. 5.46 ± 0.70 %ID/mL, p<0.05) post-injection of ^{64}Cu-GTSM. After 24 h, a significant decrease in brain ^{64}Cu concentration was found in TASTPM mice (-10.10 ± 2.23 %,

p<0.01) but not in age-matched controls (-2.04 ± 3.57 %, p>0.05). Statistical analysis also revealed significant effects of time ($F_{1,8}$ = 30.68, p = 0.0005) and group ($F_{1,8}$ = 12.23, p = 0.0081) on spine ^{64}Cu concentration, but the interaction between group and time was found to be non-significant ($F_{1,8}$ = 4.35, p = 0.07). Post-hoc tests indicated significantly higher ^{64}Cu concentration in the spinal cord of TASTPM mice as compared with controls at both 30 min (5.20 ± 0.67 %ID/mL vs. 3.73 ± 0.54 %ID/mL, p<0.01) and 24 h (4.65 ± 0.46 %ID/mL vs. 3.48 ± 0.46 %ID/mL, p<0.05) post-injection of the tracer. Figure 3.15 shows mean brain and spinal cord concentrations of ^{64}Cu in TASTPM mice and healthy controls at 30 min and 24 h post-injection of ^{64}Cu-GTSM, and the kinetic behaviour of the radiocopper in both tissues for each individual animal.

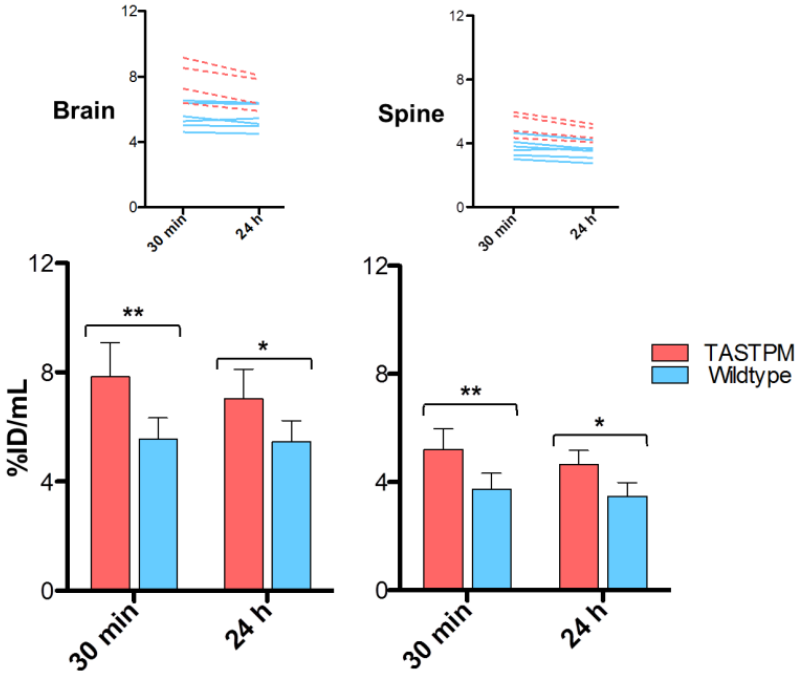

Figure 3.15: *In vivo* brain (left) and spine (right) concentration of ^{64}Cu, expressed as %ID/mL, in 6-8-month-old TASTPM mice and age-matched controls as measured by PET ROI analysis. Time-activity curves illustrating clearance of ^{64}Cu radioactivity over time for each individual mouse are shown at the top of the figure. TASTPM mice showed significantly higher concentration of ^{64}Cu in the brain and spine at 30 min and 24 h post-injection of ^{64}Cu-GTSM and a faster ^{64}Cu clearance rate from brain tissue compared to controls. Statistically significant differences from healthy controls are indicated by * (p<0.05) and ** (p<0.01). Data are mean (n = 4 for TASTPM mice; n = 6 for controls) ± SD.

Two-way ANOVA analysis also revealed a significant effect of group ($F_{1,4}$ = 16.25, p = 0.0157) on brain ^{64}Cu concentration in 13-15-month-old male TASTPM mice and age-matched controls, but did not show significant effects of time ($F_{1,4}$ = 1.230, p = 0.3296) and group by time interaction ($F_{1,4}$ = 7.687, p = 0.0502). As observed for the 6-8 month-old age group, global concentration of ^{64}Cu in the brain was significantly greater in 13-15-month-old TASTPM mice

than in age-matched controls at 30 min (6.11 ± 0.42 %ID/mL vs. 4.51 ± 0.42 %ID/mL, p<0.01) and 24 h (5.83 ± 0.25 %ID/mL vs. 4.63 ± 0.30 %ID/mL, p<0.05) post-injection of ^{64}Cu-GTSM (Figure 3.16). Brain concentration of ^{64}Cu increased slightly (2.96 ± 2.73 %) in the control group over 24 h, while it was found to decrease in TASTPM mice (-4.48 ± 2.59 %). However, this difference in ^{64}Cu biokinetics between the two groups did not reach statistical significance. A significant effect of group ($F_{1,4}$ = 34.48, p = 0.0042) was also observed on spine concentration of ^{64}Cu in 13-15-month-old TASTPM mice and age-matched controls. Post-hoc evaluation showed that spinal cord concentration of ^{64}Cu was significantly higher in the TASTPM group compared to controls at both 30 min (4.32 ± 0.32 %ID/mL vs. 2.98 ± 0.17 %ID/mL, p<0.001) and 24 h (4.09 ± 0.17 %ID/mL vs. 3.04 ± 0.21 %ID/mL, p<0.01) post-injection of ^{64}Cu-GTSM. No significant effects of time ($F_{1,4}$ = 0.7930, p = 0.4235) and interaction ($F_{1,4}$ = 2.069, p = 0.2237) on spinal cord ^{64}Cu concentration in TASTPM mice and controls at 13-15 months of age were detected.

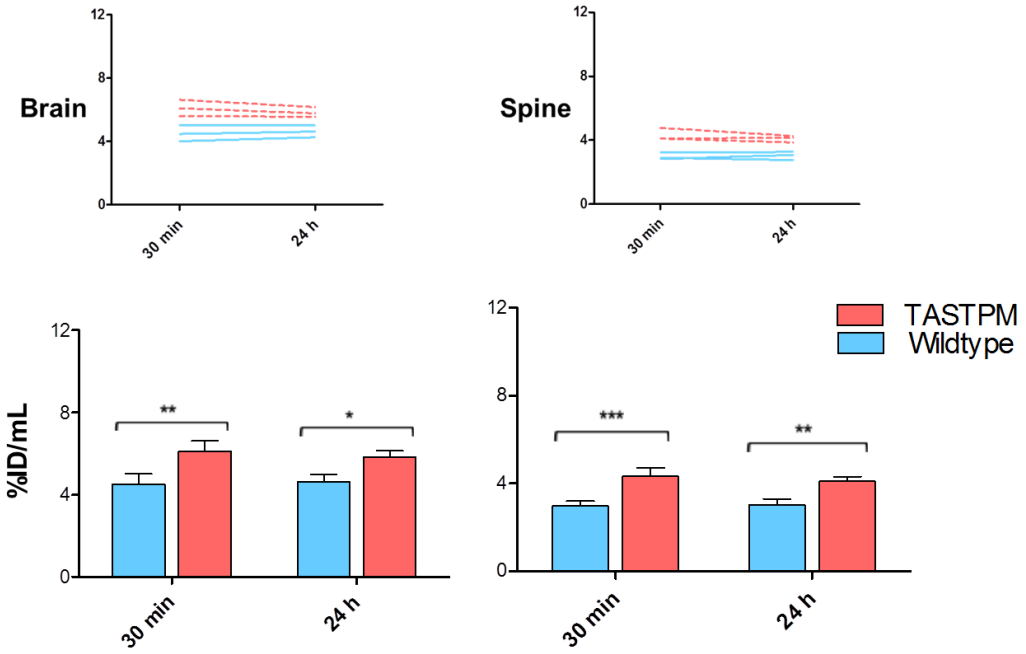

Figure 3.16: *In vivo* brain (left) and spine (right) concentration of ^{64}Cu, expressed as %ID/mL, in 13-15-month-old TASTPM mice and age-matched controls as measured by PET ROI analysis. Time-activity curves illustrating clearance of ^{64}Cu radioactivity over time for each individual mouse are shown at the top of the figure. TASTPM mice showed significantly higher concentration of ^{64}Cu in the brain and spine at 30 min and 24 h post-injection of ^{64}Cu-GTSM. Statistically significant differences from healthy controls are indicated by * (p<0.05), ** (p<0.01) and *** (p<0.001). Data are mean (n=3/group) ± SD.

Brain and spinal cord concentrations of ^{64}Cu were found to decrease with age, particularly in the TASTPM group, but this trend did not reach statistical significance. However, a significant effect of group by time interaction ($F_{1,5}$ = 7.510, p = 0.0408) on brain ^{64}Cu concentration was detected

between 6-8- and 13-15-month-old TASTPM transgenic mice, indicating a modest variation in the clearance rate of ^{64}Cu from brain tissue in the TASTPM group with age. No significant difference in ^{64}Cu radioactivity clearance from the brain was found between 6-8- and 13-15-month-old wildtype mice.

3.4.5.1 Atlas-based image analysis of regional brain concentration of ^{64}Cu

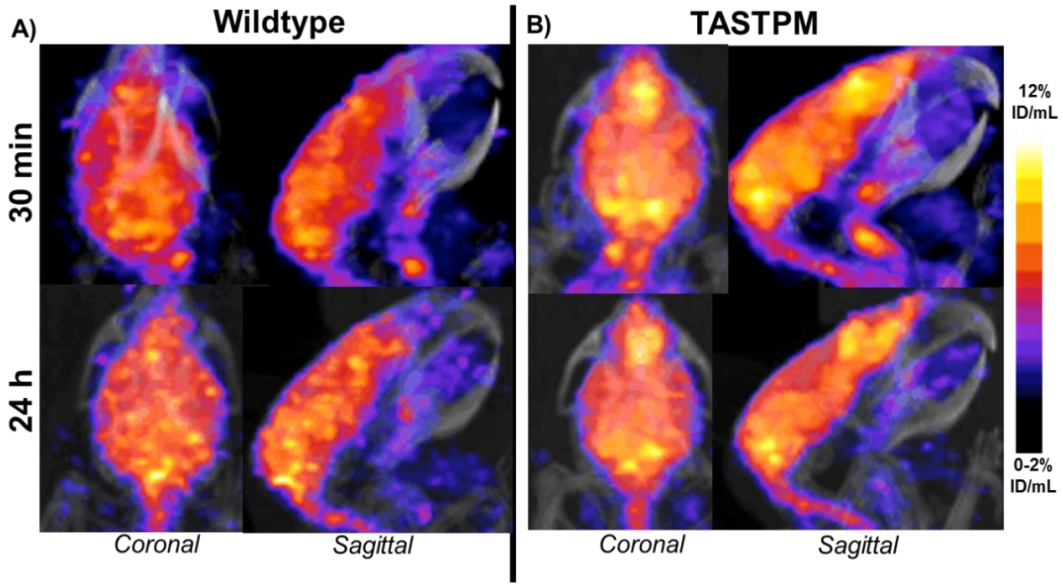

Figure 3.17: Representative coronal and sagittal section PET/CT MIP images illustrating ^{64}Cu distribution in the brain and spinal cord of 6-8-month-old C57BL/6J wild-type controls (**A**) and age-matched TASTPM mice (**B**) at 30 min (top) and 24 h (bottom) post-injection of ^{64}Cu-GTSM. PET/CT scans revealed increased uptake and prolonged retention of ^{64}Cu in the brains of TASTPM and wild-type mice, as well as heterogeneous distribution of the radiolabel at 30 min and 24 h post-injection of the tracer. All MIPs were scaled to 0-2 %ID/mL (min) and 12 %ID/mL (max).

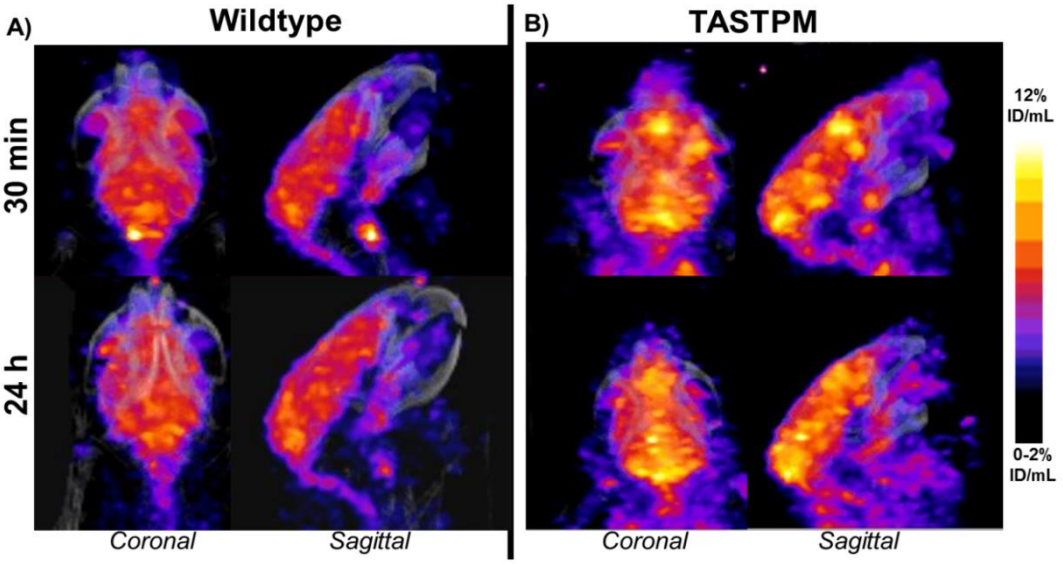

Figure 3.18: Representative coronal and sagittal section PET/CT MIP images showing ^{64}Cu distribution in the brain and spinal cord of 13-15-month-old C57BL/6J wild-type controls (**A**) and age-matched TASTPM mice (**B**) at 30 min (top) and 24 h (bottom) post-injection of ^{64}Cu-GTSM. All MIPs were scaled to 0-2 %ID/mL (min) and 12 %ID/mL (max).

As depicted in Figures 3.17 and 3.18, ^{64}Cu-GTSM administration resulted in the heterogeneous distribution of ^{64}Cu in the brains of both wildtype and TASTPM mice at all imaging time-points. On visual assessment, PET images showed both higher brain uptake and greater inhomogeneity, with more concentration of ^{64}Cu hotspots, in the TASTPM AD model when compared to healthy controls.

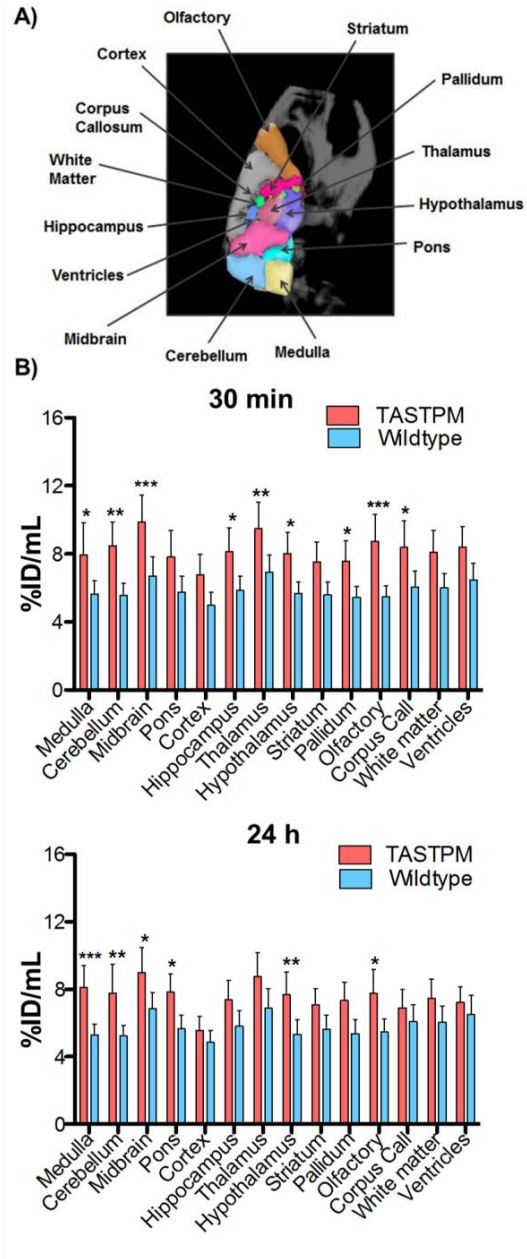

Figure 3.19: (**A**) 3D mouse brain atlas; (**B**) Regional brain distribution of ^{64}Cu in 6-8-month-old TASTPM transgenic mice and age-matched controls at 30 min (top) and 24 h (bottom) post-injection of ^{64}Cu-GTSM. Statistically significant differences from healthy controls are indicated by * ($p<0.05$), ** ($p<0.01$) and *** ($p<0.001$). Data are mean ($n = 4$ for TASTPM mice; $n = 6$ for controls) ± SD.

In order to quantify ^{64}Cu uptake heterogeneity in a functional context, brain PET images were analysed using a 3D mouse brain atlas. Statistical analysis revealed significant effects of group, region and group by region interaction on brain regional ^{64}Cu accumulation in 6-8-month-old

TASTPM mice and age-matched controls at both 30 min ($F_{1,8}$ = 12.68, p = 0.0074; $F_{1,8}$ = 21.64, p<0.0001; $F_{1,8}$ = 2.971, p=0.001) and 24 h ($F_{1,8}$ = 7.701, p = 0.0241; $F_{1,8}$ = 40.87, p<0.0001; $F_{1,8}$ = 11.69, p<0.0001) post-injection of the tracer. Post-hoc tests were used to identify brain regions of significantly different ^{64}Cu concentration between these two groups. At 30 min post-injection of the tracer, TASTPM mice showed significantly higher ^{64}Cu concentration than controls in the medulla (p<0.05), cerebellum (p<0.01), midbrain (p<0.001), hippocampus (p<0.05), thalamus (p<0.01), hypothalamus (p<0.05), pallidum (p<0.05), olfactory bulb (p<0.001) and corpus callosum (p<0.05). The TASTPM group maintained significantly higher ^{64}Cu concentration than controls in the medulla (p<0.001), cerebellum (p<0.01), midbrain (p<0.05), hypothalamus (p<0.01) and olfactory bulb (p<0.05), as well as pons (p<0.05), at 24 h after injection of the tracer (Figure 3.19). Standard deviations of mean regional uptake values were noticeably larger for TASTPM mice when compared to controls, revealing a greater inter-individual variability in the disease group.

In a similar manner to the 6-8-month-old group, significant effects of group, region and interaction on brain regional ^{64}Cu concentration were found in 13-15-month-old TASTPM mice and age-matched controls at 30 min ($F_{1,8}$ = 14.86, p = 0.0182; $F_{1,8}$ = 20.69, p<0.0001; $F_{1,8}$ = 4.835, p<0.0001) and 24 h ($F_{1,8}$ = 19.24, p = 0.0118; $F_{1,8}$ = 13.80, p<0.0001; $F_{1,8}$ = 4.446, p<0.0001) post-injection of ^{64}Cu-GTSM. Post-hoc evaluation revealed significantly greater concentrations of ^{64}Cu in the cerebellum (p<0.001), midbrain (p<0.001), pons (p<0.05), thalamus (p<0.05), hypothalamus (p<0.01), pallidum (p<0.05), olfactory bulb (p<0.001), corpus callosum (p<0.05) and ventricles (p<0.05) of TASTPM mice compared to controls at 30 min post-administration of the tracer. After 24 h, 13-15-month-old TASTPM mice exhibited significantly higher ^{64}Cu concentrations than controls in the cerebellum (p<0.001), midbrain (p<0.001), thalamus (p<0.01), olfactory bulb (p<0.001), corpus callosum (p<0.01) and ventricles (p<0.001) (Figure 3.20).

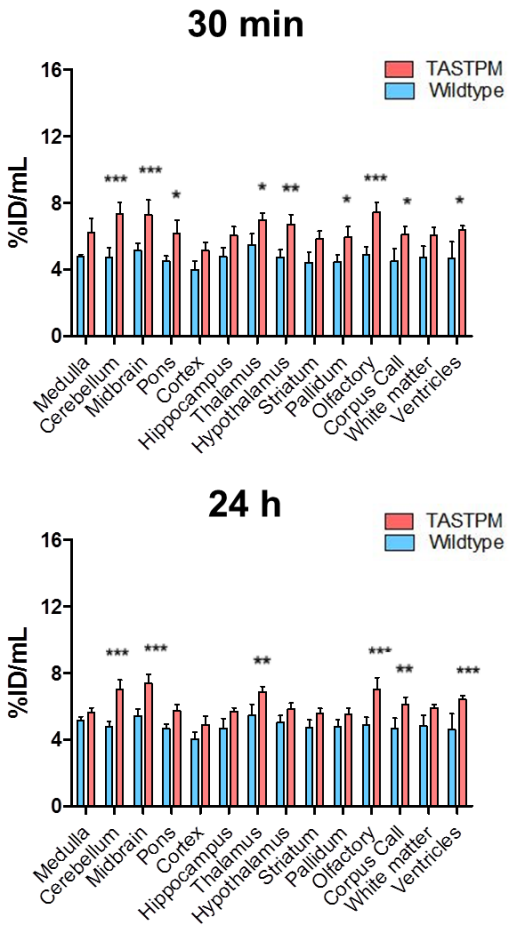

Figure 3.20: Atlas-based quantification of brain regional ^{64}Cu accumulation in 13-15-month-old TASTPM mice and age-matched controls. Statistically significant differences between groups are indicated by * ($p<0.05$), ** ($p<0.01$) and *** ($p<0.001$). Data are mean (n=3/group) ± SD.

Additionally, statistical analysis detected significant differences in brain regional ^{64}Cu concentration between the different age groups of mice. Ventricular uptake was found to be significantly higher in wildtype mice at 6-8 months of age when compared to the 13-15-month-old group at both 30 min ($p<0.05$) and 24 h ($p<0.05$) post-injection of ^{64}Cu-GTSM. Contrarily, 6-8 month-old TASTPM mice exhibited significantly greater ^{64}Cu uptake than their older counterparts in the medulla at 24 h after injection ($p<0.05$).

3.4.5.2 Texture analysis

Because the regional distribution of the tracer within the brain is at or beyond the resolution limits of the PET/CT scanner, the heterogeneity in the distribution of ^{64}Cu within the brain will have been underestimated by atlas-based quantification due to the partial volume effect. For this reason, PET brain signal heterogeneity was alternatively quantified using texture analysis, which does not rely on the use of predefined structural templates and instead focuses on the

study of the spatial interrelationships of the image voxels. First-order parameters (mean, minimum/maximum, median, range, percentiles, standard deviation, skewness, kurtosis, coefficient of variation, energy and entropy), describing global texture features of tracer uptake that relate to the inhomogeneity of voxel intensity distribution within a predefined whole-brain ROI, were measured (Figure 3.21).

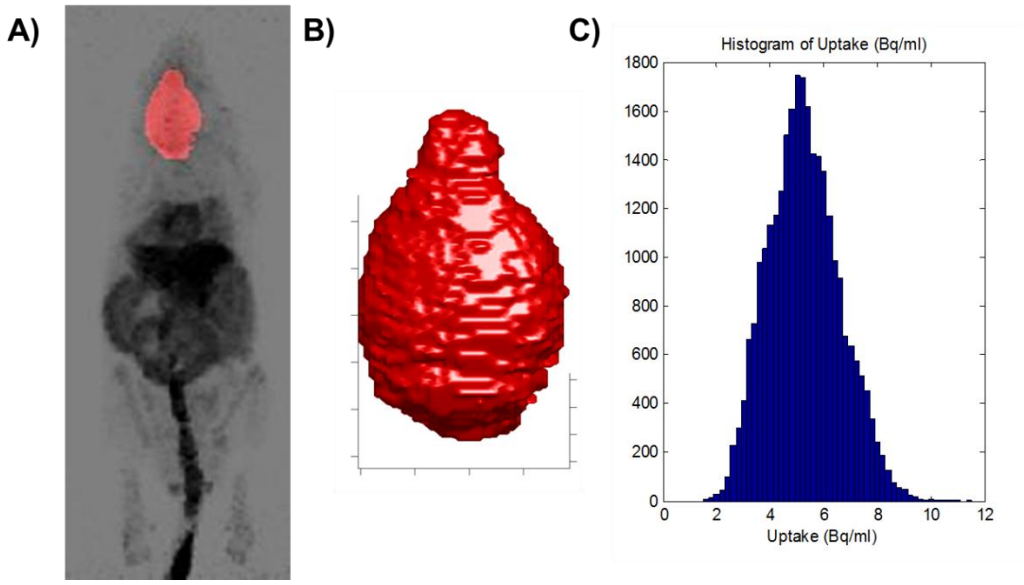

Figure 3.21: (**A**) Brain ROI drawn in a CT image and applied to a PET image of a 13-15-month-old TASTPM mouse at 24 h post-injection of the tracer for texture analysis; (**B**) 3D brain ROI; (**C**) Histogram showing the distribution of radioactivity concentration voxel values (in units Bq/mL) within brain ROI.

Two-way repeated measures ANOVA revealed significant differences between 6-8-month-old TASTPM transgenic mice and age-matched wildtype controls in standard deviation ($p<0.05$), skewness ($p<0.01$), kurtosis ($p<0.01$), coefficient of variation ($p<0.01$), entropy ($p<0.01$) and energy ($p<0.05$) (Table 3.2). The TASTPM group showed increased standard deviation and coefficient of variation compared to controls, demonstrating a higher spread and non-uniformity in voxel intensity values. Furthermore, TASTPM brain images had higher entropy (measure of spatial randomness) than those of wild-type mice, revealing an increased level of disorder in voxel intensity distribution. The energy (measure of uniformity) of TASTPM brain images was lower compared to that of control datasets, suggesting a broader histogram and spread of voxel intensity values. The TASTPM group also showed a lower kurtosis (kurtosis < 3) than controls, which is indicative of a voxel intensity distribution less clustered around the mean and more spread, when compared to the control group, which tended more towards a normal distribution (kurtosis~ 3). Skewness (a measure of asymmetry and deviation from a normal distribution) was

found to be more negative for controls than for TASTPM mice, indicating a greater spread for voxel intensity values lower than the median than for those higher than the median in wild-type datasets. All measures of central tendency of the datasets (mean, median, maximum, minimum, range and percentiles) were found to be higher for the TASTPM group than for wild-type mice, which is indicative of increased tracer uptake in the brains of TASTPM mice compared to controls.

Table 3.2: Texture features of brain PET images of 6-8-month-old TASTPM mice and age-matched controls at 30 min and 24 h post-injection of ^{64}Cu-GTSM.

	TASTPM		**Wildtype**		Group	Time	
	30 min	*24 h*	*30 min*	*24 h*	Effect	Effect	Interaction
Mean	5.46 ± 1.87	4.90 ± 1.53	4.28 ± 0.85	4.29 ± 0.82	ns	**	**
Max	10.00 ± 2.86	10.56 ± 2.37	7.61 ± 1.47	8.38 ± 1.39	ns	ns	ns
Min	1.02 ± 0.72	0.67 ± 0.12	0.94 ± 0.35	0.78 ± 0.20	ns	ns	ns
Range	8.98 ± 2.26	9.89 ± 2.27	6.68 ± 1.22	7.60 ± 1.26	ns	**	ns
St. Dev.	1.35 ± 0.39	1.45 ± 0.40	0.95 ± 0.15	1.05 ± 0.17	*	ns	ns
Skewness	-0.07 ± 0.14	-0.04 ± 0.21	-0.35 ± 0.11	-0.35 ± 0.18	**	ns	ns
Kurtosis	2.97 ± 0.11	2.78 ± 0.20	3.09 ± 0.06	3.12 ± 0.19	**	ns	ns
Coef. of Variation	0.25 ± 0.02	0.30 ± 0.02	0.22 ± 0.01	0.25 ± 0.02	**	***	*
Median	5.49 ± 1.94	4.95 ± 1.59	4.37 ± 0.83	4.39 ± 0.86	ns	*	*
10th%	3.65 ± 1.28	2.93 ± 0.93	2.95 ± 0.68	2.80 ± 0.58	ns	***	**
25th%	4.59 ± 1.64	3.92 ± 1.33	3.70 ± 0.75	3.65 ± 0.75	ns	**	**
50th%	5.49 ± 1.94	4.95 ± 1.59	4.37 ± 0.83	4.39 ± 0.86	ns	*	*
75th%	6.39 ± 2.14	5.95 ± 1.85	4.93 ± 0.94	5.01 ± 0.94	ns	ns	ns
90th%	7.11 ± 2.30	6.70 ± 1.95	5.43 ± 1.05	5.52 ± 0.98	ns	ns	*
Entropy	1.71 ± 0.27	1.77 ± 0.27	1.39 ± 0.15	1.48 ± 0.14	**	ns	ns
Energy	0.22 ± 0.06	0.20 ± 0.05	0.30 ± 0.05	0.27 ± 0.04	*	***	ns

Statistically significant group, time and group by time interaction effects are indicated by * ($p<0.05$), ** ($p<0.01$) and *** ($p<0.001$). Data are mean (n = 4 for TASTPM mice; n = 6 for controls) ± SD.

Although no significant effects of group and interaction on first-order texture parameters were detected in 13-15-month-old TASTPM mice and age-matched controls, similar trends to those of the younger age groups were observed. TASTPM transgenic mice exhibited higher central tendency measures as a result of their greater brain ^{64}Cu uptake relative to controls. TASTPM datasets also showed higher standard deviation and entropy, and lower energy than wildtype controls, demonstrating a higher spread and non-uniformity in the distribution of voxel intensity values. Voxel intensity values in the TASTPM group tended towards a highly peaked, heavy-tailed distribution (kurtosis > 3), while the control group was closer to a normal distribution

behaviour (kurtosis ~ 3). The skewness value was positive for both groups and slightly higher at both imaging time-points for wildtypes, revealing a higher spread for voxel intensity values greater than the median than for those lower than the median in this group. However, in this age range, standard deviations of texture parameters were considerably larger for the TASTPM group compared to controls, and therefore a larger number of datasets is required to determine the relevance of these trends in image heterogeneity.

Table 3.3: Texture features of brain PET images of 13-15-month-old TASTPM mice and age-matched controls at 30 min and 24 h post-injection of ^{64}Cu-GTSM.

	TASTPM		**Wildtype**		Group	Time	
	30 min	*24 h*	*30 min*	*24 h*	Effect	Effect	Interaction
Mean	7.49 ± 3.24	5.88 ± 2.35	6.56 ± 1.47	4.05 ± 1.42	ns	*	ns
Max	21.49 ± 9.55	14.14 ± 2.38	14.73 ± 2.55	9.27 ± 0.96	ns	ns	ns
Min	1.13 ± 0.62	1.04 ± 0.56	1.21 ± 0.27	0.76 ± 0.27	ns	ns	ns
Range	20.36 ± 9.05	13.10 ± 2.42	13.52 ± 2.63	8.51 ± 0.72	ns	ns	ns
St. Dev.	2.54 ± 1.20	1.77 ± 0.59	2.19 ± 0.33	1.34 ± 0.32	ns	ns	ns
Skewness	0.59 ± 0.21	0.34 ± 0.37	0.61 ± 0.31	0.48 ± 0.45	ns	ns	ns
Kurtosis	3.87 ± 0.51	3.37 ± 0.81	3.25 ± 0.21	3.30 ± 0.91	ns	ns	ns
Coef. of Variation	0.33 ± 0.05	0.32 ± 0.07	0.34 ± 0.06	0.35 ± 0.07	ns	ns	ns
Median	7.28 ± 3.16	5.87 ± 2.48	6.28 ± 1.66	3.85 ± 1.49	ns	*	ns
10th%	4.31 ± 1.66	3.56 ± 1.48	3.95 ± 1.01	2.47 ± 1.06	ns	*	ns
25th%	5.76 ± 2.49	4.67 ± 1.98	5.01 ± 1.39	3.09 ± 1.32	ns	*	ns
50th%	7.28 ± 3.16	5.88 ± 2.48	6.28 ± 1.66	3.85 ± 1.48	ns	*	ns
75th%	9.01 ± 3.93	7.04 ± 2.84	7.83 ± 1.67	4.99 ± 1.64	ns	*	ns
90th%	10.77 ± 4.74	8.14 ± 2.97	9.59 ± 1.61	5.92 ± 1.76	ns	*	ns
Entropy	3.05 ± 1.88	2.74 ± 1.01	2.14 ± 0.16	1.64 ± 0.26	ns	*	ns
Energy	0.09 ± 0.04	0.13 ± 0.06	0.14 ± 0.02	0.23 ± 0.07	ns	ns	ns

Statistically significant group, time and group by time interaction effects are indicated by * ($p<0.05$), ** ($p<0.01$) and *** ($p<0.001$). Data are mean (n=3/group) ± SD.

3.4.6 *Ex vivo* biodistribution

Following PET/CT imaging, the *ex vivo* biodistribution of ^{64}Cu at 24 h post-injection of ^{64}Cu-GTSM was evaluated via gamma-counting of explanted organs in all groups of mice (Figures 3.22 and 3.23). As expected from the PET images, high accumulation of ^{64}Cu was observed in the lungs, heart, liver, kidneys, intestines and brain in both TASTPM and wildtype controls at both ages.

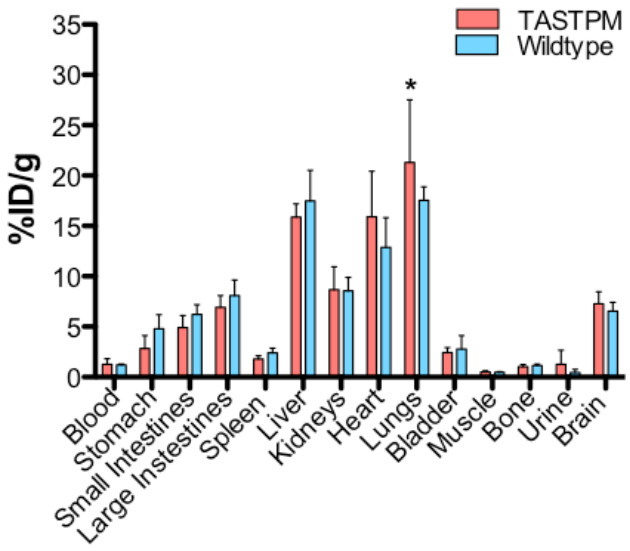

Figure 3.22: Tissue biodistribution of ^{64}Cu in 6-8-month-old TASTPM mice and age-matched controls at 24 h post-injection of ^{64}Cu-GTSM. Statistically significant differences from controls are indicated by * ($p<0.05$). Data are mean (n = 4 for TASTPM mice; n = 6 for controls) ± SD.

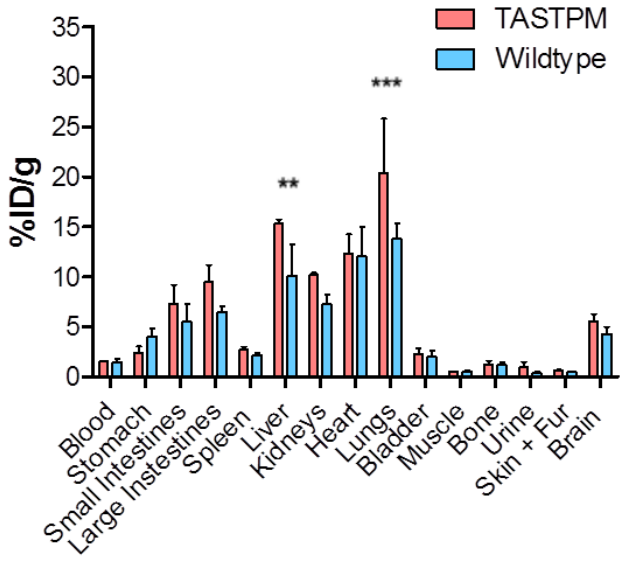

Figure 3.23: Tissue biodistribution of ^{64}Cu in 13-15-month-old TASTPM mice and age-matched controls at 24 h post-injection of ^{64}Cu-GTSM. Statistically significant differences from controls are indicated by ** ($p<0.01$) and *** ($p<0.001$). Data are mean (n=3/group) ± SD.

Two-way repeated measures ANOVA revealed significant effects of organ ($F_{1,8}$ = 121.4, $p<0.0001$) and organ by group interaction ($F_{1,8}$ = 2.06, p = 0.023) on ^{64}Cu *ex vivo* biodistribution in 6-8-month-old TASTPM transgenic mice and age-matched controls but did not show a significant overall group effect ($F_{1,8}$ = 0.057, p = 0.82). Only lung tracer uptake was found to be significantly different by post-hoc analysis between the two groups ($p<0.05$), with TASTPM mice

exhibiting a higher mean concentration of ^{64}Cu than controls (21.30 ± 5.39 %ID/g vs. 17.54 ± 1.22 %ID/g).

Statistical analysis also demonstrated significant effects of organ ($F_{1,4}$ = 85.24, p<0.0001) and interaction ($F_{1,4}$ = 3.688, p=0.0002) and a non-significant group effect ($F_{1,4}$ = 6.200, p=0.0675) on ^{64}Cu *ex vivo* concentration in 13-15-month-old TASTPM mice and healthy controls. Post-hoc evaluation revealed significantly higher ^{64}Cu concentrations in the liver (15.30 ± 0.42 %ID/g vs. 10.13 ± 3.08 %ID/g, p<0.01) and lungs (20.42 ± 5.41 %ID/g vs. 13.82 ± 1.50 %ID/g, p<0.001) of 13-15-month-old TASTPM mice when compared to age-matched controls. These significant differences were found to result from an age-dependent decrease in liver (p<0.001) and lung (p<0.01) uptake of ^{64}Cu in wildtype mice between 6-8 and 13-15 months of age. No significant age effects were measured in TASTPM transgenic mice.

Gamma-counting results revealed a small increase in global brain uptake of ^{64}Cu in TASTPM mice compared to controls at both ages, which did not reach statistical significance by the tests employed. The brain %ID/g values determined by *ex vivo* organ counting showed a strong correlation (R^2 = 0.6891) with whole-brain ^{64}Cu uptake measured by PET expressed as %ID/mL, with two outliers included (Figure 3.24).

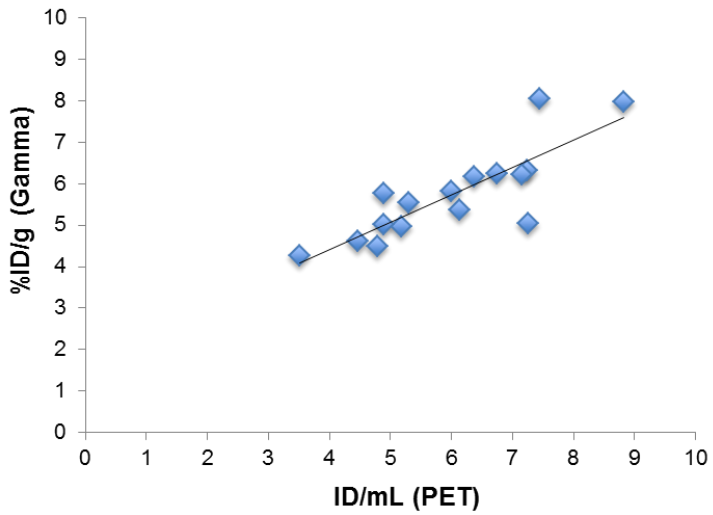

Figure 3.24: Comparison of brain uptake of ^{64}Cu as measured by PET imaging and by *ex vivo* gamma-counting at 24 h post-injection of ^{64}Cu-GTSM in 6-8-/13-15-month-old TASTPM transgenic mice and wildtype controls. All TASTPM (n = 7) and wildtype (n = 9) mice were included in the correlation.

Ex vivo gamma-counting also confirmed hepatobiliary excretion as the main route of elimination of the radiocopper from the body (~ 90 % of excreted ^{64}Cu radioactivity in faeces).

3.4.7 *Ex vivo* brain autoradiography

To evaluate further the heterogeneity in the brain distribution of ^{64}Cu visualised by PET, sagittal brain slices of TASTPM and control mice sacrificed 24 h after ^{64}Cu-GTSM injection were imaged by phosphor imaging autoradiography. The results are summarised in Figure 3.25. *Ex vivo* autoradiographs confirmed the heterogeneity of ^{64}Cu uptake within brain tissue in both animal groups and the presence of prominent radioactive hotspots in the medulla, cerebellum, midbrain, caudate putamen and olfactory bulb (Figure 3.25.A) in 6-8-month-old TASTPM mice. The highest accumulation of ^{64}Cu in wildtype brain tissue was found in the caudate putamen and cerebellum. Visual inspection of representative digital autoradiographs showed increased tracer uptake and a higher degree of heterogeneity in brain ^{64}Cu distribution in the disease model when compared to healthy controls (Figure 3.25.B).

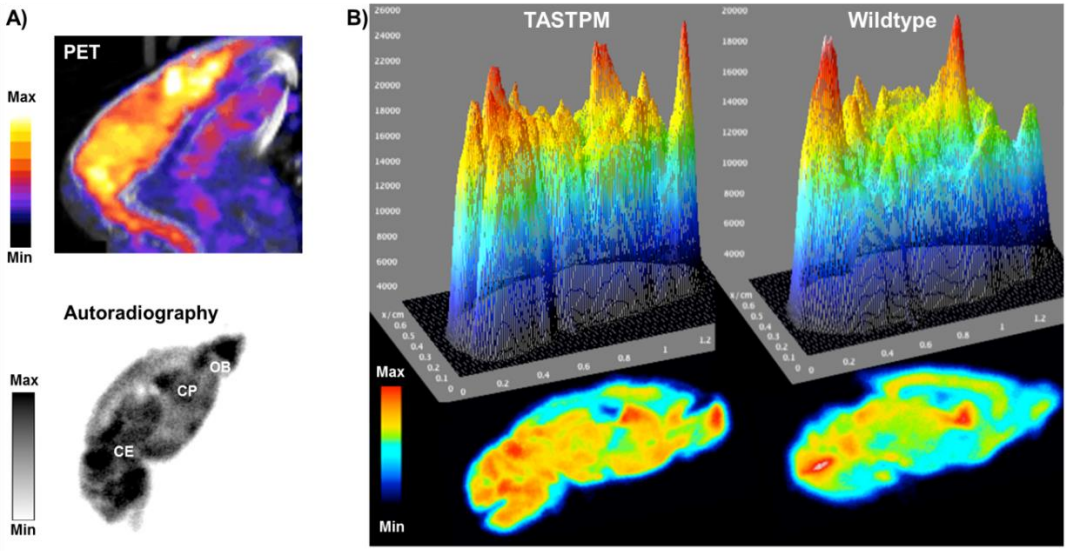

Figure 3.25: (**A**) Sagittal section of PET/CT MIP image of the head of a 6-8-month-old TASTPM mouse at 24 h post-injection of ^{64}Cu-GTSM (top) and *ex vivo* autoradiograph of representative sagittal brain section from the same animal (bottom). (**B**) Surface plots of brain autoradiographs from a 6-8-month-old TASTPM (left) and control (right) mice sacrificed 24 h after administration of ^{64}Cu-GTSM. *Ex vivo* autoradiography confirmed the heterogeneous pattern of ^{64}Cu accumulation in the brain suggested by PET imaging. Visual examination of autoradiographs showed higher and patchier brain uptake of ^{64}Cu in TASTPM mice compared to healthy controls. CE = cerebellum; CP = caudate putamen; OB = olfactory bulb.

3.4.8 Histology

The extent of cerebral Aβ plaque deposition in the TASTPM AD mouse model was evaluated via Congo red staining of brain sections previously autoradiographed. As expected from

previous reports (Howlett *et al.*, 2004; Howlett *et al.*, 2008) and our own immunohistochemical studies, Congo red-stained Aβ plaque deposits were predominantly found in the hippocampus, cortex and thalamus in 6-8- and 13-15-month-old TASTPM transgenic mice. No Aβ deposits were detected in age-matched wildtype controls. To determine whether there was a relationship between brain regional distribution of ^{64}Cu and Aβ plaque deposition in TASTPM mice, Congo red-stained brain slices and their respective autoradiographs were inspected visually. Figures 3.26 and 3.27 show exemplar brain slices of TASTPM mice at 6-8 and 13-15 months of age imaged by autoradiography and subsequently stained with Congo red. Although ^{64}Cu was taken up by all brain regions, visual assessment of the paired images revealed that the areas predominantly affected by Aβ plaque load (red-orange stain; hippocampus, thalamus and cerebral cortex) did not correspond to the regions with the most prominent radioactive hotspots, as depicted by autoradiography (olfactory bulb, medulla, cerebellum, midbrain and caudate putamen), suggesting that other metabolic/pathological factors besides Aβ plaque deposition influence brain regional ^{64}Cu accumulation.

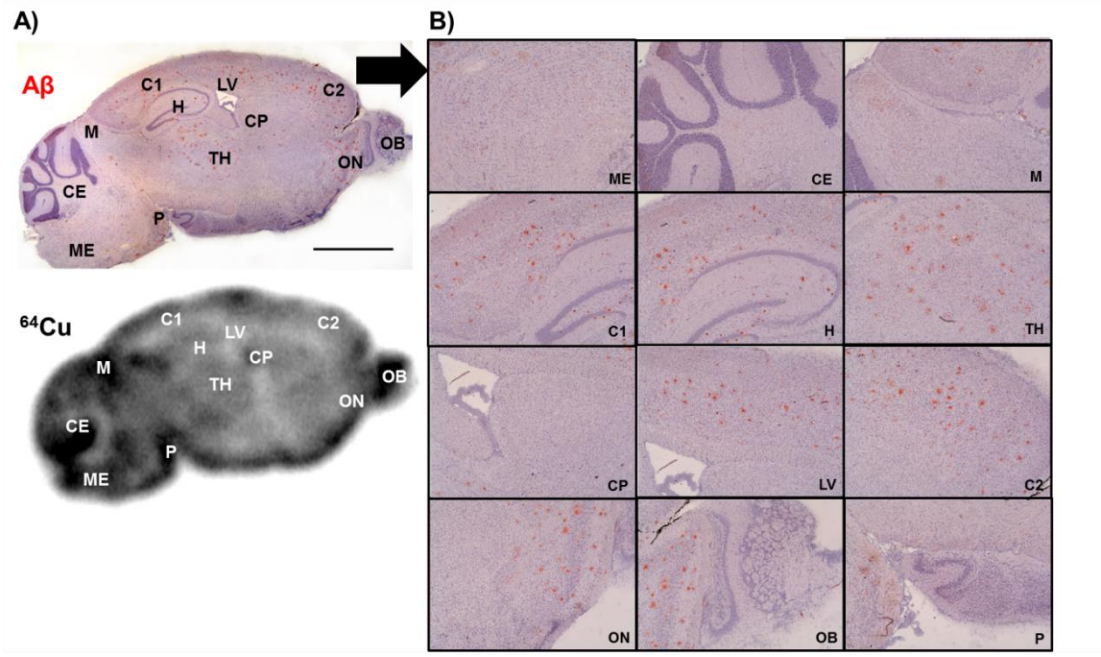

Figure 3.26: (**A**) Photomicrograph of a Congo red-stained sagittal brain section from a 6-8-month old TASTPM mouse (top) and corresponding autoradiograph at 24 h post-injection of ^{64}Cu-GTSM (bottom). (**B**) Magnified views of representative brain regions shown in Figure 3.26.A. ^{64}Cu was found to accumulate in the whole brain, including plaque-rich regions (red-orange stain; hippocampus, thalamus and cerebral cortex). However, the most prominent ^{64}Cu hotspots were observed in areas with low plaque density (olfactory bulb, medulla, cerebellum, midbrain and caudate putamen), suggesting the influence of additional factors other than Aβ plaque deposition on brain regional ^{64}Cu accumulation. From top left to bottom right: ME = medulla; CE = cerebellum; M = midbrain; C1 = cerebral cortex; H = hippocampus; TH = thalamus; CP = caudate putamen; LV = lateral ventricle; C2 = cerebral cortex; ON = anterior olfactory nucleus; OB = olfactory bulb; P = pons. The scale bar represents 1 mm.

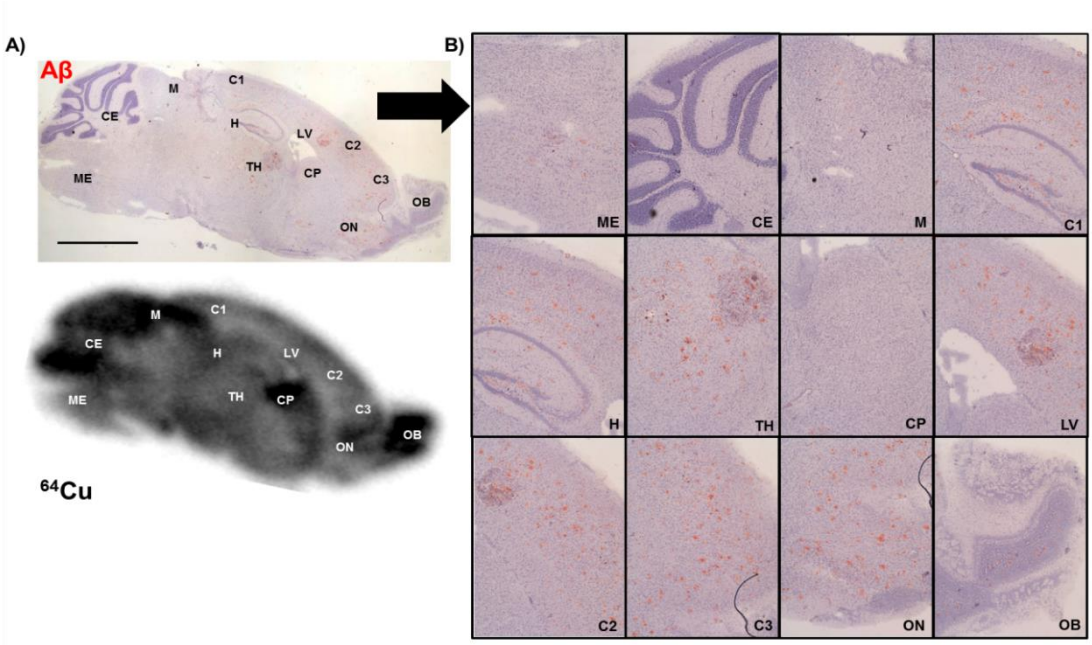

Figure 3.27: (**A**). Photomicrograph of sagittal brain section from a 13-15-month old TASTPM mouse (top) and corresponding brain autoradiograph (bottom) at 24 h post-injection of ^{64}Cu-GTSM (**B**) Magnified views of representative brain regions shown in Figure 3.27.A. As observed in 6-8-month-old TASTPM mice, ^{64}Cu accumulated most prominently within brain regions with low Aβ plaque load (olfactory bulb, medulla, cerebellum, midbrain and caudate putamen) at 24 h post-injection of ^{64}Cu-GTSM. From top left to bottom right: ME = medulla; CE = cerebellum; M = midbrain; C1 = cerebral cortex; H = hippocampus; TH = thalamus; CP = caudate putamen; LV = lateral ventricle; C2 = cerebral cortex; ON = anterior olfactory nucleus; OB = olfactory bulb. The scale bar represents 1 mm.

3.5 DISCUSSION

Non-invasive monitoring of brain copper trafficking *in vivo* by PET could provide unique insight into the role of copper metabolism in AD biology, and may have potential as a diagnostic marker of disease progression and response to therapy, particularly in the context of metal chelation treatments. In this study, we aimed to explore brain copper trafficking in TASTPM transgenic mice at early and middle stages of AD-like pathology by PET imaging using the Cu-BTSC complex ^{64}Cu-GTSM.

The chosen route of administration of ^{64}Cu-GTSM was intravenous injection, which does not mimic the gastrointestinal uptake and biodistribution of endogenous copper but ensures rapid delivery of the radiotracer into the brain. In order to confirm the ability of the tracer to release radiocopper intracellularly within the brain, we used solvent extraction to measure the amount of intact ^{64}Cu-GTSM complex present in brain homogenates of mice injected with the tracer, at different time-points after injection (30 min, 24 h). The results revealed that less than 4 % of ^{64}Cu radioactivity was associated with the octanol-extractable fraction already at 30 min post-

injection, consistent with the proposed cellular uptake and non-selective bioreductive trapping of ^{64}Cu-GTSM (142, 150, 365). The low ^{64}Cu radioactivity present in the octanol-extractable fraction, and the lack of ^{64}Cu-GTSM complex detectable by radio-TLC of that fraction, indicated that ^{64}Cu-GTSM was almost completely dissociated by 30 min. Alongside our *in vivo* blood sampling and dynamic PET/CT imaging experiments, which revealed short blood half-life and remarkably high and rapid uptake of the tracer into the brain, the results obtained are consistent with a process in which the lipophilic nature of the ^{64}Cu-GTSM complex facilitates its passage across the BBB and into cells, where it dissociates, releasing ^{64}Cu intracellularly, as previously suggested for this compound (413). This mechanism is the basis for the selection of ^{64}Cu-GTSM as a vehicle for the intracellular delivery of imageable amounts of ^{64}Cu into the brain. The use of radioactive copper salts, which enter the brain via active transport mechanisms, would mimic brain copper metabolism much more closely but would not allow the delivery of sufficient radiocopper to study copper trafficking processes within the CNS, as shown in previous studies (179). The speciation of the ^{64}Cu radiolabel of ^{64}Cu-GTSM in the intracellular copper pool has not been elucidated but it probably follows the same metabolic pathways as endogenous copper.

As well as efficient delivery of ^{64}Cu into the brain, ^{64}Cu-GTSM-PET imaging also demonstrated that clearance of radiocopper from the brain is considerably slower than that of most other tissues (e.g. heart, kidneys). The biological significance of this observation is not yet clear but it could be due to brain tissue showing greater active sequestration of copper ions driven by increased metabolic demands associated with regular brain function, or less active copper efflux mechanisms.

PET/CT imaging of copper trafficking with ^{64}Cu-GTSM revealed significantly increased brain and spine uptake of ^{64}Cu in male TASTPM mice at both 6-8 and 13-15 months of age compared to age-matched controls at 30 min and 24 h post-injection of the tracer. Despite differences in the animal model, age ranges and methodology used, these results agree with those of Fodero-Tavoletti *et al.*, who reported that ^{64}Cu uptake in the brain was nearly two-fold higher in APP/PS1 transgenic mice compared to healthy controls at 60 min post-injection of ^{64}Cu-GTSM (155). However, enhanced brain uptake of ^{64}Cu in TASTPM mice was found to be much less

marked (~1.3-fold increase in the 6-8-month-old group and ~1.4-fold increase in the 13-15-month-old group) than that previously reported for the APP/PS1 model. This may be partially due to inherent differences in phenotype severity and disease progression between the two AD models.

Unlike PET, the increase in ^{64}Cu brain uptake in TASTPM mice compared to controls at 24 h post-injection of the tracer did not reach statistical significance when measured by *ex vivo* gamma-counting. *Ex vivo* organ counting is subject to greater opportunities for non-systematic error (e.g. cross contamination between tissues during dissection, weighing errors, incomplete explantation) that may account for this discrepancy. It should be also noted that the total injected dose used to quantify *ex vivo* biodistribution of ^{64}Cu may have been underestimated due to activity loss during dissection and urine/faeces collection. These potential opportunities for error may explain why gamma-counting measurements did not show a stronger linear correlation with PET quantitative data ($R^2 = 0.6891$).

While ^{64}Cu clearance from brain was found to be slower than that from other tissues in both TASTPM and wildtype mice, it was also observed that tracer washout was faster in TASTPM mice when compared to healthy controls (-10 % vs. -2 % at 6-8 months of age; -4.5 % vs +3 % at 13-15 months of age). Despite this faster ^{64}Cu clearance rate, TASTPM mice still had significantly increased ^{64}Cu concentration in the brain than controls both at 30 min and 24 h post-injection of ^{64}Cu-GTSM. These differences in brain copper trafficking between the two groups may be explained by the combination of more active copper influx and efflux mechanisms in the TASTPM model, or by different patterns of copper bioavailability to these processes. The molecular mechanisms underlying the increased concentration of ^{64}Cu in the brains of AD mice have yet to be deciphered but may be driven by the regulation of total brain copper levels in an effort to maintain brain copper homeostasis and/or enhance copper-dependent antioxidant enzyme activity as a response to oxidative stress. Another possibility to consider is the existence of pathological alterations of cerebral vasculature in this AD model. No perturbations of BBB integrity and permeability have been reported for the TASTPM model but morphological and architectural alterations of cerebral vasculature caused by Aβ plaque pathology, as evidenced for APP23 transgenic mice, could result in abnormal regional blood

flow and affect global tracer uptake (414, 415). On the other hand, faster brain clearance of ^{64}Cu in TASTPM transgenic mice may be caused by the overexpression of APP, which has been suggested to play a role in normal copper metabolism as an efflux transporter (256, 353, 416).

An age-dependent decrease in global ^{64}Cu brain uptake was observed in both TASTPM and wildtype mice between 6-8 and 13-15 months of age. This could be due to reductions in cerebral blood flow associated with aging, but could also result from regulatory mechanisms of the CNS aimed at maintaining copper homeostasis at a constant level. The latter possibility was first suggested by Wang and co-workers after observing increased cerebral copper content and reduced active $^{67}CuCl_2$ brain uptake in aging mice (196, 417).

Both PET/CT imaging and *ex vivo* brain autoradiography demonstrated that the accumulation of ^{64}Cu within the brain at 30 min and 24 h after ^{64}Cu-GTSM administration was heterogeneous. In an attempt to rationalise ^{64}Cu brain signal heterogeneity, we measured ^{64}Cu uptake in 14 predefined brain regions using a 3D mouse brain atlas. ^{64}Cu concentration was found to be higher in all brain regions in TASTPM mice compared to controls, with differences between the two groups reaching statistical significance in specific areas at 30 min and 24 h post-injection of the tracer. Whether these differences in ^{64}Cu regional brain uptake are a consequence of localised AD-like pathology or result from globally higher ^{64}Cu accumulation in the brains of TASTPM mice is unknown. However, it should be noted that many of these brain regions are very small compared to the limited spatial resolution of the PET/CT scanner; this means that the heterogeneity in ^{64}Cu concentration within the brain will have been underestimated by atlas-based quantification due to the partial volume effect; combined with the lack of flexibility of segmentation boundaries and the potential for imperfect matching of the atlas regions onto the real brain regions, these results must be interpreted cautiously.

In order to avoid overinterpreting regional variations in brain uptake of ^{64}Cu as a result of these limitations, PET brain signal heterogeneity was alternatively measured by texture analysis. This type of analysis investigates the spatial interrelationships of the image voxels that reflect global and regional patterns of image heterogeneity, without an underlying biological or structural

model. Statistical analysis of first-order texture parameters revealed a higher spread, asymmetry and non-uniformity of the voxel intensity distribution in TASTPM brain images, indicating a greater degree of image heterogeneity in the disease model compared to controls. Nevertheless, larger sample sizes are needed in order to determine the significance of these trends in PET image heterogeneity, particularly in the 13-15-month old age group, in which standard deviation of texture parameters was found to be higher. While this type of image analysis does not offer insight into the biological interpretation of differences in brain uptake of ^{64}Cu between the two animal groups, it does offer a basis for parameterisation of imaging for clinical diagnostic purposes.

The molecular mechanisms responsible for the increased heterogeneity of ^{64}Cu distribution within the brain (evidenced both via atlas-based quantification and texture analysis) have yet to be elucidated. Brain copper metabolism is based on a complex network of uptake, trafficking and efflux processes and a delicate balance between “free” and protein-bound copper species. Whether higher ^{64}Cu accumulation in certain regions results from endogenous metabolic demands of each brain region, enhanced regional BBB permeability and/or microvessel density, or localised AD-like pathology remains unknown. Metabolite analysis studies will be necessary to determine the fate of the ^{64}Cu radiolabel and the biological significance of its heterogeneous distribution within brain tissue.

The ability of Aβ plaques to bind copper has been extensively reported in the literature (418-420). The sequestration of copper by extracellular Aβ plaque deposits is thought to contribute to brain copper dyshomeostasis in AD by reducing the intracellular bioavailability of copper ions (341, 398, 400, 421). In order to determine whether a correlation existed between the regional distribution of ^{64}Cu in the brain and Aβ plaque deposition in 6-8- and 13-15-month-old TASTPM transgenic mice, brain tissue was imaged by autoradiography and subsequently stained with the Aβ-binding Congo red dye. We observed that, although ^{64}Cu was taken up by the whole brain, the main radioactive hotspots (cerebellum, midbrain, caudate putamen, olfactory bulb) did not co-localise with the regions of highest Aβ plaque load (cerebral cortex, hippocampus, thalamus). This distribution pattern does not preclude the possibility that Aβ plaques serve as a

sink for copper ions, but highlights the influence of additional metabolic/pathological factors other than Aβ plaque deposition on the regional accumulation of ^{64}Cu in the brain.

3.6 CONCLUSIONS

This study demonstrated that ^{64}Cu-GTSM is a suitable vehicle for the efficient delivery of ^{64}Cu into the brain, and revealed the potential for application of ^{64}Cu-GTSM-PET to study changes in copper ion trafficking associated with various neurological disorders (e.g. AD, PD, ALS, HD). PET/CT imaging with ^{64}Cu-GTSM showed statistically significant differences in ^{64}Cu brain uptake and biokinetics between TASTPM transgenic mice at early and middle stages of the disease and age-matched controls. Furthermore, atlas-based PET quantification and texture analysis demonstrated substantial variations in regional brain concentration of ^{64}Cu and PET image heterogeneity, respectively, between the two groups of mice. The present study provides an initial set of PET imaging parameters (global brain concentration of ^{64}Cu; rate of clearance of ^{64}Cu from brain; degree of heterogeneity of brain ^{64}Cu distribution) that could be evaluated in early human trials. These results support further evaluation of PET imaging of brain copper trafficking both as a tool to investigate alterations in copper trafficking that might have added value in the diagnosis of AD, and as a possible diagnostic biomarker to monitor disease progression and response to treatment, especially in the context of copper chelation therapies.

Chapter 4- Imaging active copper trafficking in a mouse model of Alzheimer's disease by XRF and ^{64}Cu-acetate-PET

4.1 AIMS

The aim of this chapter is to investigate active copper transport in the brain and whole-body in the TASTPM mouse model of AD by synchrotron radiation X-ray fluorescence (XRF) and ^{64}Cu-acetate-PET in order to identify potential copper metabolism abnormalities that may be associated with the pathology.

4.2 INTRODUCTION

For many years, radioactive copper salts have played a crucial role in the understanding of the physiology of copper metabolism in health and disease. The assessment of tissue radioactivity in small animals after radiocopper administration contributed to the early characterisation of copper absorption, distribution and excretion in living organisms (109, 422-425). The measurement of radiocopper accumulation in body fluids and tissues using nuclear scintillation systems was also performed in human subjects and used to identify copper metabolism abnormalities associated with genetic conditions, such as WD (426-430). However, the limited spatial resolution of nuclear scintillation cameras in the 1960s hindered temporarily the application of radioactive copper salts to investigate whole-body copper fluxes *in vivo*.

With the advent of high-resolution PET scanners and increasing availability of copper radioisotopes, the feasibility of using radioactive copper salts as PET radiotracers for the real-time assessment of active copper transport at the whole-body level in living organisms has been demonstrated. Bissig and co-workers first reported the use of a high-resolution PET system to image copper trafficking in a rat model of WD, although prolonged retention of orally administered radiocopper in the gastrointestinal tract did not allow the detection of abnormalities

in copper hepatic processing (431). Subsequent studies by Peng *et al.* demonstrated the utility of $^{64}CuCl_2$-PET to characterise copper metabolism imbalance in an ATP7B knockout mouse model of WD (153, 179). Peng and co-workers also used $^{64}CuCl_2$ to visualise prostate cancer and hepatoma xenografts, and reported abnormally high accumulation of radiocopper in both tumour types compared to soft tissue (184, 185).

With growing evidence supporting the existence of abnormalities in copper metabolism in many neurological disorders (e.g. AD, PD, HD, ALS), the application of radioactive copper salts as radiotracers offers great potential not only to study active copper transport in these diseases but also as a diagnostic tool to assess disease status and progression. To date, only Fodero-Tavoletti and co-workers have used copper radioisotopes to image copper trafficking by PET in a mouse model of AD (155). However, their study focused on the evaluation of brain copper fluxes by using the BBB-permeable ^{64}Cu-GTSM complex as a radiocopper delivery vehicle, and did not provide any information on active copper transport at the whole-body level. Although in AD research much focus has been on the dysregulation of copper homeostasis in the brain, serum copper levels have also been shown to be altered in AD, which could have an effect on copper trafficking at the level of the whole organism (349, 432). PET imaging of whole-body copper trafficking using radioactive copper salts would enable the identification and characterisation of metabolic abnormalities that might have added value for the diagnosis of AD and other neurological disorders.

The potential of radioactive copper salts as PET radiotracers extends beyond the detection of copper metabolism abnormalities associated with disease. In the context of copper chelation therapies, radiocopper can be used to evaluate the mechanism of action of a particular copper chelating drug and even monitor response to treatment. Nomura *et al.* demonstrated the utility of $^{64}CuCl_2$-PET to evaluate the copper trafficking efficacy of chelating agent disulfiram in a mouse model of MD (154). The development of copper chelating drugs (e.g. CQ, PBT2) aimed at restoring copper homeostasis in several pathological conditions (e.g. AD, HD, PD, brain cancer) encourages the application of PET imaging using ionic radiocopper as a tool for assessing their therapeutic effect.

Hence, in this study we examine the potential of ^{64}Cu-acetate-PET to evaluate the short-term dynamics of copper at the level of the whole organism in the TASTPM mouse model of AD, and assess the effects of CQ treatment on whole-body copper trafficking. In addition to monitoring whole-body copper trafficking in the acute time scale by PET, the endogenous distribution of copper in the brain resulting from prolonged active transport was imaged in AD transgenic mice by XRF. The characterisation of acute and chronic copper distribution at brain and whole-body levels in the TASTPM mouse model will allow the detection of potential trafficking abnormalities that can be used as diagnostic markers of the pathology.

4.3 MATERIALS AND METHODS

4.3.1 Radiochemistry

All reagents were purchased from Sigma-Aldrich, Alfa Aesar, Interlink Scientific Services or VWR International Ltd. and were used without further purification, unless otherwise stated. ^{64}Cu was produced as previously reported on a CTI RDS 112 biomedical cyclotron at the Clinical PET Centre of St Thomas' Hospital in the form of $^{64}CuCl_2$ in 0.1 N HCl solution (4.8 GBq/µg) (99). Radioactivity was measured using a Capintec CRC-25R dose calibrator. Radio-TLC was performed on a LabLogic Flow-Count scanner (scan speed: 0.25 mm/s), using MERCK 60 F_{254} silica gel plates as the stationary phase and ethyl acetate as the mobile phase. ^{64}Cu-acetate was prepared by buffering $^{64}CuCl_2$ (~300 MBq) with a 3 M solution of sodium acetate to pH 6 (R_f= 0, 100 % radiochemical purity) and administered in physiological saline. CQ doses (50 mg/kg) were suspended in 4 % (w/v) (2-hydroxypropyl)-β-cyclodextrin for intraperitoneal administration (≤400 µL). Sham doses were made with 4 % (w/v) (2-hydroxypropyl)-β-cyclodextrin (≤400 µL).

4.3.2 Animals

All animal experiments were performed in accordance with the Animals (Scientific Procedures) Act, 1986 and approved by the local ethics committee. Animals were kept in standard BSU conditions (21°C, 50 % humidity) and fed *ad libitum* with regular animal feed.

Double-mutant TASTPM mice on a C57BL/6J background were bred in-house from mice provided by GlaxoSmithKline (GSK). Additional information on the TASTPM mouse model is included in Chapter III. C57BL/6J wildtype controls were obtained from Charles River Laboratories International, Inc.

4.3.3 XRF

Elemental copper maps of brain tissue sections from TASTPM and wildtype mice (4- and 8-month age groups, n=3/group) were obtained using XRF. Animals were sacrificed by cervical dislocation and their brains removed and hemisected. All dissection instruments were previously wiped down with alcohol in order to avoid metal contamination of the tissue. Brain hemispheres were incubated in a 30 % (w/v) sucrose solution until they sank, and stored at -80°C overnight. Frozen left hemispheres were sectioned (40 µm) in the sagittal plane using a Bright 5040 cryotome. Two representative brain slices were taken per animal (sections 109 and 129 in Paxinos and Franklin's mouse brain atlas) (433). Tissue slices were placed on XRF film (4 µm thick, Ultralene®, SPEX SamplePrep, NJ, USA) and allowed to dry at room temperature.

XRF was performed at the Diamond Light Source synchrotron facility (Harwell Science and Innovation Campus, Didcot, UK) by Dr Po-Wah So (Institute of Psychiatry, Psychology and Neuroscience, King's College London). Elemental copper maps were acquired at 100 µm spatial resolution using the I18-Microfocus Spectroscopy beamline. Fluorescence measurements were performed with the sample surface positioned at 45° with respect to the incoming X-ray beam in order to reduce the scatter contribution to the detected signal. 2D copper maps were quantified using ImageJ (NIH) software. Fixed-volume ROIs (12 mm^2) were drawn on several brain regions of the elemental copper maps to compare mean pixel intensity values between control and TASTPM samples.

4.3.4 *In vivo* blood sampling

Following inhalation induction with isoflurane (2 % [v/v]) and surgical exposure of the left external jugular vein, C57BL/6J controls (n=3, 6-8 months old) were intravenously injected with ^{64}Cu-acetate via the lateral tail vein (5 MBq, ~100 µL). Blood samples (~10 µL) were withdrawn from the jugular vein at different time-points after injection (1, 2, 5, 10, 15, 20, 30, and 60 min

post-injection), and were subsequently weighed and gamma-counted. Time-activity curves were plotted to determine the blood half-life of the tracer.

4.3.5 PET/CT imaging

Imaging experiments were performed using a nanoScan® PET/CT (Mediso Medical Imaging Systems, Budapest, Hungary). ^{64}Cu-acetate-PET was conducted in 6-8- (n=3) and 13-15-month-old (n=3) male TASTPM transgenic mice and age-matched C57BL/6J controls (n=4 and n=3, respectively). Animals were anaesthetised by isoflurane inhalation (3 % [v/v], Vet Tech Solutions Ltd.) and injected with ^{64}Cu-acetate (40 MBq, ≤200 µL) via lateral tail vein. Immediately after injection, mice were placed on the scan bed in the prone position and maintained under inhalation anaesthesia (2 % isoflurane). A 30-min PET scan was subsequently acquired (400-600 keV energy window; 5 ns coincidence window, 0.30 x 0.30 x 0.30 mm^3 voxel size), followed by a CT scan (180 projections, 45 KVp, 0.25 x 0.25 x 0.21 mm^3 voxel size). Animals were allowed to recover from anaesthesia and housed overnight. Mice were then scanned again at 24 h post-injection of the tracer for 1 h. PET imaging of copper trafficking with ^{64}Cu-acetate after CQ/sham treatment was performed in 2-month-old male C57BL/6J wildtype mice (n=2/treatment). Mice were intraperitoneally injected with CQ or sham doses (see section 4.3.1) and anaesthetised 30 min after injection. Animals were then injected with ^{64}Cu-acetate via lateral tail vein and scanned by PET for 30 min (400-600 keV energy window; 5 ns coincidence window, 0.30 x 0.30 x 0.30 mm^3 voxel size), followed by a CT scan (180 projections, 45 KVp, 0.25 x 0.25 x 0.21 mm^3 voxel size). Mice were re-imaged at 24.5 h post-injection of the tracer for 30 min. Respiration rate and bed temperature were monitored throughout all scans.

4.3.5.1 PET image analysis

All PET/CT datasets were reconstructed using the Tera-Tomo 3D iterative algorithm (8 iterations, 6 subsets, 0.25 x 0.25 x 0.25 mm^3 voxel size). Decay, dead-time, and intercrystal scatter corrections were applied. A CT-derived attenuation map was used for PET attenuation compensation. The 0-30 min PET datasets were reconstructed into 5-min bins and binned images corresponding to 25–30 min post-injection were used for ROI analysis. Static 24-25 h and 24.5-25 h PET datasets were reconstructed into single bins representing the average

radiotracer biodistribution during each time frame. All reconstructed datasets were analysed using VivoQuant 1.21 software (InviCRO, LLC). Software-driven PET/CT co-registration was applied and corrected using manual reorientation functions when inaccurate. To measure ^{64}Cu concentration in the spine, heart, liver and kidneys, fixed-volume ROIs (~15 mm^3) were delineated within each organ. The sum of activity (MBq) within each organ ROI was divided by the sum of the whole-body ID (excluding tail) and normalised by the volume of the ROI to yield %ID/mL.

To quantify global and regional brain concentration of ^{64}Cu, a mouse brain atlas NM/CT module (inviCRO, LLC) was automatically overlaid onto all PET/CT datasets. Atlas-based measurements of ^{64}Cu brain concentration were expressed as %ID/mL. Ventricular uptake of ^{64}Cu was alternatively measured by drawing a fixed-volume ROI (0.3125 mm^3) within the lateral ventricles. The mean and maximum concentration of activity per voxel in the ventricle ROI were divided by the ID normalised by the weight of the mouse to give mean and maximum standardised uptake values (SUV_{mean} and SUV_{max}), respectively.

4.3.6 *Ex vivo* biodistribution

After imaging, animals were sacrificed by cervical dislocation immediately and all major organs were explanted, weighed and gamma-counted (LKB Wallac 1282). The activity in the urine and faeces collected from the recovery cages was also measured. ^{64}Cu concentration in each organ was expressed as %ID/g. The total ID was defined as the sum of all whole-body counts (excluding tail) and excreted activity (urine and faeces).

4.3.7 *Ex vivo* brain autoradiography and histology

Brain tissue removed from imaged mice was incubated in a 30 % (w/v) sucrose solution until it sank and stored at -80°C overnight. Cryopreserved brains were sectioned (10 µm) in the sagittal plane using a Bright 5040 cryotome. Tissue sections were thaw-mounted onto Superfrost PLUS glass microscope slides (Menzel-Glaser, Thermo Scientific) and allowed to dry at room temperature. The slides were then exposed to a storage phosphor screen (PerkinElmer, Super Resolution, 12.5 x 25.2 cm) in a standard X-ray cassette for 15 h. The phosphor screen was

then imaged using a Typhoon 8600 scanner (Molecular Dynamics) and images were analysed with OptiQuant 5.0 (PerkinElmer) and ImageJ (NIH).

Following autoradiography, brain slices were stored at -80°C. After decay, the sections were stained with hematoxylin for visualisation of tissue morphology. Frozen brain slices were fixed in 4 % (w/v) PFA for 45 min and washed with distilled water. Subsequently, tissue sections were immersed in Harris' hematoxylin (Sigma Aldrich) for 15 s. Brain slices were then washed with tap water for 2 min, followed by a rinse in acid alcohol solution (1 mL 3M HCl in 200 mL 70 % IMS [v/v]) for 1 min. Finally, brain slices were incubated in 95 % (v/v) alcohol (3 min, 2 changes) and 100 % alcohol (3 min, 2 changes) for dehydration, cleared in Histo-Clear II solution (National Diagnostics; 2 changes, 3 min) and mounted with DPX mounting medium (Merck Millipore). All cover-slipped slides were examined under bright-field microscopy using a light microscope (DM6000 B; Leica Microsystems Ltd., Bucks, UK).

4.3.8 Statistical analysis

All data are reported as mean ± SD. Statistical analysis was performed using GraphPad Prism 5 (GraphPad Software Inc.). Two-way repeated measures ANOVA with post-hoc analyses using the Bonferroni multiple comparison correction was used to determine statistically significant differences between TASTPM mice and controls at different imaging time-points. Student t-test (2-tailed, unpaired) was used to compare individual datasets.

4.4 RESULTS

4.4.1 XRF

To examine the distribution of endogenous copper in the brains of TASTPM transgenic mice and wildtype controls, elemental copper maps from representative brain sections were generated by XRF. We initially aimed to perform XRF analysis on brain sections of 6-8- and 13-15-month-old TASTPM mice and age-matched controls, but the lack of availability of aged AD mice did not allow copper distribution to be evaluated in the latter age group. Instead, copper mapping was conducted on brain sections of 4-month-old TASTPM and wildtype mice in order to assess the effect of disease progression and aging on brain copper distribution.

Slices 109 and 129 from the Paxinos and Franklin's mouse brain atlas were used as reference points for the sectioning. Figure 4.1 depicts representative photomicrographs of the 109 and 129 sagittal brain sections stained with acetylcholinesterase, showing the main brain structures present at each level.

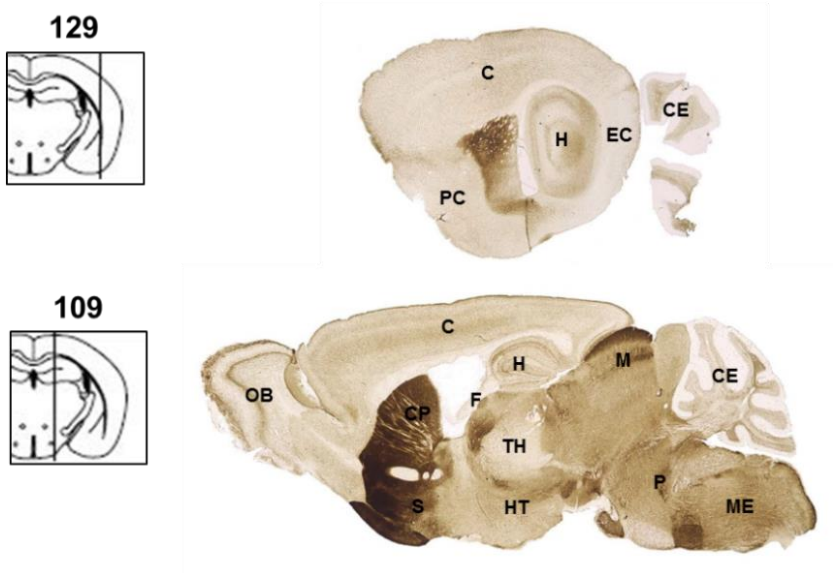

Figure 4.1: Photomicrographs of the 129 (top) and 109 (bottom) sagittal brain sections from the Paxinos and Franklin's mouse brain atlas stained with acetylcholinesterase. Left-hand side illustrations depict the location of the brain slice with respect to the bregma (129: 3.36 mm; 109: 0.96 mm) (433). C = cerebral cortex; PC = piriform cortex; H = hippocampus; EC = entorrhinal cortex; CE = cerebellum; OB = olfactory bulb; CP = caudate putamen; F = fimbria of the hippocampus; TH = thalamus; HT = hypothalamus; M = midbrain; P = pons; ME = medulla.

Representative brain sections of 4- and 8-month-old TASTPM transgenic mice and age-matched controls were scanned by synchrotron-based XRF to produce quantitative elemental copper maps. Visual inspection of the XRF maps revealed that copper distribution in the selected brain sections was heterogeneous in all groups, with particularly high copper levels around the CSF spaces (Figures 4.2 and 4.3).

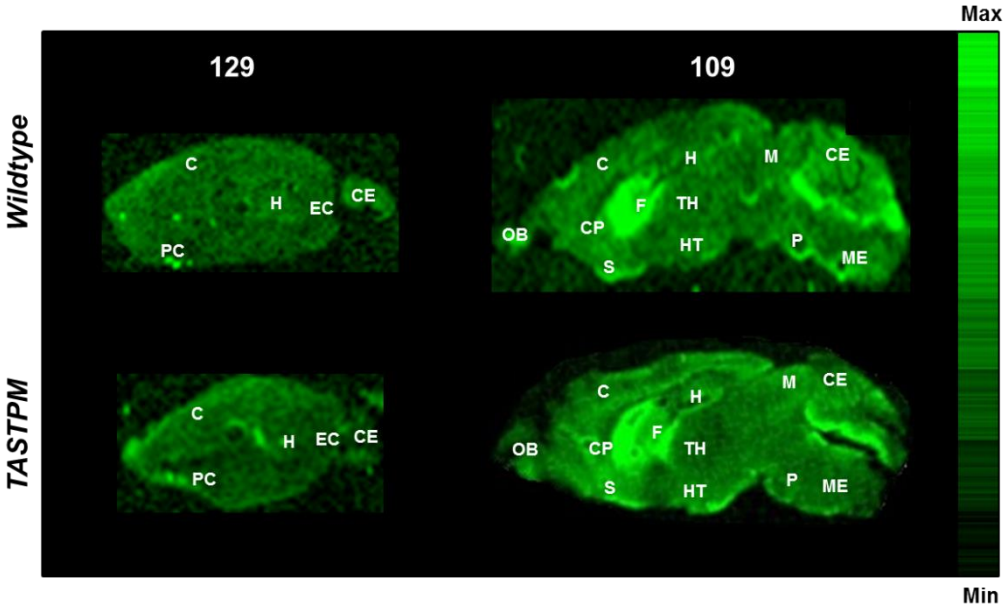

Figure 4.2: Elemental copper maps from sagittal brain sections 129 (left) and 109 (right) of 4-month-old TASTPM mice and age-matched controls acquired by synchrotron-based XRF. On visual assessment, copper accumulation seemed to be particularly prominent in the areas surrounding the lateral and fourth ventricles (fimbria of the hippocampus, caudate putamen and cerebellum). C = cerebral cortex; PC = piriform cortex; H = hippocampus; EC = entorrhinal cortex; CE = cerebellum; OB = olfactory bulb; CP = caudate putamen; F = fimbria of the hippocampus; TH = thalamus; HT = hypothalamus; M = midbrain; P = pons; ME = medulla.

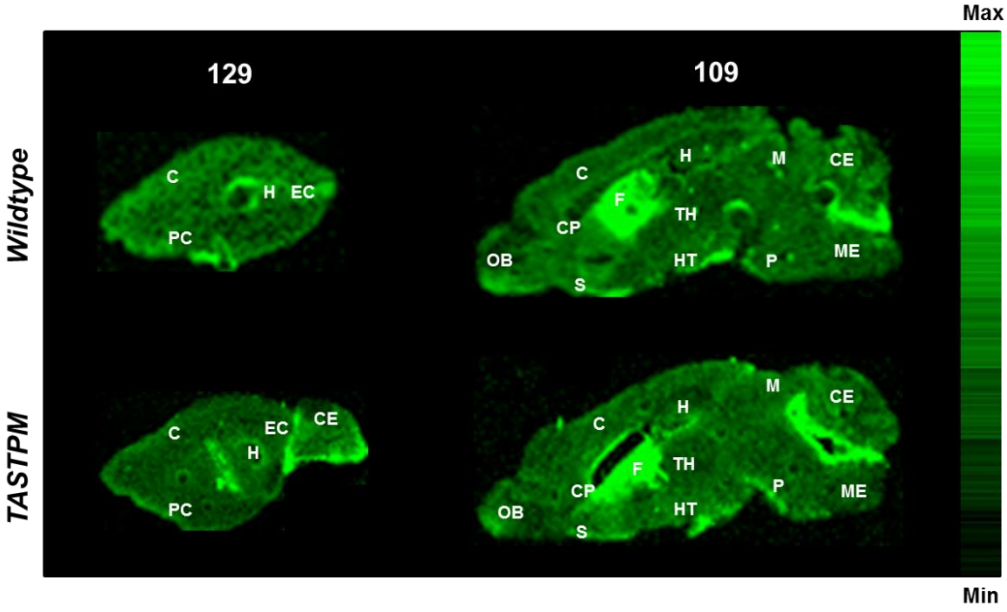

Figure 4.3: Elemental copper maps from sagittal brain sections 129 (left) and 109 (right) of 8-month-old TASTPM mice and age-matched controls acquired by synchrotron-based XRF. As observed in the 4-month-old mouse groups, copper accumulated primarily in periventricular regions in both TASTPM and control mice. C = cerebral cortex; PC = piriform cortex; H = hippocampus; EC = entorrhinal cortex; CE = cerebellum; OB = olfactory bulb; CP = caudate putamen; F = fimbria of the hippocampus; TH = thalamus; HT = hypothalamus; M = midbrain; P = pons; ME = medulla.

Fixed-volume ROIs were drawn within the main brain regions in each section and mean pixel intensity values were compared between AD and control samples. Repeated measures ANOVA indicated significant effects of region ($F_{1,4}$ = 4.699, p = 0.0053) and group by region interaction

($F_{1,4}$ = 3.322, p = 0.0240) on mean copper signal intensity in section 129 of 4-month-old TASTPM and control groups (Figure 4.4). Post-hoc evaluation revealed that copper levels in the hippocampus were significantly higher in 4-month-old TASTPM transgenic mice compared to age-matched controls (8.96 ± 4.37 vs 3.15 ± 0.75, p<0.05). In section 109, significant effects of region ($F_{1,4}$ = 14.68, p<0.0001) and interaction ($F_{1,4}$ = 3.347, p = 0.0014) were also detected. XRF quantification of mean copper signal intensity in section 109 did not indicate a significant difference in hippocampal copper levels between 4-month-old TASTPM mice and age-matched controls, but showed a two-fold higher accumulation of copper in the caudate putamen of the wildtype group when compared to AD mice (18.48 ± 8.44 vs 9.07 ± 1.12, p<0.001).

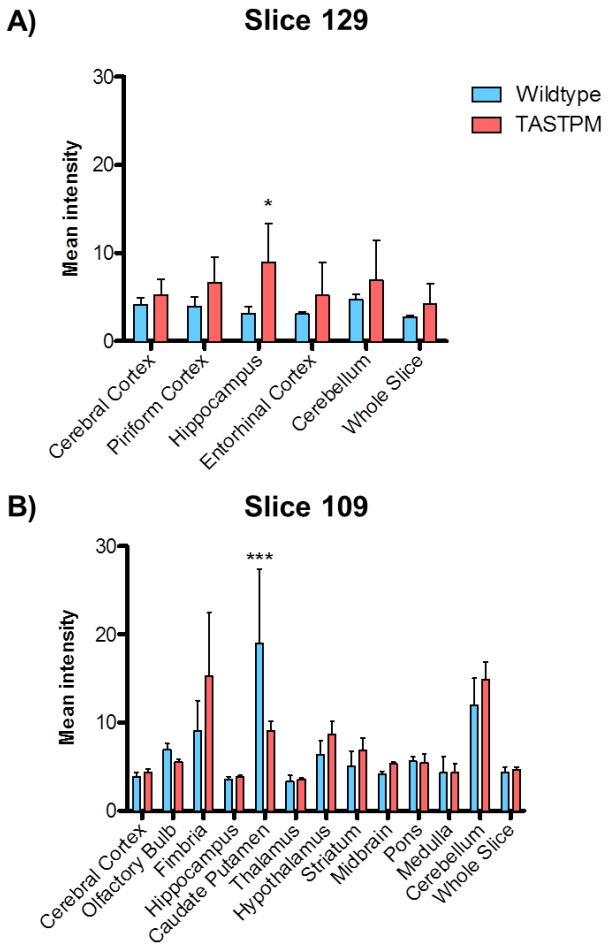

Figure 4.4: Quantification of elemental copper maps from brain sections 129 (top) and 109 (bottom) of 4-month-old TASTPM mice and age-matched controls. XRF analysis revealed statistically significant differences in mean copper signal intensity between the groups in the hippocampus (p<0.05) and caudate putamen (p<0.001). Statistically significant differences are indicated by * (p<0.05) and *** (p<0.001). Data are mean (n =3/group) ± SD.

Statistical analysis also revealed significant effects of region (129: $F_{1,4}$ = 6.901, p = 0.0007; 109: $F_{1,4}$ = 15.19, p<0.0001) and group by region interaction (129: $F_{1,4}$ = 4.377, p = 0.0075; 109: $F_{1,4}$ = 11.42, p<0.0001) on mean pixel intensity values in sections 129 and 109 of 8-month-old

TASTPM transgenic mice and wildtype controls (Figure 4.5). Post-hoc tests indicated almost four-fold higher levels of copper in the cerebellum of TASTPM mice when compared to controls (15.47 ± 8.49 vs 4.31 ± 2.87, $p<0.01$) in section 129. Quantification of section 109 also showed significantly higher mean copper signal intensity in the cerebellum of 8-month-old TASTPM mice relative to controls (30.92 ± 8.07 vs 14.30 ± 0.79, $p<0.01$), as well as a nearly seven-fold greater accumulation of copper in the thalamus of AD mice (30.06 ± 6.61 vs 4.57 ± 1.18, $p<0.001$). In addition, post-hoc evaluation revealed significantly higher mean copper signal intensity in the caudate putamen of 8-month-old wildtype controls compared to age-matched TASTPM mice (34.58 ± 18.80 vs 6.11 ± 2.01, $p<0.001$), in the same manner as for the 4-month-old mouse groups.

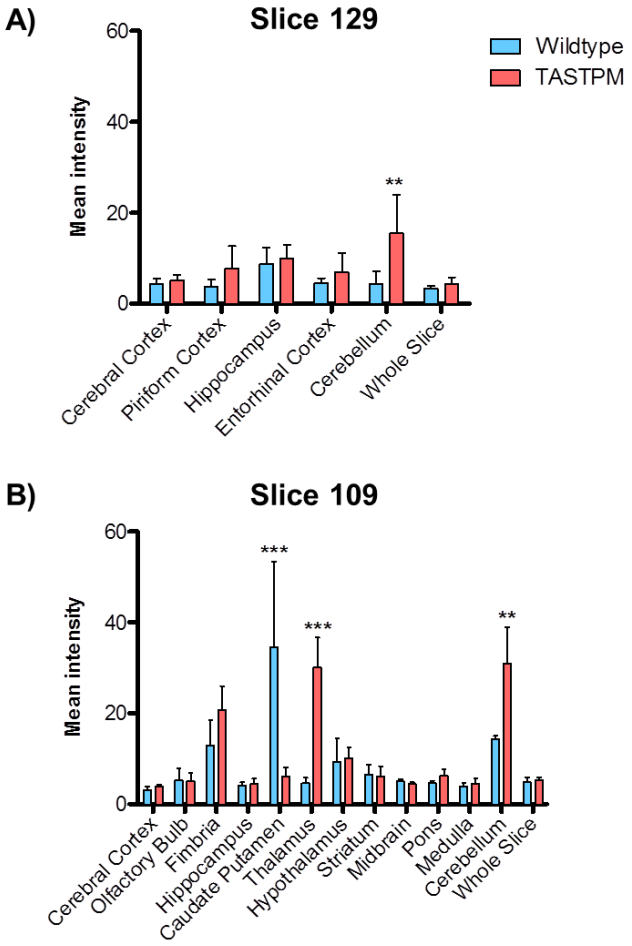

Figure 4.5: Quantification of elemental copper maps from brain sections 129 (top) and 109 (bottom) of 8-month-old TASTPM mice and age-matched controls. XRF analysis indicated statistically significant differences in mean copper signal intensity between the groups in the cerebellum ($p<0.01$), thalamus ($p<0.001$) and caudate putamen ($p<0.001$). Statistically significant differences are indicated by ** ($p<0.01$) and *** ($p<0.001$). Data are mean (n = 3/group) ± SD.

Additional ROIs were drawn around the periventricular areas of section 109 without following specific anatomical boundaries and mean pixel intensity values were compared between AD

and wildtype groups. No significant differences in mean copper signal intensity were found between the groups within the region surrounding the lateral ventricles, but TASTPM transgenic mice were found to exhibit significantly higher copper levels than controls in the area surrounding the fourth ventricle, at the junction between the pons, midbrain and cerebellum, at both 4 (11.79 ± 0.78 vs 8.41 ± 1.94, $p<0.05$) and 8 (24.65 ± 1.80 vs 12.65 ± 2.44, $p<0.01$) months of age. Global copper content in each slice was found to be slightly higher for the TASTPM group compared to age-matched controls at both ages.

The effects of aging and disease progression on the distribution of endogenous copper within the brain were also evaluated by comparing mean copper signal intensity values between the different age groups (Figure 4.6). An age-dependent increase of copper signal was observed in the maps of both TASTPM and control mice, although this effect did not reach statistical significance. For wildtype controls, copper levels in the caudate putamen were found to increase significantly from 4 to 8 months of age (18.48 ± 8.44 vs 34.58 ± 18.80, $p<0.01$). Conversely, TASTPM transgenic mice showed age-dependent increases of mean copper signal intensity in the thalamus (3.57 ± 0.15 vs 30.06 ± 6.61, $p<0.001$) and cerebellum (14.83 ± 2.05 vs 30.92 ± 8.07, $p<0.001$).

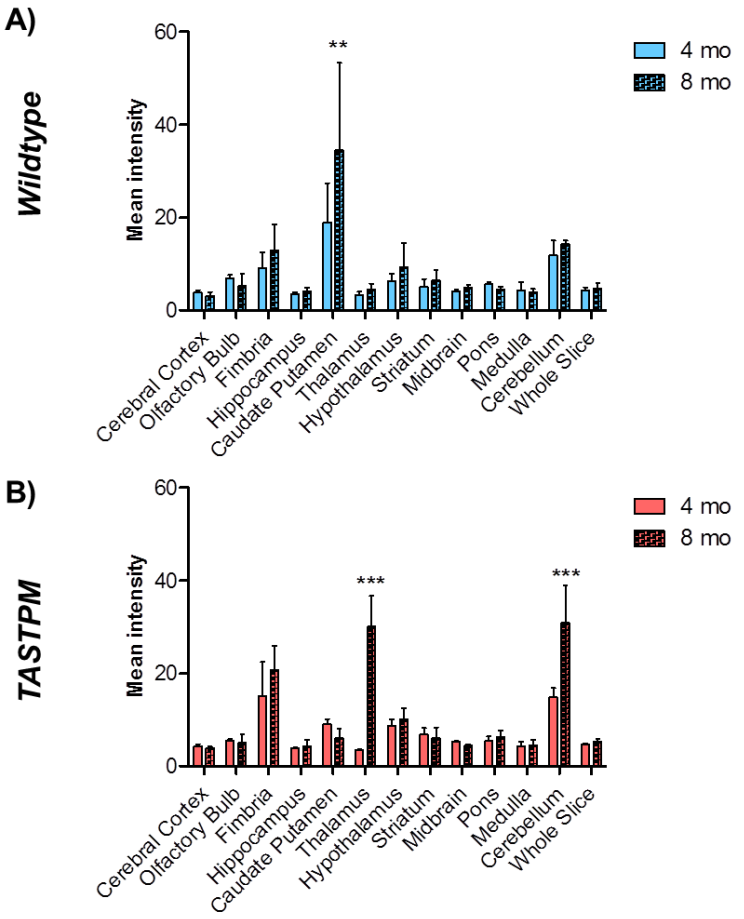

Figure 4.6: The effect of aging on brain copper distribution in TASTPM transgenic mice and wildtype controls as shown by XRF. Significant differences in copper levels between the 4- and 8-month-old age groups were found in the caudate putamen ($p<0.01$) in wildtype mice, and in the thalamus and cerebellum in the AD group. Statistically significant differences are indicated by ** ($p<0.01$) and *** ($p<0.001$). Data are mean (n =3/group) ± SD.

4.4.2 *In vivo* blood sampling

To evaluate the *in vivo* behaviour of ^{64}Cu-acetate in blood, blood samples were collected from the left external jugular vein of wildtype mice injected with the tracer at different time-points after injection. Blood aliquots were subsequently gamma-counted and time-activity curves were constructed to determine the blood half-life of the tracer. ^{64}Cu-acetate was found to follow a biexponential clearance pattern, with a fast half-life of 1.28 ± 0.47 min and a slow half-life of 9.75 ± 3.50 min.

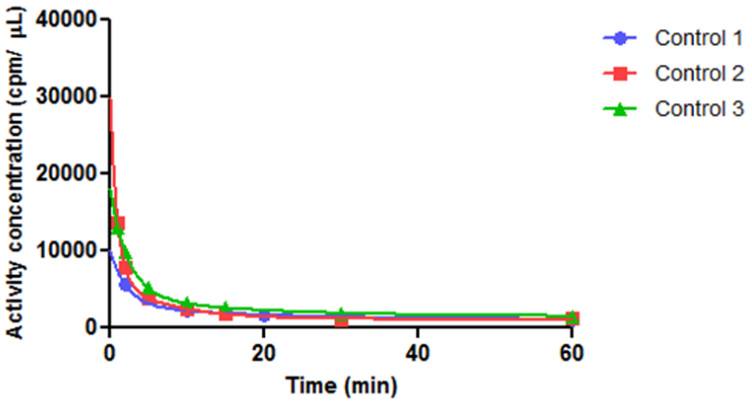

Figure 4.7: Blood time-activity curves resulting from *in vivo* blood sampling in wildtype mice injected with ^{64}Cu-acetate. Blood clearance of ^{64}Cu-acetate followed a biexponential behaviour, with a fast elimination half-time of 1.28 ± 0.47 min and a slow half-life of 9.75 ± 3.50 min.

4.4.3 Measurement of whole-body copper trafficking in AD by ^{64}Cu-acetate-PET

4.4.3.1 PET/CT imaging

After investigating the short-term dynamics of copper fluxes within the CNS in AD-like pathology with ^{64}Cu-GTSM (see Chapter III), we evaluated copper trafficking at the level of the whole organism in the TASTPM mouse model by ^{64}Cu-acetate-PET. The fate of intravenously administered radiocopper was monitored longitudinally by PET in 6-8- and 13-15- month-old male TASTPM mice and age-matched controls.

At 30 min post-injection of the tracer, ^{64}Cu radioactivity was found to accumulate predominantly in the liver of both 6-8-month-old TASTPM and wildtype mice (Figure 4.8). PET imaging also revealed high ^{64}Cu signal in the intestines and kidneys in both animal groups. Unlike ^{64}Cu-GTSM, ^{64}Cu-acetate was not taken up avidly by the lungs, heart and brain. The biodistribution of the radiocopper exhibited little change from 30 min to 24 h post-injection of the tracer, with most ^{64}Cu radioactivity concentrating in the liver, kidneys and intestines. On visual assessment, the TASTPM group appeared to exhibit higher intestinal ^{64}Cu concentration than controls at 30 min post-injection of ^{64}Cu-acetate. No obvious differences in ^{64}Cu biodistribution were observed between the two groups at the 24 h time-point.

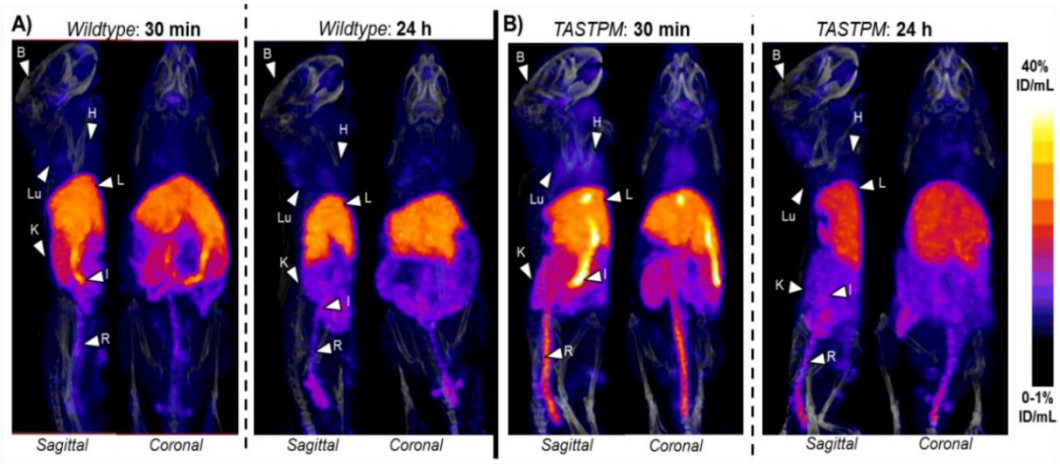

Figure 4.8: Exemplar sagittal and coronal views of PET/CT MIPs of 6-8-month-old male wild-type controls (**A**) and age-matched TASTPM transgenic mice (**B**) at 30 min and 24 h post-administration of ^{64}Cu-acetate. ^{64}Cu-acetate PET/CT scans showed high accumulation of radiocopper in the liver, kidneys and intestines of both TASTPM mice and age-matched controls at 30 min and 24 h post-injection of the tracer. High ^{64}Cu signal in the rectum at late imaging time-points seems to indicate that radiocopper was mainly excreted in the faeces. Organs are indicated by arrows: B = brain; H = heart; Lu = lungs; L = liver; K = kidneys; I = intestines; R = rectum. All MIPs were scaled to 0-1 %ID/mL (min) and 40 %ID/mL (max).

The general biodistribution of the tracer was similar for the 13-15-month-old TASTPM and wildtype groups (Figure 4.9). ^{64}Cu-acetate PET/CT scans showed high accumulation of ^{64}Cu in the liver, and to a lesser extent, in the intestines and kidneys in both TASTPM transgenic mice and wildtype controls. After 24 h, ^{64}Cu concentration decreased in all three organs in both animal groups. In a similar manner as observed in the younger age group, 13-15-month-old TASTPM mice seemed to accumulate a higher concentration of radiocopper in the intestines at 30 min post-injection of the tracer than age-matched controls. Radiocopper appeared to be mainly excreted in the faeces, as evidenced by significant accumulation of ^{64}Cu radioactivity in the rectum at 24 h post-injection of the tracer in both TASTPM and control mice.

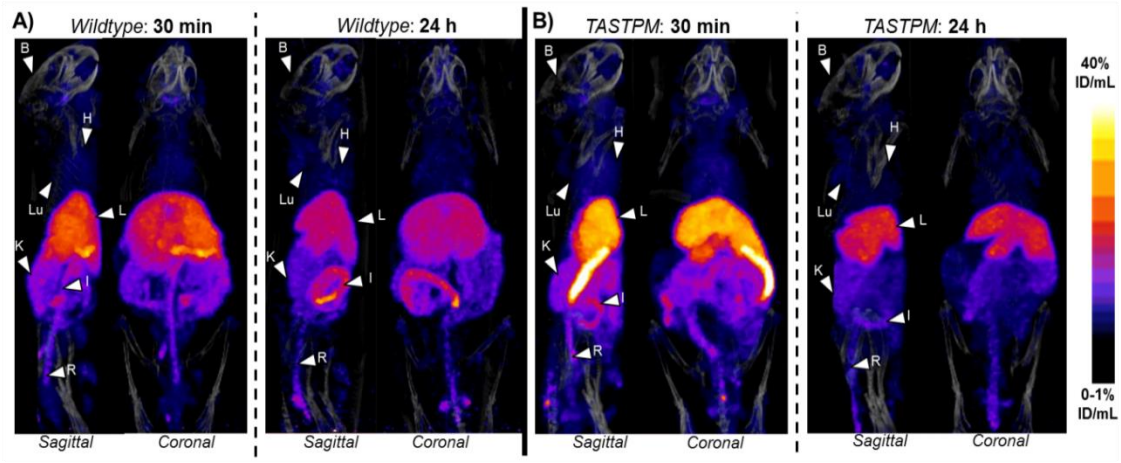

Figure 4.9: Exemplar sagittal and coronal views of PET/CT MIPs of 13-15-month-old male wild-type controls (**A**) and age-matched TASTPM transgenic mice (**B**) at 30 min and 24 h post-administration of ^{64}Cu-acetate. Radiocopper accumulated primarily in the liver, intestines and kidneys in both animal groups at 30 min and 24 h post-administration of the tracer. Radiocopper appeared to be excreted in the faeces, as evidenced by significant accumulation of ^{64}Cu in the rectum at 24 h post-injection of the tracer. Organs are indicated by arrows: B = brain; H = heart; Lu = lungs; L = liver; K = kidneys; I = intestines; R = rectum. All MIPs were scaled to 0-1 %ID/mL (min) and 40 %ID/mL (max).

The biokinetics of intravenously injected radiocopper were evaluated by PET ROI analysis and compared between TASTPM transgenic mice and healthy controls. Figure 4.10 shows time-activity curves for the main organs of interest (heart, kidneys, liver, spine and brain) illustrating clearance of ^{64}Cu radioactivity over time in 6-8-month-old TASTPM mice and age-matched controls. As expected, the liver exhibited the highest accumulation of ^{64}Cu in both animal groups. ^{64}Cu radioactivity was found to decrease over time in the liver, kidneys and heart of both TASTPM and wildtype mice, although ^{64}Cu clearance in these organs was more pronounced in the AD group (21.97 ± 15.51 vs 15.99 ± 15.95 % decrease in liver %ID/mL; 60.10 ± 4.17 vs 36.27 ± 8.91 % decrease in heart %ID/mL; 35.15 ± 8.70 vs 12.73 ± 20.71 % decrease in kidneys %ID/mL). ^{64}Cu uptake in the CNS was low in both TASTPM transgenic mice and healthy controls. Brain ^{64}Cu concentration showed a tendency to decrease over time in the AD group, while it slightly increased in wildtype controls (9.13 ± 1.28 % decrease vs 2.36 ± 5.63 % increase in brain %ID/mL). ^{64}Cu radioactivity cleared from the spine over time in both groups, although more markedly for TASTPM mice than controls (28.54 ± 2.65 vs 16.54 ± 4.83 % decrease in spine %ID/mL).

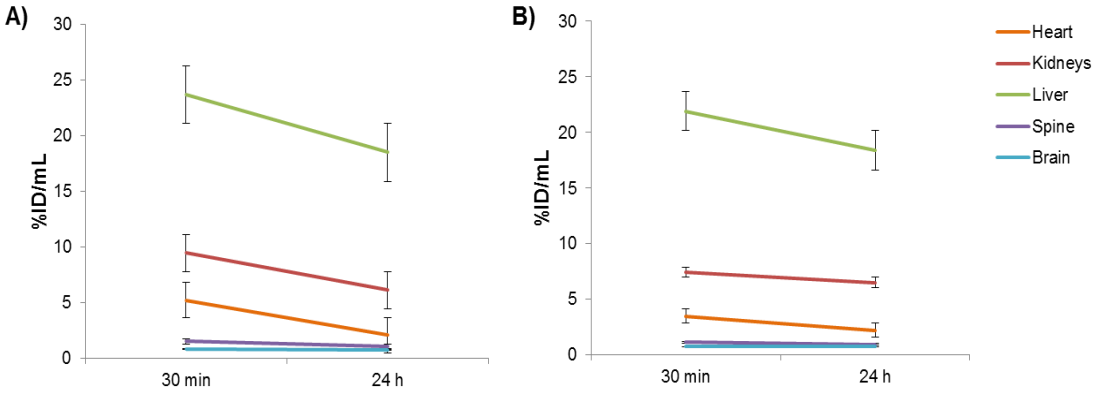

Figure 4.10: Time-activity curves extracted from PET image analysis showing ^{64}Cu concentration (expressed as %ID/mL) over time in the heart, kidneys, liver, spine and brain of 6-8-month-old male (**A**) TASTPM mice and age-matched C57BL/6J controls (**B**). PET ROI analysis revealed that clearance of ^{64}Cu radioactivity from organs of interest was more marked in TASTPM mice than controls. Data are mean (n=3 for TASTPM, n=4 for wildtype controls) ± SEM.

Repeated measures ANOVA demonstrated significant effects of time ($F_{1,5}$ = 59.04, p = 0.0006) and group by time interaction ($F_{1,5}$ = 10.78, p = 0.0219) on heart ^{64}Cu concentration in 6-8-month-old TASTPM mice and age-matched controls. Post-hoc tests revealed that ^{64}Cu concentration in the heart was significantly higher in the AD group relative to controls at 30 min after injection of ^{64}Cu-acetate (5.25 ± 1.39 %ID/mL vs. 3.49 ± 0.51 %ID/mL, p<0.05). Contrarily, no significant differences in liver and kidney ^{64}Cu concentration were found between the two

groups at any imaging time-point. Although no significant effects of time and group were measured, statistical analysis indicated a significant effect of group by time interaction ($F_{1,5}$ = 12.18, p = 0.0175) on brain ^{64}Cu concentration in 6-8-month-old TASTPM and wildtype controls, possibly associated with the faster rate of ^{64}Cu clearance exhibited by the AD group when compared to controls. Repeated measures ANOVA also showed a significant interaction effect ($F_{1,5}$ = 12.26, p = 0.0173) on spinal cord ^{64}Cu concentration, as well as significant effects of group ($F_{1,5}$ = 9.849, p = 0.0257) and time ($F_{1,5}$ = 76.63, p = 0.0003) in 6-8-month-old TASTPM and age-matched controls. Post-hoc evaluation demonstrated significantly higher ^{64}Cu concentration in the spine of TASTPM transgenic mice compared to wildtype controls (1.53 ± 0.17 %ID/mL vs. 1.14 ± 0.15 %ID/mL, p<0.01) at 30 min after injection of the tracer.

PET ROI analysis revealed similar ^{64}Cu biokinetics between the 6-8- and 13-15-month-old TASTPM and wildtype groups (Figure 4.11). The liver exhibited the highest ^{64}Cu concentration among all organs in both 13-15-month-old TASTPM mice and age-matched controls. ^{64}Cu concentration in the liver, kidneys and heart decreased over time in both animal groups, although the decline rate was more pronounced for AD mice when compared to healthy controls (32.55 ± 7.84 vs 18.67 ± 17.95 % decrease in liver %ID/mL; 58.37 ± 5.38 vs 34.64 ± 11.74 % decrease in heart %ID/mL; 28.59 ± 4.16 vs 14.83 ± 1.00 % decrease in kidneys %ID/mL). In this age range, brain ^{64}Cu concentration increased slightly over time for both TASTPM and control mice (2.26 ± 4.29 and 1.54 ± 5.58 % increase in %ID/mL, respectively). ^{64}Cu radioactivity in the spinal cord decreased from 30 min to 24 h post-injection in both 13-15-month-old TASTPM and age-matched controls but, in this case, ^{64}Cu clearance rate was faster for the control group when compared to AD mice (25.27 ± 3.16 vs 13.38 ± 5.01 % decrease in %ID/mL).

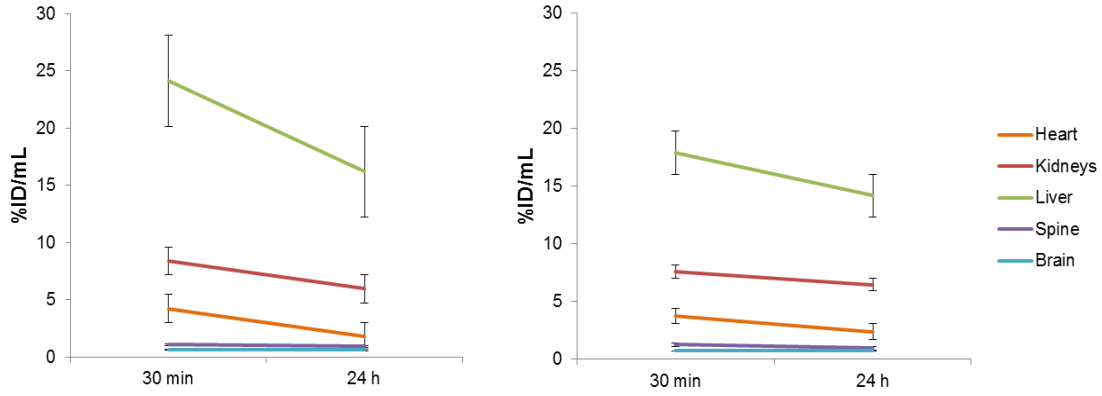

Figure 4.11: Time-activity curves extracted from PET image analysis showing ^{64}Cu concentration (expressed as %ID/mL) over time in the heart, kidneys, liver, spine and brain of 13-15-month-old male (**A**) TASTPM mice and age-matched wildtype controls (**B**). Data are mean (n=3/group) ± SEM.

Statistical analysis did not reveal significant effects of group, time or group by time interaction on ^{64}Cu concentration in the heart, brain and spinal cord in 13-15-month-old TASTPM transgenic mice and age-matched controls. Instead, repeated measures ANOVA indicated significant effects of time ($F_{1,4}$ = 14.81, p = 0.0183) and group ($F_{1,4}$ = 11.34, p = 0.0281) on hepatic ^{64}Cu concentration in this age range. Post-hoc tests demonstrated that 13-15-month-old TASTPM transgenic mice exhibited a significantly higher concentration of ^{64}Cu in the liver than their wildtype counterparts at 30 min post-injection of ^{64}Cu-acetate (24.17 ± 2.89 %ID/mL vs. 17.90 ± 2.76 %ID/mL, p<0.05). Significant effects of time ($F_{1,4}$ = 80.80, p = 0.0008) and interaction ($F_{1,4}$ = 10.82, p = 0.0302) were also observed on renal ^{64}Cu concentration, although no significant differences in specific patterns were detected by post-hoc evaluation.

The effect of age on ^{64}Cu biodistribution was also evaluated in all TASTPM and wildtype age groups. A significant effect of age ($F_{1,5}$ = 8.908, p = 0.0306) on hepatic ^{64}Cu concentration was found in wildtype controls resulting from a reduction in ^{64}Cu accumulation from 6-8 to 13-15 months of age at both 30 min and 24 h post-injection. Moreover, statistical analysis revealed significant effects of age ($F_{1,4}$ = 15.73, p = 0.0166), time ($F_{1,4}$ = 87.27, p = 0.0007) and age by time interaction ($F_{1,4}$ = 22.06, p = 0.0093) on spinal cord ^{64}Cu concentration in the TASTPM groups. Post-hoc tests showed that ^{64}Cu concentration in the spine was significantly greater in 6-8-month-old TASTPM transgenic mice than in their older counterparts at 30 min post-injection of ^{64}Cu-acetate (1.53 ± 0.17 %ID/mL vs. 1.07 ± 0.03 %ID/mL, p<0.01). The concentration of ^{64}Cu in the brain was found to decrease from 6-8 to 13-15 months of age in both animal groups, although this trend did not reach the level of statistical significance.

Unlike ^{64}Cu-GTSM, ^{64}Cu-acetate is not able to cross the BBB by passive diffusion and relies on active transport mechanisms to enter the brain. Because of this, very little ^{64}Cu radioactivity (~0.5-1 %ID/mL) was measured in the brains of both TASTPM and wildtype mice by PET at the chosen imaging time-points. While ^{64}Cu-GTSM released ^{64}Cu in all brain regions, ^{64}Cu-acetate was found to concentrate mostly around the CSF spaces. Figure 4.12 depicts the distribution of ^{64}Cu in the brain of a 13-15-month-old control mouse injected with ^{64}Cu-acetate at both 30 min and 24 h post-injection. On visual assessment, ^{64}Cu radioactivity appeared to accumulate

focally in the right and left lateral ventricles and fourth ventricle, and seemed to decrease slightly over time.

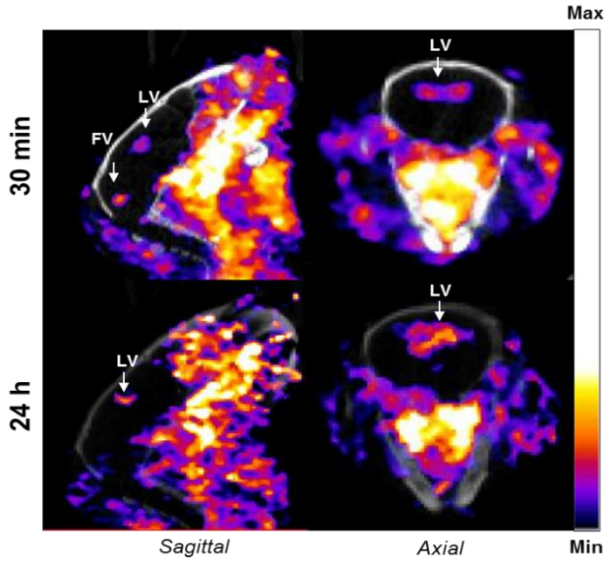

Figure 4.12: Representative sagittal and axial section PET/CT MIP images illustrating ^{64}Cu distribution in the brain of a 13-15-month-old C57BL/6J wild-type control at 30 min and 24 h post-injection of ^{64}Cu-acetate. PET/CT scans revealed that most ^{64}Cu radioactivity was concentrated in or near the ventricular system.

In order to measure the concentration of ^{64}Cu in the ventricles and other brain regions over time, we applied a 3D mouse brain atlas module to all PET/CT datasets. The ventricles and, to a lesser extent, the hypothalamus, exhibited the highest concentration of ^{64}Cu among all brain regions in 6-8-month-old TASTPM mice and age-matched controls at 30 min and 24 h post-administration of the tracer (Figure 4.13). Statistical analysis indicated significant effects of region and group by region interaction on brain regional accumulation of ^{64}Cu in 6-8-month-old TASTPM and control mice at both 30 min (region: $F_{1,5} = 18.16$, $p<0.0001$; interaction: $F_{1,5} = 2.222$, $p=0.0180$) and 24 h (region: $F_{1,5} = 35.60$, $p<0.0001$; interaction: $F_{1,5} = 3.045$, $p=0.0015$) post-injection. However, no specific significant differences in brain regional ^{64}Cu concentration were revealed by post-hoc evaluation between the two groups at any time-point.

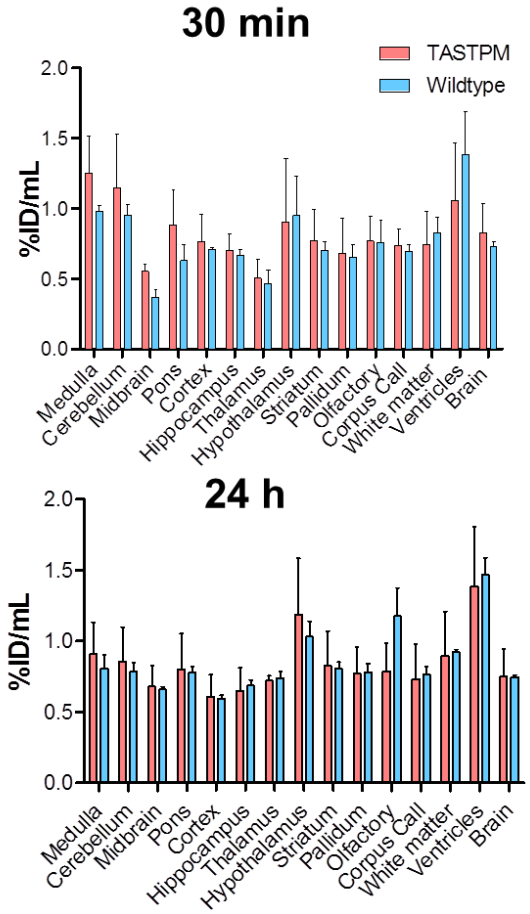

Figure 4.13: Brain regional concentration of ^{64}Cu in 6-8-month-old TASTPM mice and age-matched controls injected with ^{64}Cu-acetate at 30 min (top) and 24 h (bottom) after injection, as measured by atlas-based quantification. Data are mean (n=3 for TASTPM, n=4 for wildtype controls) ± SD.

Atlas-based quantification showed lower ^{64}Cu concentration in all brain areas and a more homogeneous ^{64}Cu distribution pattern in aged TASTPM mice and controls compared to the 6-8-month-old mouse groups (Figure 4.14). The ventricles remained the region with the highest ^{64}Cu concentration in both groups at all imaging time-points. Repeated measures ANOVA indicated significant effects of region ($F_{1,4}$ = 12.68, p<0.0001) and group by region interaction ($F_{1,4}$ = 2.092, p = 0.0306) on regional concentration of ^{64}Cu in the brain in 13-15-month-old TASTPM mice and age-matched controls at 30 min post-injection of ^{64}Cu-acetate. Post-hoc tests did not demonstrate any specific statistically significant differences in brain ^{64}Cu distribution between the two groups. No significant effects of group or interaction on brain regional concentration of ^{64}Cu were measured in the 13-15-month-old TASTPM and wildtype groups at 24 h post-administration of the tracer.

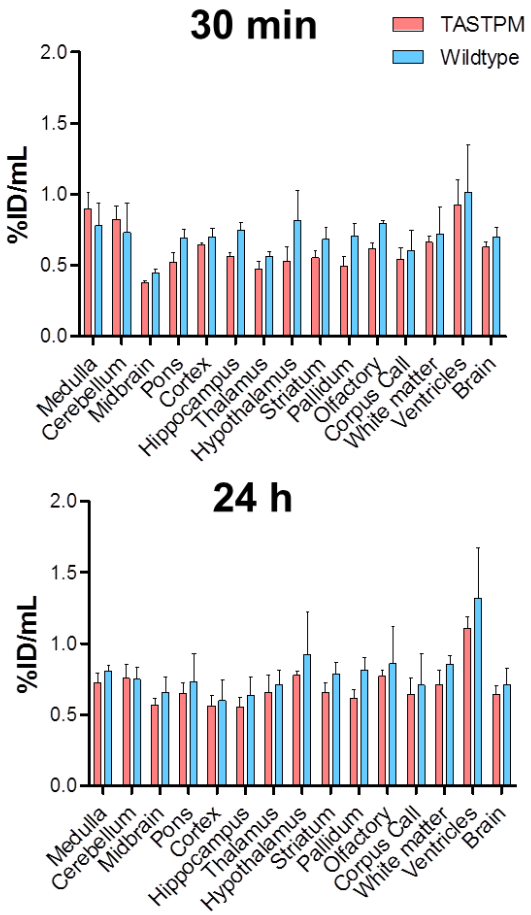

Figure 4.14: Brain regional concentration of ^{64}Cu in 13-15-month-old TASTPM mice and age-matched controls injected with ^{64}Cu-acetate at 30 min (top) and 24 h (bottom) after injection, as measured by atlas-based quantification. Data are mean (n=3/group) ± SD.

Statistical comparison of brain ^{64}Cu distribution among the different age groups revealed significant effects of region ($F_{1,5}$ = 14.44, p<0.0001) and group by region interaction ($F_{1,5}$ = 2.096, p = 0.0261) in wildtype controls from 6-8 to 13-15 months of age. Post-hoc evaluation indicated significantly higher ventricular concentration of ^{64}Cu in 6-8-month-old controls compared to their older counterparts at 30 min post-injection of ^{64}Cu-acetate (1.39 ± 0.30 %ID/mL vs. 1.01 ± 0.34 %ID/mL, p<0.05).

However, atlas-based quantification of ventricular ^{64}Cu concentration may provide inaccurate results due to the partial volume effect associated with the small size of the region and potential for imperfect matching of the atlas template onto the real ventricular system. For this reason, ventricular ^{64}Cu concentration was alternatively measured by drawing a fixed-volume ROI within the brightest hotspot of the lateral ventricles for SUV_{mean} and SUV_{max} determination.

Figure 4.15 shows the ventricular SUV_{mean} and SUV_{max} values for 6-8-month-old TASTPM and wildtype groups at 30 min and 24 h post-injection of ^{64}Cu-acetate. Average SUV_{max} and SUV_{mean} values were found to be generally higher in the wildtype group when compared to AD mice at 30 min post-injection of ^{64}Cu-acetate, although this trend did not reach statistical significance. This was consistent with atlas-based quantification, which also revealed increased early uptake of ^{64}Cu in the ventricles of 6-8-month-old C57BL/6J controls compared to age-matched TASTPM mice. The SUV parameters were found to increase over time in both groups, but with a more pronounced trend in AD mice (SUV_{max}: 74.48 ± 19.16 vs 3.15 ± 34.97 % increase; SUV_{mean}: 51.07 ± 22.13 vs 7.73 ± 22.14 % increase). This was also in agreement with the atlas-based measurements (35.58 ± 14.86 % increase in %ID/mL in TASTPM vs 11.75 ± 32.67 % increase in %ID/mL in controls). A large interindividual variability in ^{64}Cu biokinetics was observed in both TASTPM and wildtype groups.

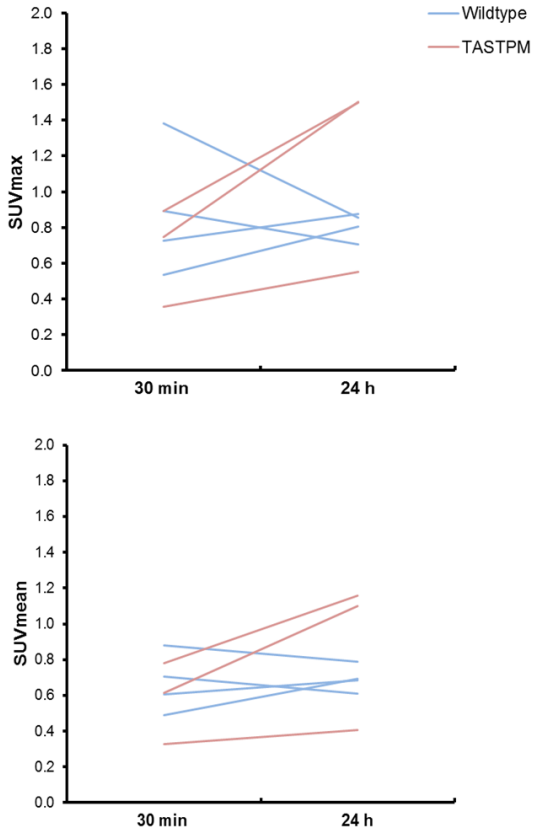

Figure 4.15: Ventricular ^{64}Cu concentration in 6-8-month-old TASTPM transgenic mice and age-matched controls at 30 min and 24 h post-injection of ^{64}Cu-acetate, expressed as SUV_{max} (top) and SUV_{mean} (bottom). Time-activity curves have been plotted for each individual mouse.

Similar results were obtained for the older TASTPM and wildtype groups (Figure 4.16). Higher ventricular SUV_{mean} and SUV_{max} values were measured for 13-15-month-old controls compared to age-matched TASTPM mice at both 30 min and 24 h post-injection. Two-way ANOVA

analysis revealed a significant effect of group ($F_{1,4}$ = 10.99, p = 0.0295) on ventricular SUV_{mean} in aged TASTPM and wildtype mice. Post-hoc evaluation indicated significantly greater SUV_{mean} values in the ventricles of 13-15-month-old C57BL/6J controls compared to TASTPM transgenic mice at all time-points after injection (30 min: 0.90 ± 0.14 vs. 0.49 ± 0.04 %ID/mL, p<0.05; 24 h: 0.97 ± 0.15 vs. 0.58 ± 0.14 %ID/mL, p<0.05). Ventricular SUV_{mean} and SUV_{max} values were found to increase over time for both groups but more markedly for TASTPM mice (SUV_{max}: 45.94 ± 8.38 vs 4.89 ± 10.76 % increase; SUV_{mean}: 17.34 ± 22.94 vs 7.96 ± 4.14 % increase), in the same manner as for their younger counterparts. No significant differences in ^{64}Cu ventricular uptake expressed as SUV were detected between the different age groups of TASTPM and wildtype mice.

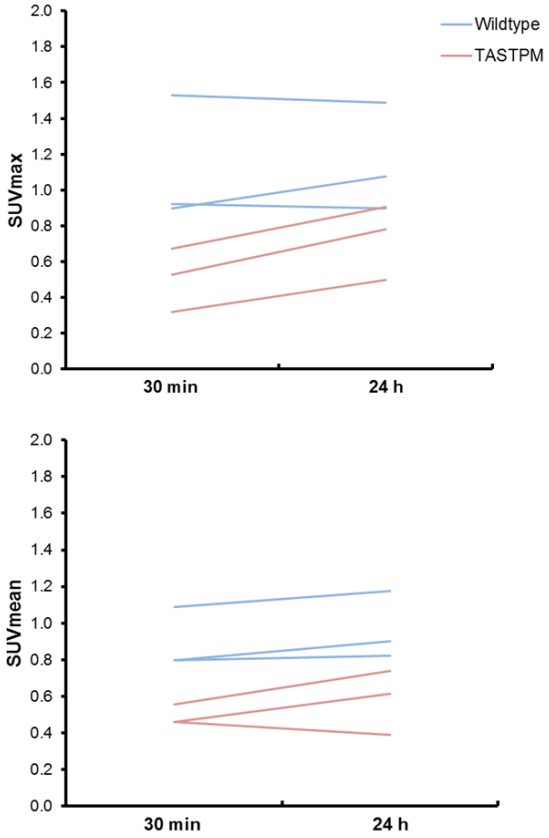

Figure 4.16: Ventricular ^{64}Cu concentration in 13-15-month-old TASTPM transgenic mice and age-matched controls at 30 min and 24 h post-injection of ^{64}Cu-acetate, expressed as SUV_{max} (top) and SUV_{mean} (bottom). Time-activity curves have been plotted for each individual mouse.

4.4.3.2 *Ex vivo* biodistribution

After imaging, all animals were sacrificed and the biodistribution of ^{64}Cu was assessed via gamma-counting of explanted organs. Figure 4.17 depicts ^{64}Cu accumulation in organs and tissues of interest of both 6-8- and 13-15-month-old TASTPM and control mice at 24 h post-injection of ^{64}Cu-acetate as measured by gamma-counting.

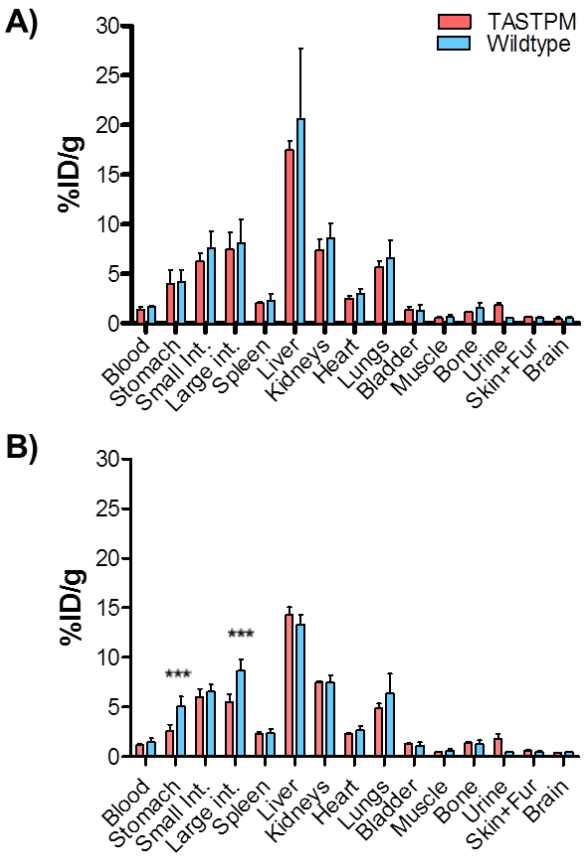

Figure 4.17: Tissue biodistribution of ^{64}Cu in 6-8- (**A**) and 13-15-month-old (**B**) TASTPM mice and age-matched controls at 24 h post-injection of ^{64}Cu-acetate. Statistically significant differences are indicated by *** ($p<0.001$). Data are mean (n=3/group) ± SD.

Gamma-counting of explanted organs revealed a similar biodistribution pattern for the 6-8- and 13-15-month-old TASTPM and wildtype groups. Similar to PET, gamma-counting showed that ^{64}Cu radioactivity was predominantly concentrated in the liver and, to a lesser extent, in the intestines and kidneys. High ^{64}Cu accumulation was also observed in the stomach and lungs.

Statistical analysis did not reveal any significant differences in *ex vivo* tissue biodistribution of ^{64}Cu between 6-8-month-old TASTPM transgenic mice and age-matched controls at 24 h post-injection of the tracer. However, two-way repeated measures ANOVA indicated significant effects of organ ($F_{1,4} = 253.4$, $p<0.0001$) and group by organ interaction ($F_{1,4} = 6.281$, $p<0.0001$) on ^{64}Cu concentration in the older TASTPM and wildtype groups. Post-hoc tests demonstrated significantly higher *ex vivo* accumulation of ^{64}Cu in the stomach (5.12 ± 0.78 %ID/mL vs. 2.58 ± 0.53 %ID/mL, $p<0.001$) and large intestine (8.65 ± 0.96 %ID/mL vs. 5.52 ± 0.65 %ID/mL, $p<0.001$) of 13-15-month-old wildtype controls when compared to their TASTPM counterparts.

Age-dependent differences in ^{64}Cu *ex vivo* biodistribution were found between 6-8- and 13-15-mont-old TASTPM and control groups. Statistical analysis revealed significant effects of organ ($F_{1,4}$ = 284.6, p<0.0001) and group by organ interaction ($F_{1,4}$ = 3.956, p = 0.0001) in 6-8- and 13-15-month-old TASTPM transgenic mice on *ex vivo* concentration of ^{64}Cu. TASTPM transgenic mice at 6-8 months of age exhibited significantly higher ^{64}Cu accumulation in the large intestines (7.46 ± 1.43 %ID/mL vs. 5.52 ± 0.65 %ID/mL, p<0.01) and liver (17.47 ± 0.78 %ID/mL vs. 14.26 ± 0.66 %ID/mL, p<0.001) than their older counterparts. Significant effects of organ ($F_{1,4}$ = 66.41, p<0.0001) and interaction ($F_{1,4}$ = 2.875, p = 0.0026) on ^{64}Cu *ex vivo* tissue biodistribution were also measured in the 6-8- and 13-15-month-old control groups. Hepatic ^{64}Cu concentration was found to be significantly greater in younger wildtype mice relative to aged controls (20.57 ± 5.79 %ID/mL vs. 13.35 ± 0.80 %ID/mL, p<0.001).

Similar to PET, gamma-counting revealed an age-dependent decrease in ^{64}Cu brain concentration in both TASTPM and control mice, although this trend did not reach statistical significance by the tests employed. *Ex vivo* measurements of ^{64}Cu concentration in the brain were found to correlate poorly (R^2 = 0.3102) with brain %ID/mL values at 24 h post-injection determined by PET ROI analysis.

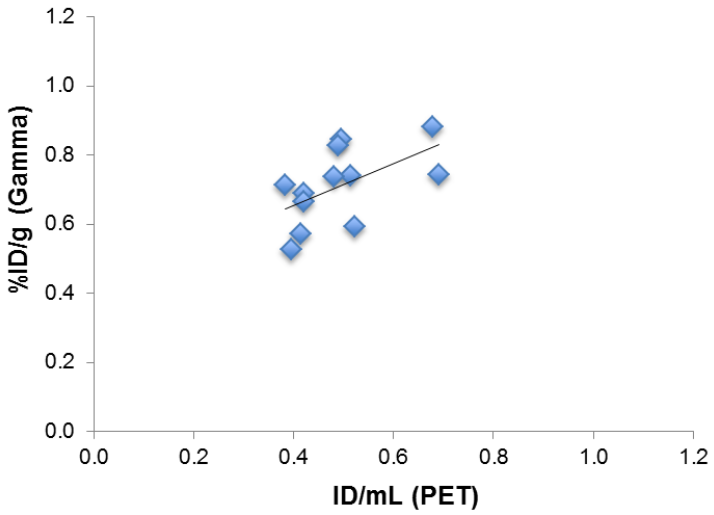

Figure 4.18: Comparison of brain uptake of ^{64}Cu as measured by PET imaging and by *ex vivo* gamma-counting at 24 h post-injection of ^{64}Cu-acetate in 6-8-/13-15-month-old TASTPM transgenic mice and age-matched controls. All TASTPM (n = 6) and wildtype (n = 6) mice were included in the correlation.

4.4.3.3 *Ex vivo* brain autoradiography and histology

In order to characterise further the distribution of ^{64}Cu in the brain resulting from ^{64}Cu-acetate administration, sections of brain tissue of TASTPM and wildtype mice sacrificed at 24 h post-

injection of the tracer were imaged by phosphor imaging autoradiography. *Ex vivo* brain autoradiography revealed a very similar ^{64}Cu distribution pattern in brain tissue for both TASTPM transgenic mice and healthy controls. As depicted in Figure 4.19, ^{64}Cu radioactivity accumulated predominantly in the area surrounding the lateral ventricles and, to a lesser extent, around the fourth ventricle and hypothalamus. This is consistent with the distribution pattern revealed by atlas-based quantification of the PET/CT datasets, which identified the ventricles and hypothalamus as the brain regions with the highest ^{64}Cu concentration at 24 h post-injection of ^{64}Cu-acetate *in vivo*.

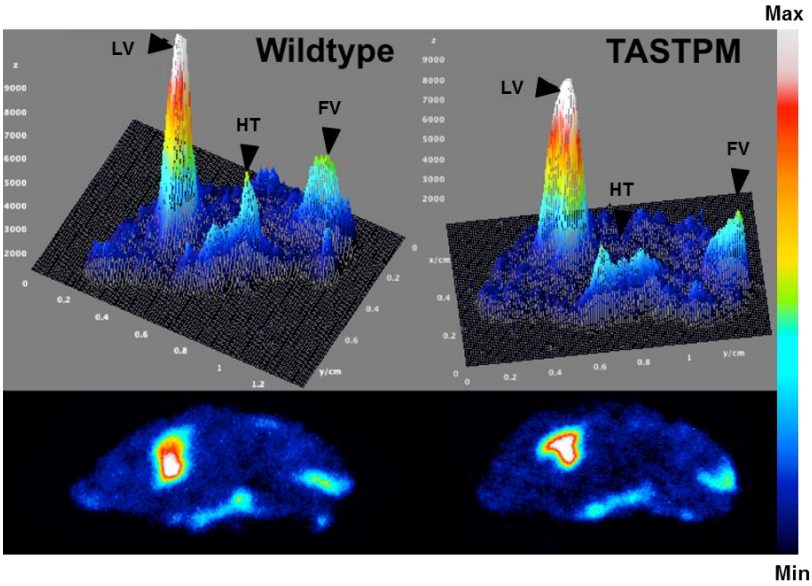

Figure 4.19: *Ex vivo* brain autoradiographs and corresponding surface plots from representative sagittal brain sections of 6-8-month-old wildtype (left) and TASTPM (right) mice sacrificed at 24 h post-injection of ^{64}Cu-acetate. *Ex vivo* autoradiography revealed a similar pattern of ^{64}Cu accumulation in the brain for both control and AD mice, with main radioactive hotspots situated near the lateral and fourth ventricles and hypothalamus. LV = lateral ventricle; FV = fourth ventricle; HT = hypothalamus.

Following radioactive decay, brain slices were stained with hematoxylin dye in order to provide an anatomical reference to their corresponding autoradiographs. Figure 4.20 shows an exemplar sagittal brain slice of a 6-8-month-old control mouse imaged by autoradiography and subsequently stained with hematoxylin. Atlas-guided identification of brain structures in histological photomicrographs and comparison of histology and autoradiography images confirmed the close association between ^{64}Cu hotspots and the ventricular system. ^{64}Cu radioactivity was found to accumulate in and around the lateral and fourth ventricles as well as in the lateral hypothalamic area. The main radioactive peak in the autoradiographic maps resulted from high accumulation of radiocopper in the lateral ventricles but also in the fimbria of the hippocampus. Previous characterisation of cerebral Aβ plaque load in the TASTPM mouse

model (see Chapter III, section 3.4.1) revealed that the areas showing high ^{64}Cu signal in the ^{64}Cu-acetate autoradiographs were traditionally not affected by Aβ plaque pathology.

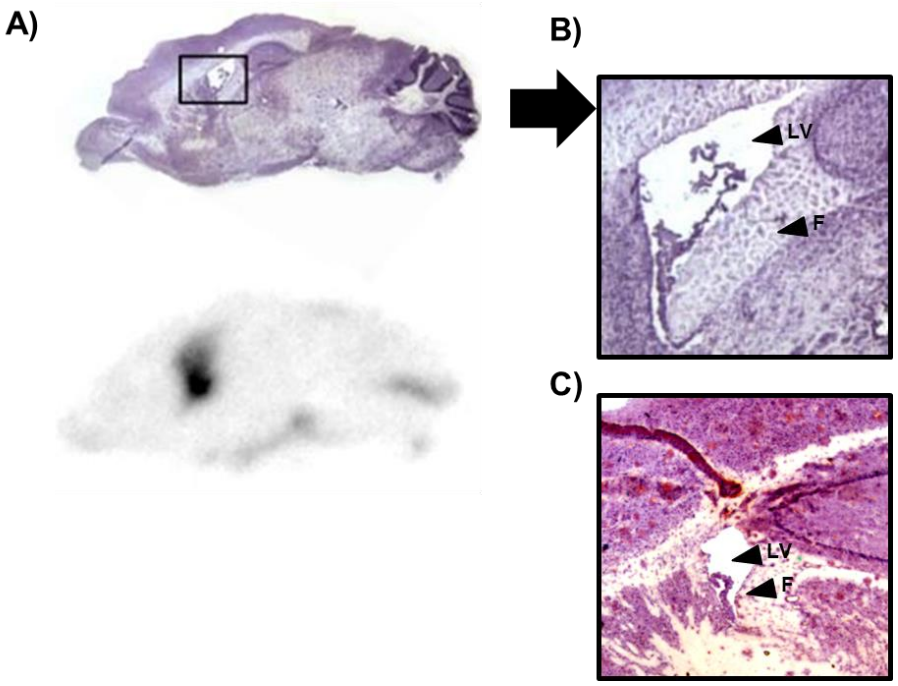

Figure 4.20: (**A**) Photomicrograph of sagittal brain section stained with hematoxylin from a 6-8-month old wildtype mouse (top) and corresponding brain autoradiograph (bottom) at 24 h post-injection of ^{64}Cu-acetate; (**B**) Magnified view of the area surrounding the lateral ventricle in hematoxylin-stained brain section; (**C**) Magnified view of the lateral ventricle area in representative sagittal brain slice stained with hematoxylin and Congo red dye from a 6-8-month old TASTPM mouse. ^{64}Cu radioactivity predominantly accumulated in the lateral ventricle and fimbria of the hippocampus and, to a lesser extent, in the fourth ventricle and lateral hypothalamic area. None of these regions showed congophilic Aβ plaque deposits (red-orange stain). LV = lateral ventricle; F = fimbria of the hippocampus.

4.4.4 Imaging the effects of CQ on copper biodistribution with ^{64}Cu-acetate-PET

4.4.4.1 PET/CT imaging

To gain insight into the mode of action of copper-zinc chelator CQ, we examined its effect on short-term copper trafficking in 2-month-old wildtype mice with ^{64}Cu-acetate-PET. Animals (n=2/treatment group) were intravenously injected with ^{64}Cu-acetate and imaged at 0-30 min and 24-24.5 h post-injection of the tracer 30 min after CQ (50 mg/kg) or 4 % (w/v) (2-hydroxypropyl)-β-cyclodextrin intraperitoneal administration (Figure 4.21).

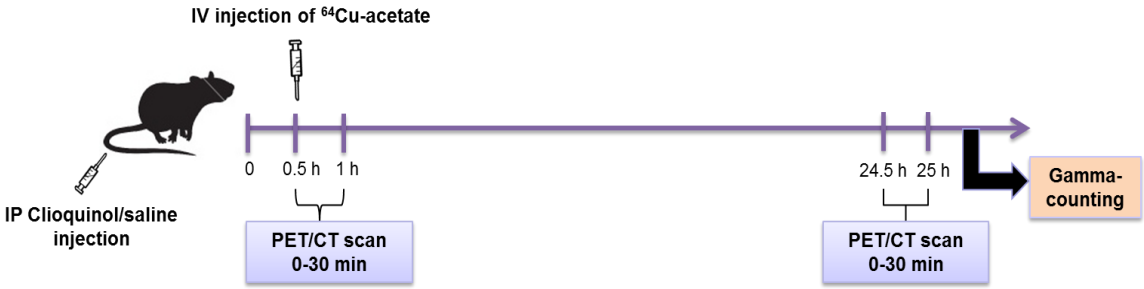

Figure 4.21: Experimental protocol for PET/CT imaging of copper trafficking with ^{64}Cu-acetate in Clioquinol- and sham-treated mice. Mice were intraperitoneally injected with CQ or saline 30 min before ^{64}Cu-acetate administration. PET/CT scans were performed at 0-30 min and 24-24.5 h post-injection of the tracer. After imaging, animals were sacrificed and *ex vivo* biodistribution of ^{64}Cu was assessed via gamma-counting of explanted organs.

The uptake and efflux of ^{64}Cu in selected organs of CQ- and sham-treated mice are shown in Figure 4.22. ^{64}Cu radioactivity accumulated predominantly in the liver and, to a lesser extent, in the kidneys and intestines in both treatment groups. ^{64}Cu concentration as measured by PET ROI analysis decreased over time in the heart, spine, kidneys and liver in both CQ- and sham-treated mice. ^{64}Cu clearance rates from spine (20.22 ± 9.07 % decrease in %ID/mL in CQ-treated mice vs. 5.01 ± 11.51 % decrease in %ID/mL in sham-treated mice) and kidneys (7.65 ± 25.43 % decrease in %ID/mL in CQ-treated mice vs. 45.78 ± 17.90 % decrease in %ID/mL in sham-treated mice) from 30 min to 24 h post-injection of the tracer were markedly different between the two treatment groups.

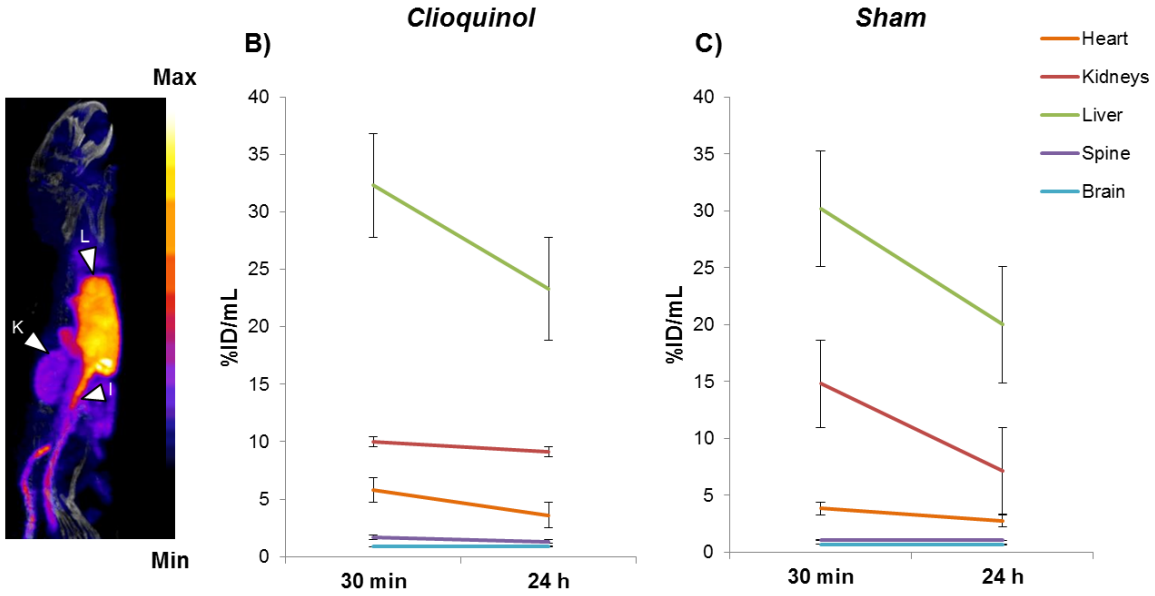

Figure 4.22: Exemplar sagittal view of the PET/CT MIP of a 2-month-old wildtype mouse pretreated with CQ at 30 min post-injection of ^{64}Cu-acetate (**A**). Time-activity curves extracted from PET ROI analysis showing ^{64}Cu concentration (expressed as %ID/mL) over time in the heart, kidneys, liver, spine and brain of CQ- (**B**) and sham-treated (**C**) C57BL6/J controls injected with ^{64}Cu-acetate. Data are mean (n=2/treatment group) ± SEM. L = liver; K = kidneys; I = intestines.

CQ-treated mice exhibited a higher concentration of ^{64}Cu in the heart (30 min: 5.79 ± 0.89 %ID/mL vs. 3.84 ± 0.17 %ID/mL; 24 h: 3.60 ± 1.03 %ID/mL vs. 2.76 ± 0.47 %ID/mL), spine (30 min: 1.66 ± 0.22 %ID/mL vs. 1.10 ± 0.007 %ID/mL; 24 h: 1.31 ± 0.04 %ID/mL vs. 1.04 ± 0.18 %ID/mL) and liver (30 min: 32.28 ± 2.20 %ID/mL vs. 30.21 ± 2.78 %ID/mL; 24 h: 23.31 ± 2.98 %ID/mL vs. 20.01 ± 3.47 %ID/mL) when compared to their sham-treated counterparts at both 30 min and 24 h post-injection of the tracer. The CQ group also showed greater accumulation of ^{64}Cu in the brain than sham-treated mice at all imaging time-points (30 min: 0.85 ± 0.11 %ID/mL vs. 0.71 ± 0.08 %ID/mL; 24 h: 0.90 ± 0.10 %ID/mL vs. 0.66 ± 0.07 %ID/mL). While ^{64}Cu radioactivity in the brain decreased slightly over time in sham-treated mice (6.12 ± 0.60 % decrease in %ID/mL), a small increase in ^{64}Cu concentration was measured between 30 min and 24 h post-injection of the tracer in the brains of CQ-treated controls (7.42 ± 18.34 % increase in %ID/mL). However, larger sample sizes are required to confirm these trends.

Atlas-based quantification of PET/CT datasets demonstrated globally higher ^{64}Cu concentration in all predefined brain regions in the CQ treatment group compared to sham-treated mice at both 30 min and 24 h post-injection of ^{64}Cu-acetate (Figure 4.23). The ventricles exhibited the highest concentration of ^{64}Cu at all imaging time-points in both CQ- and sham-treated wildtype mice.

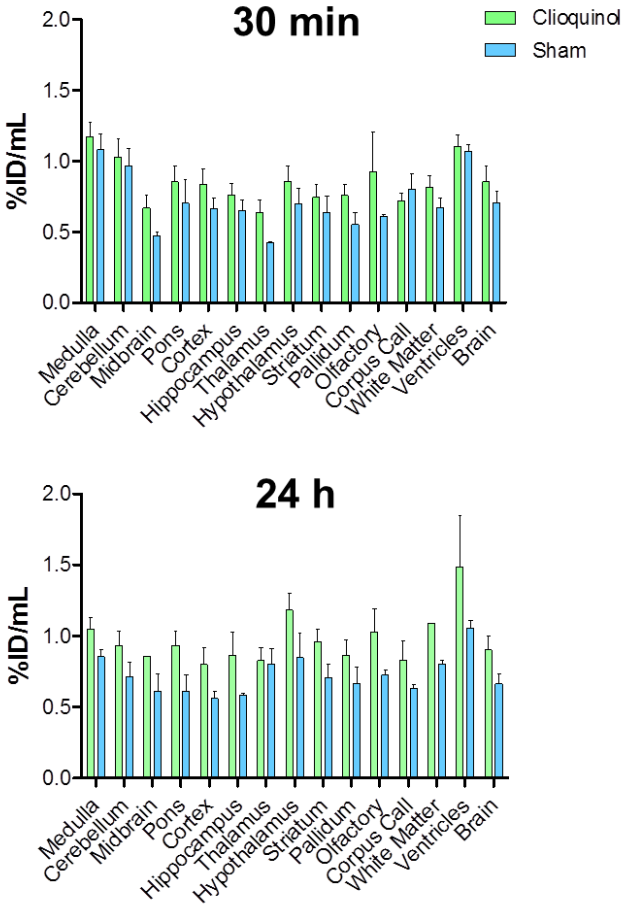

Figure 4.23: Brain regional concentration of ^{64}Cu in CQ- and sham-treated wildtype mice injected with ^{64}Cu-acetate at 30 min (top) and 24 h (bottom) after injection, as measured by atlas-based quantification. Data are mean (n=2/treatment group) ± SD.

Ventricular SUV_{mean} and SUV_{max} values were determined for CQ and sham treatment groups in order to provide a measurement alternative to atlas-based quantification (Figure 4.24). PET ROI analysis revealed similar ventricular SUV_{mean} and SUV_{max} values for CQ- and sham-treated wildtype mice at 30 min post-injection of the tracer. After 24 h, ^{64}Cu concentration in the ventricles increased in both treatment groups, although more markedly for sham-treated mice (SUV_{max}: 190.06 ± 67.43 % vs. 76.52 ± 18.21 % increase in %ID/mL; SUV_{mean}: 84.83 ± 15.91 % vs. 47.01 ± 27.38 % increase in %ID/mL).

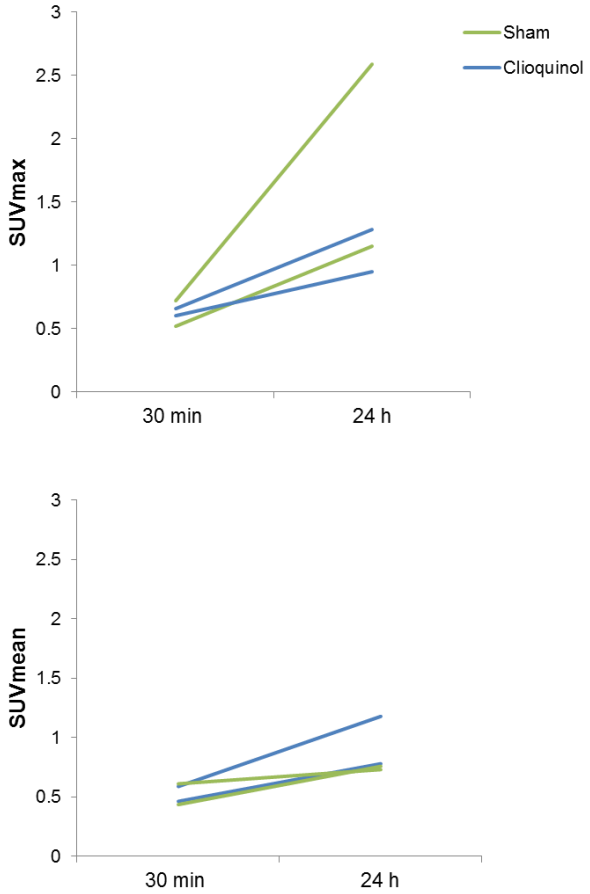

Figure 4.24: Ventricular ^{64}Cu concentration in CQ- and sham-treated C57BL/6J controls at 30 min and 24 h post-injection of ^{64}Cu-acetate, expressed as SUV_{max} (top) and SUV_{mean} (bottom). Time-activity curves have been plotted for each individual mouse.

4.4.4.2 Gamma-counting

The *ex vivo* biodistribution of ^{64}Cu in CQ- and sham-treated wildtype mice at 24 h post-injection of ^{64}Cu-acetate was evaluated via gamma-counting of explanted organs (Figure 4.25). ^{64}Cu biodistribution as measured by gamma-counting was found to be very similar for both treatment groups, with most ^{64}Cu radioactivity accumulating in the liver, intestines, kidneys and lungs. Similar to PET, gamma-counting revealed higher ^{64}Cu concentration in the heart (3.58 ± 0.07 %ID/mL vs. 2.84 ± 0.21 %ID/mL), liver (19.99 ± 2.99 %ID/mL vs. 16.98 ± 1.77 %ID/mL) and brain (0.53 ± 0.05 %ID/mL vs. 0.35 ± 0.001 %ID/mL) of CQ-treated wildtype mice compared to the sham group at 24 h post-injection of the tracer.

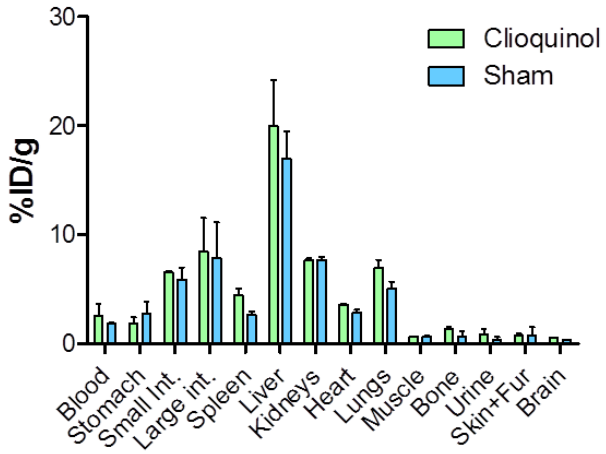

Figure 4.25: Tissue biodistribution of ^{64}Cu in CQ- and sham-treated C57BL/6J controls at 24 h post-injection of ^{64}Cu-acetate. Data are mean (n=2/treatment group) ± SD.

4.5 DISCUSSION

The evaluation of whole-body copper trafficking by PET imaging may shed new light into the pathophysiology of many neurological disorders that have been associated with copper metabolism imbalance, including AD. The feasibility of ^{64}Cu-GTSM-PET as a useful tool to investigate copper fluxes within the CNS was demonstrated in the third chapter of this dissertation. The ability of ^{64}Cu-GTSM to bypass the BBB and release its ^{64}Cu payload non-selectively into cells allows the delivery of radiocopper into the brain in sufficient amounts for the visualisation of brain copper trafficking. However, while ^{64}Cu-GTSM-PET is useful to study the short-term dynamics of copper within the CNS, it does not provide any information on the long-term accumulation of endogenous copper within the brain or the active routes of entry for copper into the CNS. In this chapter, we examined the endogenous distribution of actively transported dietary copper within the brain in the TASTPM mouse model of AD by XRF. Furthermore, we investigated acute active copper transport at the whole-body level in TASTPM transgenic mice at early and middle stages (6-8 and 13-15 months of age) of AD-like pathology by PET imaging with radioactive copper salt ^{64}Cu-acetate. The potential of ^{64}Cu-acetate-PET as a tool to assess the effects of copper chelation therapies was also evaluated in a very preliminary way.

^{64}Cu-GTSM-PET did not reveal an obvious association between regional accumulation of ^{64}Cu in the brain on a short-term time scale and cerebral Aβ plaque deposition in the TASTPM mouse model (see chapter III, section 3.4.8). However, the accumulation of copper ions in Aβ plaque-rich areas may occur more prominently over the lifetime of the animal. In order to investigate the regional distribution pattern of endogenous copper within the brain in AD-like pathology, 2D elemental copper maps from representative brain sections of TASTPM transgenic mice were generated by XRF and compared to those of age-matched healthy controls. Despite not being able to distinguish between oxidation states or chemical forms, XRF is an excellent tool to study the distribution of metals in tissue since it allows global mapping of multiple metals on the same sample (193). Although we initially intended to use the same age groups for XRF elemental analysis as those used in our ^{64}Cu-GTSM-PET imaging experiments (6-8 and 13-15 months of age), brain copper maps were finally generated for 4- and 8-month-old TASTPM transgenic mice and age-matched controls due to lack of availability of AD mice in the 13-15-month-old range. The addition of a 4-month-old age group allowed quantitative assessment of the effect of age and disease progression on brain copper distribution.

XRF mapping revealed prominent accumulation of endogenous copper around the CSF spaces and comparatively low copper concentration within the brain parenchyma in all groups. This brain copper distribution pattern had been previously observed in 2- and 7-month-old C57BL/6J wildtype mice by laser ablation inductively coupled plasma mass spectrometry (196). The focal accumulation of copper around the ventricular system underlines the importance of the BCSFB in brain copper metabolism, even though its exact role is not completely understood. Although the BBB has been proposed as the main route of entry for copper ions into the brain, the BCSFB is also thought to play a crucial role in copper transport to and from the CNS. In view of both the nutrient and secretory capacity of the CSF and the ability of the choroid plexus to sequester copper ions, the BCSFB has been suggested as the main barrier for the regulation of brain copper homeostasis (219, 434). In the ventricular system, high copper concentrations have been measured in the CSF and choroid plexus but also in the subventricular zone of the lateral ventricles, a region known to play a key role in the process of adult neurogenesis (435, 436). Fu and co-workers reported elevated copper levels and high MT expression in the subventricular zone in young, adult and old rats compared to other brain regions. The choroid

plexus was also found to accumulate high levels of copper but exhibited higher levels of expression of copper transporters (Ctr1, DMT1 and ATP7A) than storage proteins. Fu *et al.* observed that age-related increase of copper content in these regions was inversely associated with the expression of neurogenesis markers, which might indicate a regulatory role for copper in adult neurogenesis. The individual contribution of the subventricular zone, choroid plexus and CSF to the XRF copper signal is unknown (436).

Quantification of the XRF elemental copper maps revealed increased copper levels in brain sections from the TASTPM group when compared to controls, along with an age-dependent rise in brain copper content in both groups. This is consistent with the results of a previous study by Wang *et al.*, who reported elevated copper accumulation in the brains of APP/V717I transgenic AD mice and an increase in brain copper concentration with aging (437). Brain copper buildup may result in increased vulnerability of the brain to oxidative stress and enhance, as a result, the neurodegenerative phenotype in these AD models.

Despite previous evidence of elevated copper levels in human Aβ plaque deposits, our XRF results revealed an ambiguous association between plaque-rich areas and brain regional accumulation of endogenous copper in the TASTPM mouse model (341, 398). TASTPM transgenic mice exhibited significantly higher copper concentration than controls in the thalamus at 8 months of age but not in the cerebral cortex or hippocampus, which are other regions traditionally affected by Aβ plaque pathology. This could be due to a decrease in the metal binding capacity of TASTPM Aβ plaques when compared to human plaque deposits, which was evidenced in another mouse model of AD-like Aβ plaque deposition (PSAPP) (438). XRF mapping of brain copper distribution in older TASTPM transgenic mice may reveal whether there is a more obvious relationship between regional copper accumulation and Aβ plaque deposition at later stages of the disease.

ROI analysis of XRF elemental copper maps demonstrated significantly higher copper content in the cerebellum of 8-month-old TASTPM transgenic mice when compared to age-matched controls and increased levels of copper in the caudate putamen of wildtype mice at 4 and 8 months of age relative to their respective TASTPM counterparts. The effects of aging on brain

copper distribution were also different between control and AD groups. While wildtype mice showed an age-dependent increase in copper concentration in the caudate putamen, TASTPM groups exhibited a buildup of copper levels in the thalamus and cerebellum from 4 to 8 months of age. The origin of these differences in brain regional copper content is unknown. In contrast to the global understanding of brain copper metabolism, very little is known about brain regional copper metabolism, cell-specific copper handling systems or interrelationships between trace metals in the different brain areas. XRF offers the possibility of mapping several trace metals on the same sample, which would allow a better characterisation of these abnormalities in brain regional copper distribution. For example, reduced copper content in the caudate putamen of AD mice could be associated with a buildup in iron levels in the same region, which has been detected in AD subjects by MRI (439, 440). However, it should be noted that the differences in brain copper distribution reported here result from the quantification of only two XRF copper maps per age group and therefore additional brain sections need to be added to the analysis to confirm their significance.

After examining the brain distribution pattern of endogenous copper resulting from prolonged active copper transport in AD-like pathology, we evaluated the short-term dynamics of active copper trafficking at the level of the whole organism in the TASTPM model by ^{64}Cu-acetate-PET. Radioactive copper salts have only been used so far to image whole-body copper trafficking in copper metabolism genetic disorders (e.g. WD, MD) but may hold promise for identifying metabolic abnormalities in other pathological conditions associated with copper dyshomeostasis (e.g. AD, HD, PD, ALS, NPC), particularly in the context of copper chelation therapies. Although in AD research much focus has been on the disruption of copper homeostasis in the brain, increased serum copper levels have also been reported in AD, which could have an effect on the short-term dynamics of whole-body copper trafficking (349, 432). The availability of ^{64}Cu-PET offers the possibility to study the trafficking of intravenously or orally administered radiocopper in disease models as well as the dynamics of specific copper transport proteins (^{64}Cu-albumin, ^{64}Cu-ceruloplasmin) that can be purified from plasma of ^{64}Cu-injected mice.

In the present study, the chosen route of administration of the tracer was intravenous injection. Although this route does not mimic gastrointestinal absorption of dietary copper, it improves the resorption rate of the radiocopper when compared to oral administration, allowing the assessment of ^{64}Cu biokinetics in extraintestinal organs. Nevertheless, PET imaging experiments using orally administered radiocopper should also be performed to determine whether there are any abnormalities in the gastrointestinal absorption and biodistribution of dietary copper associated with AD pathology.

Blood clearance of ^{64}Cu-acetate as measured by *in vivo* blood sampling was found to follow a biexponential pattern, which probably reflects an initial wave of radiocopper uptake into organs (mainly the liver, intestines and kidneys), followed by efflux of copper back into the circulation and transfer to other organs. As expected, ^{64}Cu-acetate-PET revealed high accumulation of ^{64}Cu in the liver, intestines and kidneys of TASTPM and wildtype mice and comparatively low radiocopper uptake in the rest of organs at all imaging time-points. High ^{64}Cu signal in the rectum at late imaging time-points suggested that radiocopper was mostly excreted in the faeces. At 6-8 months of age, AD mice showed significantly increased ^{64}Cu concentration in the heart and spine when compared to controls at 30 min post-injection of ^{64}Cu-acetate. However, these differences were not detected between 13-15-month-old TASTPM and age-matched controls. Instead, aged TASTPM mice were found to exhibit significantly higher hepatic ^{64}Cu levels than wildtype controls at 30 min post-injection of the tracer. It should be noted that the reported differences in whole-body copper trafficking are significant but subtle and therefore a larger sample size is required to verify these trends in TASTPM and control mice. Higher accumulation of ^{64}Cu in the spine, heart and liver of TASTPM transgenic mice at early imaging time-points may arise from more active copper influx mechanisms driven by increased metabolic demands associated with the disease or a different profile (biokinetics, speciation) of the tracer in blood. PET ROI analysis also revealed a faster clearance rate of ^{64}Cu radioactivity from 30 min to 24 h post-injection from the liver, heart, kidneys and spine in TASTPM transgenic mice when compared to controls, which may be due to more active copper efflux mechanisms in the AD model.

Unlike ^{64}Cu-GTSM, ^{64}Cu-acetate is taken up by the brain via active copper transport mechanisms. Although this uptake route does not allow the delivery of radiocopper into the brain in sufficient quantities to monitor brain copper trafficking longitudinally, it mimics the entry mechanism of plasma copper into the brain. While ^{64}Cu-GTSM released radiocopper in all brain regions, ^{64}Cu-acetate was found to accumulate focally within and around the ventricular system, similar to the distribution pattern observed in the XRF copper maps. Whether the ventricular signal of the ^{64}Cu-acetate PET scans reflects copper influx, efflux or regulatory processes is not known. The limited spatial resolution of the PET/CT scanner does not allow the distinction between the CSF, the choroid plexus and the areas contiguous to the ventricles (e.g. fimbria of the hippocampus, subventricular zone of the lateral ventricles) and therefore these images are difficult to quantify and interpret.

PET image analysis and *ex vivo* counting revealed no significant differences in global brain ^{64}Cu concentration between TASTPM transgenic mice and wildtype controls at either age. However, despite showing similar group effects, PET and gamma-counting measurements were found to exhibit a poor correlation (R^2 = 0.3102). This discrepancy is probably due to the overestimation of brain ^{64}Cu concentration as measured by PET due to the spillover of activity from high-uptake neighbouring regions (mainly neck) into the brain ROI. In addition, gamma-counting measurements might have been subject to cross contamination between tissues, weighing errors, incomplete explantation or activity loss during dissection. Both PET and gamma-counting demonstrated an age-dependent decrease in brain ^{64}Cu concentration in both TASTPM transgenic mice and controls. These findings are consistent with those of Wang and co-workers, who reported an age-related reduction of brain $^{67}CuCl_2$ uptake in C57BL/6J wildtype mice (196). This age-dependent decrease in active brain ^{64}Cu uptake may be driven by a regulatory mechanism aiming to compensate the increase in brain endogenous copper content measured in aged TASTPM and control mice by XRF.

To assess the regional distribution of ^{64}Cu in the brains of TASTPM and wildtype mice over time, we initially applied a 3D mouse brain atlas template to all the ^{64}Cu-acetate-PET datasets. Atlas-based quantification did not indicate any significant differences in brain regional ^{64}Cu accumulation between AD mice and controls at either age. As expected, the ventricles showed

the highest ^{64}Cu concentration among all brain regions in both TASTPM and control mice at all imaging time-points. Nevertheless, atlas-based quantification may yield inaccurate measurements of the ventricular ^{64}Cu concentration due to the partial volume effect associated with the small size of the ventricles and the potential for imperfect matching of the template onto the real brain region. Hence, SUV_{mean} and SUV_{max} values were also measured within the lateral ventricles to provide an alternative estimate of the accumulation of ^{64}Cu in the ventricles. Although these SUV parameters may also be affected by the partial volume effect, they produce a more reliable measurement of the concentration of ^{64}Cu in the ventricles since they do not entail the (potentially highly inaccurate) delineation of an ROI around the boundaries of the ventricular system. Interestingly, wildtype mice exhibited higher average ventricular SUV_{mean} and SUV_{max} values than their TASTPM counterparts at both ages, although this difference only reached statistical significance between the 13-15-month-old groups. SUV quantification also demonstrated a time-dependent increase in ^{64}Cu radioactivity in the ventricles of both TASTPM and control mice at both 6-8 and 13-15 months of age, which was more prominent in the AD groups. The interpretation of these results is rather complex since the limited spatial resolution of the PET scanner does not allow the measurement of ^{64}Cu concentration within specific subregions of the ventricular system (CSF, choroid plexus, fimbria of the hippocampus, subventricular zone of the lateral ventricles). C57BL6/J controls may exhibit a greater accumulation of ^{64}Cu in the ventricles due to a higher rate of active copper transport from the blood into the choroid plexus or to a greater concentration of radiocopper in blood at early time-points than TASTPM transgenic mice. On the other hand, AD mice may show a more pronounced time-dependent increase in ventricular ^{64}Cu levels due to a leakier epithelium, increased demand for copper or different ^{64}Cu blood biokinetics than controls. It should be noted that the BCSFB could be also acting as a CSF-to-blood efflux system for copper ions and/or as a copper metabolism regulatory site, and therefore the ventricular ^{64}Cu signal may also reflect these processes. However, these results should not be overinterpreted since a high interindividual variability was observed in SUV quantification and consequently a larger sample size is needed to confirm the reported trends.

The potential of ^{64}Cu-acetate-PET as a tool to evaluate the effects of copper-zinc chelator CQ on copper biodistribution *in vivo* was also preliminarily investigated. In recent years, a number of

copper chelating agents (e.g. CQ, PBT2) aimed at minimising neurotoxic Aβ-copper interactions and correcting copper dyshomeostasis in the AD brain have been developed. Although some of these chelators have shown therapeutic effects in mouse models of AD, their mechanism of action remains to be fully characterised (441, 442). CQ has been reported to sequester copper from Aβ plaque deposits and transport it into cells, thus decreasing Aβ toxicity and restoring intracellular copper levels in the brain (371). Furthermore, it has also been shown that the intracellular release of copper ions from CQ complexes promotes the degradation of Aβ plaque deposits through the upregulation of MMP activity (364).

^{64}Cu-acetate-PET offers the possibility to visualise and quantify the effects of chelation therapies on whole-body copper dynamics *in vivo*. To date, the application of PET for the assessment of response to copper chelation treatments has only been reported in a study by Nomura *et al.*, in which PET imaging with $^{64}CuCl_2$ was used to demonstrate the efficacy of disulfiram for brain copper transport in a mouse model of MD (154). In this study, we present the results of a preliminary experiment to evaluate the effects of CQ pretreatment on the short-term dynamics of ^{64}Cu in wildtype mice. The dose (50 mg/kg) and administration route used in this experiment had been previously reported in the literature (443). The 30 min gap between CQ administration and ^{64}Cu-acetate injection was chosen based on previous studies reporting peak concentrations of CQ in the plasma and brain being reached at 15 and 60 min after intraperitoneal administration of the drug, respectively (444).

Both PET imaging and *ex vivo* gamma-counting revealed higher concentrations of ^{64}Cu in the liver, heart, spine and brain of mice pretreated with CQ when compared to the sham group. Increased ^{64}Cu accumulation in these organs in CQ-treated mice might result from the formation of the hydrophobic ^{64}Cu-CQ complex in blood, which in turn might move across biological membranes by non-saturable diffusion mechanisms at a much faster rate than active transport. Nevertheless, it should be noted that the differences in ^{64}Cu concentration observed between CQ- and sham-treated mice were relatively subtle and therefore a larger sample size is needed to confirm the significance of these trends. The low amount of radiocopper delivered by ^{64}Cu-acetate into the brain did not allow the visualisation of the effect of CQ treatment on brain copper trafficking and therefore this experiment should be repeated using ^{64}Cu-GTSM as a

delivery vehicle. Furthermore, additional experiments using different doses, administration routes and/or treatment times need to be conducted to fully evaluate the impact of CQ treatment on whole-body copper trafficking and understand the therapeutic effect of this drug in AD pathology.

4.6 CONCLUSIONS

The characterisation of active copper transport at brain and whole-body levels is key to identify copper metabolism abnormalities associated with inherited and acquired neurological disorders. In this study, we have shown the utility of XRF and ^{64}Cu-acetate-PET as tools to investigate brain and whole-body copper distribution resulting from acute and chronic active copper transport processes in a mouse model of AD-like pathology. Significant differences in brain regional distribution of endogenous copper were measured by XRF between TASTPM transgenic mice and wildtype controls. Our results showed an ambiguous association between brain regional copper accumulation as determined by XRF and cerebral Aβ plaque deposition, which supports the idea that the dysregulation of brain copper metabolism in AD extends beyond Aβ plaque pathology. PET/CT imaging using ^{64}Cu-acetate revealed subtle differences in acute whole-body ^{64}Cu trafficking between TASTPM transgenic mice at early and middle stages of the disease and age-matched controls, which need to be further examined in order to determine their importance in the pathophysiology of the disorder. The present study also demonstrated the potential of ^{64}Cu-acetate-PET to evaluate the effects of copper chelating agent CQ on whole-body copper trafficking. In the context of copper chelation therapies, ^{64}Cu-acetate-PET could be used not only to shed some light into the mechanism of action of copper chelating drugs but also to monitor response to treatment in several disorders linked to copper dyshomeostasis (e.g. AD, HD, MD, WD, PD).

Chapter 5- PET imaging of copper trafficking in a mouse model of Niemann-Pick disease type C1

5.1 AIMS

The purpose of this study is to examine the short-term dynamics of copper, particularly within the CNS, in a mouse model of NPC1 disease by ^{64}Cu-GTSM-PET, in order to delineate potential abnormalities in copper trafficking that might serve as diagnostic markers for the disorder.

5.2 INTRODUCTION

NPC1 disease is a rare lipid storage disorder predominantly caused by mutations in the gene encoding the NPC1 protein. Loss-of-function of this protein leads to the intracellular accumulation of cholesterol and other lipids in late endosomes and lysosomes. As a result of abnormal lipid storage, patients suffering from NPC1 disease show liver and spleen enlargement and progressive CNS degeneration, leading to the development of cognitive deficits and motor impairment (319). Additionally, NPC1 disease patients have been shown to develop AD-like neurofibrillary pathology, which also contributes to the neurodegenerative process (445, 446).

Analysis of NPC1 function has suggested that this protein may play a role in the regulation of lysosomal transport of endocytosed lipid cargo or function to transport lipophilic molecules, except cholesterol, out of endosomal/lysosomal compartments (447, 448). However, it remains to be clarified what the exact role of NPC1 is and how loss-of-function of this protein induces the pathological features characteristic of the disorder (e.g liver dysfunction, neurodegeneration). While the metabolism of several lipids, including cholesterol, sphingomyelin, glycosphingolipids, phospholipids and lysobisphosphatidic acid, has been reported to be disrupted in the liver and spleen of NPC1 disease patients, glycosphingolipids have been found to be the predominant

storage material in the brain (449). These two lipid storage patterns and their distinctly different pathological effects suggest multiple functional roles for the NPC1 protein in the body.

The fact that systemic and neurological disease processes follow independent courses along with the broad phenotypic variability of NPC1 disease hamper the development of successful treatment options for this disorder. To date, no curative therapy exists for NPC1 disease and the management of the disorder remains largely symptomatic (450). Treatment with miglustat, an inhibitor of glycosphingolipid biosynthesis, was shown to improve or stabilise several markers, mostly neurological, of disease severity in NPC1 patients, but was not able to halt or reverse disease progression (451).

Due to its extreme clinical heterogeneity and variable age of presentation, accurate diagnosis of NPC1 disease is often challenging. Although the disease can be detected via molecular genetic testing, there are currently no reliable independent diagnostic markers to assess disease severity and progression and monitor response to treatment. For many years, the primary diagnostic test for NPC1 disease has been invasive skin biopsy followed by biochemical testing of intracellular accumulation of exogenously derived LDL-cholesterol in cultured fibroblasts (452). Nevertheless, this diagnostic approach is complex, time-consuming and costly and may not be effective to detect NPC1 cell lines presenting only minor abnormalities (319).

Both *in vitro* and *in vivo* studies have demonstrated that abnormal lipid metabolism in NPC1 disease is accompanied by oxidative stress (453-457). As a consequence of oxidative stress, plasma and tissue levels of cholesterol oxidation products have been found to be increased in NPC1 knockout mice (457). Porter and co-workers revealed that elevation of plasma oxysterol levels correlated with the age of disease onset and disease severity in human subjects. This study additionally showed that concentration of cholesterol oxidation products in blood plasma decreased in a feline model of NPC1 disease in response to the administration of cholesterol modulator 2-hydroxypropyl-β-cyclodextrin, demonstrating the potential usefulness of this marker for monitoring response to treatment (458). However, although measurement of oxysterols in plasma is a cheap, rapid and highly sensitive diagnostic method, it cannot differentiate between NPC1 disease and other subtypes of Niemann-Pick disease (e.g. Niemann-Pick disease type

A/B, acid sphingomyelinase-deficient Niemann-Pick disease), thus requiring additional testing to confirm the diagnosis (459, 460).

The source of oxidative stress in NPC1 disease remains unknown. It is thought that mitochondrial function is disrupted in NPC1 disease, which may lead to ATP deficiency and increased production of ROS. Furthermore, it has been suggested that alterations in the activities of several antioxidant systems (e.g. peroxisomal catalase, vitamin E, glutathione peroxidase 1) may be responsible for the buildup of ROS in plasma and tissues of NPC1 patients. Finally, it has been hypothesised that dysregulation of metal homeostasis in NPC1 disease may enhance ROS production and accelerate neurodegeneration (461).

Growing evidence suggests that the metabolism of several transition metals, including copper, is disrupted in NPC1 disease (321-324, 462-465). Among other transition metal imbalances, copper content in the liver and blood has been found to be altered in both NPC1 deficient mice and human subjects (323, 324, 465). The origin of these metabolic abnormalities is not understood. The NPC1 protein may play a direct role in normal copper metabolism since it has been shown to mediate the incorporation of endosomal copper into ceruloplasmin in cultured hepatocytes (326, 327). However, copper imbalance in NPC1 disease may merely be a consequence of aberrant cholesterol storage since copper and cholesterol metabolic pathways have been shown to be interconnected (325).

Although copper dyshomeostasis is thought to contribute to neurodegeneration in NPC1 disease through the production of ROS, copper metabolism abnormalities in the CNS have not been fully characterised. Reports on CNS copper content in NPC1 disease are few and often contradictory. Whole-brain copper levels have not been measured in human brain tissue but were found to be decreased in NPC1 knockout mice compared to healthy controls (321). Copper content in the cerebellum, which is the brain structure most affected by neurodegeneration in NPC1 disease, was shown to be reduced or unchanged in NPC1 knockout mice relative to age-matched controls (321, 324). CSF copper levels were found to be significantly decreased in a very small cohort of NPC1 patients (n=2) as compared with healthy subjects (321).

A better characterisation of copper metabolism imbalance in NPC1 disease, particularly within the CNS, is needed to understand its impact on disease severity and progression and evaluate its potential as a diagnostic marker of the disorder. Hence, in the present study, we have investigated the short-term dynamics of copper in a mouse model of NPC1 disease by ^{64}Cu-GTSM-PET in order to delineate potential metabolic abnormalities associated with the disorder. By exploiting the ability of ^{64}Cu-GTSM to cross the BBB and release its copper payload non-selectively into cells, we were able visualise and quantify radiocopper trafficking *in vivo* both at CNS and whole-body level. To our knowledge, this is the first report evaluating the real-time dynamics of copper in NPC1-like pathology *in vivo* by noninvasive imaging.

5.2.1 The BALB/cNctr-*Npc1^{m1N}*/J mouse model of NPC1 disease

In the present study, *in vivo* copper trafficking was investigated by PET in the BALB/cNctr-*Npc1^{m1N}*/J mouse model of NPC1 disease. This mouse model is commonly used since is fully characterised and displays an early-onset, severe form of NPC1 disease, with lifespan limited to 12-14 weeks (49). Loss of NPC1 function in this model is caused by a spontaneous mutation arising from the insertion of a retrotransposon-like sequence in the NPC1 gene, resulting in a premature stop codon and protein truncation (466).

NPC1 knockout mice exhibit intracellular accumulation of cholesterol and glycosphingolipids, leading to hepatosplenomegaly and liver dysfunction (467-469). Similar to NPC1 patients, NPC1 deficient mice also develop progressive neurodegeneration, characterised by cerebral atrophy, demyelination of the corpus callosum, and degeneration of cerebellar Purkinje cells. As a result, NPC1 mutant mice show a staggering gait, action tremors, reduced exploratory behaviour and impaired learning and memory capacity (470). However, NPC1 knockout mice are not able to reproduce all the features of human NPC1 pathology. In contrast to the widespread occurrence of neurofibrillary tangles in patients with NPC1 disease, neurofibrillary pathology has not been detected in NPC1 deficient mice (471). NPC1$^{-/-}$ mouse models are also not able to reproduce the high phenotypic variability characteristic of human disease (319). Regarding metal homeostasis, it should be noted that Hung *et al.* reported discrepancies in the direction of trace metal abnormalities between patients with NPC1 disease and NPC1$^{-/-}$ transgenic mice, which probably reflect species-specific differences in metal metabolism.

Therefore, following preclinical evaluation, copper trafficking should also be evaluated in NPC1 patients in order to assess the status of copper metabolism in human NPC1 disease (321).

In this study, NPC1 knockout mice and their wildtype littermates have been imaged at 6 and 9 weeks of age. The 6-week-old age group was chosen as representative of the presymptomatic stage of the disease, since symptoms in this NPC1 model usually start at about 7 weeks of age, while 9-week-old mice were designated as the symptomatic group (49).

5.3 MATERIALS AND METHODS

5.3.1 Radiochemistry

All reagents were purchased from Sigma-Aldrich, Alfa Aesar, Interlink Scientific Services or VWR International Ltd. and were used without further purification, unless otherwise stated. ^{64}Cu was produced as previously reported on a CTI RDS 112 biomedical cyclotron at the Clinical PET Centre of St Thomas' Hospital in the form of $^{64}CuCl_2$ in 0.1 N HCl solution (4.8 GBq/μg) (99). Radioactivity was measured using a Capintec CRC-25R dose calibrator. Radio-TLC was performed on a LabLogic Flow-Count scanner (scan speed: 0.25 mm/s), using MERCK 60 F_{254} silica gel plates as the stationary phase and ethyl acetate as the mobile phase.

H_2GTSM was synthesised following a previously reported procedure (142, 406). ^{64}Cu-GTSM (~90 % isolated radiochemical yield, ≥ 95 % radiochemical purity) was prepared by reaction of the H_2GTSM ligand with ^{64}Cu-acetate (~100 MBq) using a previously reported radiolabelling protocol. Full experimental details for the synthesis of H_2GTSM and ^{64}Cu-GTSM are included in the third chapter of this dissertation (sections 3.31 and 3.3.2). For intravenous administration, ^{64}Cu-GTSM was diluted in sterile 0.9 % (w/v) saline solution to <10 % of total injected volume (< 200 μL).

5.3.2 Animals

All animal experiments were performed in accordance with the Animals (Scientific Procedures) Act, 1986 and approved by the local ethics committee. Animals were kept in standard BSU

conditions (21°C, 50 % humidity) and fed *ad libitum* with regular animal feed (PicoLab Rodent Diet 20 EXT IRR, LabDiet ®, US).

BALB/cNctr-*Npc1*^{m1N}/J transgenic mice (The Jackson Laboratory, Charles River, UK) were maintained by heterozygote sibling matings and genotyped as previously described (466). Animals were bred at the Department of Pharmacology of the University of Oxford and transferred to the Rayne Institute two weeks before the experiment. Food intake, natural behaviour and animal body weight were monitored weekly.

5.3.3 PET/CT imaging

Imaging experiments were performed using a nanoScan® PET/CT (Mediso Medical Imaging Systems, Budapest, Hungary). ^{64}Cu-GTSM-PET was performed in 6- and 9-week-old female NPC1$^{-/-}$ transgenic mice and age-matched wildtype controls (n=3/group). All animals were anaesthetised by isoflurane inhalation (3 % [v/v], Vet Tech Solutions Ltd.) and injected with ^{64}Cu-GTSM (~15-20 MBq, ≤200 µL) via lateral tail vein. Immediately after injection, mice were placed on the scan bed in the prone position and imaged for 30 min by PET/CT (PET: 400-600 keV energy window; 5 ns coincidence window, 0.30 x 0.30 x 0.30 mm^3 voxel size; CT: 180 projections, 45 KVp, 0.25 x 0.25 x 0.21 mm^3 voxel size). After imaging, mice were allowed to recover and housed overnight. At 15 h post-injection of ^{64}Cu-GTSM, animals were re-scanned for 30 min. Anaesthesia was maintained at 2 % isoflurane throughout the duration of the scans. Respiration rate and bed temperature were monitored during image acquisition.

5.3.3.1 PET image analysis

All PET/CT datasets were reconstructed using 3D iterative algorithms (8 iterations, 6 subsets, 0.25 x 0.25 x 0.25 mm^3 voxel size) (408). Decay, dead-time, intercrystal scatter and CT-derived attenuation corrections were applied as part of the reconstruction. The 0-30 min PET datasets were reconstructed into 5-min bins and binned images corresponding to 25–30 min post-injection were used for ROI analysis. Static 15-15.5 h PET datasets were reconstructed into single bins representing the average radiotracer biodistribution during this time frame. All reconstructed datasets were quantified using VivoQuant 1.21 software (inviCRO, LLC, Boston, USA). PET and CT images were automatically co-registered and fixed-volume 3D ROIs (~15

mm^3) were drawn to determine %ID/mL of ^{64}Cu in organs of interest. A mouse brain atlas NM/CT module (inviCRO, LLC) was automatically co-registered to all PET/CT datasets and used to measure global and regional concentration of ^{64}Cu in the brain.

5.3.4 *Ex vivo* biodistribution

After imaging (15.5 h post-injection of ^{64}Cu-GTSM), all mice were culled and dissected. Organs of interest were explanted, weighed and gamma-counted (LKB Wallac 1282) to measure ^{64}Cu concentration in each organ as %ID/g. The sum of whole-body counts (excluding tail) and excreted activity (urine and faeces) was considered as the total ID.

5.3.5 *Ex vivo* brain autoradiography

After dissection, brain tissue was cryopreserved in 30 % (w/v) sucrose solution for ~6 h and stored at -80°C overnight. Sagittal brain sections were then cut at 10 µm using a Bright 5040 cryotome and thaw-mounted onto Superfrost PLUS glass microscope slides (Menzel-Glaser, Thermo Scientific). Subsequently, tissue slices were exposed to a storage phosphor screen (PerkinElmer, Super Resolution, 12.5 x 25.2 cm) for 15 h. Finally, the plate was scanned using a Typhoon 8600 scanner (Molecular Dynamics) and the resulting autoradiographs were analysed with OptiQuant 5.0 (PerkinElmer) and ImageJ (NIH).

5.3.6 Statistical analysis

All data are reported as mean ± SD. Statistical analysis was performed using GraphPad Prism 5 (GraphPad Software Inc.). Two-way repeated measures ANOVA with post-hoc analyses using the Bonferroni multiple comparison correction was used to determine statistically significant differences between $NPC1^{-/-}$ transgenic mice and wildtype controls at different imaging time-points.

5.4 RESULTS

5.4.1 PET/CT imaging

In order to investigate short-term copper trafficking in NPC1 disease, particularly at the CNS level, $NPC1^{-/-}$ transgenic mice at 6 and 9 weeks of age and age-matched controls were

intravenously injected with ^{64}Cu-GTSM and imaged from 0-30 min and from 15-15.5 h post-injection. Figure 5.1 depicts the *in vivo* biodistribution of ^{64}Cu in 6-week-old NPC1 knockout mice and wildtype controls at 30 min and 15 h after injection. On visual assessment, ^{64}Cu radioactivity seemed to accumulate predominantly in the lungs and heart and to a lesser extent in the liver, intestines, kidneys and brain in both animal groups at 30 min post-injection of the tracer. ^{64}Cu accumulation in the lungs at 30 min after injection seemed remarkably higher for wildtype controls when compared to NPC1$^{-/-}$ transgenic mice. After 15 h, ^{64}Cu radioactivity appeared to wash out from the heart, lungs and kidneys and to increase in the liver and intestines in both NPC1$^{-/-}$ transgenic mice and wildtype controls. Brain ^{64}Cu uptake seemed to remain relatively constant over time in both groups.

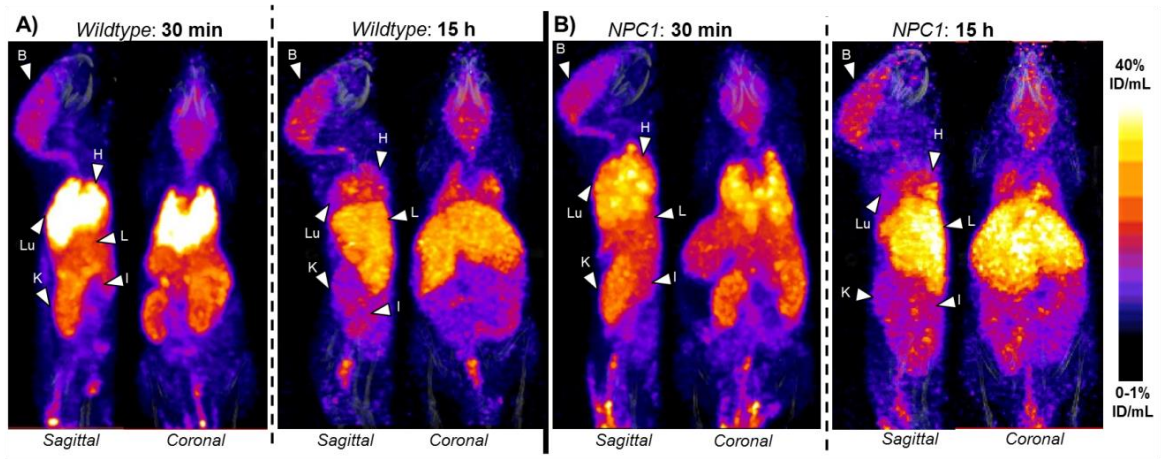

Figure 5.1: Exemplar sagittal and coronal views of PET/CT MIPs of 6-week-old female wildtype controls (**A**) and age-matched NPC1$^{-/-}$ transgenic mice (**B**) at 30 min and 15 h post-injection of ^{64}Cu-GTSM. PET imaging revealed high accumulation of ^{64}Cu radioactivity in the heart, lungs, liver, kidneys, intestines and brain at 30 min after injection of the tracer in all mice. While ^{64}Cu accumulation decreased in the heart, lungs and kidneys over time, the concentration of radiocopper in the liver and intestines increased. Brain uptake of ^{64}Cu remained relatively constant over time in both animal groups. Organs are indicated by arrows: B = brain; Sp = spine; H = heart; Lu = lungs; L = liver; K = kidneys; I = intestines. All MIPs were scaled to 0-1 %ID/mL (min) and 40 %ID/mL (max).

The *in vivo* biodistribution of ^{64}Cu in 9-week-old NPC1 knockout mice and age-matched controls at 30 min and 15 h post-injection of ^{64}Cu-GTSM was very similar to that of their younger counterparts (Figure 5.2). Based on visual inspection of PET/CT images, ^{64}Cu radioactivity accumulated mainly in the heart, lungs, liver, kidneys intestines and brain at 30 min post-injection of the tracer. At 15 h after injection, ^{64}Cu concentration decreased in the heart, lungs and kidneys and increased in the liver and intestines. Intestinal ^{64}Cu uptake at late imaging time-points appeared to be greater in NPC1 knockout mice than in wildtype controls. ^{64}Cu accumulation in the brain remained relatively constant over time in both animal groups but seemed to be higher in the NPC1 group compared to healthy controls.

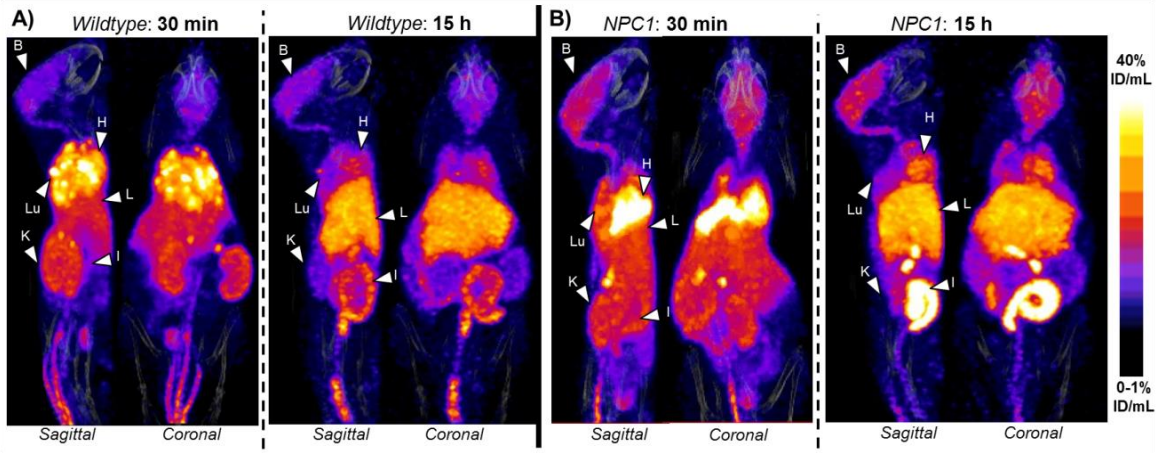

Figure 5.2: Exemplar sagittal and coronal views of PET/CT MIPs of 9-week-old female wildtype controls (**A**) and age-matched NPC1$^{-/-}$ transgenic mice (**B**) at 30 min and 15 h post-injection of ^{64}Cu-GTSM. Similar to the 6-week-old mouse groups, 9-week-old NPC1$^{-/-}$and control mice showed high concentration of ^{64}Cu in the heart, lungs, liver, kidneys, intestines and brain at 30 min after injection. From 30 min to 15 h post-injection of ^{64}Cu-GTSM, ^{64}Cu radioactivity decreased in the heart, lungs and kidneys and increased in the liver and intestines. The concentration of ^{64}Cu in the brain appeared to be higher for NPC1 knockout mice at both imaging time-points when compared to their wildtype littermates. Organs are indicated by arrows: B = brain; Sp = spine; H = heart; Lu = lungs; L = liver; K = kidneys; I = intestines. All MIPs were scaled to 0-1 %ID/mL (min) and 40 %ID/mL (max).

^{64}Cu biokinetics in the CNS (brain and spine) and other organs of interest (e.g. heart, liver) were quantified in all groups by PET ROI analysis (Figure 5.3). As expected, ^{64}Cu concentration was found to decrease markedly in the heart (NPC1$^{-/-}$: 54.24 ± 12.34 % decrease in %ID/mL; wildtype: 49.71 ± 20.50 % decrease in %ID/mL) and increase in the liver (NPC1$^{-/-}$: 64.07 ± 10.18 % increase in %ID/mL; wildtype: 33 ± 22.44 % increase in %ID/mL) from 30 min to 15 h post-injection of the tracer in both 6-week-old NPC1 knockout mice and age-matched controls. Furthermore, PET ROI analysis revealed that ^{64}Cu concentration increased slightly in the brain (NPC1$^{-/-}$: 1.71 ± 1.20 % increase in %ID/mL; wildtype: 1.42 ± 0.84 % increase in %ID/mL) and spine (NPC1$^{-/-}$: 3.07 ± 3.87 % increase in %ID/mL; wildtype: 2.15 ± 6.31 % increase in %ID/mL) in both animal groups from 30 min to 15 h post-injection of the tracer. The concentration of ^{64}Cu in the brain and spinal cord of NPC1 knockout mice was found to be slightly higher when compared to that of their wildtype littermates but this difference between the groups did not reach statistical significance by the tests employed.

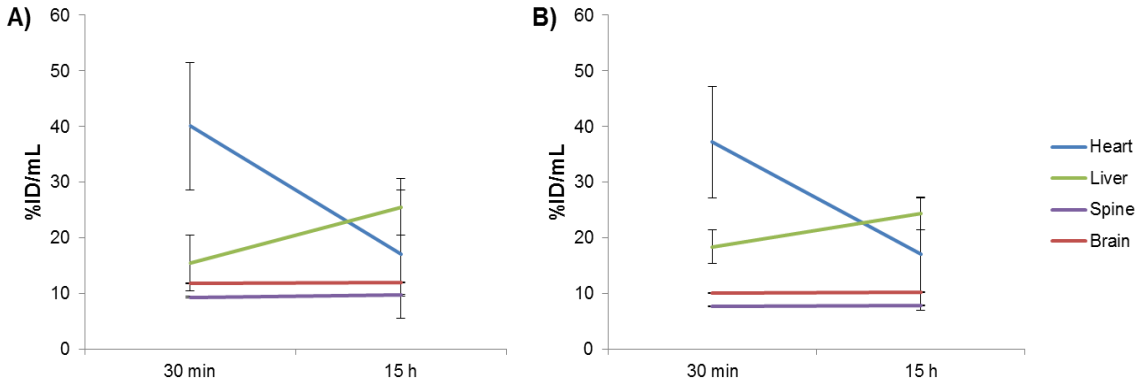

Figure 5.3: Time-activity curves extracted from PET ROI analysis depicting ^{64}Cu concentration (expressed as %ID/mL) over time in the heart, liver, spine and brain of 6-week-old NPC1$^{-/-}$ (**A**) and age-matched wildtype controls (**B**). Data are mean (n=3/group) ± SEM.

PET quantification demonstrated that the *in vivo* biokinetics of ^{64}Cu in the 9-week-old NPC1$^{-/-}$ and control groups were similar to those of their younger counterparts (Figure 5.4). A decrease in cardiac ^{64}Cu concentration was measured from 30 min to 15 h post-injection of ^{64}Cu-GTSM in both NPC1$^{-/-}$ transgenic mice (48.38 ± 10.81 % decrease in %ID/mL) and age-matched controls (52.56 ± 9.74 % decrease in %ID/mL). Hepatic ^{64}Cu content was also found to increase over time in both animal groups (NPC1$^{-/-}$: 69.42 ± 15.76 % increase in %ID/mL; wildtype: 69.77 ± 6.19 % increase in %ID/mL). Nevertheless, contrary to younger mice, 9-week-old NPC1 knockout mice and wildtype controls exhibited a decrease in spinal cord ^{64}Cu concentration over time (NPC1$^{-/-}$: 5.30 ± 2.95 % decrease in %ID/mL; wildtype: 3.95 ± 3.24 % decrease in %ID/mL). While ^{64}Cu accumulation in the brains of NPC1$^{-/-}$ transgenic mice was found to decrease slightly from 30 min to 15 h post-injection of ^{64}Cu-GTSM (0.38 ± 1.50 % decrease in %ID/mL), brain ^{64}Cu concentration in age-matched controls was shown to increase from 30 min to 15 h post-injection of the tracer (2.47 ± 1.41 % increase in %ID/mL).

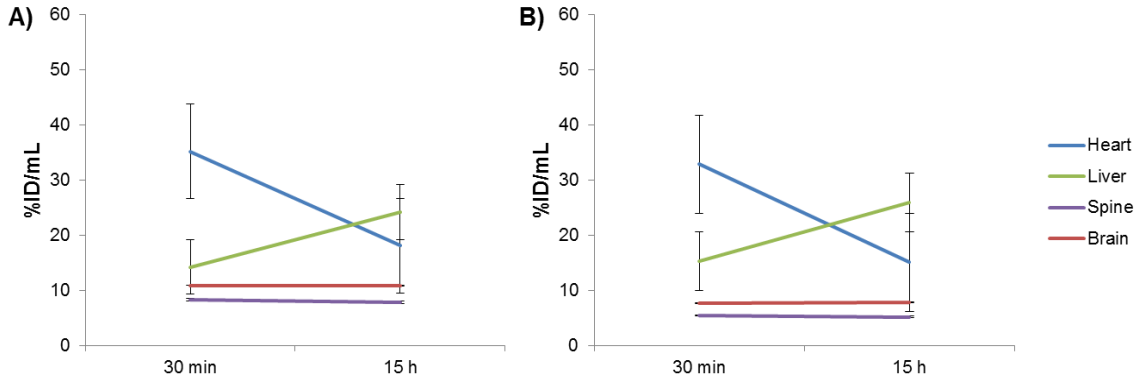

Figure 5.4: Time-activity curves extracted from PET ROI analysis showing ^{64}Cu concentration (expressed as %ID/mL) from 30 min to 15 h post-injection of ^{64}Cu-GTSM in the heart, liver, spine and brain of 9-week-old NPC1$^{-/-}$ (**A**) and age-matched wildtype controls (**B**). Data are mean (n=3/group) ± SEM.

Unlike in younger mice, significant differences in ^{64}Cu biokinetics within the CNS were detected between 9-week-old NPC1 knockout mice and age-matched controls (Figure 5.5).

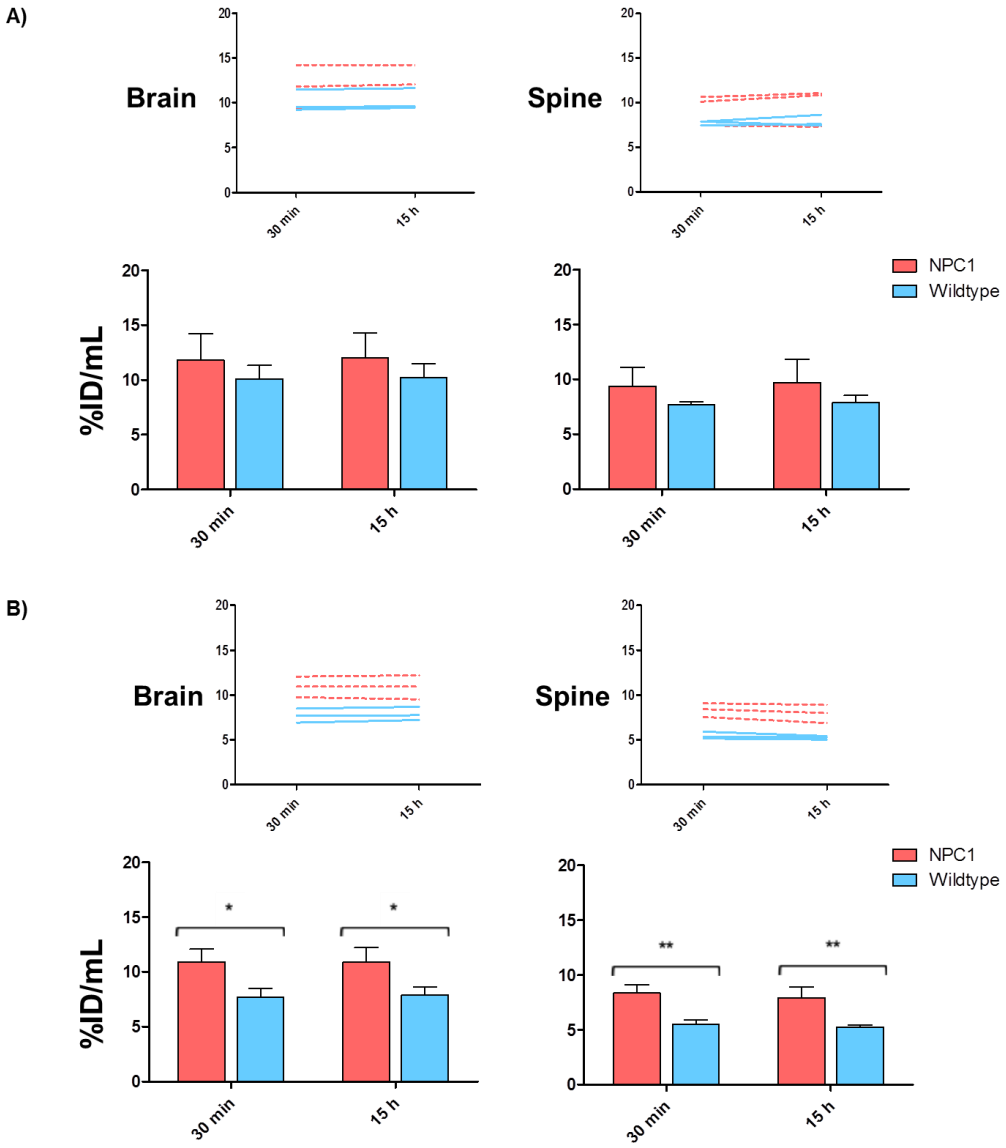

Figure 5.5: *In vivo* brain (left) and spine (right) concentration of ^{64}Cu (expressed as %ID/mL) in 6- (**A**) and 9-week-old (**B**) NPC1 knockout mice and age-matched controls, as measured by PET ROI analysis. Time-activity curves illustrating clearance of ^{64}Cu radioactivity over time for each individual mouse are shown at the top of each bar chart. NPC1$^{-/-}$ transgenic mice exhibited significantly higher ^{64}Cu concentration in the brain and spine at all imaging time-points than controls. Statistically significant differences from healthy controls are indicated by * ($p<0.05$) and ** ($p<0.01$). Data are mean (n=3/group) ± SD.

Two-way ANOVA analysis demonstrated a significant group effect on brain ^{64}Cu concentration in 9-week-old NPC1 knockout mice and wildtype controls ($F_{1,4}$ = 13.54, p = 0.0212). Post-hoc tests indicated significantly higher ^{64}Cu accumulation in the brains of NPC1$^{-/-}$ transgenic mice compared to their wildtype littermates at 30 min (10.92 ± 0.94 %ID/mL vs. 7.71 ± 0.64 %ID/mL, $p<0.05$) and 15 h (10.89 ± 1.10 %ID/mL vs. 7.89 ± 0.61 %ID/mL, $p<0.05$) post-administration of ^{64}Cu-GTSM. Statistical analysis also revealed significant effects of group ($F_{1,4}$ = 26.46, p =

0.0068) and time ($F_{1,4}$ = 10.15, p = 0.0334) on spine ^{64}Cu concentration in 9-week-old NPC1$^{-/-}$ mice and wildtype controls. NPC1 knockout mice exhibited significantly higher ^{64}Cu accumulation in the spinal cord than their wildtype littermates at all imaging time-points (30 min: 8.35 ± 0.76 %ID/mL vs. 5.48 ± 0.40 %ID/mL, p<0.01; 15 h: 7.93 ± 1.02 %ID/mL vs. 5.25 ± 0.19 %ID/mL, p<0.01).

These significant differences in brain and spine ^{64}Cu accumulation between the two animal groups result mainly from an age-dependent decrease in ^{64}Cu concentration in these organs in wildtype mice. Two-way ANOVA analysis indicated significant effects of age on brain ($F_{1,4}$ = 8.256, p = 0.0453) and spine ($F_{1,4}$ = 77.34, p = 0.0009) ^{64}Cu concentration in 6- and 9-week-old wildtype controls. Post-hoc evaluation showed significantly higher ^{64}Cu concentration in the brain (30 min: 10.11 ± 0.99 %ID/mL vs. 7.71 ± 0.64 %ID/mL, p<0.05; 15 h: 10.25 ± 0.99 %ID/mL vs. 7.89 ± 0.61 %ID/mL, p<0.05) and spinal cord (30 min: 7.73 ± 0.25 %ID/mL vs. 5.48 ± 0.40 %ID/mL, p<0.001; 15 h: 7.90 ± 0.65 %ID/mL vs. 5.25 ± 0.19 %ID/mL, p<0.001) of 6-week-old wildtype mice compared to their older counterparts at all imaging time-points. Although an age-dependent reduction in ^{64}Cu concentration was also observed in NPC1 knockout mice, this trend did not reach statistical significance.

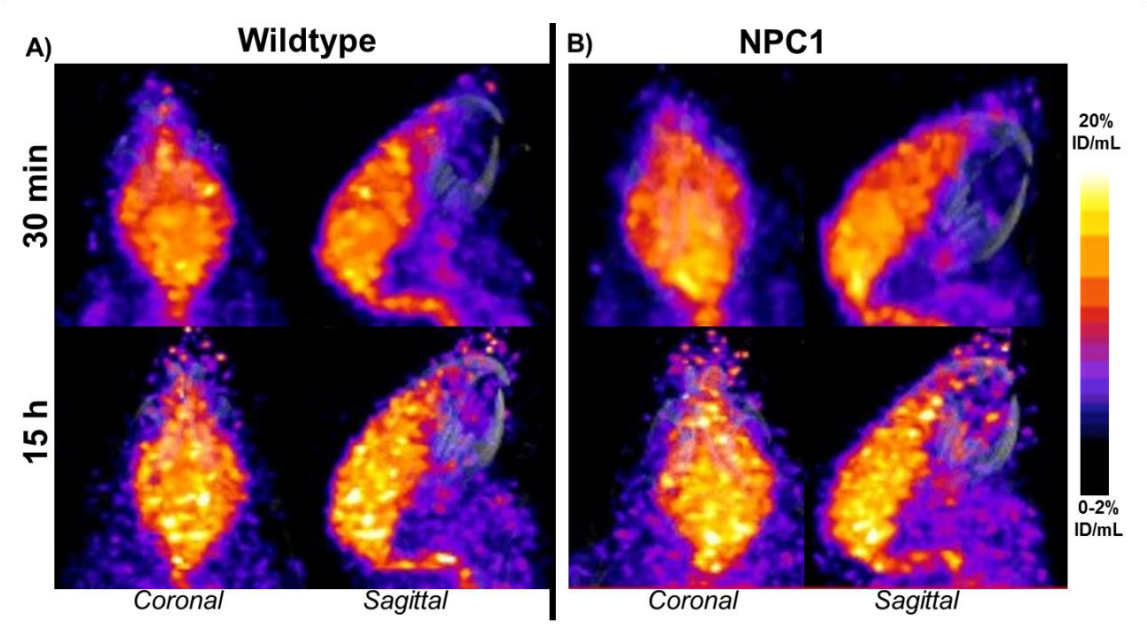

Figure 5.6: Representative coronal and sagittal section PET/CT MIP images illustrating ^{64}Cu distribution in the brains of 6-week-old wildtype controls (**A**) and age-matched NPC1 knockout mice (**B**) at 30 min (top) and 15 h (bottom) post-injection of ^{64}Cu-GTSM. Brain distribution of ^{64}Cu appeared relatively homogenous at 30 min post-injection of the tracer but became slightly more heterogeneous over time in both animal groups. All MIPs were scaled to 0-2 %ID/mL (min) and 20 %ID/mL (max).

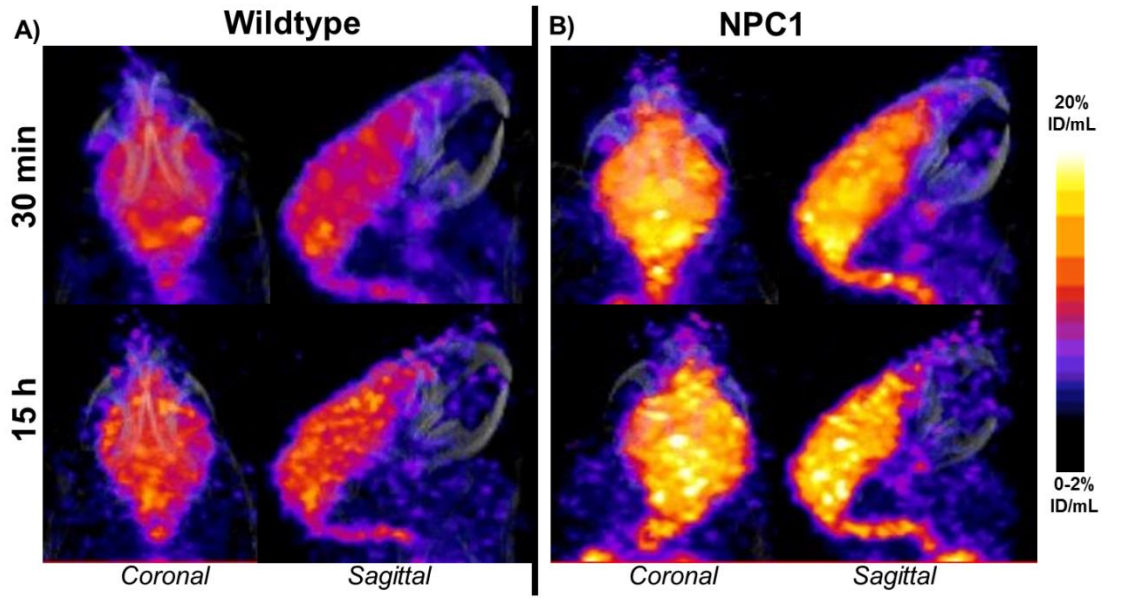

Figure 5.7: Representative coronal and sagittal section PET/CT MIP images showing the distribution of ^{64}Cu in the brains of 9-week-old wildtype controls (**A**) and age-matched NPC1 knockout mice (**B**) at 30 min (top) and 15 h (bottom) post-injection of ^{64}Cu-GTSM. NPC1 knockout mice exhibited higher brain ^{64}Cu accumulation than their wildtype littermates at all imaging time-points. The heterogeneity of the brain ^{64}Cu signal seemed to increase from 30 min to 15 h after injection in both mouse groups. All MIPs were scaled to 0-2 %ID/mL (min) and 20 %ID/mL (max).

Figures 5.6 and 5.7 depict the distribution of ^{64}Cu in the brains of 6- and 9-week-old NPC1$^{-/-}$ transgenic mice and age-matched controls at 30 min and 15 h post-injection of the tracer. Brain distribution of ^{64}Cu appeared relatively homogeneous at 30 min after injection in both 6-week-old NPC1$^{-/-}$ and wildtype mice but became slightly more heterogeneous over time in both groups. In the older mouse groups, ^{64}Cu was taken up in all brain regions at 30 min post-injection of the tracer but seemed to accumulate more prominently around the medulla. From 30 min to 15 h post-injection, the heterogeneity of the brain PET signal appeared to increase in both 9-week-old NPC1 knockout mice and wildtype controls.

Due to the low amount of activity injected and limited spatial resolution of the PET scanner, the visualisation of the regional accumulation of ^{64}Cu in the brains of NPC1$^{-/-}$ transgenic mice and wildtype controls proved difficult. To evaluate the distribution of ^{64}Cu in the brain in a functional context, our PET/CT datasets were analysed using a 3D mouse brain atlas. Two-way ANOVA analysis demonstrated only a significant effect of interaction ($F_{1,4}$ = 3.841, p = 0.0002) on brain regional concentration of ^{64}Cu in 6-week-old NPC1 knockout mice and age-matched controls at 30 min post-injection of the tracer, but did not reveal any significant differences in ^{64}Cu accumulation in specific regions between the groups at either imaging time-point (Figure 5.8).

The concentration of ^{64}Cu in all brain regions was found to be generally higher in NPC1$^{-/-}$ transgenic mice compared to age-matched controls at both 30 min and 15 h post-injection of ^{64}Cu-GTSM. The thalamus and midbrain were found to accumulate more radiocopper than the rest of brain regions in both animal groups.

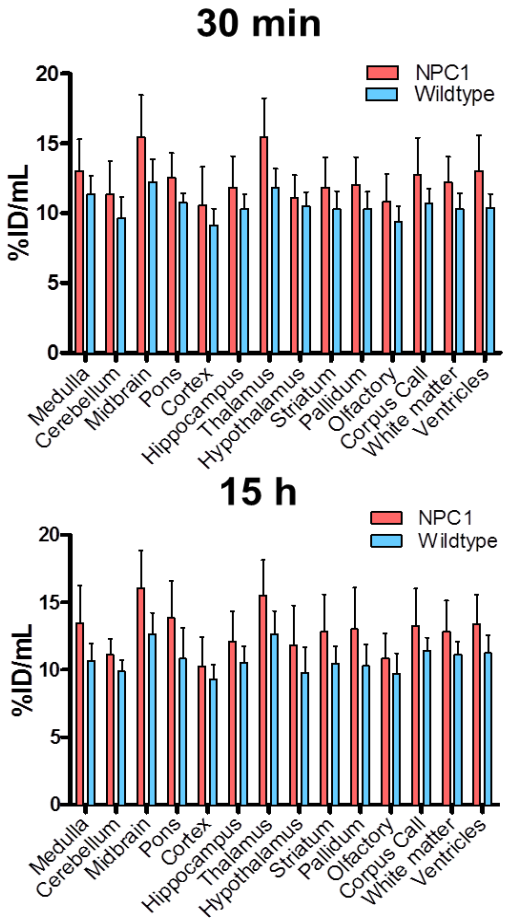

Figure 5.8: Regional brain distribution of ^{64}Cu in 6-week-old NPC1$^{-/-}$ transgenic mice and age-matched controls at 30 min (top) and 15 h (bottom) post-injection of ^{64}Cu-GTSM. No significant differences in brain regional ^{64}Cu concentration between the two groups were detected. Data are mean (n = 3/group) ± SD.

Significant effects of group, region and group-by-region interaction on brain regional accumulation of ^{64}Cu were measured in 9-week-old NPC1 knockout mice and age-matched controls at both 30 min (group: $F_{1,4}$ = 16.38, p = 0.0155; region: $F_{1,4}$ = 32.91, p<0.0001; interaction: $F_{1,4}$ = 3.840, p = 0.0002) and 15 h (group: $F_{1,4}$ = 15.17, p = 0.0176; region: $F_{1,4}$ = 41.48, p<0.0001; interaction: $F_{1,4}$ = 5.274, p<0.0001) post-injection of the tracer. Contrary to the findings in younger mice, post-hoc evaluation revealed significant differences in ^{64}Cu concentration in specific brain regions between the two animal groups at both imaging time-points (Figure 5.9). At 30 min after injection, NPC1 knockout mice exhibited significantly greater ^{64}Cu levels than their wildtype littermates in the medulla (p<0.05), cerebellum (p<0.05), midbrain (p<0.001), pons (p<0.01), hippocampus (p<0.05), thalamus (p<0.001), hypothalamus (p<0.01),

striatum (p<0.01), pallidum (p<0.01), olfactory bulb (p<0.05), corpus callosum (p<0.01), white matter (p<0.01) and ventricles (p<0.01). The NPC1$^{-/-}$ group showed significantly higher ^{64}Cu concentration than controls in the medulla (p<0.01), midbrain (p<0.001), pons (p<0.01), hippocampus (p<0.05), thalamus (p<0.001), hypothalamus (p<0.001), striatum (p<0.01), pallidum (p<0.01), corpus callosum (p<0.05), white matter (p<0.01) and ventricles (p<0.05) at 15 h post-injection of ^{64}Cu-GTSM.

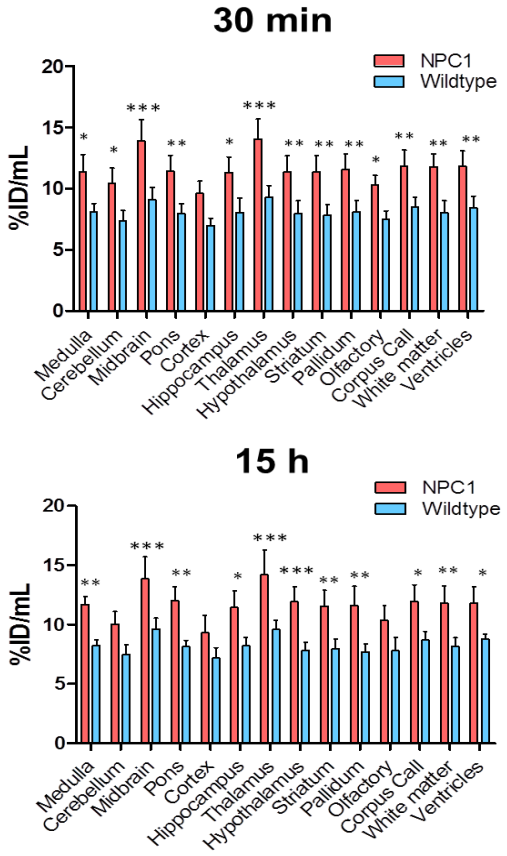

Figure 5.9: Regional brain distribution of ^{64}Cu in 9-week-old NPC1$^{-/-}$ transgenic mice and age-matched controls at 30 min (top) and 15 h (bottom) post-injection of ^{64}Cu-GTSM. Statistically significant differences from healthy controls are indicated by * (p<0.05), ** (p<0.01) and *** (p<0.001). Data are mean (n = 3/group) ± SD.

Moreover, two-way ANOVA analysis demonstrated significant effects of age ($F_{1,4}$ = 8.323, p = 0.0448), region ($F_{1,4}$ = 33.15, p<0.0001) and interaction ($F_{1,4}$ = 2.599, p = 0.0074) on brain regional concentration of ^{64}Cu in wildtype mice at 30 min post-injection of the tracer. Post-hoc tests indicated significantly higher ^{64}Cu accumulation in the medulla (p<0.01), midbrain (0<0.05) and pons (p<0.05) of 6-week-old controls when compared to their older counterparts. Significant effects of age ($F_{1,4}$ = 8.277, p = 0.0451) and region ($F_{1,4}$ = 20.23, p<0.0001) on brain regional ^{64}Cu uptake were also detected in the wildtype groups at late imaging time-points. At 15 h after injection of ^{64}Cu-GTSM, a significant reduction in ^{64}Cu concentration was measured in the

midbrain ($p<0.05$), thalamus ($p<0.05$) and white matter ($p<0.05$) of 9-week-old wildtype mice relative to young controls. On the other hand, no significant differences in brain regional ^{64}Cu accumulation as measured by atlas-based quantification were detected between 6- and 9-week-old NPC1$^{-/-}$ knockout mice.

5.4.2 *Ex vivo* biodistribution

At the end of the imaging process, the biodistribution of ^{64}Cu in NPC1 knockout mice and wildtype controls was evaluated via *ex vivo* gamma-counting of explanted organs. In this study, *ex vivo* tissue counting was only performed in 9-week-old NPC1 knockout mice and wildtype controls since their younger counterparts were kept alive for a follow-up imaging session, which could not be conducted in the end due to lack of $^{64}CuCl_2$ supply.

Figure 5.10 illustrates the *ex vivo* biodistribution of ^{64}Cu in 9-week-old NPC1 knockout mice and age-matched controls at 15 h post-injection of ^{64}Cu-GTSM. ^{64}Cu radioactivity was found to accumulate predominantly in the lungs, liver and intestines and to a lesser extent in the heart and brain in both animal groups.

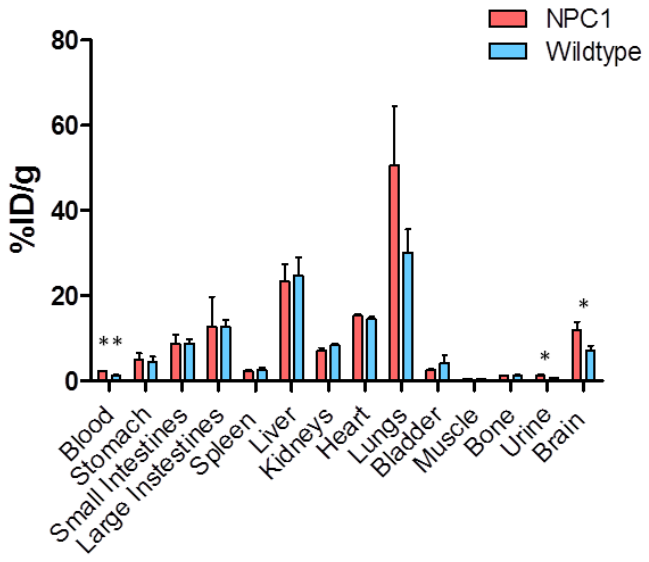

Figure 5.10: Tissue biodistribution of ^{64}Cu in 9-week-old NPC1$^{-/-}$ transgenic mice and age-matched controls at 15 h post-injection of ^{64}Cu-GTSM. Statistically significant differences from controls are indicated by * ($p<0.05$) and ** ($p<0.01$). Data are mean (n = 3/group) ± SD.

Interestingly, statistical analysis demonstrated significantly greater ^{64}Cu concentration in the blood of 9-week-old NPC1 knockout mice compared to age-matched wildtype controls (2.25 ± 0.10 %ID/mL vs. 1.38 ± 0.11 %ID/mL, $p<0.01$). The NPC1$^{-/-}$ group also showed significantly

higher ^{64}Cu concentration in urine than their wildtype littermates (1.29 ± 0.2 %ID/mL vs. 0.64 ± 0.10 %ID/mL, $p<0.05$). Furthermore, the concentration of ^{64}Cu in the brain was found to be significantly higher in NPC1$^{-/-}$ transgenic mice relative to age-matched controls (11.86 ± 1.69 %ID/mL vs. 7.03 ± 1 %ID/mL, $p<0.05$), which was consistent with our PET quantification results. Brain ^{64}Cu %ID/g values measured by *ex vivo* counting exhibited a strong correlation (R^2 = 0.7461) with whole-brain ^{64}Cu concentration estimated by PET ROI analysis (Figure 5.11).

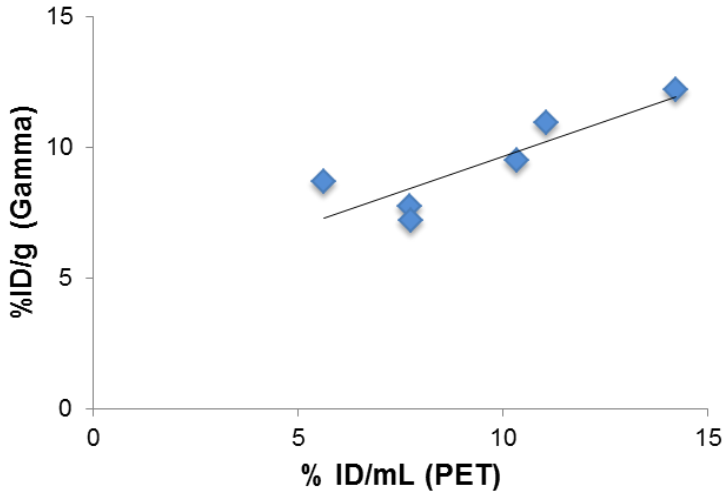

Figure 5.11: Comparison of whole-brain ^{64}Cu concentration values as measured by PET ROI analysis and *ex vivo* gamma-counting at 15 h post-injection of ^{64}Cu-GTSM in 9-week-old NPC1$^{-/-}$ transgenic mice and age-matched controls. A strong correlation was found between the two parameters (R^2 = 0.7461). All NPC1$^{-/-}$ (n = 3) and wildtype (n = 3) mice were included in the correlation.

5.4.3 *Ex vivo* brain autoradiography

In order to generate high-resolution maps of the distribution of ^{64}Cu within brain tissue, sagittal brain sections of NPC1 knockout mice and wildtype controls sacrificed at 15 h post-injection of ^{64}Cu-GTSM were imaged by phosphor imaging autoradiography. Similar to gamma-counting, *ex vivo* autoradiography could only be performed in 9-week-old NPC1$^{-/-}$ transgenic mice and age-matched controls since 6-week-old mice were kept alive for a follow-up imaging study.

Figure 5.12 shows the regional distribution of ^{64}Cu in representative sagittal brain slices of NPC1 knockout mice and wildtype controls at 15 h after injection of the tracer as measured by autoradiography. *Ex vivo* autoradiographs reflect globally higher accumulation of ^{64}Cu in the brains of 9-week-old NPC1 knockout mice compared to age-matched controls, depicted also by PET imaging. The most prominent radioactive hotspots in the NPC1$^{-/-}$ brain autoradiographs were found in the midbrain, thalamus, pons, cerebellum and medulla, consistent with the results of atlas-based PET quantification. The distribution of ^{64}Cu in wildtype brain tissue was found to

be more homogeneous compared to that in the NPC1$^{-/-}$ group, although distinct accumulation of ^{64}Cu in the thalamic area could also be observed.

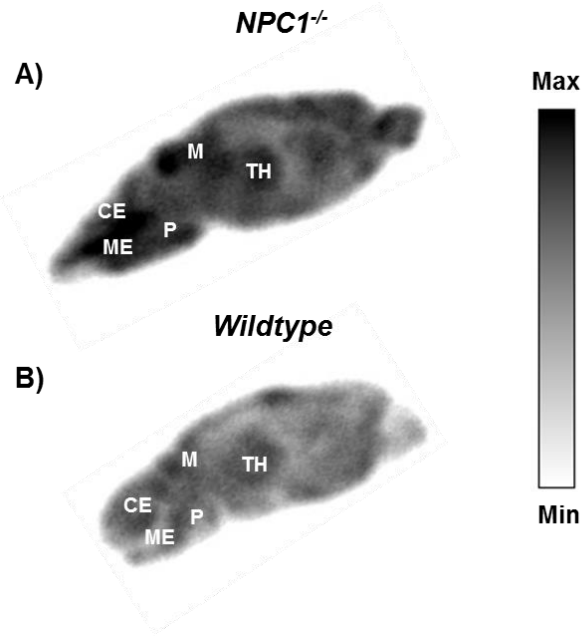

Figure 5.12: *Ex vivo* autoradiographs from representative sagittal brain sections of 9-week-old NPC1$^{-/-}$ (top) and control (bottom) mice sacrificed at 15 h post-injection of ^{64}Cu-GTSM. *Ex vivo* autoradiography demonstrated higher brain ^{64}Cu accumulation and more prominent ^{64}Cu hotspots in NPC1 knockout mice compared to controls. The main radioactive hotspots in the NPC1$^{-/-}$ brain autoradiographs were located in the thalamus, midbrain, cerebellum, medulla and pons areas. TH = thalamus; M = midbrain; ME = medulla; P = pons; CE = cerebellum.

5.5 DISCUSSION

Growing evidence has suggested that the metabolism of several trace metals, including copper, is altered in NPC1 disease (321-324, 463-465). The characterisation of trace metal abnormalities in NPC1 disease is essential to understand their impact on the severity and progression of the disorder and to determine whether they provide any added diagnostic value to the existing NPC1 biomarkers. Hence, in this study, we have studied *in vivo* copper trafficking in a mouse model of NPC1 disease at presymptomatic and symptomatic stages of the disorder by ^{64}Cu-GTSM-PET in order to identify any measurable alterations that may be associated with the pathology.

In the present study, we have focused on the delineation of copper trafficking within the CNS since transition metal imbalance has been linked to enhanced oxidative stress in NPC1 disease and is therefore thought to contribute heavily to the neurodegenerative process characteristic of this disorder (320, 324, 458). For this reason, we used the Cu-BTSC complex ^{64}Cu-GTSM as a

vehicle to deliver radioactive copper into the CNS and subsequently monitor its trafficking. The efficacy of ^{64}Cu-GTSM to transport radiocopper into the brain was demonstrated in the third chapter of this dissertation. Nevertheless, additional studies should be performed using ionic radiocopper in order to investigate active transport of dietary copper salts at the whole-body level in NPC1 disease.

The chosen route for ^{64}Cu-GTSM administration was tail vein injection, which bypasses the absorption phase of endogenous copper metabolism but facilitates the rapid deposition of radiocopper within the CNS. However, the fate of orally administered radiocopper should also be evaluated by PET in future studies in order to detect any potential abnormalities in the gastrointestinal absorption of copper that might be associated with NPC1 disease.

As expected from a previous study (see Chapter III), ^{64}Cu-GTSM rapidly released radiocopper in all major organs after injection, including heart, lungs, liver, intestines, kidneys and brain. At 15 h post-injection of the tracer, ^{64}Cu radioactivity was found to decrease in the heart, lungs and kidneys, and to accumulate in the liver and intestines, probably reflecting the excretion of radiocopper via the biliary system. Despite previous studies reporting increased copper content in the liver of NPC1 deficient mice compared to control animals, no significant differences in hepatic ^{64}Cu concentration were found between NPC1 and wildtype groups at either 6 or 9 weeks of age (320-322). This discrepancy might be explained on the basis of differences between long-term and short-term copper biodistribution in this mouse model of NPC1 disease. Increased copper levels in the liver of NPC1 knockout mice might result from prolonged accumulation of dietary copper in this organ, and might therefore not be measurable by PET, due to its limited temporal range.

As previously observed (see Chapter III), both brain and spine showed surprisingly high radiocopper sequestration capacities. Slow clearance of ^{64}Cu radioactivity from brain and spinal cord compared to other tissues might be caused by a particularly high metabolic demand for copper of the CNS and/or less active copper efflux mechanisms.

PET image analysis revealed no significant differences in whole-brain and spine ^{64}Cu concentration between presymptomatic NPC1 knockout mice and age-matched controls. Conversely, at 9 weeks of age, NPC1$^{-/-}$ transgenic mice exhibited significantly higher ^{64}Cu concentration than wildtype controls at both 30 min and 15 h post-injection of ^{64}Cu-GTSM. Interestingly, these differences in brain and spine ^{64}Cu concentration between the two animal groups were found to result from an age-dependent decrease in ^{64}Cu concentration in these organs in wildtype mice. Due to the low statistical power of this study, these results need to be interpreted cautiously. The exact role of the NPC1 protein in copper metabolism has not yet been defined and consequently the impact of its deletion on brain copper trafficking is unknown. Yanagimoto *et al.* demonstrated that NPC1 mediated copper transport from late endosomes to the secretory compartment for its subsequent incorporation into ceruloplasmin in cultured hepatocytes (326, 327). A potential role for NPC1 in the metallation and secretion of ceruloplasmin was further supported by Arguello *et al.*, who reported higher copper and lower iron content along with increased ceruloplasmin, MT-1 and transferrin receptor gene expression in the liver of NPC1 deficient mice compared to controls (322). However, the lack of benefit of chelation therapy on neurological function in NPC1 knockout mice together with reduced cerebral copper content in this model seem to suggest a different role for the NPC1 protein in brain copper metabolism (321). In this context, increased brain ^{64}Cu retention in symptomatic NPC1$^{-/-}$ transgenic mice could also be driven by a regulatory mechanism aiming to compensate for the low cerebral copper levels previously reported for this model in an effort to restore copper-dependent antioxidant enzyme activity as a response to oxidative stress (321).

Atlas-based quantification revealed no significant differences in brain regional ^{64}Cu concentration between 6-week-old NPC1 deficient mice and wildtype controls but did show significantly increased ^{64}Cu accumulation in multiple brain regions in symptomatic NPC1 knockout mice compared to age-matched controls. Whether these differences in brain regional ^{64}Cu concentration are a result of localised NPC1 disease or globally higher ^{64}Cu accumulation in the NPC1 model is not known. Considering the limitations of atlas-based quantification (e.g partial volume effect, imperfect matching between atlas regions and brain structures), these results should be considered orientative rather than definitive. Enhanced brain regional ^{64}Cu concentration in symptomatic NPC1 knockout mice might arise from an increased metabolic

demand for copper in these regions associated with the disease, higher regional BBB permeability or increased blood vessel density in this model.

Similar to PET quantification, *ex vivo* brain autoradiography demonstrated globally higher accumulation of ^{64}Cu in the brains of 9-week-old NPC1 deficient mice compared to age-matched controls. Prominent ^{64}Cu hotspots were observed in the midbrain, thalamus, medulla, cerebellum and pons regions in the NPC1$^{-/-}$ brain autoradiographs, which was also consistent with our PET imaging results. The molecular mechanisms driving the accumulation of radiocopper in these regions remain to be elucidated. The cerebellum and brainstem structures (medulla, pons and midbrain) are the regions most affected by neurodegeneration in NPC1 disease (472). Neuronal loss and oxidative damage have also been documented in the thalamus of NPC1$^{-/-}$ transgenic mice (455, 471). Consequently, increased accumulation of ^{64}Cu in these regions might be driven by a regulatory mechanism aiming to enhance their antioxidant capacity to counteract oxidative stress. Alternatively, higher ^{64}Cu uptake could be highlighting a potential copper deficiency in these brain regions caused by increased intracellular cholesterol accumulation, since an inverse relationship between copper and cholesterol concentrations has been reported in animal studies (473-476). Reduced copper content has been measured in the cerebellum of NPC1 deficient mice but copper levels in the remaining brain regions have not been reported yet (321).

After imaging, the *ex vivo* biodistribution of ^{64}Cu in symptomatic NPC1 deficient mice and age-matched controls at 15 h post-injection of ^{64}Cu-GTSM was evaluated via gamma-counting of explanted organs. NPC1 knockout mice were found to exhibit significantly higher ^{64}Cu concentration in blood than their wildtype littermates. These results are in agreement with previous research revealing increased copper content in blood plasma in 7-week-old NPC1$^{-/-}$ transgenic mice compared to healthy controls (321, 324). It should be noted that elevated blood ^{64}Cu concentration might contribute to some extent to enhanced accumulation of ^{64}Cu in the brain and spinal cord of NPC1$^{-/-}$ transgenic mice. Elevation of plasma copper in symptomatic NPC1 knockout mice (7 weeks old) has been associated with an increase in copper-bound holoceruloplasmin levels and ceruloplasmin oxidase activity, which might indicate a higher rate of synthesis/secretion of this protein in this NPC1 model (321, 324). Additional studies need to

be performed to determine whether plasma ^{64}Cu is inserted into ceruloplasmin or bound to other plasma proteins (e.g. albumin, transcuprein), whether increased blood ^{64}Cu concentration in NPC1 knockout mice can be detected at earlier time-points after injection of the tracer and stages of the disease, and whether this increase can also be measured in human NPC1 subjects. The relationship between blood copper concentration and disease severity and progression also needs to be evaluated in order to determine the potential of this parameter as a diagnostic marker of NPC1 disease.

5.6 CONCLUSIONS

This study has further demonstrated the potential of ^{64}Cu-GTSM-PET as a tool to identify alterations in copper metabolism associated with disease processes, particularly within the CNS. The characterisation of copper metabolism abnormalities in NPC1 disease is essential to understand their effect on certain pathological features of the disorder, such as oxidative stress, which is a major contributor to neurodegeneration. In this study, PET imaging has been used for the first time to evaluate the real-time dynamics of copper trafficking in a mouse model of NPC1 disease in order to identify potential metabolic abnormalities that might have added value in the diagnosis of the disorder. ^{64}Cu-GTSM-PET revealed significantly increased ^{64}Cu concentration in the brain and spine of symptomatic NPC1 deficient mice compared to healthy controls at both 30 min and 15 h post-injection of the tracer. Furthermore, atlas-based PET quantification indicated significant differences in brain regional ^{64}Cu accumulation between these two groups of mice. Symptomatic NPC1 knockout mice were additionally found to exhibit significantly higher ^{64}Cu concentration in blood than their wildtype littermates at late time-points after injection. Despite the low statistical power of this study, the origin of these metabolic abnormalities along with their relationship with disease severity and progression merit further investigation. Due to the inability of NPC1 mouse models to mimic the phenotypic variabiliaty of human NPC1 disease, PET imaging of copper trafficking should additionally be performed in human subjects in order to delineate any potential abnormalities that could be used to assess the status of the disease and even monitor response to treatment.

Chapter 6- Asymmetrical copper bis(thiosemicarbazone) complexes for PET: synthesis and characterisation

6.1 AIMS

In this chapter, we aimed to synthesise and characterise a series of new asymmetrical Cu-BTSCs for potential use in molecular imaging applications, including the measurement of copper trafficking processes. The redox potential and lipophilicity of these complexes were determined in order to provide early insight into their potential biological behaviour.

6.2 INTRODUCTION

Cu-BTSCs are a versatile family of copper (II) complexes with a wide range of pharmacological properties, including antineoplastic, antimicrobial and neuroprotective activities (288, 477-479). The most attractive feature of these complexes is that their biological behaviour can be tuned by structural modification of their ligand scaffold. For example, the addition of alkyl groups to the diimine backbone of the ligand has been reported to decrease the redox potential of the resulting copper complexes, making them less susceptible to bioreduction and metal-ligand dissociation. On the other hand, alkylation of the terminal amine groups of the ligand has been shown to increase the lipophilicity of the complexes, subsequently influencing their cell permeability, plasma protein binding and biokinetics (142, 166).

The tunability of the physicochemical properties of Cu-BTSCs via ligand structure modification offers the possibility to control the conditions under which these complexes undergo bioreduction and metal-ligand dissociation for a variety of diagnostic imaging applications. This was exploited in the third chapter of this dissertation to provide a BBB-permeable complex capable of releasing its copper payload nonselectively into cells by bioreduction (Cu-GTSM). The feasibility of using Cu-BTSC complexes as molecular imaging agents was first demonstrated by Green *et al.*, who unveiled the potential of Cu-PTSM to delineate regional blood flow. This complex, with only one alkyl group on its backbone, has a relatively high redox

potential and is therefore prone to bioreduction and metal release in all cellular environments. The intracellular reduction and metal-ligand dissociation of Cu-PTSM have been found to be so rapid that the uptake of the tracer is thought to be almost entirely dependent on blood flow. Green and co-workers reported rapid blood clearance and high brain and heart accumulation of ^{67}Cu-PTSM as well as an excellent correlation between tracer uptake and regional blood flow (assessed using [^{125}I] iodoantipyrine) in a gerbil stroke model, demonstrating the potential utility of Cu-PTSM-PET for the assessment of cerebral and myocardial perfusion (168). Cu-PTSM has shown promise in identifying perfusion abnormalities in a small clinical study performed on patients with occlusive coronary artery disease, and remains so far the Cu-BTSC gold-standard for imaging regional blood flow (174).

The effect of backbone alkylation on bioreduction and metal-ligand dissociation has also been exploited to develop Cu-BTSC radiotracers capable of releasing their copper payload selectively into hypoxic cells. This is the case of the prototype hypoxia-selective complex Cu-ATSM, which differs from Cu-PTSM only by an additional backbone methyl group. Due to its lower Cu (II/I) reduction potential, bioreduction of Cu-ATSM is harder compared to that of Cu-PTSM and the complex is able to diffuse out of the cell under normoxic conditions before reduction and dissociation occur. However, the complex gets trapped by bioreduction in more reducing environments, providing a means for delineating and quantifying hypoxia within tissues. The hypoxia selectivity of Cu-ATSM has been repeatedly demonstrated both *in vitro* and *in vivo* and the tracer has been shown to be useful in depicting hypoxic tissue and predicting response to therapy in a small number of cancer clinical trials (89, 142, 147, 158, 159, 166).

Nevertheless, despite initial promise, both Cu-PTSM- and Cu-ATSM-PET suffer from major drawbacks that significantly hamper their clinical use. Cu-PTSM has been found to exhibit significant interspecies variability in the strength of its binding to serum albumin, which results in the underestimation of regional blood flow in humans (175, 412). On the other hand, the cellular uptake of Cu-ATSM has been shown to be hypoxia-selective only in certain types of tumours, which seems to suggest that other factors besides tissue hypoxia might contribute to the retention mechanism of this tracer *in vivo* (160). Furthermore, the *in vivo* stability of Cu-ATSM has been found to be poor, as evidenced by the similar biodistribution profiles obtained for ^{64}Cu-

ATSM and ^{64}Cu-acetate in tumour-bearing mice at early and late imaging time-points (480). Finally, although Cu-ATSM may be suitable to delineate tumour hypoxia, its hypoxia-selective threshold has been shown to be too low to identify hypoxically compromised but salvageable myocardium underlying chronic cardiovascular disease (481).

Because to these limitations as well as the possibility to use Cu-BTSCs for new imaging applications (e.g. imaging of copper trafficking/ cerebral oxidative stress), there is growing interest in developing new Cu-BTSC radiotracers with improved imaging properties for clinical use. For this reason, in collaboration with the University of Kent (Dr Oliver C. Brown and Prof Michael Went), we have synthesised and characterised a library of new asymmetrical Cu-BTSC complexes with a variety of alkylation patterns. Asymmetrical BTSC ligands, although harder to synthesise and purify, offer greater structural diversity than symmetrical BTSCs and therefore may facilitate the fine-tuning of the physicochemical properties of the Cu-BTSC complexes needed for specific imaging applications (482). The measurement of the redox potential and lipophilicity of the new Cu-BTSC complexes was included as part of their characterisation as these two properties are the most influential in determining their biodistribution and selectivity, and the most tunable by regional alkylation. However, it should be noted that additional physicochemical parameters (acid dissociation coefficient [pK_a], dissociation constant [K_d]) need to be determined in order to fully define the biological behaviour of the new Cu-BTSC complexes as well as their potential as molecular imaging agents.

6.3 MATERIALS AND METHODS

6.3.1 Chemistry

6.3.1.1 General directions

All reagents were purchased from Sigma-Aldrich, Alfa Aesar, Interlink Scientific Services and VWR International Ltd. and were used without further purification, unless otherwise stated. NMR spectra were recorded on a Bruker Ultrashield 400WB PLUS 9.4 T spectrometer (^{1}H NMR at 400 MHz). All chemical shifts were referenced to residual solvent peaks and are quoted in ppm relative to tetramethylsilane. High-performance liquid chromatography (HPLC) was performed

using an Agilent Technologies 1200 series unit with a C_{18} column and UV/VIS detection at 254 nm and a gradient mobile phase consisting of water + 0.1 % (v/v) trifluoroacetic acid (TFA) (A) and acetonitrile + 0.1 % (v/v) TFA (B) (0 min: 95% A / 5% B; 15 min: 5% A / 95% B; 20 min: 5% A / 95% B; 25 min: 95% A / 5% B; 30 min: 95% A / 5% B). Mass spectra were recorded on an Agilent Technologies 6520 Accurate-Mass Q-TOF LC-MS mass spectrometer using the positive ion electrospray technique (ESI^+ MS). Thin layer chromatography (TLC) was performed using MERCK 60 F_{254} silica gel TLC plates as the stationary phase and ethyl acetate as the mobile phase.

6.3.1.2 Synthesis of BTSC ligands

Table 6.1: Structure of BTSC ligands

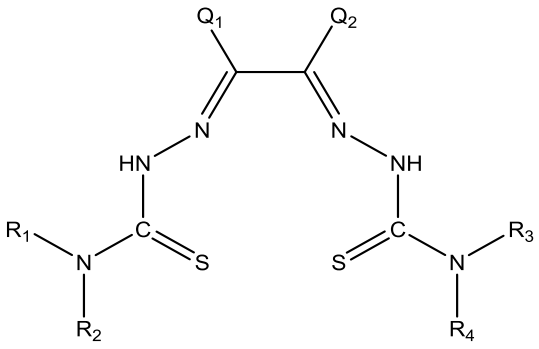

Ligand	R_1	R_2	Q_1	Q_2	R_3	R_4	New?
1	CH_3	H	H	H	CH_3	H	No (142, 155, 365)
2	C_2H_5	H	H	H	C_2H_5	H	No (365)
3	CH_3	H	CH_3	H	CH_3	CH_3	Yes
4	C_2H_5	H	CH_3	H	CH_3	H	Yes
5	C_6H_5	H	CH_3	H	C_2H_5	H	Yes
6	CH_3	H	CH_3	H	C_6H_5	H	Yes

Ligand	R_1	R_2	Q_1	Q_2	R_3	R_4	New?
7	C_6H_5	H	CH_3	H	CH_3	H	Yes
8	C_2H_5	H	CH_3	H	CH_3	CH_3	Yes
9	C_2H_5	H	CH_3	H	C_6H_5	H	Yes
10	CH_3	H	CH_3	CH_3	CH_3	H	No (142, 304, 307)
11	C_2H_5	H	CH_3	CH_3	C_2H_5	H	No (143, 146)
12	CH_3	H	CH_3	CH_3	H	H	Yes
13	CH_3	H	CH_3	CH_3	CH_3	CH_3	No (116)
14	H	H	CH_3	CH_3	CH_3	CH_3	Yes
15	H	H	CH_3	C_2H_5	H	H	No (142, 143, 483)
16	H	H	CH_3	C_2H_5	CH_3	H	Yes
17	C_2H_5	H	CH_3	C_2H_5	H	H	Yes
18	H	H	CH_3	C_2H_5	C_2H_5	H	Yes
19	CH_3	H	CH_3	C_2H_5	H	H	Yes
20	H	H	CH_3	C_2H_5	CH_3	CH_3	Yes

Symmetric BTSC ligands (**1**, **2**, **10** and **11**) were synthesised using a common protocol, exemplified by the method for the preparation of glyoxalbis(*N*^{4}-methyl-3-thiosemicarbazone) (**1**) described in the third chapter of this dissertation (see section 3.3.1) (142, 406). **1**: IR ν_{max}/cm^{-1}: 3317, 3148, 3000, 2328, 1512, 1248, 1083, 914; ^{1}H NMR (400 MHz, DMSO-d$_6$) δ/ppm 2.965 (6H, d, 2 x NHC*H*$_3$, $^3J_{H\text{-}H}$ = 4 Hz), 7.728 (2H, s, 2 x *H*(C=)NNHC(=S)), 8.505 (2H, q, 2 x C(=S)N*H*CH$_3$ $^3J_{H\text{-}H}$ = 4 Hz), 11.770 (2H, s, 2 x H(C=)NN*H*C(=S)); HPLC: R_t = 6.15 min. ESI$^+$ MS: m/z for $[C_6H_{12}N_6S_2 + H]^+$ = 233.0638 (calc.), 233.0671 (found). **2**: IR ν_{max}/cm^{-1}: 3370, 3133, 2972, 1743, 1516, 1220, 909, 807, 623; ^{1}H NMR (400 MHz, DMSO-d$_6$) δ/ppm 1.109 (6H, t, 2 x

CH_2CH_3, $^3J_{H-H}$ = 4 Hz), 3.540 (4H, m, 2 x $NHCH_2CH_3$, $^3J_{H-H}$ = 4 Hz), 7.730 (2H, s, 2 x *H*(C=)NNHC(=S)), 8.545 (2H, t, 2 x C(=S)N*H*CH_2CH_3 $^3J_{H-H}$ = 4 Hz), 11.720 (2H, s, 2 x H(C=)NN*H*C(=S)); HPLC: R_t = 7.59 min. **10**: IR ν_{max}/cm^{-1}: 3359, 3243, 2953,1543, 1489, 1224, 1130, 1074, 817, 554. ^{1}H NMR (400MHz, DMSO-d_6) δ/ppm: 2.21 (6H, s, 2 x C*H*$_3$(C=)NNH), 3.03 (6H, d, 2 x C*H*$_3$NH, $^3J_{H-H}$ = 4 Hz), 8.37 (2H, m, 2 x CH_3N*H*, $^3J_{H-H}$ = 4 Hz), 10.21 (2H, s, H(C=)NN*H*C(=S)). HPLC: R_t = 8.46 min; ESI$^+$ MS: m/z for [$C_8H_{16}N_6S_2$ + H^+]$^+$= 261.0951 (calc.), 261.0900 (found). **11**: ^{1}H NMR (400MHz, DMSO-d_6) δ/ppm: 1.14 (6H, t, 2 x CH_2CH_3, $^3J_{H-H}$ = 4 Hz), 2.21 (6H, s, 2 x C*H*$_3$(C=)NNH)), 3.59 (4H, m, 2 x CH_3CH_2NH, $^3J_{H-H}$ = 4 Hz), 8.42 (2H, t, 2 x C(=S)N*H*CH_2CH_3, $^3J_{H-H}$ = 4 Hz), 10.15 (2H, s, 2 x H(C=)NN*H*C(=S)); ESI$^+$ MS: m/z for [$C_{10}H_{20}N_6S_2$ + H^+]$^+$ = 289.1264 (calc.), 289.1248 (found).

Asymmetric BTSC ligands **12** and **13** were prepared using a previously reported procedure, illustrated by the following method for the synthesis of diacetyl-2-(4-*N*-methyl-3-thiosemicarbazone)-3-(3-*N*-amino-3-thiosemicarbazone) (**12**, Figure 6.1) (484). 2,3-butanedione (5.26 mL, 60 mmols) was dissolved in 100 mL of cold distilled water (0 °C) in a conical flask. Five drops of concentrated HCl (97 %) were added to the reaction mixture, followed by 4-methyl-3-thiosemicarbazide (3.45 g, 32.8 mmol). After stirring for 1 hour, the resulting suspension was filtered and the residue rinsed with water (3 x 100 mL), ethanol (3 x 50 mL) and diethyl ether (3 x 10 mL) and recrystallised from warm ethanol to afford pure mono-substituted-3-thiosemicarbazone intermediate (2.4 g, 43 %). Subsequently, this intermediate (0.80 g, 4.62 mmols) was added over 2 h in portions to a solution of thiosemicarbazide in methanol (0.44 g, 4.82 mmol) previously acidified with concentrated HCl. The reaction mixture was heated under reflux (~65 °C) for 5 h, during which a whitish suspension formed. After cooling down to room temperature, the solution was filtered under vacuum and the precipitate washed with ethanol (3 x 50 mL) and diethyl ether (3 x 10 mL). The resulting solid was then recrystallised from warm DMSO/water (50:50) to yield pure **12** (0.90 g, 79 %). **12**: IR ν_{max}/cm^{-1}: 3416, 3223, 3154, 1554, 1490, 1239, 1082, 826, 566; ^{1}H NMR (400 MHz, DMSO-d_6) δ/ppm: 2.17 (3H, s, C*H*$_3$(C=)NNH(C=S)(NH_2)), 2.21 (3H, s, C*H*$_3$(C=)NNH(C=S)$NHCH_3$)), 3.03 (3H, d, C*H*$_3$NHC(=S), $^3J_{H-H}$ = 4 Hz), 7.85 (2H, s, NH(C=S)N*H*$_2$), 8.39 (1H, m, C(=S)N*H*CH_3, $^3J_{H-H}$ = 4 Hz), 10.18 (1H, s, ((C=)NN*H*(C=S)NH_2), 10.23 (1H, s, ((C=)NN*H*(C=S)$NHCH_3$); HPLC: R_t = 6.48 min. **13**: IR ν_{max}/cm^{-1}: 3361, 3242, 1487, 1243, 1131, 1072, 551; ^{1}H NMR (400MHz, DMSO-d_6) δ/ppm: 2.15

(3H, s, C*H*$_3$(C=)NNH(C=S)N(CH$_3$)$_2$), 2.20 (3H, s, C*H*$_3$(C=)NNH(C=S)NHCH$_3$), 2.21 (6H, s, CH$_3$(C=)NNH(C=S)N(C*H*$_3$)$_2$), 3.03 (3H, d, CH$_3$(C=)NNH(C=S)NHC*H*$_3$, $^3J_{H\text{-}H}$ = 4 Hz), 8.39 (1H, m, CH$_3$(C=)NNH(C=S)N*H*CH$_3$, $^3J_{H\text{-}H}$ = 4 Hz), 9.53 (1H, s, CH$_3$(C=)NN*H*(C=S)N(CH$_3$)$_2$), 10.24 (1H, s, CH$_3$(C=)NN*H*(C=S)NHCH$_3$). HPLC: R$_t$ = 8.06 min.

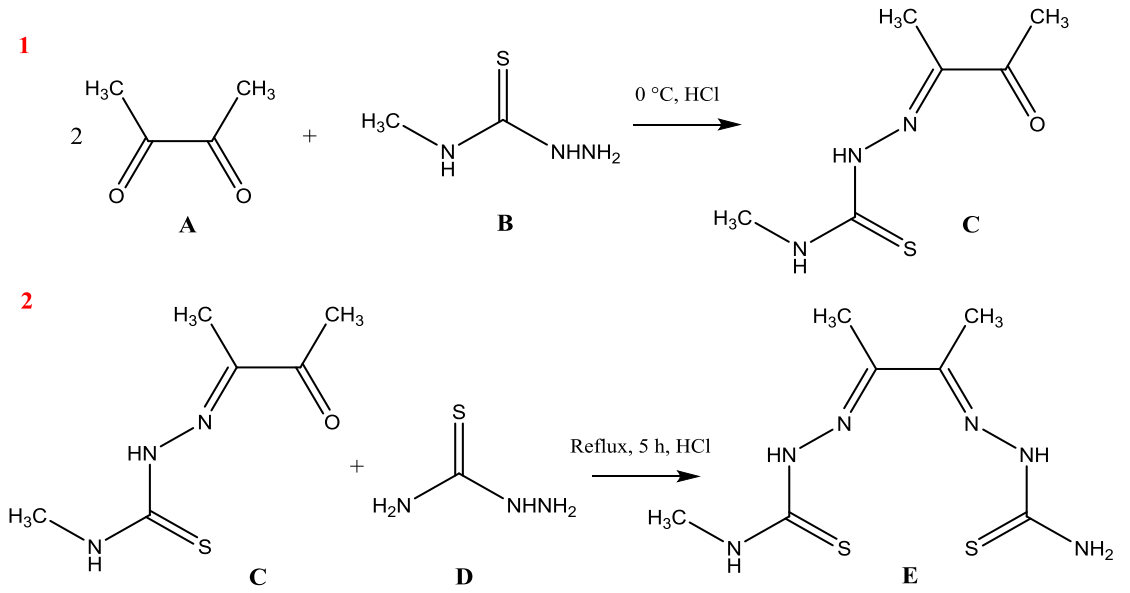

Figure 6.1: Synthesis of diacetyl-2-(4-*N*-methyl-3-thiosemicarbazone)-3-(3-*N*-amino-3-thiosemicarbazone) (**12**, **E**) from diacetyl-2-(4-N-methyl-3-thiosemicarbazone) (**C**) and thiosemicarbazide (**D**). **C** was prepared by reaction of an excess of 2,3-butanedione (**A**) and 4-methyl-3-thiosemicarbazide (**B**) (484).

BTSC ligands **3**, **4**, **5**, **6**, **7**, **8**, **9**, **14, 15**, **16**, **17**, **18**, **19** and **20** were synthesised by Dr Oliver C. Brown (School of Physical Sciences, University of Kent) and sent to King's College London for characterisation of the physicochemical properties of their corresponding copper (II) complexes. **15** was prepared following the synthetic approach for symmetric BTSC ligands by Gingras *et al.* previously described (406). Asymmetrical ligands **14**, **16**, **17**, **18**, **19** and **20** were prepared via the previously reported non-protected diketone strategy used for the synthesis of **12** (484). On the other hand, asymmetric ligands **3**, **4**, **5**, **6**, **7**, **8** and **9** were synthesised using a protocol by Lim and co-workers based on the use of an acetal as a protecting group in order to ensure that only one carbonyl group of the diketone reactant condenses with the first thiosemicarbazide (Figure 6.2) (482). After this first step, the acetal group is cleaved with a mild Lewis acid (e.g. lithium tetrafluoroborate) and the deprotected intermediate reacts with a dissimilar thiosemicarbazide to afford the desired asymmetric BTSC ligand. Characterisation data for all these ligands is included in the PhD thesis of Dr Oliver C. Brown (485).

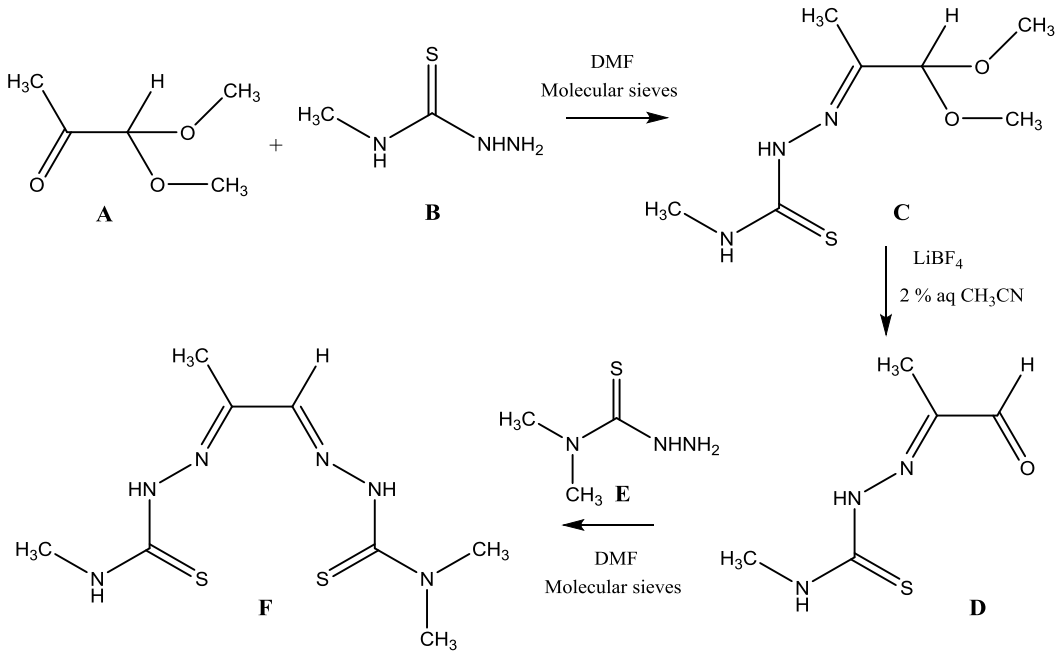

Figure 6.2: Synthesis of pyruvaldehyde-2-(4-*N*-methyl-3-thiosemicarbazone)-3-(3-*N*-dimethyl-3-thiosemicarbazone) (**3**, **F**) following a previously reported protocol by Lim *et al*.(482). Pyruvic aldehyde dimethyl acetal (**A**) first reacts with 4-methyl-3-thiosemicarbazide (**B**) to yield pyruvaldehyde dimethyl acetal 2-(4-*N*-methyl-3-thiosemicarbazone) (**C**). Subsequently, **C** is deprotected with lithium tetrafluoroborate ($LiBF_4$) to give pyruvaldehyde 2-(4-*N*-methyl-3-thiosemicarbazone) (**D**), which is finally condensed with 4,4-dimethyl-3-thiosemicarbazide (**E**) to afford **F**.

6.3.1.3 Synthesis of Cu-BTSC complexes

Table 6.2: Structure of Cu-BTSC complexes

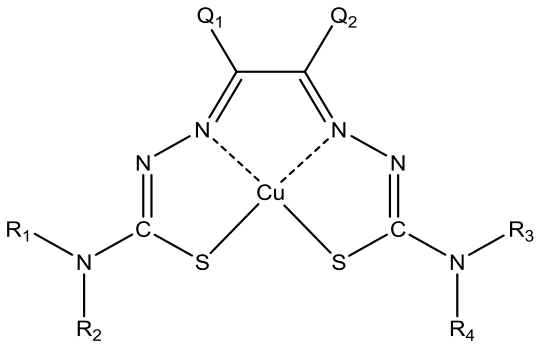

Complex	R_1	R_2	Q_1	Q_2	R_3	R_4	New?
Cu(1)	CH_3	H	H	H	CH_3	H	No (142, 155, 365)
Cu(2)	C_2H_5	H	H	H	C_2H_5	H	No (365)
Cu(3)	CH_3	H	CH_3	H	CH_3	CH_3	Yes

Complex	R_1	R_2	Q_1	Q_2	R_3	R_4	New?
Cu(4)	C_2H_5	H	CH_3	H	CH_3	H	Yes
Cu(5)	C_6H_5	H	CH_3	H	C_2H_5	H	Yes
Cu(6)	CH_3	H	CH_3	H	C_6H_5	H	Yes
Cu(7)	C_6H_5	H	CH_3	H	CH_3	H	Yes
Cu(8)	C_2H_5	H	CH_3	H	CH_3	CH_3	Yes
Cu(9)	C_2H_5	H	CH_3	H	C_6H_5	H	Yes
Cu(10)	CH_3	H	CH_3	CH_3	CH_3	H	No (142, 304, 307)
Cu(11)	C_2H_5	H	CH_3	CH_3	C_2H_5	H	No (143, 146)
Cu(12)	CH_3	H	CH_3	CH_3	H	H	Yes
Cu(13)	CH_3	H	CH_3	CH_3	CH_3	CH_3	No (116)
Cu(14)	H	H	CH_3	CH_3	CH_3	CH_3	Yes
Cu(15)	H	H	CH_3	C_2H_5	H	H	No (142, 143, 166)
Cu(16)	H	H	CH_3	C_2H_5	CH_3	H	Yes
Cu(17)	C_2H_5	H	CH_3	C_2H_5	H	H	Yes
Cu(18)	H	H	CH_3	C_2H_5	C_2H_5	H	Yes
Cu(19)	CH_3	H	CH_3	C_2H_5	H	H	Yes
Cu(20)	H	H	CH_3	C_2H_5	CH_3	CH_3	Yes

All copper (II) complexes were synthesised using a common procedure, exemplified by the method for the preparation of **Cu(1)** described in the third chapter of this thesis (see section

3.3.1) (142). **Cu(1)**: HPLC: R_t = 5.57 min; ESI^+ MS: m/z for $[CuC_6H_{10}N_6S_2 + H]^+$= 293.9777 (calc.), 293.9805 (found); TLC: R_f = 0.36. **Cu(2)**: HPLC: R_t = 8.14 min; ESI^+ MS: m/z for $[CuC_8H_{14}N_6S_2 + H]^+$ = 322.0090 (calc.), 322.0093 (found); TLC: R_f = 0.58. **Cu(3)**: ESI^+ MS: m/z for $[CuC_8H_{14}N_6S_2 + H]^+$ = 322.0090 (calc.), 322.0093 (found); TLC: R_f = 0.38. **Cu(4)**: HPLC: R_t = 7.51 min; ESI^+ MS: m/z for $[CuC_8H_{14}N_6S_2 + H]^+$ = 322.0090 (calc.), 322.0098 (found); **Cu(5)**: HPLC: R_t = 12.11 min; ESI^+ MS: m/z for $[CuC_{13}H_{16}N_6S_2 + H]^+$ = 384.0247 (calc.), 384.0247 (found); TLC: R_f = 0.52. **Cu(6)**: HPLC: R_t = 13.51 min; ESI^+ MS: m/z for $[CuC_{12}H_{14}N_6S_2 + H]^+$ = 370.0090 (calc.), 370.0093 (found); TLC: R_f = 0.54. **Cu(7)**: HPLC: R_t = 10.37 min; ESI^+ MS: m/z for $[CuC_{12}H_{14}N_6S_2 + H]^+$ = 370.0090 (calc.), 370.0095 (found); TLC: R_f = 0.41. **Cu(8)**: ESI^+ MS: m/z for $[CuC_9H_{16}N_6S_2 + H]^+$ = 336.0247 (calc.), 336.0255 (found); TLC: R_f = 0.34. **Cu(9)**: ESI^+ MS: m/z for $[CuC_{13}H_{16}N_6S_2 + H]^+$ = 384.0247 (calc.), 384.0247 (found); TLC: R_f = 0.59. **Cu(10)**: HPLC: R_t = 7.36 min; ESI^+ MS: m/z for $[CuC_8H_{14}N_6S_2 + H]^+$ = 322.0090 (calc.), 322.0101 (found); TLC: R_f = 0.52. **Cu(11)**: ESI^+ MS: m/z for $[CuC_{10}H_{18}N_6S_2 + H]^+$ = 350.0403 (calc.), 350.0957 (found); TLC: R_f = 0.55. **Cu(12)**: HPLC: R_t = 6.03 min; ESI^+ MS: m/z for $[CuC_7H_{12}N_6S_2 + H]^+$ = 307.9934 (calc.), 307.9935 (found); TLC: R_f = 0.39. **Cu(13)**: HPLC: R_t = 9.54 min; ESI^+ MS: m/z for $[CuC_9H_{16}N_6S_2 + H]^+$ = 336.0247 (calc.), 336.0249; TLC: R_f = 0.42. **Cu(14)**: HPLC: R_t = 8.12 min; ESI^+ MS: m/z for $[CuC_8H_{14}N_6S_2 + H]^+$ = 322.0090 (calc.), 322.0085 (found). **Cu(15)**: HPLC: R_t = 5.27 min; ESI^+ MS: m/z for $[CuC_7H_{12}N_6S_2 + H]^+$ = 307.9934 (calc.), 307.9934 (found); TLC: R_f = 0.40. **Cu(16)**: HPLC: R_t = 7.05 min; ESI^+ MS: m/z for $[CuC_8H_{14}N_6S_2 + H]^+$ = 322.0090 (calc.), 322.0080 (found); TLC: R_f = 0.53. **Cu(17)**: HPLC: R_t = 7.52 min; ESI^+ MS: m/z for $[CuC_9H_{16}N_6S_2 + H]^+$ = 336.0247 (calc.), 336.0248 (found); TLC: R_f = 0.54. **Cu(18)**: HPLC: R_t = 8.07 min; ESI^+ MS: m/z for $[CuC_9H_{16}N_6S_2 + H]^+$ = 336.0247 (calc.), 336.0287 (found); TLC: R_f = 0.47. **Cu(19)**: HPLC: R_t = 6.49 min; ESI^+ MS: m/z for $[CuC_8H_{14}N_6S_2 + H]^+$ = 322.0090 (calc.), 322.0093 (found); TLC: R_f = 0.53. **Cu(20)**: HPLC: R_t = 9.02 min; ESI^+ MS: m/z for $[CuC_9H_{16}N_6S_2 + H]^+$ = 336.0247 (calc.), 336.0247 (found); TLC: R_f = 0.57.

6.3.2 Electrochemistry

All cyclic voltammograms were recorded using a μAUTOLAB potentiostat (Metrohm Autolab B. V., Netherlands) and General Purpose Electrochemical System (GPES) acquisition and analysis software. Cyclic voltammetry measurements were performed at a scan rate of 0.1 V/s under an inert atmosphere of argon using a glassy carbon working electrode, a silver wire

pseudo-reference electrode and a platinum auxiliary electrode. All experiments were carried out in anhydrous deoxygenated DMSO (5 mL) using tetrabutylammonium hexafluorophosphate (0.1 M, Sigma Aldrich) as a support electrolyte and a Cu-BTSC concentration of 0.5 mM. Ferrocene (Sigma Aldrich) was used as an internal reference and all potentials were referenced to the ferrocene/ferrocenium couple. The Cu(II)/Cu(I) and Cu(II)/Cu(III) potentials were calculated as the midpoint between the reduction and oxidation peaks. All electrochemical experiments were performed under the supervision of Dr Katherine Holt (Department of Chemistry, University College London).

6.3.3 HPLC determination of lipophilicity

Log P values of new Cu-BTSC complexes were estimated by reversed-phase HPLC using an Eclipse XDB-C_{18} column (4.6 x 150 mm, 5 µm) as the stationary phase and an isocratic mobile phase consisting of water + 0.1 % (v/v) TFA (60 %) and acetonitrile + 0.1 % (v/v) TFA (40 %). A number of Cu-BTSC complexes of known logP values (**Cu(10)**, **Cu(11)**, **Cu(21)**, **Cu(22)** and **Cu(23)**, determined by octanol-water extraction) were chromatographed by HPLC and the logarithms of their retention factors (logKs) plotted against their literature logP values to construct a calibration curve (Table 6.3) (143). LogK values were calculated using the equation $\log K = \log(t_r\text{-}t_o/t_o)$, where t_r is the retention time of the complex and t_o is the retention time of the solvent front (DMSO) (486). The calibration equation was then used to calculate the logP values of the new Cu-BTSC complexes using their experimental retention factors. Complexes **Cu(21)**, **Cu(22)** and **Cu(23)** were synthesised and characterised by Dr Maxwell G. Handley (Department of Imaging Chemistry and Biology, King's College London) (487).

Table 6.3: Structure and literature logP values of reference Cu-BTSC complexes (143).

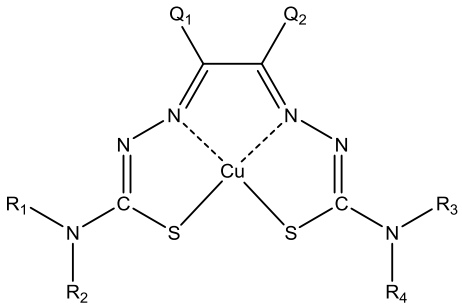

Complex	R_1	R_2	Q_1	Q_2	R_3	R_4	Molecular weight (g)	LogP
Cu(10)	CH_3	H	CH_3	CH_3	CH_3	H	321.91	1.69
Cu(11)	C_2H_5	H	CH_3	CH_3	C_2H_5	H	349.97	1.86
Cu(21)	CH_3	H	CH_3	H	CH_3	H	307.89	1.52
Cu(22)	C_2H_5	H	CH_3	H	C_2H_5	H	335.94	1.74
Cu(23)	CH_3	H	C_2H_5	C_2H_5	CH_3	H	349.97	2.01

6.4 RESULTS

6.4.1 Chemistry

All symmetric BTSC ligands (**1**, **2**, **10**, **11** and **15)** were prepared following a previously reported procedure by Gingras *et al.* and obtained in high yield and purity (>95 %) (406). Conversely, the synthesis of asymmetric BTSC ligands via protected (**3**, **4**, **5**, **6**, **7**, **8** and **9**) and unprotected (**12**, **14**, **16**, **17**, **18**, **19** and **20**) diketone methods proved to be more challenging, often resulting in low reaction yields and mixtures of isomers and undesired by-products. Moreover, asymmetrical BTSCs were difficult to isolate and purify due to their low solubility in common solvents, which limited the amount of pure ligand that could be used for characterisation (485).

All Cu-BTSC complexes were easily synthesised and purified following a previously reported protocol by Dearling and co-workers (142). ESI^+ MS characterisation of the complexes was

consistent with the proposed formulations and HPLC analysis revealed no significant impurities (<5 %) in the final product.

6.4.2 Electrochemistry

Table 6.4 shows the electrochemical reduction and oxidation potentials of complexes **Cu(1)**-**Cu(20)** as measured by cyclic voltammetry. Cyclic voltammograms were acquired in a three-electrode configuration using a glassy carbon electrode as the working electrode, a platinum wire as the auxiliary electrode and a silver wire as the reference electrode. To be able to compare electrochemical potentials for different Cu-BTSC complexes, ferrocene was used as an internal standard.

Table 6.4: Half-wave potentials ($E_{1/2}$) and peak separations (ΔE_p) of **Cu(1)**-**Cu(20)** complexes in anhydrous DMSO at 298 K normalised with respect to ferrocene. All measurements were performed at 0.1 V/s scan rate.

Complex	$E_{1/2}$ Cu(II/I) (V)[a]	Cu(II/I) ΔE_p (mV)[b]	$E_{1/2}$ Cu(III/II) (V)[a]	Cu(III/II) ΔE_p (mV)[b]
Cu(1)	-0.96	65	0.22	170
Cu(2)	-1.06	63	0.13	131
Cu(3)	-1.01	73	0.24	97
Cu(4)	-1.08	72	0.18	90
Cu(5)	-0.97	61	----	----
Cu(6)	-0.93	69	----	----
Cu(7)	-1.04	93	----	----
Cu(8)	-1.05	68	0.20	95
Cu(9)	-1.06	60	----	----
Cu(10)	-1.12	90	0.19	81

Complex	$E_{1/2}$ Cu(II/I) (V)[a]	Cu(II/I) ΔE_p (mV)[b]	$E_{1/2}$ Cu(III/II) (V)[a]	Cu(III/II) ΔE_p (mV)[b]
Cu(11)	-1.13	88	0.18	84
Cu(12)	-1.12	75	0.18	83
Cu(13)	-1.05	65	0.26	87
Cu(14)	-1.13	79	0.19	82
Cu(15)	-1.16	51	0.14	66
Cu(16)	-1.13	74	0.14	84
Cu(17)	-1.14	53	0.21	66
Cu(18)	-1.11	72	0.17	79
Cu(19)	-1.13	73	0.15	81
Cu(20)	-1.10	72	0.18	80

[a] Half-wave potentials were calculated by averaging the anodic and cathodic peak potentials: $E_{1/2} = (E_{pa} + E_{pc})/2$. [b] Peak separations are given by $\Delta E_p = |E_{pa} - E_{pc}|$.

All Cu-BTSC complexes underwent reversible or nearly reversible one-electron Cu(II/I) reductions, as exemplified by the voltammogram of complex **Cu(17)** (Figure 6.3). The magnitudes of the anodic and cathodic current peaks were found to be approximately equal, demonstrating chemical reversibility for the Cu(II/I) couple. The behaviour of the Cu(III/II) redox couple was only found to be reversible for Cu-BTSC complexes with two alkyl groups at the diimine backbone (except for **Cu(14)** and **Cu(16)**), while CuBTSCs with less than two alkyl substituents showed reduced peak current for the return potential scan (**Cu(1)**, **Cu(2)**, **Cu(3)**, **Cu(4)** and **Cu(8)**), or were not oxidisable within the potential range studied (**Cu(5)**, **Cu(6)**, **Cu(7)** and **Cu(9)**).

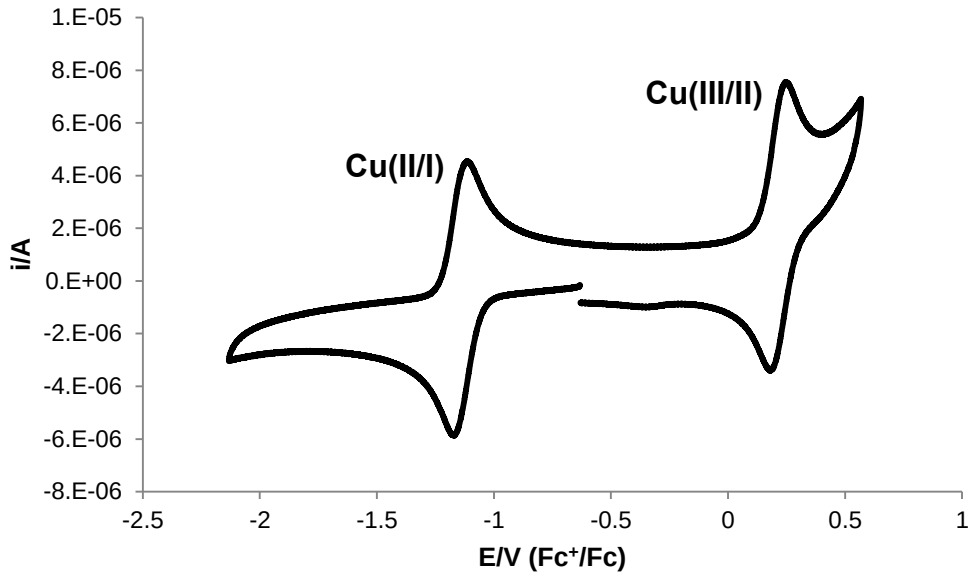

Figure 6.3: Cyclic voltammogram of **Cu(17)** in anhydrous DMSO at 0.1 V/s scan rate. A silver wire served as pseudo-reference electrode and ferrocene was used as an internal standard. i/A = current in amperes E/V (Fc^+/Fc) = applied potential in volts versus ferrocene/ferrocenium couple.

Anodic to cathodic peak separations ranged from 51 to 93 mV for the Cu(II/I) redox processes and from 66 to 131 mV for the Cu(III/II) couple (except **Cu(1)**, 170 mV), similar to the peak separation range for the reversible one-electron oxidation of the ferrocene/ferrocinium couple under the same experimental conditions (79-145 mV). Cyclic voltammograms of all Cu-BTSC complexes are included in the appendix of this chapter.

As expected, a correlation was found between the alkylation pattern of the ligand backbone and the Cu(II/I) redox potential, although less pronounced than previously reported (142) (Figure 6.4). Alkylation of the diimine backbone of the ligand appeared to lower the half-wave potential of the Cu(II/I) couple. Half-wave potentials for Cu-BTSC complexes with zero (**Cu(1)** and **Cu(2)**) and one alkyl substituent (**Cu(3)**-**Cu(9)**) on the backbone were found to be relatively similar, ranging from -0.96 to -1.06 and from -0.93 to -1.08 V respectively. Complexes with two methyl groups at Q_1 and Q_2 (**Cu(10)**-**Cu(14)**) had $E_{1/2}$ Cu(II/I) potentials in the range of -1.05 to -1.13 V, while CuBTSCs with ethyl and methyl substituents on the ligand backbone (**Cu(15)**-**Cu(20)**) had slightly lower redox potentials, ranging from -1.10 to -1.16 V.

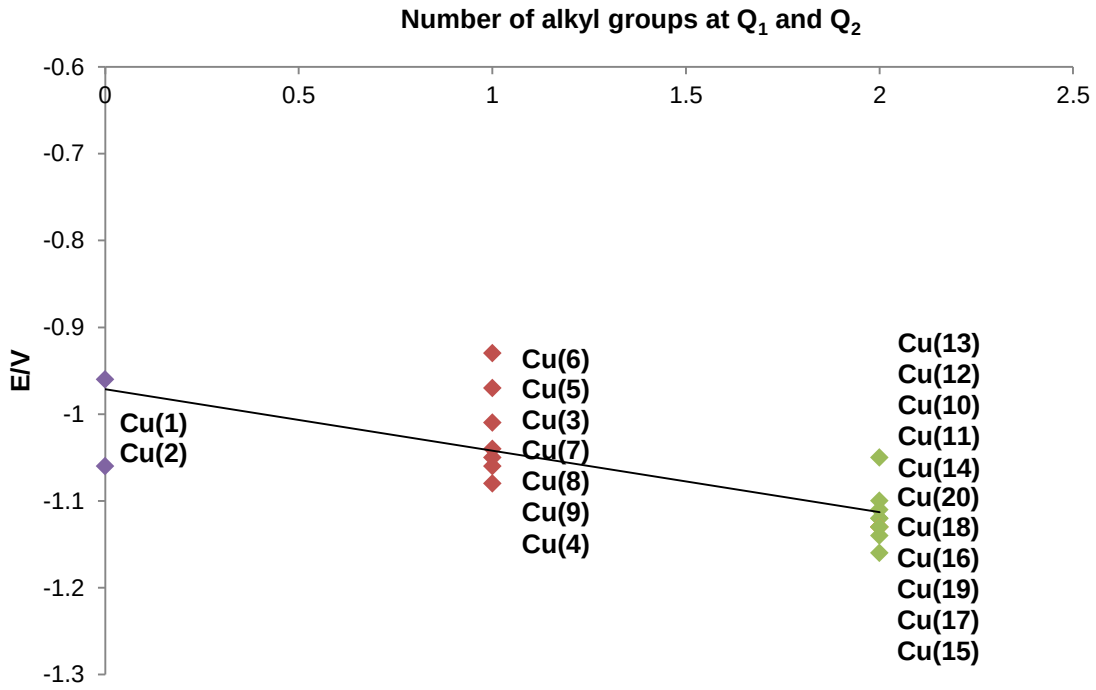

Figure 6.4: Effect of ligand backbone alkylation on $E_{1/2}$ Cu(II/I) potential of Cu-BTSC complexes. Half-wave potential values for Cu-BTSCs were found to decrease with increasing number of backbone alkyl groups.

6.4.3 HPLC determination of lipophilicity

Due to the lack of availability of ^{64}Cu at the time of these experiments, reversed-phase HPLC was used to estimate the lipophilicity of the newly synthesised Cu-BTSC complexes as an alternative to octanol-water partitioning. Lipophilicity assessment by reversed-phase HPLC assumes a linear relationship between the logarithm of the retention factor of the compound (logK) and its logP. Thus, a number of reference Cu-BTSC complexes (**Cu(10)**, **Cu(11)**, **Cu(21)**, **Cu(22)** and **Cu(23)**) were chromatographed and their experimental logK values correlated directly with their known experimental logPs to create a calibration curve (Figure 6.5).

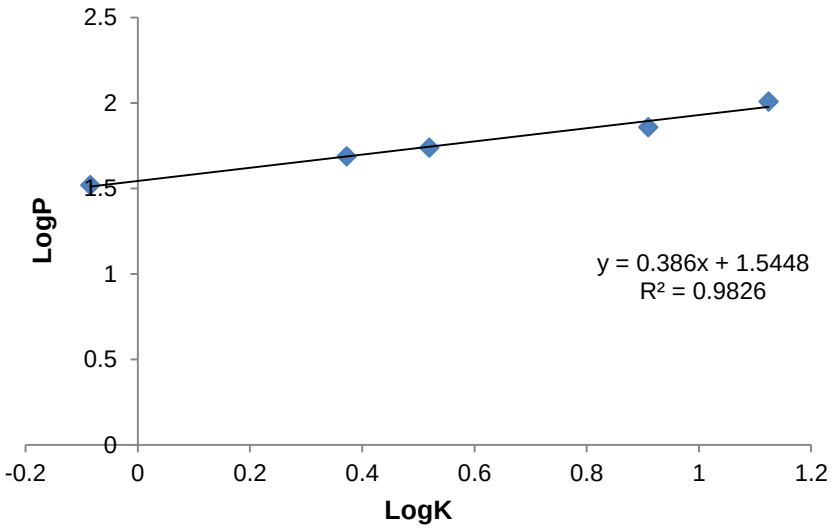

Figure 6.5: Correlation between the literature logP values of **Cu(10)**, **Cu(11)**, **Cu(21)**, **Cu(22)** and **Cu(23)** and their experimental logKs measured by HPLC. A C_{18} column was used as the stationary phase and a water + 0.1 % (v/v) TFA (60 %) / acetonitrile + 0.1 % (v/v) TFA (40 %) isocratic system as the mobile phase.

The calibration equation was then applied to calculate the logPs of the new Cu-BTSC complexes using their experimental logK values. The logP values obtained for complexes **Cu(1)**-**Cu(20)** are summarised in Table 6.5.

Table 6.5: LogP values for complexes **Cu(1)**-**Cu(20)** estimated by reversed-phase HPLC.

Complex	Molecular weight (g)	R_t (min)	LogK	LogP
Cu(1)	293.86	2.42	-0.68	1.28
Cu(2)	321.91	4.42	0.08	1.58
Cu(3)	321.91	7.17	0.41	1.70
Cu(4)	321.91	5.49	0.24	1.64
Cu(5)	383.98	27.57	1.11	1.97
Cu(6)	369.96	19.17	0.93	1.91

Complex	Molecular weight (g)	R_t (min)	LogK	LogP
Cu(7)	369.96	16.05	0.85	1.87
Cu(8)	335.94	11.72	0.69	1.81
Cu(9)	383.98	28.9	1.13	1.98
Cu(12)	307.89	3.46	-0.14	1.49
Cu(13)	335.94	16.01	0.85	1.87
Cu(14)	321.91	6.43	0.34	1.68
Cu(15)	307.89	2.85	-0.37	1.40
Cu(16)	321.91	5.36	0.23	1.63
Cu(17)	335.94	7.68	0.45	1.72
Cu(18)	335.94	8.12	0.49	1.73
Cu(19)	321.91	4.96	0.17	1.61
Cu(20)	335.94	11.96	0.70	1.81

As expected, higher logP values correlated with greater molecular weight, with complexes having phenyl groups in their structure being the most lipophilic. Alkylation of both the diimine backbone and pendant amino arms contributed to enhancing the lipophilicity of Cu-BTSCs.

Figure 6.6 shows the total $E_{1/2}$ Cu(II/I) potential and lipophilicity range covered by the new library of Cu-BTSC complexes. This plot demonstrates that **Cu(3)**, **Cu(5)** and **Cu(6)**, although more lipophilic, have an electrochemical behaviour similar to that of **Cu(1)** (Cu-GTSM). On the other hand, complexes **Cu(14)** and **Cu(16)**-**Cu(20)** show relatively similar redox potential and

lipophilicity characteristics as hypoxia-selective **Cu(10)** (Cu-ATSM) and **Cu(11)** (Cu-ATSE). **Cu(12)** is considerably less lipohilic than the previous complexes but its $E_{1/2}$ Cu(II/I) potential lies within the same range, similarly to **Cu(15)**. Complexes **Cu(2)**, **Cu(4)**, **Cu(7)-(9)** and **Cu(13)** have redox potentials intermediate between those of the two previous groups of complexes and variable lipophilicity.

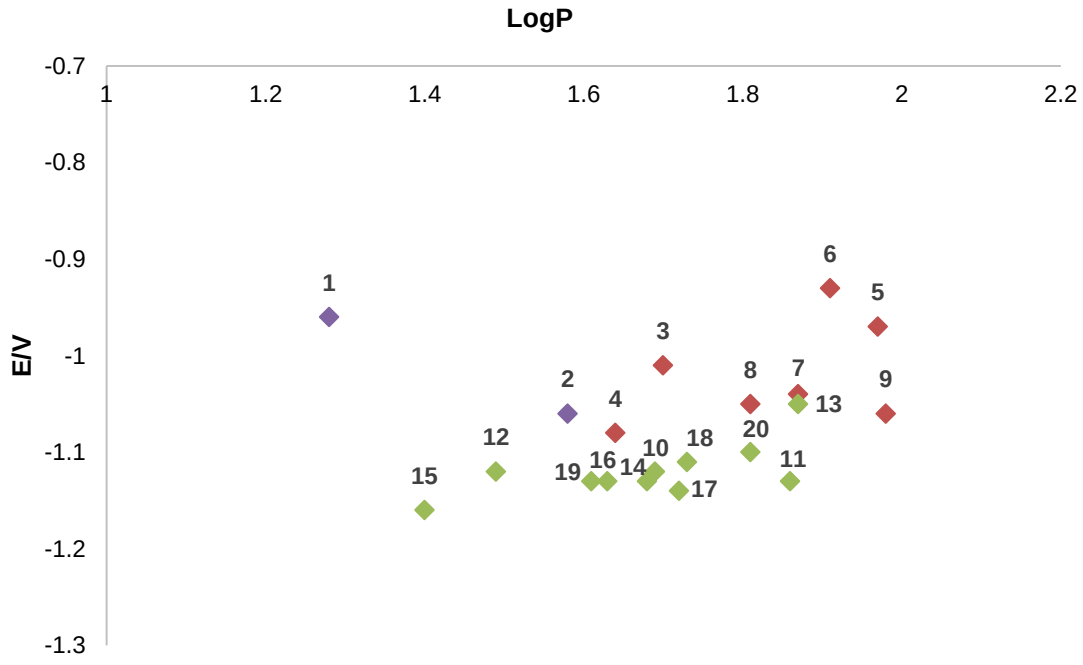

Figure 6.6: Scatter plot showing the relationship between $E_{1/2}$ Cu(II/I) potential and logP values of Cu-BTSCs **Cu(1)**-**Cu(20)**. *Purple*: no backbone alkyl groups; *red*: one backbone alkyl group; *green*: two backbone alkyl groups.

6.5 DISCUSSION

The sensitivity of the biodistribution properties of Cu-BTSC radiopharmaceuticals to the structural modification of their ligand scaffold has favoured their adaptability to a diverse range of imaging applications. It has been shown that Cu-BTSC complexes with two alkyl substituents at the diimine backbone are bioreduced and irreversibly trapped only under reductive cellular environments, which facilitates their use as hypoxia imaging agents. Conversely, Cu-BTSCs with less than two alkyl groups on their backbone tend to be taken up by all cells and thus hold potential for imaging blood flow or copper trafficking processes. For many years, symmetrical complexes Cu-ATSM and Cu-PTSM, which differ from one another only by one backbone alkyl substituent, have been investigated as imaging probes for the delineation of tissue hypoxia and

perfusion, respectively (147, 158, 170, 488). However, despite much promise, these tracers remain prototypes since some of their imaging characteristics (e.g. *in vivo* stability, plasma protein binding, hypoxia sensitivity, liver and kidney uptake) are far from optimal (143, 175, 480, 489). Hence, there is great interest in developing alternative Cu-BTSC radiotracers with improved imaging characteristics for clinical use. Despite the ease of synthesis of symmetrical BTSCs, asymmetrical ligands offer greater structural diversity, which allows the fine-tuning of the physicochemical properties of the final Cu-BTSC complexes, facilitating the optimisation of their biodistribution and pharmacokinetics for specific imaging applications. In collaboration with the University of Kent (Dr Oliver C. Brown and Prof Michael Went), we have synthesised an extended library of asymmetric Cu-BTSCs with a variety of ligand alkylation patterns, and determined their redox potential and lipohilicity values. Although the measurement of these two parameters is not sufficient for predicting the biological behaviour of these complexes, it is an important step in their characterisation and a useful indicator of their imaging potential.

A strong correlation has been repeatedly reported between the Cu(II/I) redox potential of Cu-BTSCs and their hypoxia selectivity. Symmetrical Cu-BTSC complexes with two backbone alkyl substituents and reduction potentials lower than -0.5 V have been found to be selectively retained in cultured cells under hypoxic conditions, whereas that Cu-BTSCs with less than two alkyl groups on their backbone and higher redox potentials have been shown to be irreversibly trapped within cells under both normoxia and hypoxia (142, 166). These observations support the idea that hypoxia selectivity in Cu-BTSCs is a function of redox potential, which in turn has been shown to be strikingly dependent on the backbone alkylation pattern of these complexes. However, it should be noted that redox potential is probably not the only factor controlling hypoxia-selective targeting, as evidenced by the variations in the degree of hypoxia selectivity observed in Cu-BTSCs exhibiting similar redox behaviour (483).

In this study, the electrochemical behaviour of Cu-BTSCs was investigated by cyclic voltammetry using a three-electrode system (glassy carbon, silver and platinum electrodes), tetrabutylammonium hexafluorophosphate as a support electrolyte and ferrocene as an internal standard. Due to the low solubility of Cu-BTSCs in water, all electrochemical measurements were carried out in DMSO, despite the fact that this solvent has the ability to coordinate to

copper (II) centres. As previously reported for symmetrical Cu-BTSC complexes, the addition of alkyl groups to the diimine backbone of the complexes generally resulted in the lowering of their Cu(II/I) reduction potential (142). Asymmetrical Cu-BTSCs with two alkyl substituents on the diimine backbone (**Cu(10)**-**Cu(20)**) were found to exhibit lower redox potentials than complexes with zero or one backbone alkyl groups (**Cu(1)**-**Cu(9)**). Blower and co-workers suggested that this structural effect on the redox behaviour of Cu-BTSCs might arise from the lengthening of the backbone C-C bond on alkylation, which might allow the copper ion to fit better into the ligand cavity, thus enhancing the stability of the complex and decreasing the susceptibility to reduction of Cu (II) to Cu (I) (145). It has been suggested that increased C-C bond length upon alkylation might result from either steric repulsion between the backbone alkyl groups or overlapping between the lowest energy unoccupied molecular orbital and the alkyl C-H bonds (144, 145).

Compared to previously reported literature values, the Cu(II/I) reduction potentials of standard symmetrical Cu-BTSCs were found to be considerably lower in this study (**Cu(1)**: -0.43 vs -0.96 V; **Cu(10)**: -0.59 vs -1.12 V; **Cu(15)**: -0.59 vs -1.16 V) (142). This could be due to the use of a pseudo-reference electrode (silver wire) instead of a true reference electrode (e.g Ag/AgCl). Pseudo-reference electrodes are often used in non-aqueous electrochemistry in place of true reference systems to avoid the formation of liquid junction potentials between aqueous and nonaqueous medium and prevent leakage of reference electrolyte from the electrode into the cell, which could affect the electrochemical processes occurring in the analyte solution. The main disadvantage of pseudo-reference systems is the lack of thermodynamic equilibrium between the electrode and the electrolyte because of the absence of common ionic species in the two adjacent phases. Nevertheless, this type of electrode can be calibrated by adding a reference redox system (e.g. ferrocene) into the electrolyte after the experiment and measuring its potential (490). Despite variation among studies in reduction potential values, the shift in redox potential per alkyl group was found to be roughly the same.

Although the number of alkyl groups on the ligand backbone (Q_1, Q_2) is thought to be the main structural determinant of the redox behaviour of Cu-BTSCs, the spread of redox potential values observed within each backbone group seems to suggest that the alkylation pattern of the

pendant amino arms also influences the reduction potential of asymmetrical Cu-BTSC complexes (142). Despite having a less significant impact than backbone alkylation, the number of alkyl substituents at the terminal amino positions of the ligand may affect the susceptibility of Cu-BTSCs to bioreduction as well as the stability of the resulting Cu (I) complexes by either steric or electronic effects. Asymmetrical Cu-BTSCs with zero and one alkyl groups on their diimine backbone were found to exhibit higher variability in Cu (II/I) reduction potential values (0.13 V spread) when compared to complexes with two alkyl substituents (0.05 V spread).

All asymmetrical Cu-BTSC complexes showed reversible or nearly reversible one-electron Cu(II/I) reductions, in which the peak currents for the cathodic and anodic processes were found to be approximately equal. On the other hand, the electrochemical behaviour of the Cu(III/II) redox couple was only found to be reversible for Cu-BTSCs with two alkyl groups on their diimine backbone, with the exception of **Cu(14)** and **Cu(16)**, which showed loss of peak current on the reverse scan. Complexes **Cu(1)**, **Cu(2)**, **Cu(3)**, **Cu(4)** and **Cu(8)**, with zero or one backbone alkyl substituents, exhibited reduced peak current for the return Cu(III/II) reduction process, suggesting partial dissociation upon oxidation. Interestingly, the cathodic current peak was not observed in the cyclic voltammograms of Cu-BTSCs with one backbone alkyl substituent and a phenyl group in their structure (**Cu(5)**, **Cu(6)**, **Cu(7)** and **Cu(9)**), which may indicate that these complexes undergo an irreversible decomposition reaction following oxidation.

Based on the proposed structure-activity relationship for Cu-BTSCs, the hypoxia-targeting ability of backbone-alkylated complexes **Cu(12)**, **Cu(14)** and **Cu(16)-Cu(20)** should be investigated, since the Cu(II/I) reduction potentials of these (-1.12, -1.13, -1.13, -1.14, -1.11, -1.13 and -1.10 V) fall within the same range as those of **Cu(10)** (Cu-ATSM, -1.12 V), **Cu(11)** (-1.13 V) and **Cu(15)** (-1.16 V), which have previously shown hypoxia selectivity *in vitro* (142, 143, 146). On the other hand, **Cu(3)**, **Cu(5)** and **Cu(6)** (-1.01, -0.97 and -0.93 V), although considerably more lipophilic, showed similar Cu(II/I) reduction potential values as non-selective **Cu(1)** (Cu-GTSM, -0.96 V), and therefore might hold potential as imaging agents for the visualisation of copper trafficking processes at brain or whole-body level. **Cu(2)**, **Cu(4)**, **Cu(7)-Cu(9)** and **Cu(13)** have moderate lipophilicities, which may promote rapid diffusion of the

complexes into tissues, and $E_{1/2}$ Cu(II/I) potential values intermediate between those of the two previous groups of Cu-BTSCs (-1.06, -1.08, -1.04, -1.05, -1.06 and -1.05 V), which may facilitate non-selective copper release into cells. These complexes should be therefore evaluated for perfusion imaging applications. However, it should be noted that the trapping mechanism of Cu-BTSCs is complex and relies on other parameters besides redox potential, such as the pK_a and K_d of Cu(I)-BTSC complexes (144, 491). Lipophilicity is thought to considerably influence the hypoxia selectivity of Cu-BTSCs *in vivo*. Handley *et al.* recently demonstrated that **Cu(15)** (Cu-CTS), a Cu-BTSC complex with similar redox behaviour and lower lipophilicity than hypoxia-selective **Cu(10)** (Cu-ATSM), delivered a better hypoxic-to-normoxic contrast than the latter (17:1 vs. 8:1) in the Langendorff isolated perfused heart system. It is therefore important to also assess these properties to fully define the potential of these Cu-BTSC radiotracers as hypoxia, copper trafficking or blood flow imaging agents.

Lipophilicity is a critical parameter for Cu-BTSC radiotracers since it has a strong influence on membrane permeability, plasma protein binding and kinetic behaviour. Lipophilicity is often expressed as a the logarithm of the partition coefficient (logP) of a compound between two immiscible phases at equilibrium, an octanol layer and an aqueous buffer. This lipophilicity index can be measured by several methods, including the “shake-flask” test, potentiometric titration and reversed-phase chromatography (486). Although the “shake-flask” method remains the reference procedure for assessing the lipophilicity of radiopharmaceuticals, it is time-consuming, sensitive to impurities and requires the use of radioactivity. Due to the limited availability of ^{64}Cu, we determined the logP values of the new asymmetrical Cu-BTSC complexes by reversed-phase HPLC using the linear regression equation between the logK values of reference Cu-BTSC complexes and their experimental logPs, measured by the “shake-flask” method. Reversed-phase HPLC is an easy, rapid and reproducible method to quantify the logP values of a library of compounds. Since HPLC-based lipophilicity measures do not rely on the partitioning of the analyte between two phases, they are not affected by the presence of impurities and do not require the use of radioactive material.

In this study, we measured the retention factors of new asymmetrical Cu-BTSC complexes by reversed-phase HPLC using a C_{18} column as the stationary phase and an isocratic

water/acetonitrile gradient as the mobile phase. Although this method is rapid and reproducible, it also has some disadvantages. For example, HPLC silica-based stationary phases do not mimic biological membranes and are therefore not able to provide information about the membrane permeability and plasma protein binding of a compound. For this reason, the use of biomimetic stationary phases (e.g. immobilised artificial membrane system, human serum albumin column) should be considered in future work (492, 493). Another drawback is that only a single mobile phase composition (60 % water/ 40 % acetonitrile) was used in this study, which does not allow the extrapolation of the logK values to elution with 100 % water (486, 494). However, despite these limitations, this method is a useful tool to estimate the lipophilicity of a library of radiotracers without radioactivity.

As previously reported for symmetrical Cu-BTSCs, a correlation was found between the molecular weight of asymmetrical Cu-BTSC complexes and their logP values (142). Increased alkylation of both the diimine backbone and pendant amino arms resulted in enhanced lipophilicity of the complexes. Regarding tracer biokinetics, it is expected that Cu-BTSCs with high logPs (e.g. **Cu(5)**, **Cu(9)**, **Cu(13)**) will show slower tissue clearance and higher non-specific binding than less lipophilic complexes (e.g. **Cu(2)**, **Cu(12)**), as exemplified by the differences in kinetic profiling found between **Cu(10)** (Cu-ATSM) and **Cu(15)** (Cu-CTS) (143). However, further research is needed to characterise the pharmacokinetic profile of these new complexes *in vivo* and additional parameters (e.g. pK_a, K_d) need to be determined to elucidate their utility for specific imaging applications.

6.6 CONCLUSIONS

In an attempt to develop new Cu-BTSC radiotracers with improved imaging characteristics for a range of diagnostic applications, we synthesised fourteen asymmetrical Cu-BTSC complexes with a variety of alkylation patterns. The electrochemical behaviour and lipophilicity of these complexes were investigated by cyclic voltammetry and reversed-phase HPLC, respectively. Our results showed a correlation between the Cu(II/I) half-wave potential of Cu-BTSCs and the number of alkyl groups on their ligand backbone (Q_1, Q_2), which supports the notion that the redox behaviour of these complexes can be tuned by ligand scaffold modification. Our

electrochemical measurements revealed that a number of Cu-BTSCs (**Cu(12)**, **Cu(14)**, **Cu(16)**-**Cu(20)**) had Cu(II/I) reduction potentials within the range that could potentially confer hypoxia selectivity. The hypoxia-targeting ability of these complexes should be therefore examined *in vitro* and *in vivo* in future experiments. On the other hand, **Cu(3)**, **Cu(5)** and **Cu(6)** showed a similar redox behavior to that of non-selective Cu-GTSM and may hold promise as imaging agents for the visualisation of copper trafficking processes at brain or whole-body level. Although many other parameters (e.g. pK_a, K_d, plasma protein binding) need to be determined to fully delineate the biological behaviour and pharmacokinetics of these complexes, the measurement of their redox potential and lipophilicity is an essential step in their characterisation and provides early insight into their potential imaging application.

Chapter 7- Summary and future work

7.1 SUMMARY

The primary aim of this thesis was to evaluate the utility of ^{64}Cu-PET as a tool to detect changes in copper trafficking associated with the pathophysiology of copper–related neurological disorders. In the last decade, a large number of studies have reported the existence of alterations in the levels of copper and other trace metals in a wide spectrum of neurodegenerative diseases (e.g. AD, PD, ALS, HD, NPC1). Although aberrant copper homeostasis has been shown to enhance the severity of neurodegeneration by contributing to common pathological processes such as protein aggregation or ROS production, copper metabolism abnormalities remain relatively poorly characterised in these disorders. The work presented in this thesis contributes towards this area of research by providing quantitative and longitudinal measurements of short-term copper trafficking in animal models of AD and NPC1 disease. Preclinical assessment of copper trafficking by PET allowed the identification of alterations in radiocopper distribution and biokinetics that may have added value for the diagnosis, prognosis and treatment of these conditions.

In this study, copper trafficking processes were investigated using two different radioactive copper tracers, the Cu-BTSC complex ^{64}Cu-GTSM and the uncomplexed ^{64}Cu-acetate salt. While ^{64}Cu-acetate was used to visualise the uptake of copper into tissues via active transport mechanisms, ^{64}Cu-GTSM was chosen as a vehicle to deliver radiocopper into the CNS to enable the measurement of copper retention, efflux and redistribution within the brain and spinal cord. The Cu-GTSM complex has been repeatedly shown to release its copper payload non-selectively into cells through a putative bioreductive mechanism (142, 150, 365, 366, 495). However, the ability of this complex to cross the BBB by passive diffusion and deliver radiocopper into the brain in imageable quantities had only been previously demonstrated by Fodero-Tavoletti *et al.*, who used ^{64}Cu-GTSM to assess brain ^{64}Cu uptake in the APP/PS1 mouse model of AD at early time-points post-injection of the tracer (155). Our PET quantification results revealed that ^{64}Cu-GTSM uptake into the brain was remarkably high (~5 %ID/mL in

wildtype mice) and rapid, reaching a plateau 10 min after injection. The tracer was found to clear rapidly from blood ($t_{1/2}$ ~ 5 min) and release most of its radiocopper cargo (>95 %) into brain cells within 30 min post-injection. These characteristics make ^{64}Cu-GTSM an ideal radiotracer for detecting alterations in copper transport and distribution within the CNS as well as variations in early tracer uptake due to disease-related blood flow changes.

^{64}Cu-GTSM-PET was used to investigate copper trafficking processes within the CNS in the TASTPM mouse model of AD plaque pathology at early and moderate-to-severe stages of the disease (6-8 and 13-15 months of age, respectively). PET ROI analysis revealed significantly increased brain and spine ^{64}Cu concentration in 6-8- (brain: 1.3-fold; spine: 1.4-fold) and 13-15-month-old TASTPM transgenic mice (brain: 1.4-fold; spine: 1.4-fold) compared to wildtype controls at 30 min and 24 h post-injection of the tracer. These results are in accordance with those by Fodero-Tavoletti and co-workers, who also reported significantly higher brain ^{64}Cu uptake in the APP/PS1 model of AD compared to the control group at 1 h post-injection of ^{64}Cu-GTSM. The molecular mechanism underlying increased brain ^{64}Cu accumulation in these AD models remains to be elucidated but may be driven by disease-related alterations in cerebral vasculature or enhanced physiological demand for copper in response to brain copper dyshomeostasis.

In addition to showing higher brain ^{64}Cu accumulation, TASTPM transgenic mice were also found to exhibit faster ^{64}Cu clearance from brain tissue than healthy controls from 30 min to 24 h post-injection of the tracer. This difference in the washout rate of ^{64}Cu may arise from APP overexpression in the TASTPM model since this protein is thought to act as an efflux transporter for copper ions in the brain (256, 353, 416). Interestingly, although AD mice showed faster ^{64}Cu clearance from the brain than wildtype controls, the rate of radiocopper efflux from brain tissue over 24 h was found to be remarkably slower when compared to that of other organs in both animal groups. This finding had not been previously reported and may reflect a greater copper sequestration capacity of the brain driven by increased metabolic demands or the presence of less active copper efflux mechanisms.

TASTPM transgenic mice and their wildtype counterparts showed differences not only in global ^{64}Cu concentration and biokinetics in the CNS but also at regional brain level. Both PET imaging and *ex vivo* brain autoradiography revealed that the distribution of ^{64}Cu within brain tissue was heterogeneous in TASTPM and control mice injected with ^{64}Cu-GTSM at both early and late time-points post-injection of the tracer. In order to assess the heterogeneity of the PET brain signal in a functional context, we initially chose to measure the concentration of ^{64}Cu in several brain regions using a 3D mouse brain atlas. This approach enabled quantitative mapping of brain regional ^{64}Cu uptake in all PET scans, and demonstrated significantly greater radiocopper concentration in some brain regions of TASTPM transgenic mice at both early and moderate-to-severe stages of the disease compared to age-matched controls. Whether these regional differences in ^{64}Cu concentration result from globally higher brain ^{64}Cu uptake in the TASTPM model or truly reflect functional metabolic changes associated with AD-like pathology remains unknown. Nevertheless, it is important to note that the accuracy of the quantification of small structures in PET images may be hampered by the limited spatial resolution of the PET imaging system, which can cause spill-in and spill-out of activity to and from neighbouring regions.

In order to minimise the quantitative bias introduced by the partial volume effect, we alternatively assessed the heterogeneity of the PET brain signal by texture analysis. This method does not rely on the use of a structural template and provides information on the spatial distribution of voxel intensities within a ROI, rather than mean parameter values. Although the pathophysiological interpretation of image texture remains unclear, the application of this type of analysis in our study allowed the detection of changes in the textural features of the ^{64}Cu-GTSM-PET images caused by alterations in brain radiocopper distribution potentially associated with AD-like pathology. Our results revealed a higher degree of image heterogeneity in the TASTPM scans compared to the images of the control group, although the differences in texture properties only reached significance between the 6-8-month-old groups. Taken together, our findings support the evaluation of PET image heterogeneity, global brain and spine ^{64}Cu concentration and rate of clearance of radiocopper from brain tissue in early clinical studies.

Another key finding from our ^{64}Cu-GTSM work is the ambiguous relationship observed between brain regional ^{64}Cu accumulation and Aβ plaque deposition in the TASTPM mouse model. The

ability of human Aβ plaque deposits to accumulate copper and other trace metals has served as a major pillar of the “metal hypothesis of AD”, which suggests that the interaction between Aβ plaque aggregates and metal ions leads to enhanced Aβ neurotoxicity and reduced intracellular metal bioavailability in the brain (339, 341, 360, 398). While radiocopper was found to accumulate in the entire brain (including plaque-rich areas), *ex vivo* autoradiography of TASTPM brain tissue showed that the main ^{64}Cu hotspots (cerebellum, midbrain, olfactory bulb and caudate putamen) did not coincide with the regions containing the highest Aβ plaque load (cerebral cortex, thalamus and hippocampus) as depicted by Congo red staining. The quantification of XRF brain elemental copper maps from 8-month-old TASTPM transgenic mice also did not show a clear association between the regional distribution of endogenous copper in the brain and cerebral Aβ plaque deposition in this AD model. TASTPM transgenic mice exhibited significantly greater copper concentration than controls in the thalamus but not in other plaque-rich regions such as the cerebral cortex or hippocampus. These results may indicate a lower metal binding capacity of TASTPM Aβ plaques compared to human plaque deposits but may also highlight the contribution of other metabolic/pathological factors (besides Aβ plaque deposition) to copper dyshomeostasis in the AD brain.

XRF mapping of representative brain sections from TASTPM and control mice also showed that endogenous copper accumulated mostly around the CSF spaces in both animal groups. Similarly, PET imaging of active copper trafficking with ^{64}Cu-acetate evidenced focal accumulation of radiocopper in the ventricular areas of the brain and comparatively low uptake in the brain parenchyma in both TASTPM transgenic mice and wildtype controls. This distribution pattern for endogenous copper and actively transported radiocopper had been previously reported by Wang *et al.* in C57BL6/J wildtype mice and underlines the importance of the BCSFB in brain copper metabolism (196). Unfortunately, the limited resolution of both XRF and PET imaging did not allow the assessment of the individual contribution of the CSF, choroid plexus and periventricular areas to the global ventricular signal. ROI-based analysis of ^{64}Cu-acetate-PET images interestingly showed greater mean ventricular SUV_{mean} and SUV_{max} values for 6-8- and 13-15-month-old wildtype controls compared to age-matched TASTPM mice at 30 min and 24 h post-injection of the tracer. SUV quantification also revealed a time-dependent increase in ventricular SUV_{mean} and SUV_{max} values in both animal groups, which was

considerably more prominent in AD mice. These results, however, are difficult to interpret since the BCSFB is thought to act as a major regulatory site to maintain copper homeostasis in the brain and therefore the ventricular ^{64}Cu signal likely reflects a combination of copper influx, efflux and storage processes (196, 219, 496). Furthermore, it should be noted that a high interindividual variability was observed in both TASTPM and control groups and thus a larger sample size is necessary to confirm the reported trends.

^{64}Cu-acetate-PET was also used to examine the short-term dynamics of active copper trafficking in TASTPM transgenic mice at early and moderate-to-severe stages of the disease (6-8 and 13-15-months of age, respectively) and age-matched controls at the whole-body level. Our PET quantification results revealed subtle but significant differences in ^{64}Cu concentration and/or clearance between AD mice and healthy controls in various organs (liver, heart, kidneys and spine). These variations in active copper trafficking had not been previously identified in preclinical AD models or human patients and therefore deserve further investigation, if confirmed with a larger sample size.

In this study, we also aimed to evaluate the utility of ^{64}Cu-acetate-PET to assess the effect of chelation therapies on whole-body copper trafficking. Considering the evaluation of copper chelating agents as potential treatment options for neurological disorders (e.g. AD, HD, MD), ^{64}Cu-acetate-PET may prove to be a useful tool to characterise the mechanism of action of these drugs and even monitor response to therapy. In a preliminary experiment, we investigated the effect of BBB-permeable copper/zinc chelator CQ (50 mg/kg) on the biodistribution of ^{64}Cu in wildtype mice. Wildtype mice pretreated with CQ were found to exhibit increased ^{64}Cu concentration in the liver, heart, spine and brain when compared to mice receiving the sham treatment. This effect may arise from the formation of the lipophilic ^{64}Cu-CQ complex in blood, which may diffuse across biological membranes at a much faster rate than radiocopper mobilised by active transport mechanisms. However, the limited availability of ^{64}Cu did not allow the evaluation of the effect of different experimental conditions (CQ dose, administration route, radioactive copper tracer, treatment time, animal model) on ^{64}Cu trafficking and therefore further research is needed to fully elucidate the mechanism of action of this drug.

The potential of ^{64}Cu-GTSM-PET as a tool to detect alterations in brain copper trafficking associated with disease was not only evaluated in a transgenic mouse strain of AD but also in a mouse model of NPC1 disease, a rare lipid storage disorder predominantly caused by mutations in the gene encoding the NPC1 protein. Although endogenous copper levels have been previously measured in preclinical NPC1 models, this is the first report on real-time *in vivo* copper trafficking in NPC1 knockout mice at presymptomatic and symptomatic stages of the disorder (6 and 9 weeks of age, respectively) (321, 324). PET image analysis revealed significantly increased ^{64}Cu concentration in the brain and spine of symptomatic NPC1 knockout mice compared to age-matched controls at both 30 min and 15 h post-injection of ^{64}Cu-GTSM (brain: 1.4-fold; spine: 1.5-fold). This difference in brain ^{64}Cu concentration may arise from a regulatory mechanism aiming to compensate for the low brain endogenous copper content previously reported for NPC1 knockout mice, the disruption of a specific function of the NPC1 protein in brain copper trafficking or blood flow alterations associated with the disease (321). Interestingly, symptomatic NPC1 deficient mice were also found to exhibit significantly greater blood ^{64}Cu concentration than their wildtype littermates at late time-points post-injection of the tracer. This finding is consistent with previous reports that demonstrated an elevation in plasma copper content in symptomatic NPC1$^{-/-}$ transgenic mice, as well as increased copper-bound holoceruloplasmin levels and ceruloplasmin oxidase activity (321, 324). Although a larger sample size is required to confirm these trends, the differences in copper trafficking reported in this thesis merit further investigation in order to determine their diagnostic value and relation to the progression and severity of NPC1 disease.

In the last chapter of this thesis, we reported on the synthesis and characterisation of fourteen new asymmetrical Cu-BTSC complexes for potential use in molecular imaging applications, including the delineation of copper trafficking processes. Although symmetrical Cu-BTSC complexes, like Cu-GTSM, are easier to synthesise and able to display distinct biological behaviours for a variety of imaging applications, asymmetrical Cu-BTSCs offer greater structural diversity and therefore the possibility of further refining the imaging characteristics of these radiotracers (e.g. *in vivo* stability, plasma protein binding, hypoxia sensitivity) for potential clinical use. In collaboration with the University of Kent (Dr Oliver C. Brown and Prof Michael Went), we synthesised a library of asymmetric Cu-BTSC complexes with a variety of ligand

alkylation patterns, and determined their redox potential and lipophilicity. Our cyclic voltammetry results showed a correlation between the Cu(II/I) half-wave potential of Cu-BTSCs and the number of alkyl groups on their ligand backbone, in agreement with previous observations by Dearling *et al* (142). Nevertheless, the spread of redox potential values observed within each backbone group seems to indicate that the alkylation pattern of the pendant amino arms also affects the reduction potential of Cu-BTSCs, which supports the idea that asymmetrical BTSC ligands enable fine-tuning of the physicochemical properties of these complexes. The new Cu-BTSC complexes exhibited a wide range of logP values as a result of the varying alkylation patterns of the diimine backbone and thiosemicarbazide arms of the ligand scaffold. Although the measurement of the redox potential and lipophilicity of these asymmetrical Cu-BTSC complexes is an essential first step in their characterisation, further work is needed to determine their biological behaviour and pharmacokinetics *in vivo* and thus their potential for specific imaging applications.

7.2 FUTURE WORK

While this thesis has demonstrated the potential of ^{64}Cu-PET as a tool to identify copper trafficking abnormalities associated with neurological disorders, many opportunities for extending the scope of this research remain. First and foremost, we believe that a case for a clinical study to test the utility of this approach in human subjects has been made by the results presented. Our study revealed a series of copper trafficking alterations imageable by PET in mouse models of AD and NPC1 disease that may have added value in the diagnosis of these conditions. However, although the preclinical models of AD and NPC1 disease used in this study were able to mimic specific features of human pathology, the best “model” to investigate the diagnostic value of measuring copper trafficking is human disease itself, since (i) no animal model closely reflects all aspects of the natural history and pathophysiology of human AD/ NPC1 disease, and (ii) species differences in copper metabolism exist between mice and humans. Hence, a clinical study should be planned to evaluate the potential of copper trafficking as a diagnostic marker of AD/NPC1 disease, and determine its relationship with disease severity and progression.

In addition to this and directly following on from the work presented in this thesis, our suggestions for the future are as follows:

- **Continuation of the AD project**

The work presented in this thesis described the biodistribution and trafficking kinetics of intravenously administered radiocopper in a mouse model of AD-like Aβ plaque pathology at brain and whole-body level. Nevertheless, since endogenous copper enters the body ultimately via the diet, a similar study should also be performed in mice after oral administration of ^{64}Cu. This will enable the assessment of *in vivo* copper trafficking via natural routes in AD-like pathology and the detection of potential abnormalities in intestinal copper absorption associated with the disease. It is expected that only a small amount of orally administered radiocopper will be taken up by the brain within the time-scale of the experiment, which may not be quantitatively imageable by PET. However, this experiment will provide necessary information to understand the pathways of distribution of copper via normal biological routes in this model of AD-like disease.

Although the intravenous administration route facilitated rapid delivery of radioactive copper into tissues, it did not allow the evaluation of the dynamics of specific plasma copper-binding proteins in AD-like pathology. Since copper is expected to reach tissues predominantly via ceruloplasmin, *in vivo* imaging of ^{64}Cu-ceruloplasmin by PET in the TASTPM model would allow the identification of potential alterations in this pathway that may affect the delivery of copper ions into organs. The long half-life of ^{64}Cu offers the possibility of isolating ^{64}Cu-ceruloplasmin from plasma or liver tissue of mice orally treated with radioactive copper, and injecting it intravenously into other mice to monitor its trafficking and tissue uptake *in vivo*.

Having identified quantitative global changes in radiocopper uptake, biokinetics and distribution, an important issue to address in the future is the fate of the administered radiocopper at the molecular level. Answering this question will provide crucial information to better characterise the copper trafficking abnormalities measured in this study and understand their link to AD-like pathology. Gel electrophoresis and size-exclusion chromatography of tissue samples (e.g. plasma, CSF, brain region homogenates) from mice injected with radioactive copper can be

performed to gain further information on the speciation of the radiocopper in TASTPM and control mouse groups. To achieve a better quantification of the abundance of copper-binding species in tissue samples from TASTPM and control mice, speciation analysis could alternatively be conducted by size-exclusion chromatography coupled to ICP-MS. This technique could be performed in biological samples from mice injected with isotopically enriched ^{65}Cu-GTSM, thus eliminating the need for ^{64}Cu radioactivity.

Despite the inability of current AD animal models to mimic human pathology, they remain useful tools for studying specific pathological features of the disease (e.g. Aβ plaque deposition, neurofibrillary tangle formation, neuroinflammation, neuronal loss). Since the nature of the copper/tau protein interactions is currently poorly understood, it would also be interesting to evaluate copper trafficking by PET in a model of AD-like tau pathology (e.g. PS19, THY-Tau22) in order to determine the effect of cerebral neurofibrillary tangle accumulation on the distribution and biokinetics of copper in the brain (497, 498).

- **Continuation of the NPC1 and CQ projects**

Although the data reported in this thesis demonstrated significant copper trafficking abnormalities in NPC1 knockout mice and provided some insight into the mode of action of copper/zinc chelator CQ, a continuation of both of these preclinical projects is warranted. This is to supply currently missing data (e.g. *ex vivo* biodistribution and brain autoradiography in 6-week-old NPC1$^{-/-}$ mice and controls) and increase the number of animals per group to confirm the trends observed in these studies.

Additional experiments to provide the missing data for the 6-week-old NPC1$^{-/-}$ and wildtype groups are currently being performed by a postdoctoral researcher in the Imaging Chemistry and Biology department under the supervision of Prof. Philip Blower. Considering the two-fold difference in blood ^{64}Cu concentration detected between 9-week-old NPC1 knockout mice and age-matched controls, emphasis should also be placed on investigating the speciation of ^{64}Cu in blood by size-exclusion chromatography and SDS-PAGE, in order to identify metabolic changes in copper-binding plasma protein levels resulting from the disease phenotype.

Due to lack of availability of ^{64}Cu, the sample size used in our preliminary CQ study was too small for statistical analysis. Therefore, in order to validate the reported trends, it is necessary to perform this experiment in a larger sample of mice. Furthermore, since only one set of experimental conditions was used, different doses, chelator administration routes, treatment times and even radioactive copper tracers should be tested in order to fully evaluate the impact of CQ treatment on copper biodistribution.

- **Continuation of the Cu-BTSC library project**

In this thesis, we reported the synthesis of a new library of asymmetrical Cu-BTSCs and the measurement of their redox potential and lipophilicity. This work was only the first step in the characterisation of these complexes as potential PET imaging agents. In order to assess the pharmacokinetics and normoxia or hypoxia selectivity of the new Cu-BTSC complexes, our library will be screened in the triple γ-detector system for isolated perfused hearts developed in the Imaging Chemistry and Biology department. This *ex vivo* model enables the measurement of real-time rates of tracer delivery, cardiac uptake and washout under normoxic and hypoxic conditions. After determining their pharmacokinetics and hypoxia selectivity, the most promising tracer candidates for specific imaging applications (e.g. hypoxia delineation, blood flow assessment, imaging of copper trafficking) will be evaluated *in vivo*. PET imaging, *ex vivo* biodistribution and *in vivo* stability studies will be performed in wildtype mice and appropiate disease models to assess the suitability of these asymmetrical complexes as PET imaging probes.

Appendix- Asymmetrical Cu-BTSC complexes for PET: synthesis and characterisation

Cyclic voltammograms of **Cu(1)**-**Cu(20)** in anhydrous DMSO at 0.1 V/s scan rate:

Cu(1)

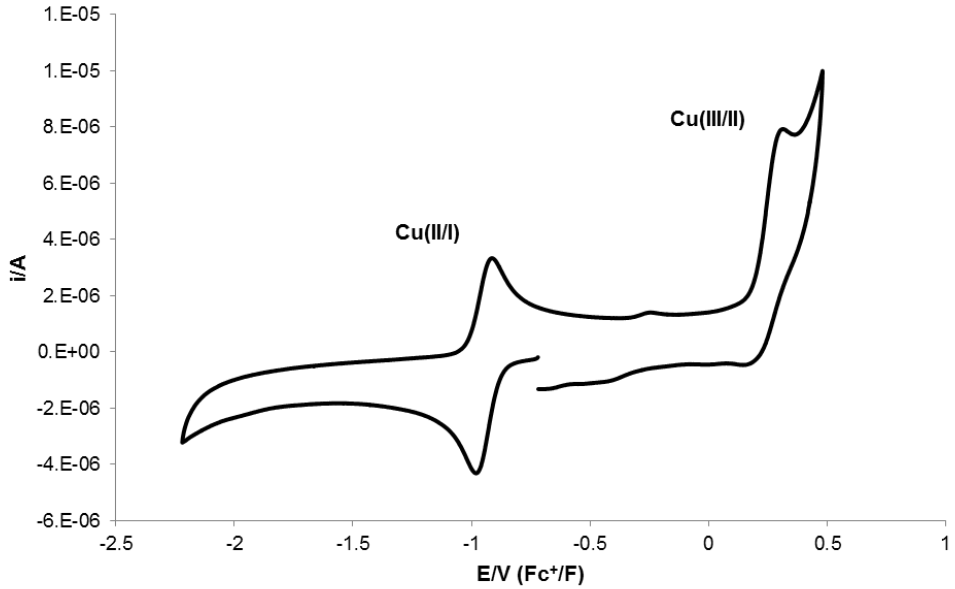

Cu(2)

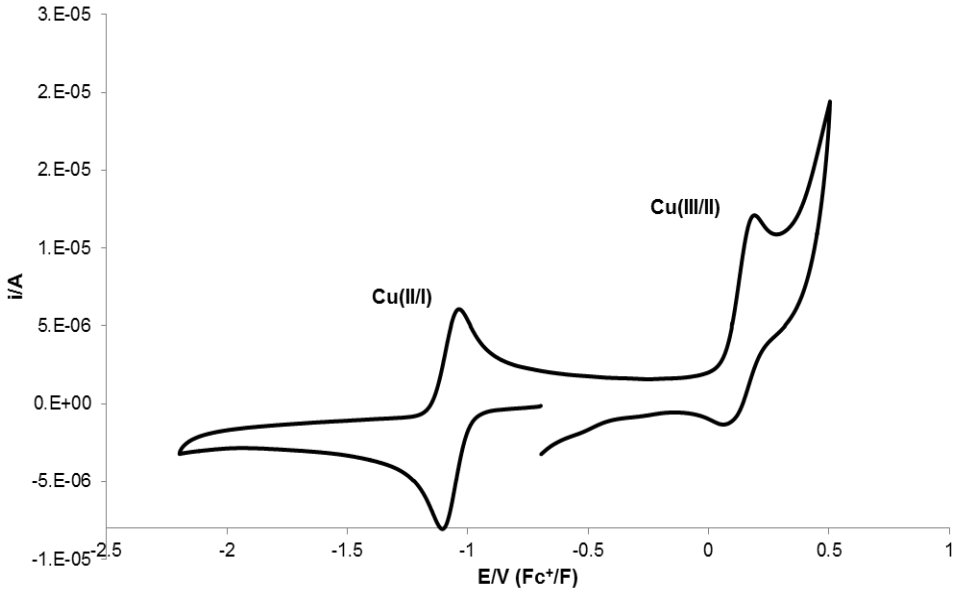

Cu(3)

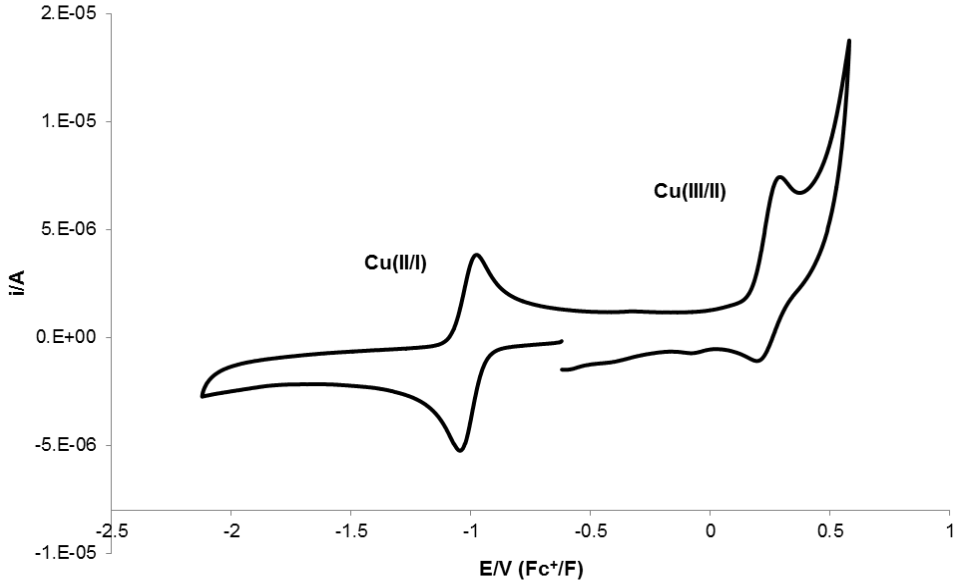
2.E-05
1.E-05
5.E-06
0.E+00
-5.E-06
-1.E-05
i/A
-2.5
-2
-1.5
-1
-0.5
0
0.5
1
E/V (Fc+/F)
Cu(II/I)
Cu(III/II)

Cu(4)

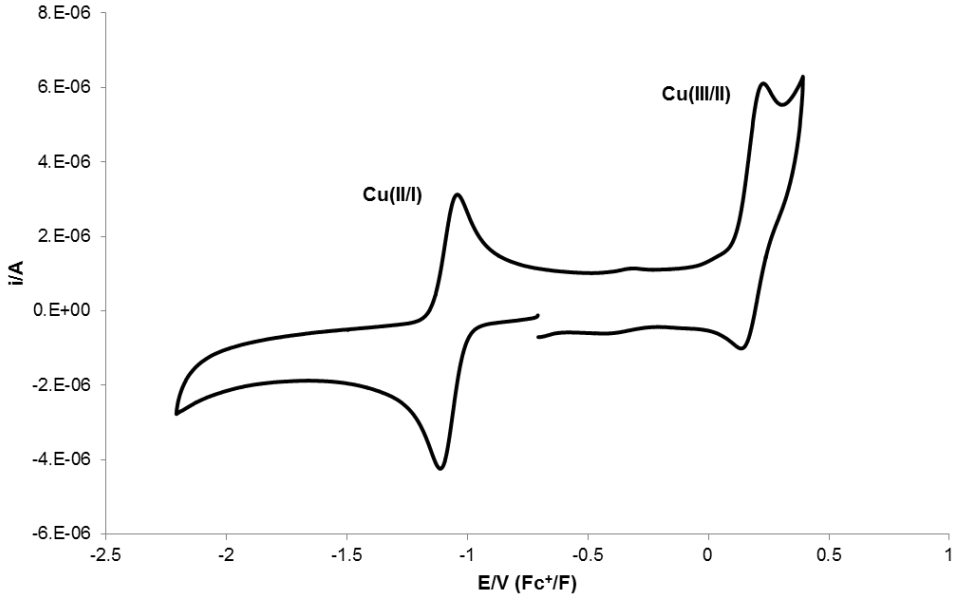
8.E-06
6.E-06
4.E-06
2.E-06
0.E+00
-2.E-06
-4.E-06
-6.E-06
i/A
-2.5
-2
-1.5
-1
-0.5
0
0.5
1
E/V (Fc+/F)
Cu(II/I)
Cu(III/II)

Cu(5)

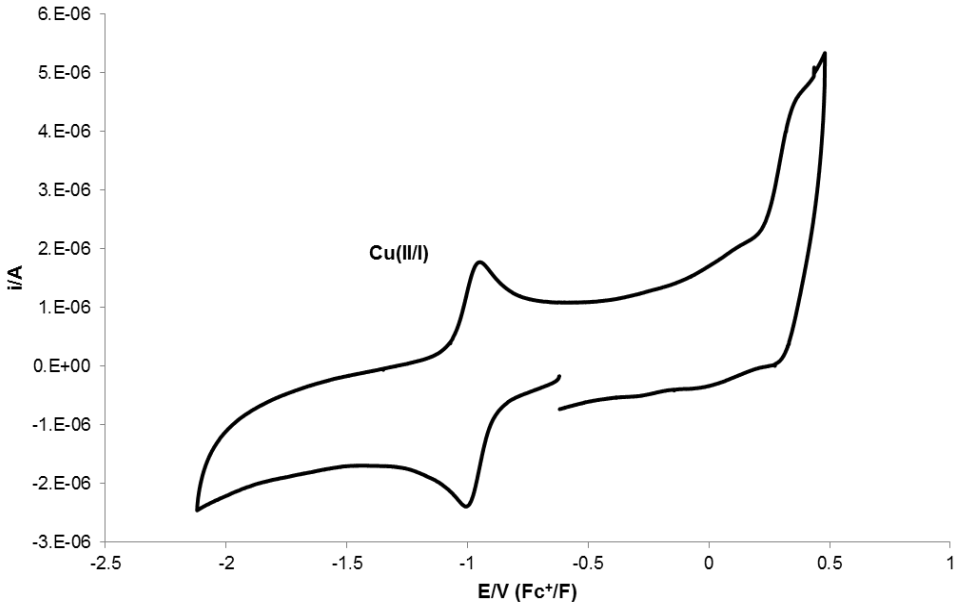
6.E-06
5.E-06
4.E-06
3.E-06
2.E-06
1.E-06
0.E+00
-1.E-06
-2.E-06
-3.E-06
i/A
Cu(II/I)
-2.5
-2
-1.5
-1
-0.5
0
0.5
1
E/V (Fc+/F)

Cu(6)

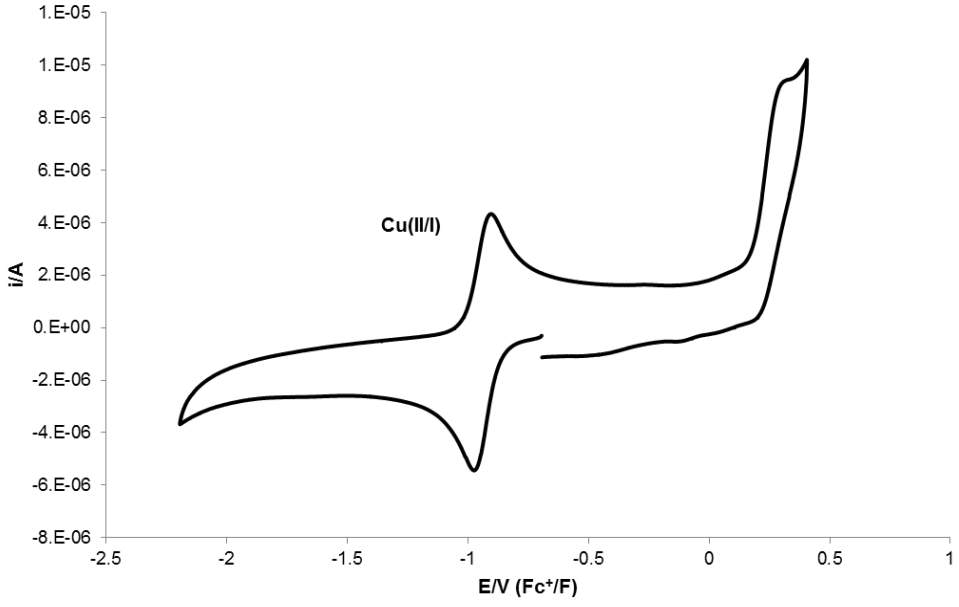
1.E-05
1.E-05
8.E-06
6.E-06
4.E-06
2.E-06
0.E+00
-2.E-06
-4.E-06
-6.E-06
-8.E-06
i/A
Cu(II/I)
-2.5
-2
-1.5
-1
-0.5
0
0.5
1
E/V (Fc+/F)

Cu(7)

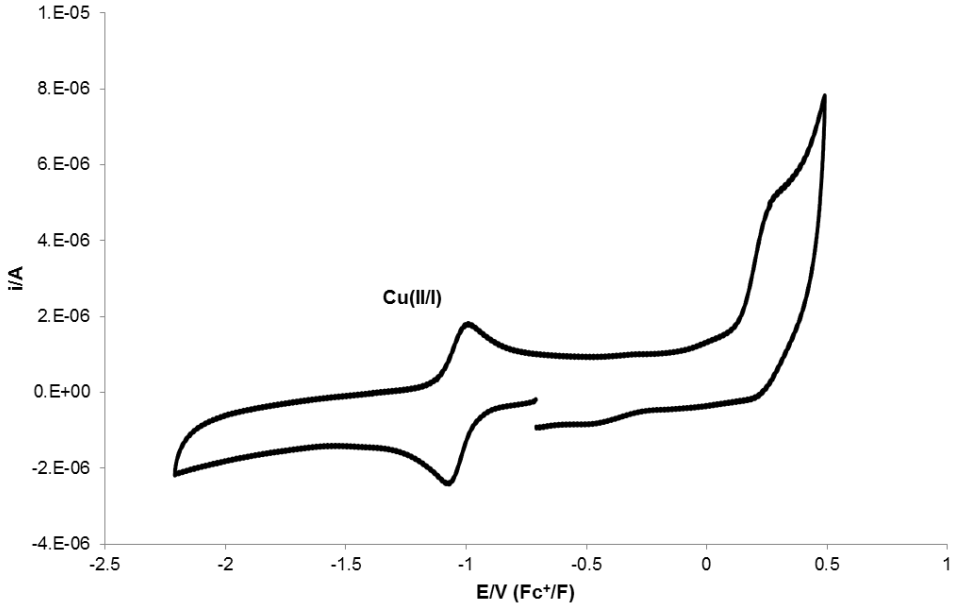
1.E-05
8.E-06
6.E-06
4.E-06
2.E-06
0.E+00
-2.E-06
-4.E-06
i/A
Cu(II/I)
-2.5
-2
-1.5
-1
-0.5
0
0.5
1
E/V (Fc+/F)

Cu(8)

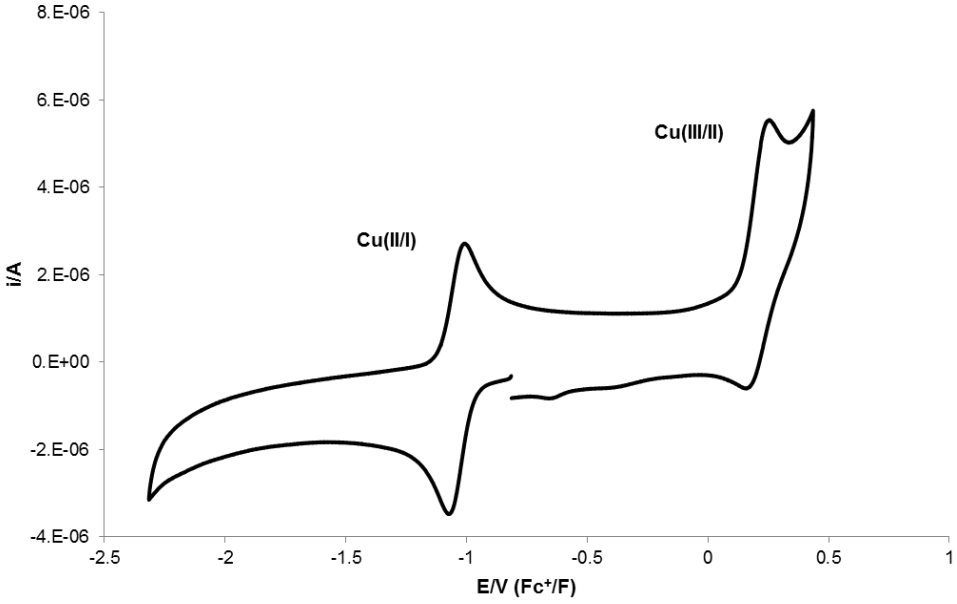
8.E-06
6.E-06
4.E-06
2.E-06
0.E+00
-2.E-06
-4.E-06
i/A
Cu(III/II)
Cu(II/I)
-2.5
-2
-1.5
-1
-0.5
0
0.5
1
E/V (Fc+/F)

Cu(9)

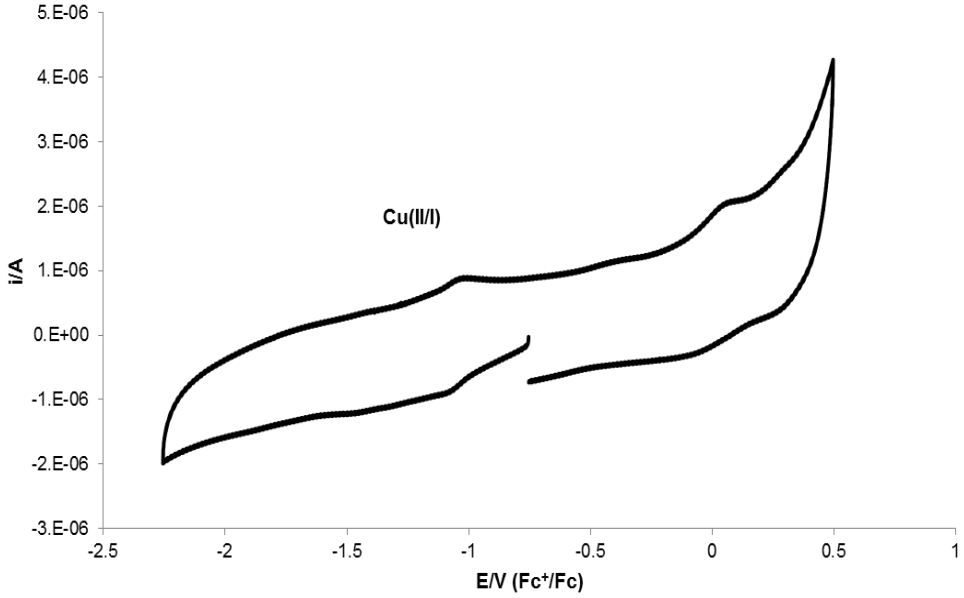
5.E-06
4.E-06
3.E-06
2.E-06
1.E-06
0.E+00
-1.E-06
-2.E-06
-3.E-06
i/A
Cu(II/I)
-2.5
-2
-1.5
-1
-0.5
0
0.5
1
E/V (Fc+/Fc)

Cu(10)

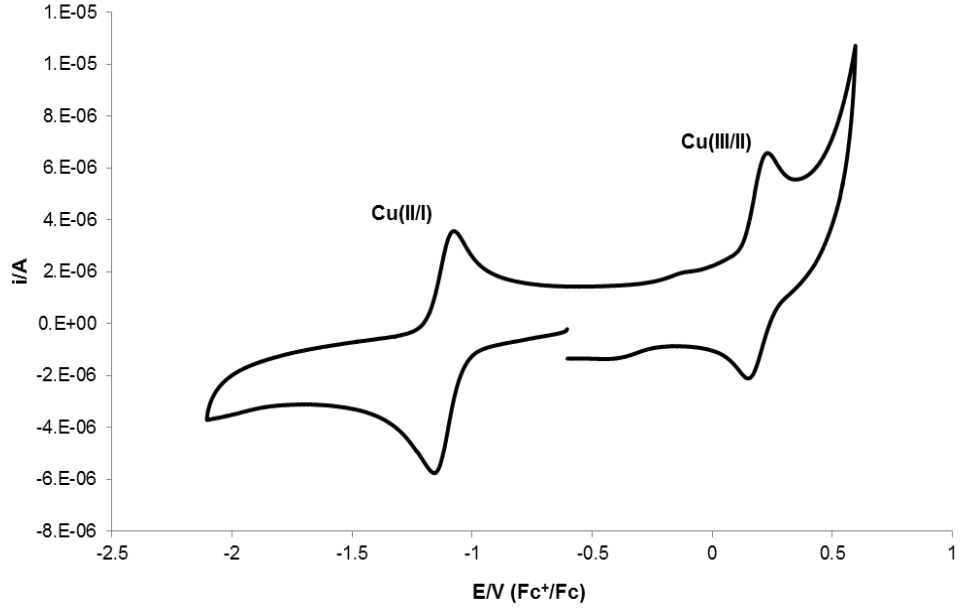
1.E-05
1.E-05
8.E-06
6.E-06
4.E-06
2.E-06
0.E+00
-2.E-06
-4.E-06
-6.E-06
-8.E-06
i/A
Cu(III/II)
Cu(II/I)
-2.5
-2
-1.5
-1
-0.5
0
0.5
1
E/V (Fc+/Fc)

Cu(11)

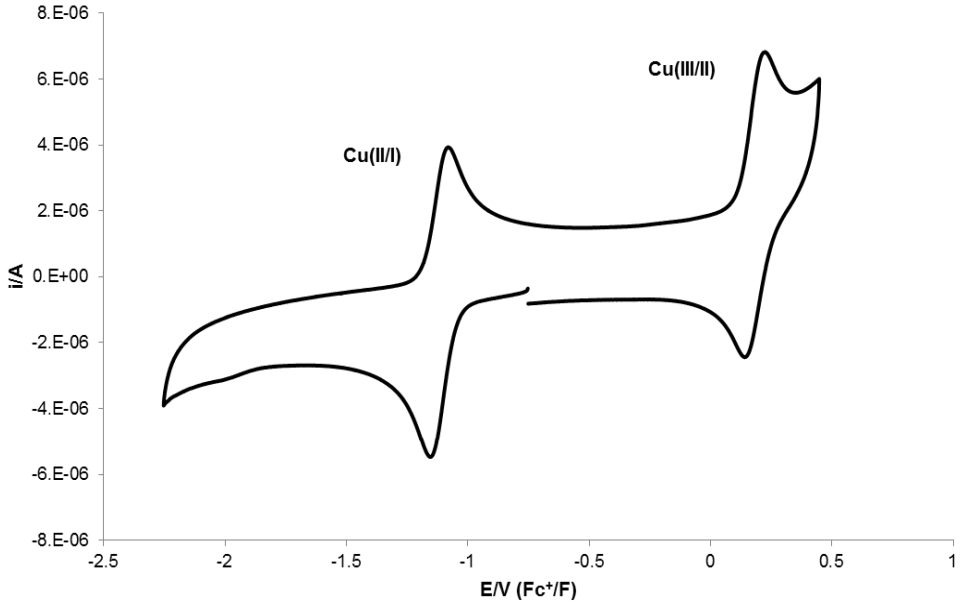
8.E-06
6.E-06
4.E-06
2.E-06
0.E+00
-2.E-06
-4.E-06
-6.E-06
-8.E-06
i/A
-2.5
-2
-1.5
-1
-0.5
0
0.5
1
E/V (Fc+/F)
Cu(II/I)
Cu(III/II)

Cu(12)

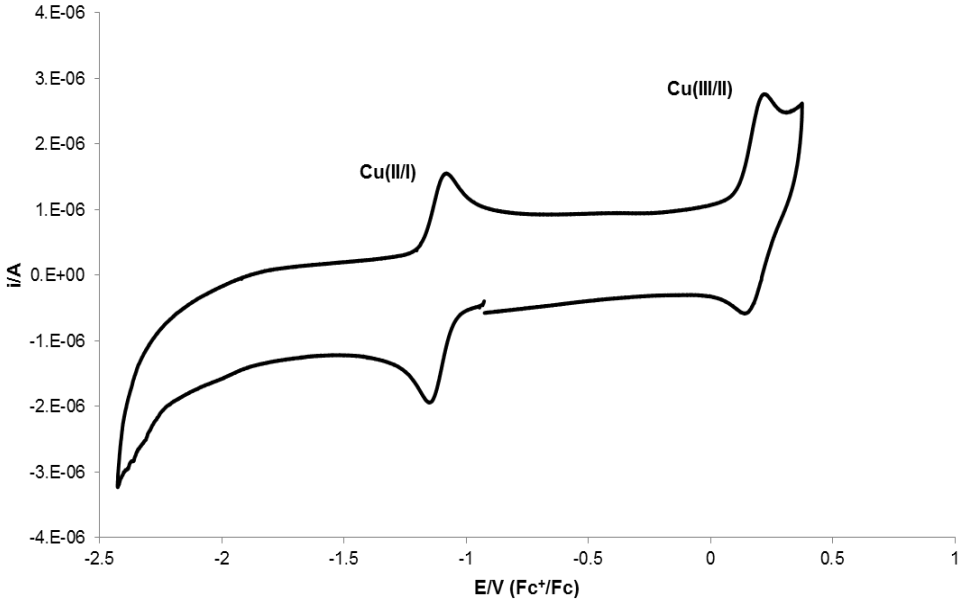
4.E-06
3.E-06
2.E-06
1.E-06
0.E+00
-1.E-06
-2.E-06
-3.E-06
-4.E-06
i/A
-2.5
-2
-1.5
-1
-0.5
0
0.5
1
E/V (Fc+/Fc)
Cu(II/I)
Cu(III/II)

Cu(13)

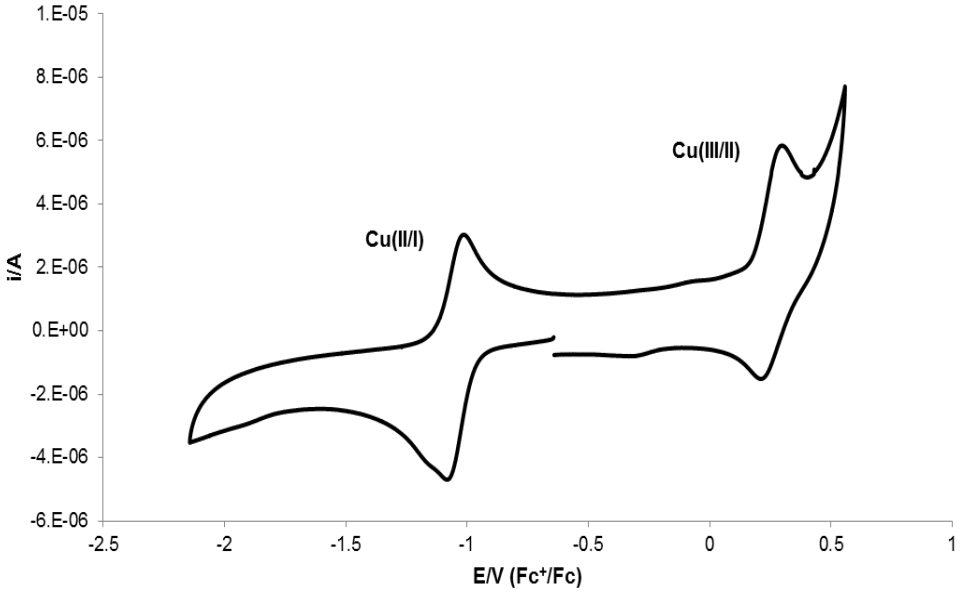
1.E-05
8.E-06
6.E-06
4.E-06
2.E-06
0.E+00
-2.E-06
-4.E-06
-6.E-06
i/A
Cu(III/II)
Cu(II/I)
-2.5
-2
-1.5
-1
-0.5
0
0.5
1
E/V (Fc+/Fc)

Cu(14)

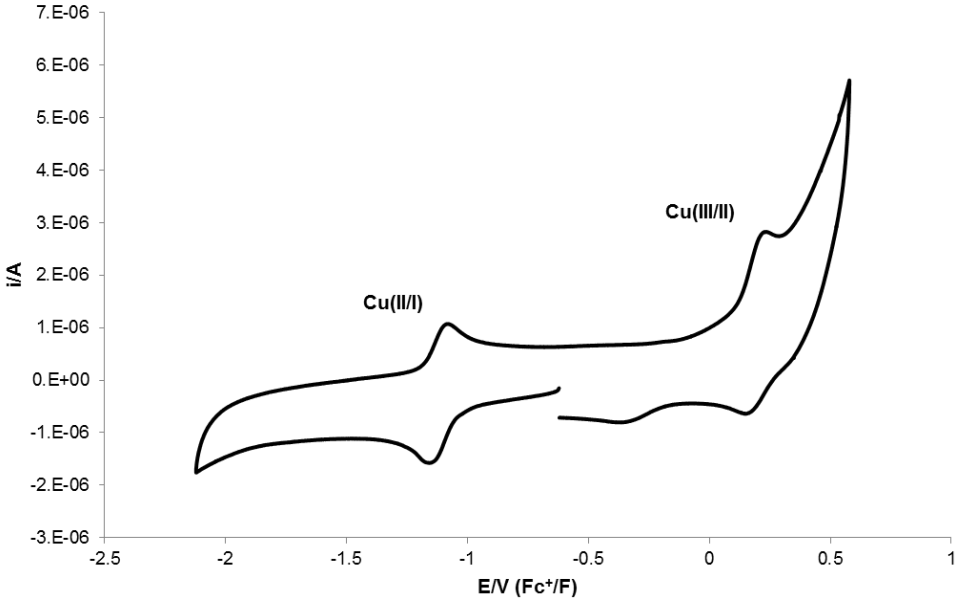
7.E-06
6.E-06
5.E-06
4.E-06
3.E-06
2.E-06
1.E-06
0.E+00
-1.E-06
-2.E-06
-3.E-06
i/A
Cu(III/II)
Cu(II/I)
-2.5
-2
-1.5
-1
-0.5
0
0.5
1
E/V (Fc+/F)

Cu(15)

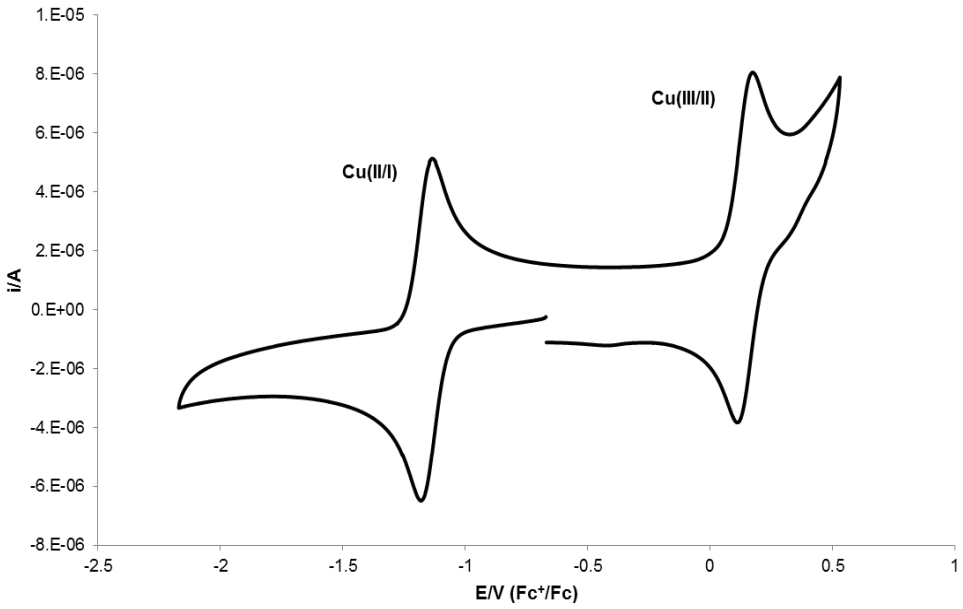
1.E-05
8.E-06
6.E-06
4.E-06
2.E-06
0.E+00
-2.E-06
-4.E-06
-6.E-06
-8.E-06
i/A
-2.5
-2
-1.5
-1
-0.5
0
0.5
1
E/V (Fc+/Fc)
Cu(II/I)
Cu(III/II)

Cu(16)

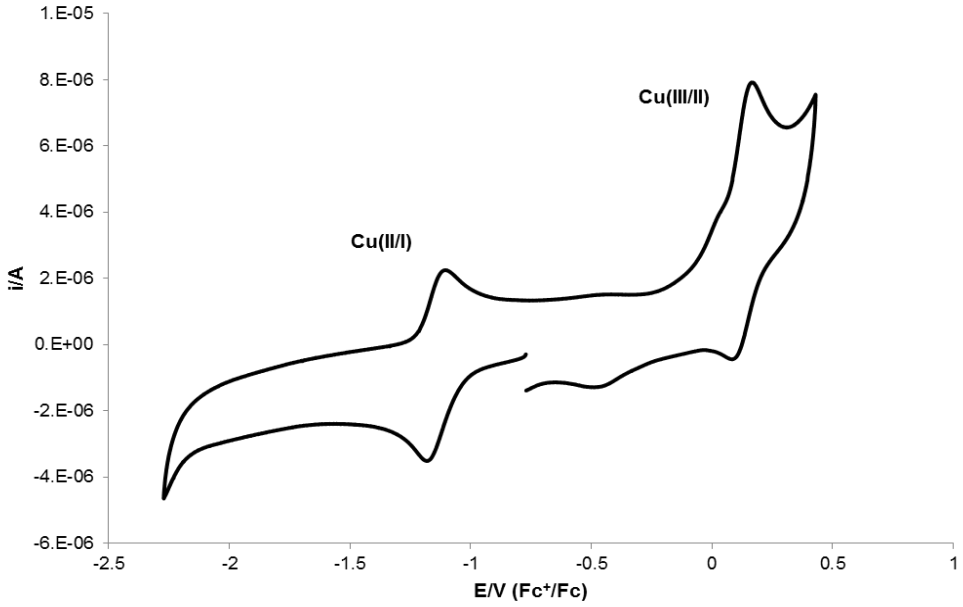
1.E-05
8.E-06
6.E-06
4.E-06
2.E-06
0.E+00
-2.E-06
-4.E-06
-6.E-06
i/A
-2.5
-2
-1.5
-1
-0.5
0
0.5
1
E/V (Fc+/Fc)
Cu(II/I)
Cu(III/II)

Cu(17)

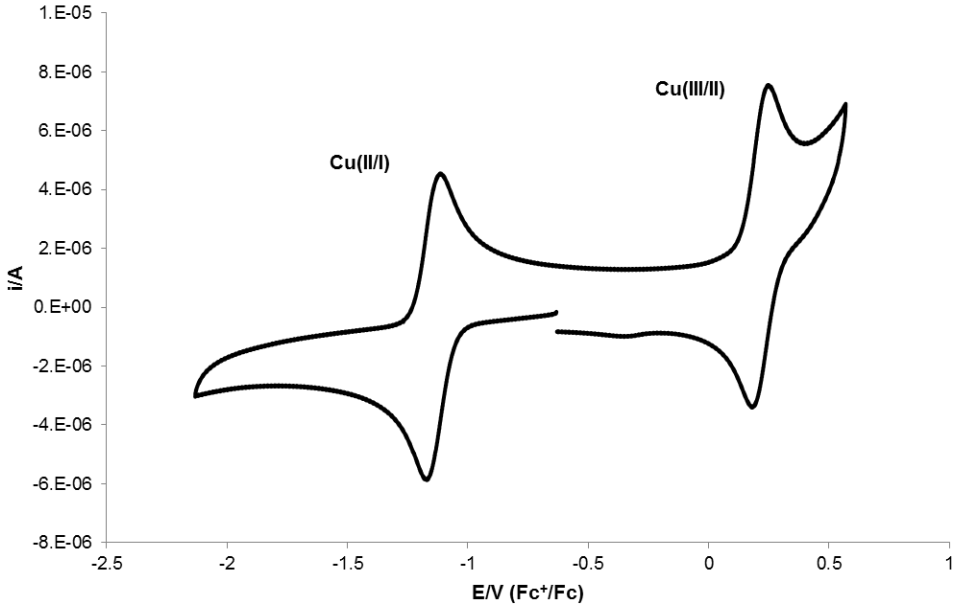
1.E-05
8.E-06
6.E-06
4.E-06
2.E-06
0.E+00
-2.E-06
-4.E-06
-6.E-06
-8.E-06
i/A
-2.5
-2
-1.5
-1
-0.5
0
0.5
1
E/V (Fc+/Fc)
Cu(II/I)
Cu(III/II)

Cu(18)

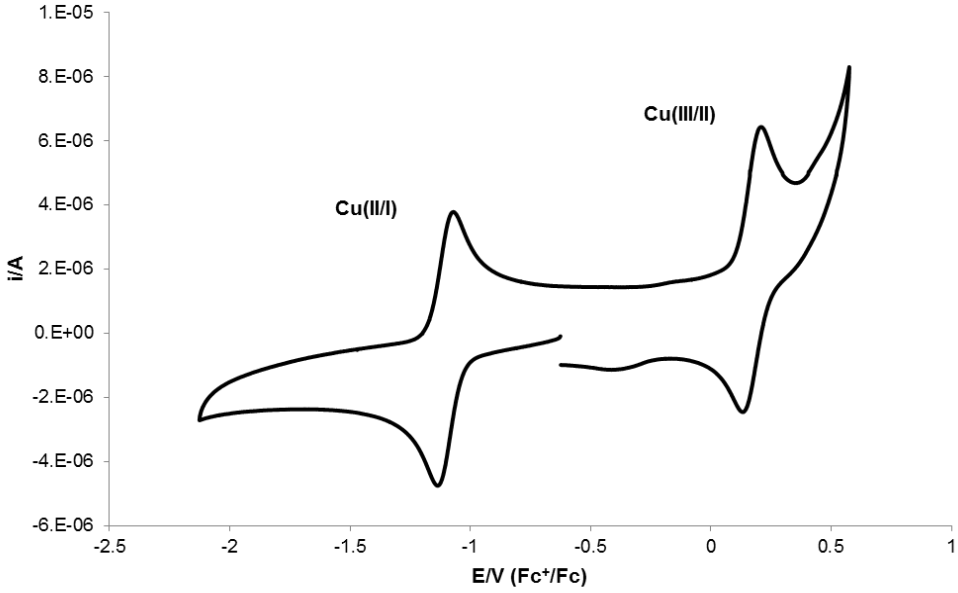
1.E-05
8.E-06
6.E-06
4.E-06
2.E-06
0.E+00
-2.E-06
-4.E-06
-6.E-06
i/A
-2.5
-2
-1.5
-1
-0.5
0
0.5
1
E/V (Fc+/Fc)
Cu(II/I)
Cu(III/II)

Cu(19)

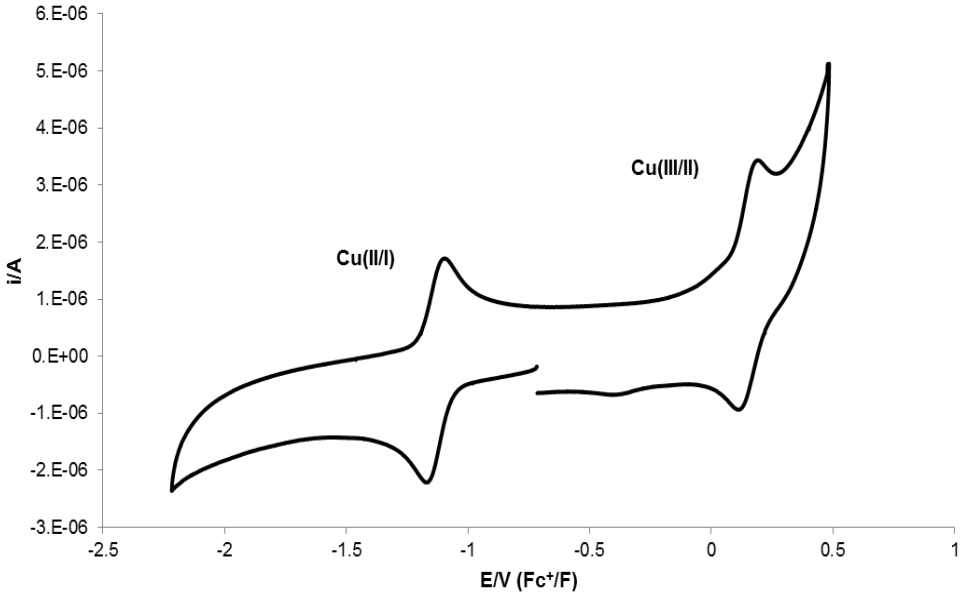
6.E-06
5.E-06
4.E-06
3.E-06
2.E-06
1.E-06
0.E+00
-1.E-06
-2.E-06
-3.E-06
i/A
Cu(III/II)
Cu(II/I)
-2.5
-2
-1.5
-1
-0.5
0
0.5
1
E/V (Fc+/F)

Cu(20)

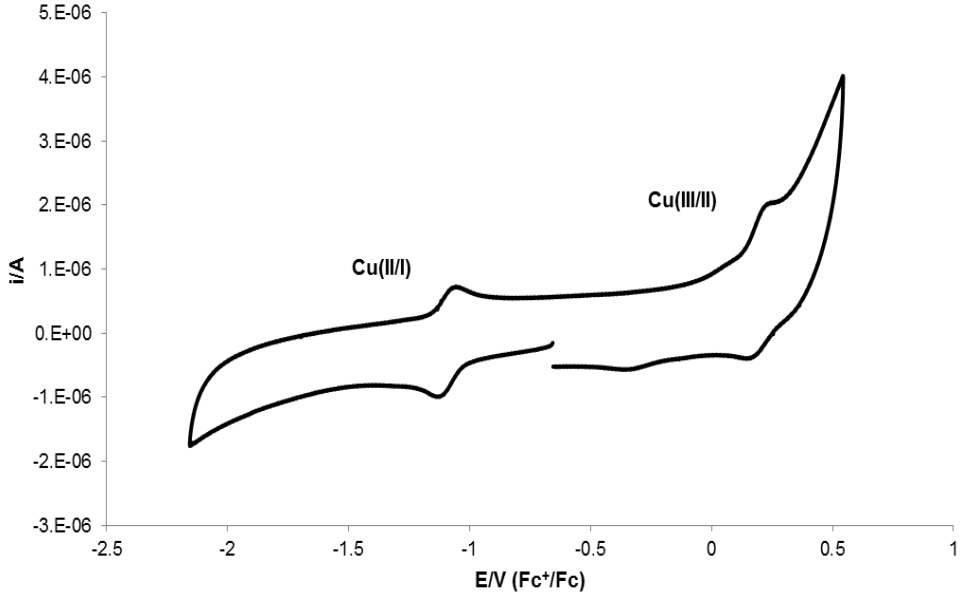
5.E-06
4.E-06
3.E-06
2.E-06
1.E-06
0.E+00
-1.E-06
-2.E-06
-3.E-06
i/A
Cu(III/II)
Cu(II/I)
-2.5
-2
-1.5
-1
-0.5
0
0.5
1
E/V (Fc+/Fc)

REFERENCES

1. McHargue JS. The occurrence of copper, manganese, zinc, nickel and cobalt, in soils, plants and animals, and their possible function as vital factors. J Agric Res. 1925;30:193-6.

2. McHargue JS. Further evidence that small quantities of copper, manganese and zinc are factors in the metabolism of animals. Am J Physiol.192;77:245-55.

3. Popova TV, Aksenova NV. Complexes of copper in unstable oxidation states. Russ J Coord Chem. 2003;29(11):743-65.

4. Bollermann T, Prabusankar G, Gemel C, Seidel RW, Winter M, Fischer RA. First dinuclear copper/gallium complexes: supporting Cu0 and CuI centres by low-Valent organogallium ligands. Chem Eur J. 2010;16(29):8846-53.

5. Kaim W, Rall J. Copper- a “modern” bioelement. Angew Chem Int Ed Eng. 1996;35(1):43-60.

6. Pearson RG. Hard and soft acids and bases. J Am Chem Soc. 1963;85(22):3533-9.

7. Cotton AF, Wilkinson G, Bochmann M, Murillo CA. Advanced inorganic chemistry. 6th ed. New Delhi, India: Wiley; 1999.

8. Liu CW, Stubbs T, Staples RJ, Fackler JP. Syntheses and structural characterizations of two new Cu-S clusters of dialkyl dithiophosphates: a sulfide-centered CuI8 cube, {Cu8[S2P(OiPr)2]6(.mu.8-S)}, and a distorted octahedral {Cu6[S2P(OEt)2]6.cntdot.2H2O} cluster. J Am Chem Soc. 1995;117(38):9778-9.

9. Cai Z, Anderson CJ. Chelators for copper radionuclides in positron emission tomography radiopharmaceuticals. J Labelled Compd Radiopharm. 2014;57(4):224-30.

10. Blower PJ, Lewis JS, Zweit J. Copper radionuclides and radiopharmaceuticals in nuclear medicine. Nucl Med Biol. 1996;23(8):957-80.

11. Puig S, Thiele DJ. Molecular mechanisms of copper uptake and distribution. Curr Opin Chem Biol. 2002;6(2):171-80.

12. Kim B-E, Nevitt T, Thiele DJ. Mechanisms for copper acquisition, distribution and regulation. Nat Chem Biol. 2008;4(3):176-85.

13. Zimmermann M, Clarke O, Gulbis JM, Keizer DW, Jarvis RS, Cobbett CS, et al. Metal binding affinities of Arabidopsis zinc and copper transporters: selectivities match the relative, but not the absolute, affinities of their amino-terminal domains. Biochemistry. 2009;48(49):11640-54.

14. Halliwell B, Gutteridge JM. Oxygen toxicity, oxygen radicals, transition metals and disease. Biochem J. 1984;219(1):1-14.

15. Linder MC, Wooten L, Cerveza P, Cotton S, Shulze R, Lomeli N. Copper transport. Am J Clin Nutr. 1998;67(5):965s-71s

.

16. Linder MC, Hazegh-Azam M. Copper biochemistry and molecular biology. Am J Clin Nutr. 1996;63(5):797s-811s.

17. Linder MC. Biochemistry of copper. 1st ed. New York, United States: Plenum Press; 1991.

18. Boal AK, Rosenzweig AC. Structural biology of copper trafficking. Chem Rev. 2009;109(10):4760-79.

19. Rosenzweig AC, O'Halloran TV. Structure and chemistry of the copper chaperone proteins. Curr Opin Chem Biol. 2000;4(2):140-7.

20. Lutsenko S, Barnes NL, Bartee MY, Dmitriev OY. Function and regulation of human copper-transporting ATPases. Physiol Rev. 2007;87(3):1011-46.

21. Leary SC, Winge DR, Cobine PA. "Pulling the plug" on cellular copper: The role of mitochondria in copper export. Biochim Biophys Acta. 2009;1793(1):146-53.

22. Beaino W, Guo Y, Chang AJ, Anderson CJ. Roles of Atox1 and p53 in the trafficking of copper-64 to tumor cell nuclei: implications for cancer therapy. J Biol Inorg Chem. 2014;19(3):427-38.

23. Maryon EB, Molloy SA, Kaplan JH. Cellular glutathione plays a key role in copper uptake mediated by human copper transporter 1. Am J Physiol Cell Physiol. 2013;304(8):C768-C79.

24. De Feo CJ, Aller SG, Siluvai GS, Blackburn NJ, Unger VM. Three-dimensional structure of the human copper transporter hCTR1. Proc Natl Acad Sci U.S.A. 2009;106(11):4237-42.

25. Puig S, Lee J, Lau M, Thiele DJ. Biochemical and genetic analyses of yeast and human high affinity copper transporters suggest a conserved mechanism for copper uptake. J Biol Chem. 2002;277(29):26021-30.

26. Lee J, Peña MMO, Nose Y, Thiele DJ. Biochemical characterization of the human copper transporter Ctr1. J Biol Chem. 2002;277(6):4380-7.

27. Ishida S, Lee J, Thiele DJ, Herskowitz I. Uptake of the anticancer drug cisplatin mediated by the copper transporter Ctr1 in yeast and mammals. Proc Natl Acad Sci U.S.A. 2002;99(22):14298-302.

28. Petris MJ, Smith K, Lee J, Thiele DJ. Copper-stimulated endocytosis and degradation of the human copper transporter, hCtr1. J Biol Chem. 2003;278(11):9639-46.

29. Nose Y, Kim B-E, Thiele DJ. Ctr1 drives intestinal copper absorption and is essential for growth, iron metabolism, and neonatal cardiac function. Cell Metab. 2006;4(3):235-44.

30. Arredondo M, Munoz P, Mura CV, Nunez MT. DMT1, a physiologically relevant apical Cu1+ transporter of intestinal cells. Am J Physiol Cell Physiol. 2003;284(6):C1525-30.

31. Espinoza A, Le Blanc S, Olivares M, Pizarro F, Ruz M, Arredondo M. Iron, copper, and zinc transport: inhibition of divalent metal transporter 1 (DMT1) and human copper transporter 1 (hCTR1) by shRNA. Biol Trace Elem Res. 2012;146(2):281-6.

32. Jiang L, Garrick MD, Garrick LM, Zhao L, Collins JF. Divalent metal transporter 1 (DMT1) mediates copper transport in the duodenum of iron-deficient rats and when overexpressed in iron-deprived HEK-293 cells. J Nutr. 2013;143(12):1927-33.

33. Lin C, Zhang Z, Wang T, Chen C, James Kang Y. Copper uptake by DMT1: a compensatory mechanism for CTR1 deficiency in human umbilical vein endothelial cells. Metallomics. 2015;7(8):1285-9.

34. Rees EM, Thiele DJ. Identification of a vacuole-associated metalloreductase and its role in Ctr2-mediated intracellular copper mobilization. J Biol Chem. 2007;282(30):21629-38.

35. van den Berghe PV, Folmer DE, Malingre HE, van Beurden E, Klomp AE, van de Sluis B, et al. Human copper transporter 2 is localized in late endosomes and lysosomes and facilitates cellular copper uptake. Biochem J. 2007;407(1):49-59.

36. Atkinson A, Winge DR. Metal acquisition and availability in the mitochondria. Chem Rev. 2009;109(10):4708-21.

37. Vest K, Cobine P. Copper in mitochondria. In: Maret W, Wedd AG, editors. Binding, transport and storage of metal ions in biological cells. 1st ed. Cambridge, United Kingdom: The Royal Society of Chemistry; 2014. 500-23.

38. Wang B, Dong D, Kang YJ. Copper chaperone for superoxide dismutase-1 transfers copper to mitochondria but does not affect cytochrome c oxidase activity. Exp Biol Med. 2013;238(9):1017-23.

39. Horng Y-C, Cobine PA, Maxfield AB, Carr HS, Winge DR. Specific copper transfer from the Cox17 Metallochaperone to both Sco1 and Cox11 in the assembly of yeast cytochrome c oxidase. J Biol Chem. 2004;279(34):35334-40.

40. Petris MJ, Mercer JF, Culvenor JG, Lockhart P, Gleeson PA, Camakaris J. Ligand-regulated transport of the Menkes copper P-type ATPase efflux pump from the Golgi apparatus to the plasma membrane: a novel mechanism of regulated trafficking. EMBO J. 1996;15(22):6084-95.

41. Cater MA, La Fontaine S, Shield K, Deal Y, Mercer JF. ATP7B mediates vesicular sequestration of copper: insight into biliary copper excretion. Gastroenterology. 2006;130(2):493-506.

42. Balamurugan K, Schaffner W. Copper homeostasis in eukaryotes: teetering on a tightrope. Biochim Biophys Acta. 2006;1763(7):737-46.

43. Rosenzweig AC. Copper delivery by metallochaperone proteins. Acc Chem Res. 2001;34(2):119-28.

44. Furukawa Y, Torres AS, O'Halloran TV. Oxygen-induced maturation of SOD1: a key role for disulfide formation by the copper chaperone CCS. EMBO J. 2004;23(14):2872-81.

45. Bertinato J, L'Abbe MR. Copper modulates the degradation of copper chaperone for Cu,Zn superoxide dismutase by the 26 S proteosome. J Biol Chem. 2003;278(37):35071-8.

46. Carroll MC, Girouard JB, Ulloa JL, Subramaniam JR, Wong PC, Valentine JS, et al. Mechanisms for activating Cu- and Zn-containing superoxide dismutase in the absence of the CCS Cu chaperone. Proc Natl Acad Sci U.S.A. 2004;101(16):5964-9.

47. Qin Z, Itoh S, Jeney V, Ushio-Fukai M, Fukai T. Essential role for the Menkes ATPase in activation of extracellular superoxide dismutase: implication for vascular oxidative stress. FASEB J. 2006;20(2):334-6.

48. Weiss KC, Linder MC. Copper transport in rats involving a new plasma protein. Am J Physiol. 1985;249(1 Pt 1):E77-88.

49. Donley SA, Ilagan BJ, Rim H, Linder MC. Copper transport to mammary gland and milk during lactation in rats. Am J Physiol Endocrinol Metab. 2002;283(4):E667-E75.

50. Moriya M, Ho Y-H, Grana A, Nguyen L, Alvarez A, Jamil R, et al. Copper is taken up efficiently from albumin and α(2)-macroglobulin by cultured human cells by more than one mechanism. Am J Physiol Cell Physiol. 2008;295(3):C708-C21.

51. Rozga M, Sokolowska M, Protas AM, Bal W. Human serum albumin coordinates Cu(II) at its N-terminal binding site with 1 pM affinity. J Biol Inorg Chem. 2007;12(6):913-8.

52. McArdle HJ, Guthrie JR, Ackland ML, Danks DM. Albumin has no role in the uptake of copper by human fibroblasts. J Inorg Biochem. 1987;31(2):123-31.

53. Vargas EJ, Shoho AR, Linder MC. Copper transport in the Nagase analbuminemic rat. Am J Physiol. 1994;267(2 Pt 1):G259-69.

54. Wirth PL, Linder MC. Distribution of copper among components of human serum. J Natl Cancer Inst. 1985;75(2):277-84.

55. Kim H, Son H-Y, Bailey SM, Lee J. Deletion of hepatic Ctr1 reveals its function in copper acquisition and compensatory mechanisms for copper homeostasis. Am J Physiol Gastrointest Liver Physiol. 2009;296(2):G356-G64.

56. Fedoseienko A, Bartuzi P, van de Sluis B. Functional understanding of the versatile protein copper metabolism MURR1 domain 1 (COMMD1) in copper homeostasis. Ann N Y Acad Sci. 2014;1314:6-14.

57. Holmberg CGL, Laurell C-B. Investigations in serum copper. II. Isolation of the copper containing protein, and a description of some of its properties. Acta Chem Scand. 1948;2:550-6.

58. Harris ZL, Takahashi Y, Miyajima H, Serizawa M, MacGillivray RT, Gitlin JD. Aceruloplasminemia: molecular characterization of this disorder of iron metabolism. Proc Natl Acad Sci U.S.A. 1995;92(7):2539-43.

59. Bielli P, Calabrese L. Structure to function relationships in ceruloplasmin: a 'moonlighting' protein. Cell Mol Life Sci. 2002;59(9):1413-27.

60. Stevens MD, DiSilvestro RA, Harris ED. Specific receptor for ceruloplasmin in membrane fragments from aortic and heart tissues. Biochemistry. 1984;23(2):261-6.

61. Campbell CH, Brown R, Linder MC. Circulating ceruloplasmin is an important source of copper for normal and malignant animal cells. Biochim Biophys Acta. 1981;678(1):27-38.

62. Hellman NE, Gitlin JD. Ceruloplasmin metabolism and function. Annu Rev Nutr. 2002;22:439-58.

63. Percival SS, Harris ED. Copper transport from ceruloplasmin: characterization of the cellular uptake mechanism. Am J Physiol. 1990;258(1 Pt 1):C140-6.

64. Osaki S, Johnson DA, Frieden E. The possible significance of the ferrous oxidase activity of ceruloplasmin in normal human serum. J Biol Chem. 1966;241(12):2746-51.

65. Ragan HA, Nacht S, Lee GR, Bishop CR, Cartwright GE. Effect of ceruloplasmin on plasma iron in copper-deficient swine. Am J Physiol. 1969;217(5):1320-3.

66. Lindley PF, Card G, Zaitseva I, Zaitsev V, Reinhammar B, Selin-Lindgren E, et al. An X-ray structural study of human ceruloplasmin in relation to ferroxidase activity. J Biol Inorg Chem. 1997;2(4):454-63.

67. McCord JM, Fridovich I. Superoxide dismutase. An enzymic function for erythrocuprein (hemocuprein). J Biol Chem. 1969;244(22):6049-55.

68. Tainer JA, Getzoff ED, Richardson JS, Richardson DC. Structure and mechanism of copper, zinc superoxide dismutase. Nature. 1983;306(5940):284-7.

69. Tainer JA, Getzoff ED, Beem KM, Richardson JS, Richardson DC. Determination and analysis of the 2 Å structure of copper, zinc superoxide dismutase. J Mol Biol. 1982;160(2):181-217.

70. Banci L, Bertini I, Cantini F, D'Amelio N, Gaggelli E. Human SOD1 before harboring the catalytic metal: solution structure of copper-depleted, disulfide-reduced form. J Biol Chem. 2006;281(4):2333-7.

71. Kaim W, Schwederski B, Klein A. Bioinorganic Chemistry-Inorganic elements in the chemistry of life: an introduction and guide. 2nd ed. Chichester, United Kingdom: John Wiley & Sons; 2013.

72. Roberts BR, Tainer JA, Getzoff ED, Malencik DA, Anderson SR, Bomben VC, et al. Structural characterization of zinc-deficient human superoxide dismutase and implications for ALS. J Mol Biol. 2007;373(4):877-90.

73. Murakami K, Murata N, Noda Y, Tahara S, Kaneko T, Kinoshita N, et al. SOD1 (copper/zinc superoxide dismutase) deficiency drives amyloid beta protein oligomerization and memory loss in mouse model of Alzheimer's disease. J Biol Chem. 2011;286(52):44557-68.

74. Faxen K, Gilderson G, Adelroth P, Brzezinski P. A mechanistic principle for proton pumping by cytochrome c oxidase. Nature. 2005;437(7056):286-9.

75. Blomberg MR. Mechanism of oxygen reduction in cytochrome c oxidase and the role of the active site tyrosine. Biochemistry. 2016;55(3):489-500.

76. Yoshikawa S, Muramoto K, Shinzawa-Itoh K. Proton-pumping mechanism of cytochrome c oxidase. Annu Rev Biophys. 2011;40(1):205-23.

77. Pan LP, He QZ, Chan SI. The nature of zinc in cytochrome c oxidase. J Biol Chem. 1991;266(28):19109-12.

78. Robinson BH. Human cytochrome oxidase deficiency. Pediatr Res. 2000;48(5):581-5.

79. Cardoso SM, Proenca MT, Santos S, Santana I, Oliveira CR. Cytochrome c oxidase is decreased in Alzheimer's disease platelets. Neurobiol Aging. 2004;25(1):105-10.

80. Lucero HA, Kagan HM. Lysyl oxidase: an oxidative enzyme and effector of cell function. Cell Mol Life Sci. 2006;63(19-20):2304-16.

81. Erler JT, Bennewith KL, Nicolau M, Dornhofer N, Kong C, Le QT, et al. Lysyl oxidase is essential for hypoxia-induced metastasis. Nature. 2006;440(7088):1222-6.

82. Kaneda A, Wakazono K, Tsukamoto T, Watanabe N, Yagi Y, Tatematsu M, et al. Lysyl oxidase is a tumor suppressor gene inactivated by methylation and loss of heterozygosity in human gastric cancers. Cancer Res. 2004;64(18):6410-5.

83. Yoshizawa K, Kihara N, Kamachi T, Shiota Y. Catalytic mechanism of dopamine beta-monooxygenase mediated by Cu(III)-oxo. Inorg Chem. 2006;45(7):3034-41.

84. Robertson D, Haile V, Perry SE, Robertson RM, Phillips JA, 3rd, Biaggioni I. Dopamine beta-hydroxylase deficiency. A genetic disorder of cardiovascular regulation. Hypertension. 1991;18(1):1-8.

85. Jepma M, Deinum J, Asplund CL, Rombouts SA, Tamsma JT, Tjeerdema N, et al. Neurocognitive function in dopamine-beta-hydroxylase deficiency. Neuropsychopharmacology. 2011;36(8):1608-19.

86. Cross AJ, Crow TJ, Perry EK, Perry RH, Blessed G, Tomlinson BE. Reduced dopamine-beta-hydroxylase activity in Alzheimer's disease. Br Med J (Clin Res Ed).1981;282(6258):93-4.

87. Kim YJ, Uyama H. Tyrosinase inhibitors from natural and synthetic sources: structure, inhibition mechanism and perspective for the future. Cell Mol Life Sci. 2005;62(15):1707-23.

88. Blower PJ. Other radioelements. In: Theobald T, editor. Sampson's textbook of radiopharmacy. 4th ed. London, United Kingdom: Pharmaceutical Press; 2011. 189-99.

89. Lewis JS, Laforest R, Buettner TL, Song S-K, Fujibayashi Y, Connett JM, et al. Copper-64-diacetyl-bis (*N*^{4}-methylthiosemicarbazone): an agent for radiotherapy. Proc Natl Acad Sci U.S.A. 2001;98(3):1206-11.

90. Smith SV. Molecular imaging with copper-64. J Inorg Biochem. 2004;98(11):1874-901.

91. McCarthy DW, Bass LA, Cutler PD, Shefer RE, Klinkowstein RE, Herrero P, et al. High purity production and potential applications of copper-60 and copper-61. Nucl Med Biol. 1999;26(4):351-8.

92. Tolmachev V, Lundqvist H, Einarsson L. Production of ^{61}Cu from a natural nickel target. Appl Radiat Isot. 1998;49(1–2):79-81.

93. Williams H, Robinson S, Julyan P, Zweit J, Hastings D. A comparison of PET imaging characteristics of various copper radioisotopes. Eur J Nucl Med Mol Imaging. 2005;32(12):1473-80.

94. Smith NA, Bowers DL, Ehst DA. The production, separation, and use of ^{67}Cu for radioimmunotherapy: A review. Appl Radiat Isot. 2012;70(10):2377-83.

95. Novak-Hofer I, Schubiger A. Copper-67 as a therapeutic nuclide for radioimmunotherapy. Eur J Nucl Med Mol Imaging. 2002;29(6):821-30.

96. Lacy JL, Guerrero L, Chiu R, Liang S, Hall L, Stone CK, editors. PET Imaging with ^{62}Cu-ETS in a human clinical trial at the university of wisconsin-madison. IEEE Nucl Sci Symp Conf Rec. 2007;5:4027-4030.

97. Haynes NG, Lacy JL, Nayak N, Martin CS, Dai D, Mathias CJ, et al. Performance of a ^{62}Zn/^{62}Cu generator in clinical trials of PET perfusion agent ^{62}Cu-PTSM. J Nucl Med. 2000;41(2):309-14.

98. Wong TZ, Lacy JL, Petry NA, Hawk TC, Sporn TA, Dewhirst MW, et al. PET of hypoxia and perfusion with ^{62}Cu-ATSM and ^{62}Cu-PTSM using a ^{62}Zn/^{62}Cu generator. Am J Roentgenol. 2008;190(2):427-32.

99. McCarthy DW, Shefer RE, Klinkowstein RE, Bass LA, Margeneau WH, Cutler CS, et al. Efficient production of high specific activity ^{64}Cu using a biomedical cyclotron. Nucl Med Biol. 1997;24(1):35-43.

100. Obata A, Kasamatsu S, McCarthy DW, Welch MJ, Saji H, Yonekura Y, et al. Production of therapeutic quantities of ^{64}Cu using a 12 MeV cyclotron. Nucl Med Biol. 2003;30(5):535-9.

101. Piel H, Qaim, S.M., & Stoecklin, G. Excitation functions of (p,xn)-reactions on natNi and highly enriched ^{62}Ni: Possibility of production of medically important radioisotope ^{62}Cu at a small cyclotron. Radiochim Acta. 1992;57(1):1-5.

102. Hilgers K, Stoll T, Skakun Y, Coenen HH, Qaim SM. Cross-section measurements of the nuclear reactions natZn(d,x)^{64}Cu, ^{66}Zn(d,α)^{64}Cu and ^{68}Zn(p,αn)^{64}Cu for production of ^{64}Cu and technical developments for small-scale production of ^{67}Cu via the ^{70}Zn(p,α)^{67}Cu process. Appl Radiat Isot. 2003;59(5–6):343-51.

103. Abbas K, Kozempel J, Bonardi M, Groppi F, Alfarano A, Holzwarth U, et al. Cyclotron production of ^{64}Cu by deuteron irradiation of ^{64}Zn. Appl Radiat Isot. 2006;64(9):1001-5.

104. Thieme S, Walther M, Preusche S, Rajander J, Pietzsch H-J, Lill J-O, et al. High specific activity ^{61}Cu via ^{64}Zn(p,α)^{61}Cu reaction at low proton energies. Appl Radiat Isot. 2013;72:169-76.

105. Rowshanfarzad P, Sabet M, Reza Jalilian A, Kamalidehghan M. An overview of copper radionuclides and production of ^{61}Cu by proton irradiation of natZn at a medical cyclotron. Appl Radiat Isot. 2006;64(12):1563-73.

106. Sun X, Anderson CJ. Production and applications of copper-64 radiopharmaceuticals. Methods Enzymol. 2004; 386:237-61.

107. Yagi M, Kondo K. Preparation of carrier-free ^{67}Cu by the ^{68}Zn(γ,p) reaction. Int J Appl Radiat Isot. 1978;29(12):757-9.

108. Jamriska D, Taylor W, Ott M, Fowler M, Heaton R. Production of high specific activity copper-67. United States; US6490330 B1, 2002.

109. Owen CA, Jr. Metabolism of radiocopper (Cu-64) in the rat. Am J Physiol. 1965;209(5):900-4.

110. Schultze MO, Simmons SJ. The use of radioactive copper in studies on nutritional anemia of rats. J Biol Chem. 1942;142(1):97-106.

111. Gibbs K, Walshe JM, Osborn SB. Simultaneous use of two radioisotopes of copper (^{64}Cu and ^{67}Cu) in the study of copper turnover in man. Clin Sci. 1969;37(3):877-8.

112. Holland JP, Ferdani R, Anderson CJ, Lewis JS. Copper-64 radiopharmaceuticals for oncologic imaging. PET Clin. 2009;4(1):49-67.

113. Cole WC, DeNardo SJ, Meares CF, McCall MJ, DeNardo GL, Epstein AL, et al. Comparative serum stability of radiochelates for antibody radiopharmaceuticals. J Nucl Med. 1987;28(1):83-90.

114. Cole WC, DeNardo SJ, Meares CF, McCall MJ, DeNardo GL, Epstein AL, et al. Serum stability of ^{67}Cu chelates: comparison with ^{111}In and ^{57}Co. Int J Rad Appl Instrum B. 1986;13(4):363-8.

115. Hueting R, Christlieb M, Dilworth JR, Garcia Garayoa E, Gouverneur V, Jones MW, et al. Bis(thiosemicarbazones) as bifunctional chelators for the room temperature 64-copper labeling of peptides. Dalton Trans. 2010;39(15):3620-32.

116. Paterson BM, Karas JA, Scanlon DB, White JM, Donnelly PS. Versatile new bis(thiosemicarbazone) bifunctional chelators: synthesis, conjugation to bombesin(7−14)-NH_2, and copper-64 radiolabeling. Inorg Chem. 2010;49(4):1884-93.

117. Cooper MS, Ma MT, Sunassee K, Shaw KP, Williams JD, Paul RL, et al. Comparison of ^{64}Cu-complexing bifunctional chelators for radioimmunoconjugation: labeling efficiency, specific activity, and in vitro/in vivo stability. Bioconjug Chem. 2012;23(5):1029-39.

118. McQuade P, Miao Y, Yoo J, Quinn TP, Welch MJ, Lewis JS. Imaging of melanoma using ^{64}Cu− and ^{86}Y−DOTA−ReCCMSH(Arg11), a cyclized peptide analogue of α-MSH. J Med Chem. 2005;48(8):2985-92.

119. Ghosh SC, Pinkston KL, Robinson H, Harvey BR, Wilganowski N, Gore K, et al. Comparison of DOTA and NODAGA as chelators for ^{64}Cu-labeled immunoconjugates. Nucl Med Biol. 2015;42(2):177-83.

120. Bass LA, Wang M, Welch MJ, Anderson CJ. In vivo transchelation of copper-64 from TETA-octreotide to superoxide dismutase in rat liver. Bioconjug Chem. 2000;11(4):527-32.

121. Prasanphanich AF, Nanda PK, Rold TL, Ma L, Lewis MR, Garrison JC, et al. [^{64}Cu-NOTA-8-Aoc-BBN(7-14)NH_2] targeting vector for positron-emission tomography imaging of gastrin-releasing peptide receptor-expressing tissues. Proc Natl Acad Sci U.S.A.2007;104(30):12462-7.

122. Liu D, Overbey D, Watkinson LD, Smith CJ, Daibes-Figueroa S, Hoffman TJ, et al. Comparative evaluation of three ^{64}Cu-labeled E. coli heat-stable enterotoxin analogues for PET imaging of colorectal cancer. Bioconjug Chem. 2010;21(7):1171-6.

123. Sun X, Wuest M, Weisman GR, Wong EH, Reed DP, Boswell CA, et al. Radiolabeling and in vivo behavior of copper-64-labeled cross-bridged cyclam ligands. J Med Chem. 2002;45(2):469-77.

124. Garrison JC, Rold TL, Sieckman GL, Figueroa SD, Volkert WA, Jurisson SS, et al. In vivo evaluation and small-animal PET/CT of a prostate cancer mouse model using ^{64}Cu bombesin analogs: side-by-side comparison of the CB-TE2A and DOTA chelation systems. J Nucl Med. 2007;48(8):1327-37.

125. Wadas TJ, Eiblmaier M, Zheleznyak A, Sherman CD, Ferdani R, Liang K, et al. Preparation and biological evaluation of (64)Cu-CB-TE2A-sst(2)-ANT, a somatostatin antagonist for PET imaging of somatostatin receptor–positive tumors. J Nucl Med. 2008;49(11):1819-27.

126. Wei L, Ye Y, Wadas TJ, Lewis JS, Welch MJ, Achilefu S, et al. (64)Cu-labeled CB-TE2A and diamsar-conjugated RGD peptide analogs for targeting angiogenesis: comparison of their biological activity. Nucl Med Biol. 2009;36(3):277-85.

127. Wadas TJ, Anderson CJ. Radiolabeling of TETA- and CB-TE2A-conjugated peptides with copper-64. Nat Protoc. 2007;1(6):3062-8.

128. Guo Y, Ferdani R, Anderson CJ. Preparation and biological evaluation of ^{64}Cu labeled Tyr3-octreotate using a phosphonic acid-based cross-bridged macrocyclic chelator. Bioconjug Chem. 2012;23(7):1470-7.

129. Jiang M, Ferdani R, Shokeen M, Anderson CJ. Comparison of two cross-bridged macrocyclic chelators for the evaluation of ^{64}Cu-labeled-LLP2A, a peptidomimetic ligand targeting VLA-4-positive tumors. Nucl Med Biol. 2013;40(2):245-51.

130. Di Bartolo N, Sargeson AM, Smith SV. New ^{64}Cu PET imaging agents for personalised medicine and drug development using the hexa-aza cage, SarAr. Org Biomol Chem. 2006;4(17):3350-7.

131. Wu Z, Liu S, Nair I, Omori K, Scott S, Todorov I, et al. (64)Cu labeled sarcophagine exendin-4 for microPET imaging of glucagon like peptide-1 receptor expression. Theranostics. 2014;4(8):770-7.

132. Paterson BM, Roselt P, Denoyer D, Cullinane C, Binns D, Noonan W, et al. PET imaging of tumours with a ^{64}Cu labeled macrobicyclic cage amine ligand tethered to Tyr3-octreotate. Dalton Trans. 2014;43(3):1386-96.

133. Paterson BM, Buncic G, McInnes LE, Roselt P, Cullinane C, Binns DS, et al. Bifunctional (64)Cu-labelled macrobicyclic cage amine isothiocyanates for immuno-positron emission tomography. Dalton Trans. 2015;44(11):4901-9.

134. Cai W, Chen K, Li Z-B, Gambhir SS, Chen X. Dual-function probe for PET and near-infrared fluorescence imaging of tumor vasculature. J Nucl Med. 2007;48(11):1862-70.

135. Rossin R, Muro S, Welch MJ, Muzykantov VR, Schuster DP. In vivo imaging of ^{64}Cu-labeled polymer nanoparticles targeted to the lung endothelium. J Nucl Med. 2008;49(1):103-11.

136. Torres Martin de Rosales R, Tavaré R, Paul RL, Jauregui-Osoro M, Protti A, Glaria A, et al. Synthesis of (64)Cu(II)–bis(dithiocarbamatebisphosphonate) and its conjugation with superparamagnetic iron oxide nanoparticles: in vivo evaluation as dual-modality PET–MRI agent. Angew Chem Int Ed Engl. 2011;50(24):5509-13.

137. Petersen AL, Binderup T, Rasmussen P, Henriksen JR, Elema DR, Kjær A, et al. ^{64}Cu loaded liposomes as positron emission tomography imaging agents. Biomaterials. 2011;32(9):2334-41.

138. Berry DJ, Torres Martin de Rosales R, Charoenphun P, Blower PJ. Dithiocarbamate complexes as radiopharmaceuticals for medical imaging. Mini Rev Med Chem. 2012;12(12):1174-83.

139. Ujjani B, Lyman S, Winkelmann D, Antholine W, Petering DH, Jones MM. Enhancement of cytotoxicity of bleomycin by dithiocarbamates: formation of bis(dithiocarbamato) Cu(II). J Inorg Biochem. 1990;38(1):81-93.

140. Charoenphun PRP, R.; Weeks, A.; Berry, D.; Shaw, K.; Mullen, G.; Ballinger, J.; Blower. PET tracers for cell labelling with the complexes of copper-64 with lipophilic ligands. Eur J Nucl Med Mol Imaging. 2011;38(2 Supplement):S294.

141. Matsumoto K, Fujibayashi Y, Konishi J, Yokoyama A. Radiolabeling and biodistribution of ^{62}Cu-dithiocarbamate--an application for the new ^{62}Zn/^{62}Cu generator. Radioisotopes. 1990;39(11):482-6.

142. Dearling JL, Lewis JS, Mullen GE, Welch MJ, Blower PJ. Copper bis(thiosemicarbazone) complexes as hypoxia imaging agents: structure-activity relationships. J Biol Inorg Chem. 2002;7(3):249-59.

143. Handley MG, Medina RA, Mariotti E, Kenny GD, Shaw KP, Yan R, et al. Cardiac hypoxia imaging: second-generation analogues of ^{64}Cu-ATSM. J Nucl Med. 2014;55(3):488-94.

144. Maurer RI, Blower PJ, Dilworth JR, Reynolds CA, Zheng Y, Mullen GE. Studies on the mechanism of hypoxic selectivity in copper bis (thiosemicarbazone) radiopharmaceuticals. J Med Chem. 2002;45(7):1420-31.

145. Blower PJ, Castle TC, Cowley AR, Dilworth JR, Donnelly PS, Labisbal E, et al. Structural trends in copper (II) bis (thiosemicarbazone) radiopharmaceuticals. Dalton Trans. 2003(23):4416-25.

146. McQuade P, Martin KE, Castle TC, Went MJ, Blower PJ, Welch MJ, et al. Investigation into ^{64}Cu-labeled bis(selenosemicarbazone) and bis(thiosemicarbazone) complexes as hypoxia imaging agents. Nucl Med Biol. 2005;32(2):147-56.

147. Fujibayashi Y, Taniuchi H, Yonekura Y, Ohtani H. Copper-62-ATSM: a new hypoxia imaging agent with high membrane permeability and low redox potential. J Nucl Med. 1997;38(7):1155.

148. Burgman P, O'Donoghue JA, Lewis JS, Welch MJ, Humm JL, Ling CC. Cell line-dependent differences in uptake and retention of the hypoxia-selective nuclear imaging agent Cu-ATSM. Nucl Med Biol. 2005;32(6):623-30.

149. Dearling JL, Packard AB. Some thoughts on the mechanism of cellular trapping of Cu (II)-ATSM. Nucl Med Biol. 2010;37(3):237-43.

150. Xiao Z, Donnelly PS, Zimmermann M, Wedd AG. Transfer of copper between bis(thiosemicarbazone) ligands and intracellular copper-binding proteins. Insights into mechanisms of copper uptake and hypoxia selectivity. Inorg Chem. 2008;47(10):4338-47.

151. Shaughnessy F, Mariotti E, Shaw K, Eykyn T, Blower P, Siow R, et al. Modification of intracellular glutathione status does not change the cardiac trapping of ^{64}Cu(ATSM). EJNMMI Res. 2014;4(1):1-10.

152. Denoyer D, Masaldan S, La Fontaine S, Cater MA. Targeting copper in cancer therapy: 'Copper That Cancer'. Metallomics. 2015;7(11):1459-76.

153. Peng F, Lutsenko S, Sun X, Muzik O. Positron emission tomography of copper metabolism in the Atp7b(−/−) knock-out mouse model of Wilson's disease. Mol Imaging Biol. 2012;14(1):70-8.

154. Nomura S, Nozaki S, Hamazaki T, Takeda T, Ninomiya E, Kudo S, et al. PET imaging analysis with ^{64}Cu in disulfiram treatment for aberrant copper biodistribution in Menkes disease mouse model. J Nucl Med. 2014;55(5):845-51.

155. Fodero-Tavoletti MT, Villemagne VL, Paterson BM, White AR, Li QX, Camakaris J, et al. Bis(thiosemicarbazonato) Cu-64 complexes for positron emission tomography imaging of Alzheimer's disease. J Alzheimers Dis. 2010;20(1):49-55.

156. Petering HG, Buskirk HH, Underwood GE. The anti-tumor activity of 2-keto-3-ethoxybutyraldehyde bis(thiosemicarbazone) and related compounds. Cancer Res. 1964;24(3 Part 1):367-72.

157. Strauss HW, Nunn A, Linder K. Nitroimidazoles for imaging hypoxic myocardium. J Nucl Cardiol. 1995;2(5):437-45.

158. Lewis JS, McCarthy DW, McCarthy TJ, Fujibayashi Y, Welch MJ. Evaluation of ^{64}Cu-ATSM in vitro and in vivo in a hypoxic tumor model. J Nucl Med. 1999;40(1):177-83.

159. O'Donoghue JA, Zanzonico P, Pugachev A, Wen B, Smith-Jones P, Cai S, et al. Assessment of regional tumor hypoxia using ^{18}F-fluoromisonidazole and ^{64}Cu (II)-diacetyl-bis (N^4-methylthiosemicarbazone) positron emission tomography: comparative study featuring microPET imaging, PO_2 probe measurement, autoradiography, and fluorescent microscopy in the R3327-AT and FaDu rat tumor models. Int J Radiat Oncol Biol Phys. 2005;61(5):1493-502.

160. Yuan H, Schroeder T, Bowsher JE, Hedlund LW, Wong T, Dewhirst MW. Intertumoral differences in hypoxia selectivity of the PET imaging agent ^{64}Cu(II)-diacetyl-bis(N^4-methylthiosemicarbazone). J Nucl Med. 2006;47(6):989-98.

161. Takahashi N, Fujibayashi Y, Yonekura Y, Welch M, Waki A, Tsuchida T, et al. Evaluation of ^{62}Cu labeled diacetyl-bis(*N*^{4}-methylthiosemicarbazone) as a hypoxic tissue tracer in patients with lung cancer. Ann Nucl Med. 2000;14(5):323-8.

162. Dehdashti F, Grigsby PW, Mintun MA, Lewis JS, Siegel BA, Welch MJ. Assessing tumor hypoxia in cervical cancer by positron emission tomography with ^{60}Cu-ATSM: relationship to therapeutic response—a preliminary report. Int J Radiat Oncol Biol Phys. 2003;55(5):1233-8.

163. Dehdashti F, Mintun MA, Lewis JS, Bradley J, Govindan R, Laforest R, et al. In vivo assessment of tumor hypoxia in lung cancer with ^{60}Cu-ATSM. Eur J Nucl Med Mol Imaging. 2003;30(6):844-50.

164. Takahashi N, Fujibayashi Y, Yonekura Y, Welch M, Waki A, Tsuchida T, et al. Copper-62 ATSM as a hypoxic tissue tracer in myocardial ischemia. Ann Nucl Med. 2001;15(3):293-6.

165. Medina RA, Mariotti E, Pavlovic D, Shaw KP, Eykyn TR, Blower PJ, et al. ^{64}Cu-CTS: a promising radiopharmaceutical for the identification of low-grade cardiac hypoxia by PET. J Nucl Med. 2015;56(6):921-6.

166. Dearling JL, Lewis JS, Mullen GE, Rae MT, Zweit J, Blower PJ. Design of hypoxia-targeting radiopharmaceuticals: selective uptake of copper-64 complexes in hypoxic cells in vitro. Eur J Nucl Med. 1998;25(7):788-92.

167. Green MA. A potential copper radiopharmaceutical for imaging the heart and brain: copper-labeled pyruvaldehyde bis(*N*^{4}-methylthiosemicarbazone). Int J Rad Appl Instrum B. 1987;14(1):59-61.

168. Green MA, Klippenstein DL, Tennison JR. Copper(II) bis(thiosemicarbazone) complexes as potential tracers for evaluation of cerebral and myocardial blood flow with PET. J Nucl Med. 1988;29(9):1549-57.

169. Barnhart AJ, Voorhees WD, Green MA. Correlation of Cu(PTSM) localization with regional blood flow in the heart and kidney. Int J Rad Appl Instrum B. 1989;16(7):747-8.

170. Shelton ME, Green M, Mathias C, Welch M, Bergmann S. Assessment of regional myocardial and renal blood flow with copper-PTSM and positron emission tomography. Circulation. 1990;82(3):990-7.

171. Mathias CJ, Green MA, Morrison WB, Knapp DW. Evaluation of Cu-PTSM as a tracer of tumor perfusion: comparison with labeled microspheres in spontaneous canine neoplasms. Nucl Med Biol. 1994;21(1):83-7.

172. Okazawa H, Yonekura Y, Fujibayashi Y, Nishizawa S, Magata Y, Ishizu K, et al. Clinical application and quantitative evaluation of generator-produced copper-62-PTSM as a brain perfusion tracer for PET. J Nucl Med. 1994;35(12):1910-5.

173. Flower MA, Zweit J, Hall AD, Burke D, Davies MM, Dworkin MJ, et al. ^{62}Cu-PTSM and PET used for the assessment of angiotensin II-induced blood flow changes in patients with colorectal liver metastases. Eur J Nucl Med. 2001;28(1):99-103.

174. Wallhaus TR, Lacy J, Stewart R, Bianco J, Green MA, Nayak N, et al. Copper-62-pyruvaldehyde bis(*N*^{4}-methyl-thiosemicarbazone) PET imaging in the detection of coronary artery disease in humans. J Nucl Cardiol. 2001;8(1):67-74.

175. Mathias CJ, Bergmann SR, Green MA. Species-dependent binding of copper(II) bis(thiosemicarbazone) radiopharmaceuticals to serum albumin. J Nucl Med. 1995;36(8):1451-5.

176. Desai V, Kaler SG. Role of copper in human neurological disorders. Am J Clin Nutr. 2008;88(3):855s-8s.

177. Linder MC, Roboz M. Turnover and excretion of copper in rats as measured with ^{67}Cu. Am J Physiol. 1986;251(5 Pt 1):E551-5.

178. Bahde R, Kapoor S, Bhargava KK, Schilsky ML, Palestro CJ, Gupta S. PET with ^{64}Cu–histidine for noninvasive diagnosis of biliary copper excretion in Long–Evans Cinnamon rat model of Wilson's disease. J Nucl Med. 2012;53(6):961-8.

179. Peng F, Lutsenko S, Sun X, Muzik O. Imaging copper metabolism imbalance in Atp7b (-/-) knockout mouse model of Wilson's disease with PET-CT and orally administered $^{64}CuCl_2$. Mol Imaging Biol. 2012;14(5):600-7.

180. Gray LW, Peng F, Molloy SA, Pendyala VS, Muchenditsi A, Muzik O, et al. Urinary copper elevation in a mouse model of Wilson's disease is a regulated process to specifically decrease the hepatic copper load. PLoS ONE. 2012;7(6):E38327.

181. Munakata M, Kodama H, Fujisawa C, Hiroki T, Kimura K, Watanabe M, et al. Copper-trafficking efficacy of copper-pyruvaldehyde bis(*N*^{4}-methylthiosemicarbazone) on the macular mouse, an animal model of Menkes disease. Pediatr Res. 2012;72(3):270-6.

182. Kodama H, Sato E, Gu YH, Shiga K, Fujisawa C, Kozuma T. Effect of copper and diethyldithiocarbamate combination therapy on the macular mouse, an animal model of Menkes disease. J Inherit Metab Dis. 2005;28(6):971-8.

183. Gupte A, Mumper RJ. Elevated copper and oxidative stress in cancer cells as a target for cancer treatment. Cancer Treat Rev. 2009;35(1):32-46.

184. Peng F, Liu J, Wu JS, Lu X, Muzik O. Mouse extrahepatic hepatoma detected on MicroPET using copper (II)-64 chloride uptake mediated by endogenous mouse copper transporter 1. Mol Imaging Biol. 2005;7(5):325-9.

185. Peng F, Lu X, Janisse J, Muzik O, Shields AF. PET of human prostate cancer xenografts in mice with increased uptake of $^{64}CuCl_2$. J Nucl Med. 2006;47(10):1649-52.

186. Jorgensen JT, Persson M, Madsen J, Kjaer A. High tumor uptake of (64)Cu: implications for molecular imaging of tumor characteristics with copper-based PET tracers. Nucl Med Biol. 2013;40(3):345-50.

187. Qin C, Liu H, Chen K, Hu X, Ma X, Lan X, et al. Theranostics of malignant melanoma with $^{64}CuCl_2$. J Nucl Med. 2014;55(5):812-7.

188. Capasso E, Durzu S, Piras S, Zandieh S, Knoll P, Haug A, et al. Role of $^{64}CuCl_2$ PET/CT in staging of prostate cancer. Ann Nucl Med. 2015;29(6):482-8.

189. Stöckel J, Safar J, Wallace AC, Cohen FE, Prusiner SB. Prion protein selectively binds copper(II) ions. Biochemistry. 1998;37(20):7185-93.

190. Nischwitz V, Berthele A, Michalke B. Speciation analysis of selected metals and determination of their total contents in paired serum and cerebrospinal fluid samples: An approach to investigate the permeability of the human blood-cerebrospinal fluid-barrier. Anal Chim Acta. 2008;627(2):258-69.

191. Prohaska JR. Functions of trace elements in brain metabolism. Physiol Rev. 1987;67(3):858-901.

192. Hare DJ, Lee JK, Beavis AD, van Gramberg A, George J, Adlard PA, et al. Three-dimensional atlas of iron, copper, and zinc in the mouse cerebrum and brainstem. Anal Chem. 2012;84(9):3990-7.

193. Popescu BFG, Nichol H. Mapping brain metals to evaluate therapies for neurodegenerative disease. CNS Neurosci Ther. 2011;17(4):256-68.

194. Dexter DT, Wells FR, Lee AJ, Agid F, Agid Y, Jenner P, et al. Increased nigral iron content and alterations in other metal ions occurring in brain in Parkinson's disease. J Neurochem. 1989;52(6):1830-6.

195. Massie HR, Aiello VR, Iodice AA. Changes with age in copper and superoxide dismutase levels in brains of C57BL/6J mice. Mech Ageing Dev. 1979;10(1–2):93-9.

196. Wang LM, Becker JS, Wu Q, Oliveira MF, Bozza FA, Schwager AL, et al. Bioimaging of copper alterations in the aging mouse brain by autoradiography, laser ablation inductively coupled plasma mass spectrometry and immunohistochemistry. Metallomics. 2010;2(5):348-53.

197. Rossi L, De Martino A, Marchese E, Piccirilli S, Rotilio G, Ciriolo MR. Neurodegeneration in the animal model of Menkes' disease involves Bcl-2-linked apoptosis. Neuroscience. 2001;103(1):181-8.

198. Abad E, Rommel JB, Kästner J. Reaction mechanism of the bicopper enzyme peptidylglycine α-hydroxylating monooxygenase. J Biol Chem. 2014;289(20):13726-38.

199. Southan C, Kruse LI. Sequence similarity between dopamine beta-hydroxylase and peptide alpha-amidating enzyme: evidence for a conserved catalytic domain. FEBS Lett. 1989;255(1):116-20.

200. Eipper BA, Milgram SL, Jean Husten E, Yun HY, Mains RE. Peptidylglycine α-amidating monooxygenase: a multifunctional protein with catalytic, processing, and routing domains. Prot Sci. 1993;2(4):489-97.

201. Kim CH, Zabetian CP, Cubells JF, Cho S, Biaggioni I, Cohen BM, et al. Mutations in the dopamine beta-hydroxylase gene are associated with human norepinephrine deficiency. Am J Med Genet. 2002;108(2):140-7.

202. Senard J-M, Rouet P. Dopamine beta-hydroxylase deficiency. Orphanet J Rare Dis. 2006;1(7):1-4.

203. Czyzyk TA, Ning Y, Hsu M-S, Peng B, Mains RE, Eipper BA, et al. Deletion of peptide amidation enzymatic activity leads to edema and embryonic lethality in the mouse. Dev Biol. 2005;287(2):301-13.

204. Harris ZL, Klomp L, Gitlin JD. Aceruloplasminemia: an inherited neurodegenerative disease with impairment of iron homeostasis. Am J Clin Nutr. 1998;67(5):972S-7S.

205. Aldred AR, Brack CM, Schreiber G. The cerebral expression of plasma protein genes in different species. Comp Biochem Physiol B Biochem Mol Biol. 1995;111(1):1-15.

206. Klomp L, Farhangrazi ZS, Dugan LL, Gitlin JD. Ceruloplasmin gene expression in the murine central nervous system. J Clin Invest. 1996;98(1):207.

207. Patel BN, David S. A novel glycosylphosphatidylinositol-anchored form of ceruloplasmin is expressed by mammalian astrocytes. J Biol Chem. 1997;272(32):20185-90.

208. Patel BN, Dunn RJ, David S. Alternative RNA splicing generates a glycosylphosphatidylinositol-anchored form of ceruloplasmin in mammalian brain. J Biol Chem. 2000;275(6):4305-10.

209. Colburn RW, Maas JW. Adenosine triphosphate—metal--norepinephrine ternary complexes and catecholamine binding. Nature. 1965;208(5005):37-41.

210. Hartter DE, Barnea A. Evidence for release of copper in the brain: depolarization-induced release of newly taken-up ^{67}Cu. Synapse. 1988;2(4):412-5.

211. Trombley PQ, Shepherd GM. Differential modulation by zinc and copper of amino acid receptors from rat olfactory bulb neurons. J Neurophysiol. 1996;76(4):2536-46.

212. Zhu HL, Wang DS, Li JS. Cu^{2+} suppresses GABA(A) receptor-mediated responses in rat sacral dorsal commissural neurons. Neurosignals. 2002;11(6):322-8.

213. Weiser T, Wienrich M. The effects of copper ions on glutamate receptors in cultured rat cortical neurons. Brain Res. 1996;742(1-2):211-8.

214. Doreulee N, Yanovsky Y, Haas HL. Suppression of long-term potentiation in hippocampal slices by copper. Hippocampus. 1997;7(6):666-9.

215. Peters C, Munoz B, Sepulveda FJ, Urrutia J, Quiroz M, Luza S, et al. Biphasic effects of copper on neurotransmission in rat hippocampal neurons. J Neurochem. 2011;119(1):78-88.

216. Schlief ML, Craig AM, Gitlin JD. NMDA receptor activation mediates copper homeostasis in hippocampal neurons. J Neurosci. 2005;25(1):239-46.

217. Schlief ML, West T, Craig AM, Holtzman DM, Gitlin JD. Role of the Menkes copper-transporting ATPase in NMDA receptor-mediated neuronal toxicity. Proc Natl Acad Sci U.S.A. 2006;103(40):14919-24.

218. Schlief ML, Gitlin JD. Copper homeostasis in the CNS: a novel link between the NMDA receptor and copper homeostasis in the hippocampus. Mol Neurobiol 2006;33(2):81-90.

219. Choi BS, Zheng W. Copper transport to the brain by the blood-brain barrier and blood-CSF barrier. Brain Res. 2009;1248:14-21.

220. Monnot AD, Behl M, Ho S, Zheng W. Regulation of brain copper homeostasis by the brain barrier systems: Effects of Fe-overload and Fe-deficiency. Toxicol Appl Pharmacol. 2011;256(3):249-57.

221. Lee J, Prohaska JR, Thiele DJ. Essential role for mammalian copper transporter Ctr1 in copper homeostasis and embryonic development. Proc Natl Acad Sci U.S.A. 2001;98(12):6842-7.

222. Qian Y, Tiffany-Castiglioni E, Welsh J, Harris ED. Copper efflux from murine microvascular cells requires expression of the menkes disease Cu-ATPase. J Nutr. 1998;128(8):1276-82.

223. Ke B-X, Llanos RM, Wright M, Deal Y, Mercer JFB. Alteration of copper physiology in mice overexpressing the human Menkes protein ATP7A. Am J Physiol Regul Integr Comp Physiol. 2006;290(5):R1460-R7.

224. Kaler SG. ATP7A-related copper transport diseases--emerging concepts and future trends. Nat Rev Neurol. 2011;7(1):15-29.

225. Davies KM, Hare DJ, Cottam V, Chen N, Hilgers L, Halliday G, et al. Localization of copper and copper transporters in the human brain. Metallomics. 2013;5(1):43-51.

226. Sofroniew MV, Vinters HV. Astrocytes: biology and pathology. Acta Neuropathol. 2010;119(1):7-35.

227. Abbott NJ, Ronnback L, Hansson E. Astrocyte-endothelial interactions at the blood-brain barrier. Nat Rev Neurosci. 2006;7(1):41-53.

228. Scheiber IF, Mercer JFB, Dringen R. Copper accumulation by cultured astrocytes. Neurochem Int. 2010;56(3):451-60.

229. Scheiber IF, Dringen R. Copper-treatment increases the cellular GSH content and accelerates GSH export from cultured rat astrocytes. Neurosci Lett. 2011;498(1):42-6.

230. Brown DR. Role of the prion protein in copper turnover in astrocytes. Neurobiol Dis. 2004;15(3):534-43.

231. Haywood S, Paris J, Ryvar R, Botteron C. Brain copper elevation and neurological changes in North Ronaldsay sheep: a model for neurodegenerative disease? J Comp Pathol. 2008;139(4):252-5.

232. Young JK, Garvey JS, Huang PC. Glial immunoreactivity for metallothionein in the rat brain. Glia. 1991;4(6):602-10.

233. Carrasco J, Giralt M, Molinero A, Penkowa M, Moos T, Hidalgo J. Metallothionein (MT)-III: generation of polyclonal antibodies, comparison with MT-I+II in the freeze lesioned rat brain and in a bioassay with astrocytes, and analysis of Alzheimer's disease brains. J Neurotrauma. 1999;16(11):1115-29.

234. Penkowa M, Nielsen H, Hidalgo J, Bernth N, Moos T. Distribution of metallothionein I + II and vesicular zinc in the developing central nervous system: correlative study in the rat. J Comp Neurol. 1999;412(2):303-18.

235. Telianidis J, Hung YH, Materia S, Fontaine SL. Role of the P-Type ATPases, ATP7A and ATP7B in brain copper homeostasis. Front Aging Neurosci. 2013;5:44.

236. Kodama H, Meguro Y, Abe T, Rayner MH, Suzuki KT, Kobayashi S, et al. Genetic expression of Menkes disease in cultured astrocytes of the macular mouse. J Inherit Metab Dis. 1991;14(6):896-901.

237. Nishihara E, Furuyama T, Yamashita S, Mori N. Expression of copper trafficking genes in the mouse brain. Neuroreport. 1998;9(14):3259-63.

238. Hevner RF, Liu S, Wong-Riley MT. A metabolic map of cytochrome oxidase in the rat brain: histochemical, densitometric and biochemical studies. Neuroscience. 1995;65(2):313-42.

239. Rothstein JD, Dykes-Hoberg M, Corson LB, Becker M, Cleveland DW, Price DL, et al. The copper chaperone CCS is abundant in neurons and astrocytes in human and rodent brain. J Neurochem. 1999;72(1):422-9.

240. Kako K, Tsumori K, Ohmasa Y, Takahashi Y, Munekata E. The expression of Cox17p in rodent tissues and cells. Eur J Biochem. 2000;267(22):6699-707.

241. Del Maestro R, McDonald W. Distribution of superoxide dismutase, glutathione peroxidase and catalase in developing rat brain. Mech Ageing Dev. 1987;41(1-2):29-38.

242. Mackenzie NC, Brito M, Reyes AE, Allende ML. Cloning, expression pattern and essentiality of the high-affinity copper transporter 1 (ctr1) gene in zebrafish. Gene. 2004;328:113-20.

243. Ohgami RS, Campagna DR, McDonald A, Fleming MD. The Steap proteins are metalloreductases. Blood. 2006;108(4):1388-94.

244. Multhaup G, Schlicksupp A, Hesse L, Beher D, Ruppert T, Masters CL, et al. The amyloid precursor protein of Alzheimer's disease in the reduction of copper(II) to copper(I). Science. 1996;271(5254):1406-9.

245. Naeve GS, Vana AM, Eggold JR, Kelner GS, Maki R, DeSouza EB, et al. Expression profile of the copper homeostasis gene, rAtox1, in the rat brain. Neuroscience. 1999;93(3):1179-87.

246. Niciu MJ, Ma XM, El Meskini R, Ronnett GV, Mains RE, Eipper BA. Developmental changes in the expression of ATP7A during a critical period in postnatal neurodevelopment. Neuroscience. 2006;139(3):947-64.

247. Saito T, Okabe M, Hosokawa T, Kurasaki M, Hata A, Endo F, et al. Immunohistochemical determination of the Wilson Copper-transporting P-type ATPase in the brain tissues of the rat. Neurosci Lett. 1999;266(1):13-6.

248. Angeletti B, Waldron KJ, Freeman KB, Bawagan H, Hussain I, Miller CC, et al. BACE1 cytoplasmic domain interacts with the copper chaperone for superoxide dismutase-1 and binds copper. J Biol Chem. 2005;280(18):17930-7.

249. Kong GW, Miles L, Crespi GN, Morton C, Ng H, Barnham K, et al. Copper binding to the Alzheimer's disease amyloid precursor protein. Eur Biophys J. 2008;37(3):269-79.

250. Millhauser GL. Copper binding in the prion protein. Acc Chem Res. 2004;37(2):79-85.

251. Brown DR, Qin K, Herms JW, Madlung A, Manson J, Strome R, et al. The cellular prion protein binds copper in vivo. Nature. 1997;390(6661):684-7.

252. Pauly PC, Harris DA. Copper stimulates endocytosis of the prion protein. J Biol Chem. 1998;273(50):33107-10.

253. Vassallo N, Herms J. Cellular prion protein function in copper homeostasis and redox signalling at the synapse. J Neurochem. 2003;86(3):538-44.

254. Brown DR, Wong BS, Hafiz F, Clive C, Haswell SJ, Jones IM. Normal prion protein has an activity like that of superoxide dismutase. Biochem J. 1999;344(Pt 1):1-5.

255. Suazo M, Hodar C, Morgan C, Cerpa W, Cambiazo V, Inestrosa NC, et al. Overexpression of amyloid precursor protein increases copper content in HEK293 cells. Biochem Biophys Res Commun. 2009;382(4):740-4.

256. Treiber C, Simons A, Strauss M, Hafner M, Cappai R, Bayer TA, et al. Clioquinol mediates copper uptake and counteracts copper efflux activities of the amyloid precursor protein of Alzheimer's disease. J Biol Chem. 2004;279(50):51958-64.

257. Bayer TA, Schäfer S, Simons A, Kemmling A, Kamer T, Tepests R, et al. Dietary Cu stabilizes brain superoxide dismutase 1 activity and reduces amyloid Aβ production in APP23 transgenic mice. Proc Natl Acad Sci U.S.A. 2003;100(24):14187-92.

258. Maynard CJ, Cappai R, Volitakis I, Cherny RA, White AR, Beyreuther K, et al. Overexpression of Alzheimer's disease amyloid-β opposes the age-dependent elevations of brain copper and iron. J Biol Chem. 2002;277(47):44670-6.

259. Que EL, Domaille DW, Chang CJ. Metals in neurobiology: probing their chemistry and biology with molecular imaging. Chem Rev. 2008;108(5):1517-49.

260. Irani DN. Cerebrospinal fluid in clinical practice. 1st ed. Philadelphia, United States: Saunders; 2009.

261. Hidalgo J, Aschner M, Zatta P, Vašák M. Roles of the metallothionein family of proteins in the central nervous system. Brain Res Bull. 2001;55(2):133-45.

262. Wake SA, Mercer JF. Induction of metallothionein mRNA in rat liver and kidney after copper chloride injection. Biochem J. 1985;228(2):425-32.

263. Hidalgo J, García A, Oliva AM, Giralt M, Gasull T, González B, et al. Effect of zinc, copper and glucocorticoids on metallothionein levels of cultured neurons and astrocytes from rat brain. Chem Biol Interact. 1994;93(3):197-219.

264. Nishimura N, Nishimura H, Ghaffar A, Tohyama C. Localization of metallothionein in the brain of rat and mouse. J Histochem Cytochem. 1992;40(2):309-15.

265. Masters BA, Quaife CJ, Erickson JC, Kelly EJ, Froelick GJ, Zambrowicz BP, et al. Metallothionein III is expressed in neurons that sequester zinc in synaptic vesicles. J Neurosci. 1994;14(10):5844-57.

266. Erickson JC, Hollopeter G, Thomas SA, Froelick GJ, Palmiter RD. Disruption of the metallothionein-III gene in mice: analysis of brain zinc, behavior, and neuron vulnerability to metals, aging, and seizures. J Neurosci. 1997;17(4):1271-81.

267. Scheiber IF, Mercer JFB, Dringen R. Metabolism and functions of copper in brain. Prog Neurobiol. 2014;116:33-57.

268. Freedman JH, Ciriolo MR, Peisach J. The role of glutathione in copper metabolism and toxicity. J Biol Chem. 1989;264(10):5598-605.

269. Kozlowski H, Luczkowski M, Remelli M, Valensin D. Copper, zinc and iron in neurodegenerative diseases (Alzheimer's, Parkinson's and prion diseases). Coord Chem Rev. 2012;256(19–20):2129-41.

270. Tumer Z. An overview and update of ATP7A mutations leading to Menkes disease and occipital horn syndrome. Hum Mutat. 2013;34(3):417-29.

271. Hung YH, Bush AI, Cherny RA. Copper in the brain and Alzheimer's disease. J Biol Inorg Chem. 2010;15(1):61-76.

272. Sarkar B, Lingertat-Walsh K, Clarke JT. Copper-histidine therapy for Menkes disease. J Pediatr. 1993;123(5):828-30.

273. Kaler SG. Diagnosis and therapy of Menkes syndrome, a genetic form of copper deficiency. Am J Clin Nutr. 1998;67(5 Suppl):1029s-34s.

274. Bhadhprasit W, Kodama H, Fujisawa C, Hiroki T, Ogawa E. Effect of copper and disulfiram combination therapy on the macular mouse, a model of Menkes disease. J Trace Elem Med Biol. 2012;26(2–3):105-8.

275. Ogawa E, Kodama H. Effects of disulfiram treatment in patients with Menkes disease and occipital horn syndrome. J Trace Elem Med Biol. 2012;26(2–3):102-4.

276. Donsante A, Yi L, Zerfas PM, Brinster LR, Sullivan P, Goldstein DS, et al. ATP7A gene addition to the choroid plexus results in long-term rescue of the lethal copper transport defect in a Menkes disease mouse model. Mol Ther. 2011.

277. Wang Y, Hodgkinson V, Zhu S, Weisman GA, Petris MJ. Advances in the understanding of mammalian copper transporters. Adv Nutr. 2011;2(2):129-37.

278. Kitzberger R, Madl C, Ferenci P. Wilson’s disease. Metab Brain Dis. 2005;20(4):295-302.

279. Sternlieb I. Perspectives on Wilson's disease. Hepatology. 1990;12(5):1234-9.

280. Roberts EA, Schilsky ML. Diagnosis and treatment of Wilson's disease: an update. Hepatology. 2008;47(6):2089-111.

281. Hall HNvW-v, Heuvel AGvd, Algra A, Hoogenraad TU, Mali WP. Wilson's disease: findings at MR imaging and CT of the brain with clinical correlation. Radiology. 1996;198(2):531-6.

282. Valentine JS, Doucette PA, Zittin Potter S. Copper-zinc superoxide dismutase and amyotrophic lateral sclerosis. Annu Rev Biochem. 2005;74:563-93.

283. Saccon RA, Bunton-Stasyshyn RKA, Fisher EMC, Fratta P. Is SOD1 loss of function involved in amyotrophic lateral sclerosis? Brain. 2013;136(8):2342-58.

284. Jonsson PA, Ernhill K, Andersen PM, Bergemalm D, Brannstrom T, Gredal O, et al. Minute quantities of misfolded mutant superoxide dismutase-1 cause amyotrophic lateral sclerosis. Brain. 2004;127(Pt 1):73-88.

285. Gaggelli E, Kozlowski H, Valensin D, Valensin G. Copper homeostasis and neurodegenerative disorders (Alzheimer's, prion, and Parkinson's diseases and amyotrophic lateral sclerosis). Chem Rev. 2006;106(6):1995-2044.

286. Mitchell JD, Borasio GD. Amyotrophic lateral sclerosis. Lancet. 2007;369(9578):2031-41.

287. Karitzky J, Ludolph AC. Imaging and neurochemical markers for diagnosis and disease progression in ALS. J Neurol Sci. 2001;191(1–2):35-41.

288. Soon CP, Donnelly PS, Turner BJ, Hung LW, Crouch PJ, Sherratt NA, et al. Cu(II) (ATSM) protects against peroxynitrite-induced nitrosative damage and prolongs survival in an amyotrophic lateral sclerosis mouse model. J Biol Chem. 2011; 286(51):44035-44.

289. Beckman JS, Carson M, Smith CD, Koppenol WH. ALS, SOD and peroxynitrite. Nature. 1993;364(6438):584.

290. McAllum EJ, Lim NK, Hickey JL, Paterson BM, Donnelly PS, Li QX, et al. Therapeutic effects of Cu(II)(atsm) in the SOD1-G37R mouse model of amyotrophic lateral sclerosis. Amyotroph Lateral Scler Frontotemporal Degener. 2013;14(7-8):586-90.

291. Roberts BR, Lim NK, McAllum EJ, Donnelly PS, Hare DJ, Doble PA, et al. Oral treatment with Cu(II)(atsm) increases mutant SOD1 in vivo but protects motor neurons and improves the phenotype of a transgenic mouse model of amyotrophic lateral sclerosis. J Neurosci. 2014;34(23):8021-31.

292. McAllum EJ, Roberts BR, Hickey JL, Dang TN, Grubman A, Donnelly PS, et al. Zn(II)(atsm) is protective in amyotrophic lateral sclerosis model mice via a copper delivery mechanism. Neurobiol Dis. 2015;81:20-4.

293. Hardiman O, van den Berg LH, Kiernan MC. Clinical diagnosis and management of amyotrophic lateral sclerosis. Nat Rev Neurol. 2011;7(11):639-49.

294. Ikawa M, Okazawa H, Tsujikawa T, Matsunaga A, Yamamura O, Mori T, et al. Increased oxidative stress is related to disease severity in the ALS motor cortex: a PET study. Neurology. 2015;84(20):2033-9.

295. Henchcliffe C, Beal MF. Mitochondrial biology and oxidative stress in Parkinson's disease pathogenesis. Nat Clin Pract Neurol. 2008;4(11):600-9.

296. Paik SR, Shin H-J, Lee J-H, Chang C-S, Kim J. Copper(II)-induced self-oligomerization of α-synuclein. Biochem J. 1999;340(3):821-8.

297. Rasia RM, Bertoncini CW, Marsh D, Hoyer W, Cherny D, Zweckstetter M, et al. Structural characterization of copper(II) binding to alpha-synuclein: insights into the bioinorganic chemistry of Parkinson's disease. Proc Natl Acad Sci U.S.A. 2005;102(12):4294-9.

298. Wang C, Liu L, Zhang L, Peng Y, Zhou F. Redox reactions of the α-synuclein−Cu^{2+} complex and their effects on neuronal cell viability. Biochemistry. 2010;49(37):8134-42.

299. Davies KM, Bohic S, Carmona A, Ortega R, Cottam V, Hare DJ, et al. Copper pathology in vulnerable brain regions in Parkinson's disease. Neurobiol Aging. 2014;35(4):858-66.

300. Olivieri S, Conti A, Iannaccone S, Cannistraci CV, Campanella A, Barbariga M, et al. Ceruloplasmin oxidation, a feature of Parkinson's disease CSF, inhibits ferroxidase activity and promotes cellular iron retention. J Neurosci. 2011;31(50):18568-77.

301. Pall HS, Williams AC, Blake DR, Lunec J, Gutteridge JM, Hall M, et al. Raised cerebrospinal-fluid copper concentration in Parkinson's disease. Lancet. 1987;2(8553):238-41.

302. Zhao H-W, Lin J, Wang X-B, Cheng X, Wang J-Y, Hu B-L, et al. Assessing plasma levels of selenium, copper, iron and zinc in patients of Parkinson's disease. PLoS ONE. 2013;8(12):E83060.

303. Obeso JA, Rodriguez-Oroz MC, Goetz CG, Marin C, Kordower JH, Rodriguez M, et al. Missing pieces in the Parkinson's disease puzzle. Nat Med. 2010;16(6):653-61.

304. Hung LW, Villemagne VL, Cheng L, Sherratt NA, Ayton S, White AR, et al. The hypoxia imaging agent Cu(II)(atsm) is neuroprotective and improves motor and cognitive functions in multiple animal models of Parkinson's disease. J Exp Med. 2012;209(4):837-54.

305. Massano J, Bhatia KP. Clinical approach to Parkinson's disease: features, diagnosis, and principles of management. Cold Spring Harb Perspect Med. 2012;2(6).

306. Ikawa M, Okazawa H, Kudo T, Kuriyama M, Fujibayashi Y, Yoneda M. Evaluation of striatal oxidative stress in patients with Parkinson's disease using [^{62}Cu]ATSM PET. Nucl Med Biol. 2011;38(7):945-51.

307. Donnelly PS, Liddell JR, Lim S, Paterson BM, Cater MA, Savva MS, et al. An impaired mitochondrial electron transport chain increases retention of the hypoxia imaging agent diacetylbis(4-methylthiosemicarbazonato)copper(II). Proc Natl Acad Sci U.S.A. 2012;109(1):47-52.

308. Wong BS, Chen SG, Colucci M, Xie Z, Pan T, Liu T, et al. Aberrant metal binding by prion protein in human prion disease. J Neurochem. 2001;78(6):1400-8.

309. Brown DR, Hafiz F, Glasssmith LL, Wong BS, Jones IM, Clive C, et al. Consequences of manganese replacement of copper for prion protein function and proteinase resistance. EMBO J. 2000;19(6):1180-6.

310. Kuczius T, Buschmann A, Zhang W, Karch H, Becker K, Peters G, et al. Cellular prion protein acquires resistance to proteolytic degradation following copper ion binding. Biol Chem. 2004;385(8):739-47.

311. Jobling MF, Huang X, Stewart LR, Barnham KJ, Curtain C, Volitakis I, et al. Copper and zinc binding modulates the aggregation and neurotoxic properties of the prion peptide PrP106−126. Biochemistry. 2001;40(27):8073-84.

312. Sigurdsson EM, Brown DR, Alim MA, Scholtzova H, Carp R, Meeker HC, et al. Copper chelation delays the onset of prion disease. J Biol Chem. 2003;278(47):46199-202.

313. Hijazi N, Shaked Y, Rosenmann H, Ben-Hur T, Gabizon R. Copper binding to PrPC may inhibit prion disease propagation. Brain Res. 2003;993(1–2):192-200.

314. Xiao G, Fan Q, Wang X, Zhou B. Huntington disease arises from a combinatory toxicity of polyglutamine and copper binding. Proc Natl Acad Sci U.S.A. 2013;110(37):14995-5000.

315. Dexter DT, Carayon A, Javoy-Agid F, Agid F, Agid Y, Wells FR, et al. Alterations in the levels of iron, ferritin andother trace metals in Parkinson's disease and other neuodegenerative diseases affecting the basal ganglia. Brain. 1991;114(4):1953-75.

316. Fox JH, Kama JA, Lieberman G, Chopra R, Dorsey K, Chopra V, et al. Mechanisms of copper ion mediated Huntington's disease progression. PLoS One. 2007;2(3):E334.

317. Nguyen T, Hamby A, Massa SM. Clioquinol down-regulates mutant huntingtin expression in vitro and mitigates pathology in a Huntington's disease mouse model. Proc Natl Acad Sci U.S.A. 2005;102(33):11840-5.

318. Cherny RA, Ayton S, Finkelstein DI, Bush AI, McColl G, Massa SM. PBT2 reduces toxicity in a C. elegans model of polyQ aggregation and extends lifespan, reduces striatal atrophy and improves motor performance in the R6/2 mouse model of Huntington's disease. J Huntingtons Dis. 2012;1(2):211-9.

319. Vanier MT. Niemann-Pick disease type C. Orphanet J Rare Dis. 2010;5:16.

320. Vázquez MC, del Pozo T, Robledo FA, Carrasco G, Pavez L, Olivares F, et al. Alteration of gene expression profile in Niemann-Pick type C mice correlates with tissue damage and oxidative stress. PLoS ONE. 2011;6(12):E28777.

321. Hung YH, Faux NG, Killilea DW, Yanjanin N, Firnkes S, Volitakis I, et al. Altered transition metal homeostasis in Niemann-Pick disease, type C1. Metallomics. 2014;6(3):542-53.

322. Arguello G, Martinez P, Pena J, Chen O, Platt F, Zanlungo S, et al. Hepatic metabolic response to restricted copper intake in a Niemann-Pick C murine model. Metallomics. 2014;6(8):1527-39.

323. Sakiyama Y, Narita A, Osawa S, Nanba E, Ohno K, Otsuka M. Abnormal copper metabolism in Niemann–Pick disease type C mimicking Wilson's disease. Neurol Clin Neurosci. 2014;2(6):193-200.

324. Vazquez MC, Martinez P, Alvarez AR, Gonzalez M, Zanlungo S. Increased copper levels in in vitro and in vivo models of Niemann-Pick C disease. Biometals. 2012;25(4):777-86.

325. Hung YH, Bush AI, La Fontaine S. Links between copper and cholesterol in Alzheimer's disease. Front Physiol. 2013;4:111.

326. Yanagimoto C, Harada M, Kumemura H, Koga H, Kawaguchi T, Terada K, et al. Niemann-Pick C1 protein transports copper to the secretory compartment from late endosomes where ATP7B resides. Exp Cell Res. 2009;315(2):119-26.

327. Yanagimoto C, Harada M, Kumemura H, Abe M, Koga H, Sakata M, et al. Copper incorporation into ceruloplasmin is regulated by Niemann-Pick C1 protein. Hepatol Res. 2011;41(5):484-91.

328. Hickey JL, Donnelly PS. Diagnostic imaging of Alzheimer's disease with copper and technetium complexes. Coord Chem Rev. 2012;256(19–20):2367-80.

329. O'Brien RJ, Wong PC. Amyloid precursor protein processing and Alzheimer's disease. Annu Rev Neurosci. 2011;34:185-204.

330. Ehehalt R, Keller P, Haass C, Thiele C, Simons K. Amyloidogenic processing of the Alzheimer β-amyloid precursor protein depends on lipid rafts. J Cell Biol. 2003;160(1):113-23.

331. Portelius E, Zetterberg H, Gobom J, Andreasson U, Blennow K. Targeted proteomics in Alzheimer's disease: focus on amyloid-beta. Expert Rev Proteomics. 2008;5(2):225-37.

332. McLean CA, Cherny RA, Fraser FW, Fuller SJ, Smith MJ, Konrad V, et al. Soluble pool of Aβ amyloid as a determinant of severity of neurodegeneration in Alzheimer's disease. Ann Neurol. 1999;46(6):860-6.

333. Gouras GK, Tsai J, Naslund J, Vincent B, Edgar M, Checler F, et al. Intraneuronal Aβ42 accumulation in human brain. Am J Pathol. 2000;156(1):15-20.

334. Love S. Contribution of cerebral amyloid angiopathy to Alzheimer's disease. J Neurol Neurosurg Psychiatry. 2004;75(1):1-4.

335. Hardy JA, Higgins GA. Alzheimer's disease: the amyloid cascade hypothesis. Science. 1992;256(5054):184-5.

336. Snyder EM, Nong Y, Almeida CG, Paul S, Moran T, Choi EY, et al. Regulation of NMDA receptor trafficking by amyloid-[beta]. Nat Neurosci. 2005;8(8):1051-8.

337. Jin M, Shepardson N, Yang T, Chen G, Walsh D, Selkoe DJ. Soluble amyloid beta-protein dimers isolated from Alzheimer cortex directly induce Tau hyperphosphorylation and neuritic degeneration. Proc Natl Acad Sci U.S.A. 2011;108(14):5819-24.

338. Roberson ED, Scearce-Levie K, Palop JJ, Yan F, Cheng IH, Wu T, et al. Reducing endogenous tau ameliorates amyloid beta-induced deficits in an Alzheimer's disease mouse model. Science. 2007;316(5825):750-4.

339. Bush AI, Tanzi RE. Therapeutics for Alzheimer's disease based on the metal hypothesis. Neurotherapeutics. 2008;5(3):421-32.

340. Bush AI, Pettingell WH, Jr., Paradis MD, Tanzi RE. Modulation of amyloid-beta adhesiveness and secretase site cleavage by zinc. J Biol Chem. 1994;269(16):12152-8.

341. Lovell M, Robertson J, Teesdale W, Campbell J, Markesbery W. Copper, iron and zinc in Alzheimer's disease senile plaques. J Neurol Sci. 1998;158(1):47-52.

342. Grundke-Iqbal I, Fleming J, Tung YC, Lassmann H, Iqbal K, Joshi JG. Ferritin is a component of the neuritic (senile) plaque in Alzheimer's dementia. Acta Neuropathol. 1990;81(2):105-10.

343. Akatsu H, Hori A, Yamamoto T, Yoshida M, Mimuro M, Hashizume Y, et al. Transition metal abnormalities in progressive dementias. Biometals. 2012;25(2):337-50.

344. Pajonk FG, Kessler H, Supprian T, Hamzei P, Bach D, Schweickhardt J, et al. Cognitive decline correlates with low plasma concentrations of copper in patients with mild to moderate Alzheimer's disease. J Alzheimers Dis. 2005;8(1):23-7.

345. Kessler H, Pajonk FG, Meisser P, Schneider-Axmann T, Hoffmann KH, Supprian T, et al. Cerebrospinal fluid diagnostic markers correlate with lower plasma copper and ceruloplasmin in patients with Alzheimer's disease. J Neural Transm. 2006;113(11):1763-9.

346. Squitti R, Lupoi D, Pasqualetti P, Dal Forno G, Vernieri F, Chiovenda P, et al. Elevation of serum copper levels in Alzheimer's disease. Neurology. 2002;59(8):1153-61.

347. Park JH, Lee DW, Park KS. Elevated serum copper and ceruloplasmin levels in Alzheimer's disease. Asia Pac Psychiatry. 2014;6(1):38-45.

348. Molina JA, Jimenez-Jimenez FJ, Aguilar MV, Meseguer I, Mateos-Vega CJ, Gonzalez-Munoz MJ, et al. Cerebrospinal fluid levels of transition metals in patients with Alzheimer's disease. J Neural Transm. 1998;105(4-5):479-88.

349. Bucossi S, Ventriglia M, Panetta V, Salustri C, Pasqualetti P, Mariani S, et al. Copper in Alzheimer's disease: a meta-analysis of serum,plasma, and cerebrospinal fluid studies. J Alzheimers Dis. 2011;24(1):175-85.

350. Maurer I, Zierz S, Möller HJ. A selective defect of cytochrome c oxidase is present in brain of Alzheimer disease patients. Neurobiol Aging. 2000;21(3):455-62.

351. Faller P, Hureau C. Bioinorganic chemistry of copper and zinc ions coordinated to amyloid-β peptide. Dalton Trans. 2009(7):1080-94.

352. Curtain CC, Ali F, Volitakis I, Cherny RA, Norton RS, Beyreuther K, et al. Alzheimer's disease amyloid-beta binds copper and zinc to generate an allosterically ordered membrane-penetrating structure containing superoxide dismutase-like subunits. J Biol Chem. 2001;276(23):20466-73.

353. Bayer TA, Multhaup G. Involvement of amyloid beta precursor protein (AbetaPP) modulated copper homeostasis in Alzheimer's disease. J Alzheimers Dis. 2005;8(2):201-6.

354. White AR, Reyes R, Mercer JFB, Camakaris J, Zheng H, Bush AI, et al. Copper levels are increased in the cerebral cortex and liver of APP and APLP2 knockout mice. Brain Res. 1999;842(2):439-44.

355. Sayre LM, Perry G, Harris PL, Liu Y, Schubert KA, Smith MA. In situ oxidative catalysis by neurofibrillary tangles and senile plaques in Alzheimer's disease: a central role for bound transition metals. J Neurochem. 2000;74(1):270-9.

356. Soragni A, Zambelli B, Mukrasch MD, Biernat J, Jeganathan S, Griesinger C, et al. Structural characterization of binding of Cu(II) to Tau protein. Biochemistry. 2008;47(41):10841-51.

357. Bush AI. Drug development based on the metals hypothesis of Alzheimer's disease. J Alzheimers Dis. 2008;15(2):223-40.

358. Opazo C, Huang X, Cherny RA, Moir RD, Roher AE, White AR, et al. Metalloenzyme-like activity of Alzheimer's disease β-amyloid: Cu-dependent catalytic conversion of dopamine, cholesterol, and biological reducing agents to neurotoxic H_2O_2. J Biol Chem. 2002;277(43):40302-8.

359. White AR, Bush AI, Beyreuther K, Masters CL, Cappai R. Exacerbation of copper toxicity in primary neuronal cultures depleted of cellular glutathione. J Neurochem. 1999;72(5):2092-8.

360. Bush AI. The metal theory of Alzheimer's disease. J Alzheimers Dis. 2013;33 (Suppl 1):S277-81.

361. Crouch PJ, Barnham KJ. Therapeutic redistribution of metal ions to treat Alzheimer's disease. Acc Chem Res. 2012;45(9):1604-11.

362. Manso Y, Comes G, Hidalgo J, Bush AI, Adlard PA. Copper modulation as a therapy for Alzheimer's disease? Int J Alzheimers Dis. 2011;2011:5.

363. Sparks DL, Schreurs BG. Trace amounts of copper in water induce beta-amyloid plaques and learning deficits in a rabbit model of Alzheimer's disease. Proc Natl Acad Sci U.S.A. 2003;100(19):11065-9.

364. White AR, Du T, Laughton KM, Volitakis I, Sharples RA, Xilinas ME, et al. Degradation of the Alzheimer's disease amyloid β-peptide by metal-dependent up-regulation of metalloprotease activity. J Biol Chem. 2006;281(26):17670-80.

365. Donnelly PS, Caragounis A, Du T, Laughton KM, Volitakis I, Cherny RA, et al. Selective intracellular release of copper and zinc ions from bis(thiosemicarbazonato) complexes reduces levels of Alzheimer's disease amyloid-beta peptide. J Biol Chem. 2008;283(8):4568-77.

366. Crouch PJ, Hung LW, Adlard PA, Cortes M, Lal V, Filiz G, et al. Increasing Cu bioavailability inhibits Aβ oligomers and Tau phosphorylation. Proc Natl Acad Sci U.S.A. 2009;106(2):381-6.

367. Kessler H, Bayer TA, Bach D, Schneider-Axmann T, Supprian T, Herrmann W, et al. Intake of copper has no effect on cognition in patients with mild Alzheimer's disease: a pilot phase 2 clinical trial. J Neural Transm. 2008;115(8):1181-7.

368. Cherny RA, Legg JT, McLean CA, Fairlie DP, Huang X, Atwood CS, et al. Aqueous dissolution of Alzheimer's disease Aβ amyloid deposits by biometal depletion. J Biol Chem. 1999;274(33):23223-8.

369. Squitti R, Rossini PM, Cassetta E, Moffa F, Pasqualetti P, Cortesi M, et al. D-Penicillamine reduces serum oxidative stress in Alzheimer's disease patients. Eur J Clin Invest. 2002;32(1):51-9.

370. Crapper McLachlan DR, Dalton AJ, Kruck TP, Bell MY, Smith WL, Kalow W, et al. Intramuscular desferrioxamine in patients with Alzheimer's disease. Lancet. 1991;337(8753):1304-8.

371. Cherny RA, Atwood CS, Xilinas ME, Gray DN, Jones WD, McLean CA, et al. Treatment with a copper-zinc chelator markedly and rapidly inhibits beta-amyloid accumulation in Alzheimer's disease transgenic mice. Neuron. 2001;30(3):665-76.

372. Ritchie CW, Bush AI, Mackinnon A, Macfarlane S, Mastwyk M, MacGregor L, et al. Metal-protein attenuation with iodochlorhydroxyquin (clioquinol) targeting Aβ amyloid deposition and toxicity in alzheimer disease: A pilot phase 2 clinical trial. Arch Neurol. 2003;60(12):1685-91.

373. Adlard PA, Cherny RA, Finkelstein DI, Gautier E, Robb E, Cortes M, et al. Rapid restoration of cognition in Alzheimer's transgenic mice with 8-hydroxyquinoline analogs is associated with decreased interstitial Aβ. Neuron. 2008;59(1):43-55.

374. Lannfelt L, Blennow K, Zetterberg H, Batsman S, Ames D, Harrison J, et al. Safety, efficacy, and biomarker findings of PBT2 in targeting Abeta as a modifying therapy for Alzheimer's disease: a phase IIa, double-blind, randomised, placebo-controlled trial. Lancet Neurol. 2008;7(9):779-86.

375. Faux NG, Ritchie CW, Gunn A, Rembach A, Tsatsanis A, Bedo J, et al. PBT2 rapidly improves cognition in Alzheimer's Disease: additional phase II analyses. J Alzheimers Dis. 2010;20(2):509-16.

376. Prana Biotechnology Limited. Prana Biotechnology announces top line results of Phase 2 IMAGINE trial of PBT2 in Alzheimer's disease [Internet]. Melbourne, Australia: Prana Biotechnology Limited; 2014 Mar 31 [cited 2016 Jun 6]. Available from: http://pranabio.com/news/prana-biotechnology-announces-top-line-results-phase-2-imagine-trial-pbt2-alzheimers-disease/#.WMg-92_yjcs

377. Rabin LA, Wang C, Katz MJ, Derby CA, Buschke H, Lipton RB. Predicting Alzheimer's disease: neuropsychological tests, self reports, and informant reports of cognitive difficulties. J Am Geriatr Soc. 2012;60(6):1128-34.

378. Johnson KA, Fox NC, Sperling RA, Klunk WE. Brain imaging in Alzheimer's disease. Cold Spring Harb Perspect Med. 2012;2(4).

379. Silverman DS, Small GW, Chang CY, et al. Positron emission tomography in evaluation of dementia: regional brain metabolism and long-term outcome. JAMA. 2001;286(17):2120-7.

380. Foster NL, Heidebrink JL, Clark CM, Jagust WJ, Arnold SE, Barbas NR, et al. FDG-PET improves accuracy in distinguishing frontotemporal dementia and Alzheimer's disease. Brain. 2007;130(10):2616-35.

381. Ewers M, Brendel M, Rizk-Jackson A, Rominger A, Bartenstein P, Schuff N, et al. Reduced FDG-PET brain metabolism and executive function predict clinical progression in elderly healthy subjects. Neuroimage Clin. 2014;4:45-52.

382. Blennow K. Cerebrospinal fluid protein biomarkers for Alzheimer's disease. NeuroRx. 2004;1(2):213-25.

383. Blennow K, Hampel H, Weiner M, Zetterberg H. Cerebrospinal fluid and plasma biomarkers in Alzheimer disease. Nat Rev Neurol. 2010;6(3):131-44.

384. Frisoni GB, Fox NC, Jack CR, Scheltens P, Thompson PM. The clinical use of structural MRI in Alzheimer disease. Nat Rev Neurol. 2010;6(2):67-77.

385. Dhenain M. Preclinical MRI and NMR biomarkers of Alzheimer's disease: concepts and applications. Magn Reson Insights. 2008;2:75.

386. Klunk WE, Engler H, Nordberg A, Wang Y, Blomqvist G, Holt DP, et al. Imaging brain amyloid in Alzheimer's disease with Pittsburgh Compound-B. Ann Neurol. 2004;55(3):306-19.

387. Edison P, Archer HA, Hinz R, Hammers A, Pavese N, Tai YF, et al. Amyloid, hypometabolism, and cognition in Alzheimer's disease: an [^{11}C]PIB and [^{18}F]FDG PET study. Neurology. 2007;68(7):501-8.

388. Fagan AM, Mintun MA, Mach RH, Lee S-Y, Dence CS, Shah AR, et al. Inverse relation between in vivo amyloid imaging load and cerebrospinal fluid Aβ42 in humans. Ann Neurol. 2006;59(3):512-9.

389. Archer HA, Edison P, Brooks DJ, Barnes J, Frost C, Yeatman T, et al. Amyloid load and cerebral atrophy in Alzheimer's disease: an ^{11}C-PIB positron emission tomography study. Ann Neurol. 2006;60(1):145-7.

390. Rowe CC, Villemagne VL. Brain amyloid imaging. J Nucl Med. 2011;52(11):1733-40.

391. Villemagne VL, Pike KE, Chetelat G, Ellis KA, Mulligan RS, Bourgeat P, et al. Longitudinal assessment of Abeta and cognition in aging and Alzheimer disease. Ann Neurol. 2011;69(1):181-92.

392. Aizenstein HJ, Nebes RD, Saxton JA, Price JC, Mathis CA, Tsopelas ND, et al. Frequent amyloid deposition without significant cognitive impairment among the elderly. Arch Neurol. 2008;65(11):1509-17.

393. Beach TG, Monsell SE, Phillips LE, Kukull W. Accuracy of the clinical diagnosis of Alzheimer's disease at National Institute on Aging Alzheimer's Disease Centers, 2005-2010. J Neuropathol Exp Neurol. 2012;71(4):266-73.

394. Arora A, Bhagat N. Insight into the molecular imaging of Alzheimer's disease. Int J Biomed Imaging. 2016;2016:17.

395. Eskici Gz, Axelsen PH. Copper and oxidative stress in the pathogenesis of Alzheimer's disease. Biochemistry. 2012;51(32):6289-311.

396. Ma QF, Li YM, Du JT, Kanazawa K, Nemoto T, Nakanishi H, et al. Binding of copper (II) ion to an Alzheimer's Tau peptide as revealed by MALDI-TOF MS, CD, and NMR. Biopolymers. 2005;79(2):74-85.

397. Smith DP, Smith DG, Curtain CC, Boas JF, Pilbrow JR, Ciccotosto GD, et al. Copper-mediated amyloid-β toxicity is associated with an intermolecular histidine bridge. J Biol Chem. 2006;281(22):15145-54.

398. Miller LM, Wang Q, Telivala TP, Smith RJ, Lanzirotti A, Miklossy J. Synchrotron-based infrared and X-ray imaging shows focalized accumulation of Cu and Zn co-localized with β-amyloid deposits in Alzheimer's disease. J Struct Biol. 2006;155(1):30-7.

399. Mantyh PW, Ghilardi JR, Rogers S, DeMaster E, Allen CJ, Stimson ER, et al. Aluminum, iron, and zinc ions promote aggregation of physiological concentrations of β-amyloid peptide. J Neurochem. 1993;61(3):1171-4.

400. Esposito L, Raber J, Kekonius L, Yan F, Yu G-Q, Bien-Ly N, et al. Reduction in mitochondrial superoxide dismutase modulates Alzheimer's disease-like pathology and accelerates the onset of behavioral changes in human amyloid precursor protein transgenic mice. J Neurosci. 2006;26(19):5167-79.

401. Marcus DL, Thomas C, Rodriguez C, Simberkoff K, Tsai JS, Strafaci JA, et al. Increased peroxidation and reduced antioxidant enzyme activity in Alzheimer's disease. Exp Neurol. 1998;150(1):40-4.

402. Saraceno C, Musardo S, Marcello E, Pelucchi S, Luca MD. Modeling Alzheimer's disease: from past to future. Front Pharmacol. 2013;4:77.

403. LaFerla FM, Green KN. Animal models of Alzheimer's disease. Cold Spring Harb Perspect Med. 2012;2(11).

404. Howlett DR, Richardson JC, Austin A, Parsons AA, Bate ST, Davies DC, et al. Cognitive correlates of Aβ deposition in male and female mice bearing amyloid precursor protein and presenilin-1 mutant transgenes. Brain Res. 2004;1017(1):130-6.

405. Howlett DR, Bowler K, Soden P, Riddell D, Davis J, Richardson J, et al. Amyloid-beta deposition and related pathology in an APP x PS1 transgenic mouse model of Alzheimer s disease. Histol Histopathol. 2008;23(1):67-76.

406. Gingras B, Somorjai R, Bayley C. The preparation of some thiosemicarbazones and their copper complexes. Can J Chem. 1961;39(5):973-85.

407. Szanda I, Mackewn J, Patay G, Major P, Sunassee K, Mullen GE, et al. National Electrical Manufacturers Association NU-4 performance evaluation of the PET component of the NanoPET/CT preclinical PET/CT scanner. J Nucl Med. 2011;52(11):1741-7.

408. Magdics M, Szirmay-Kalos L, Toth B, Legrady D, Cserkaszky A, Balkay L, et al. Performance evaluation of scatter modeling of the GPU-based “Tera-Tomo” 3D PET reconstruction. NSS/MIC, 2011. IEEE 2011:4086-8.

409. Chicklore S, Goh V, Siddique M, Roy A, Marsden PK, Cook GJ. Quantifying tumour heterogeneity in ^{18}F-FDG PET/CT imaging by texture analysis. Eur J Nucl Med Mol Imaging. 2013;40(1):133-40.

410. Cook GJ, Yip C, Siddique M, Goh V, Chicklore S, Roy A, et al. Are pretreatment ^{18}F-FDG PET tumor textural features in non-small cell lung cancer associated with response and survival after chemoradiotherapy? J Nucl Med. 2013;54(1):19-26.

411. Jarrett JT, Berger EP, Lansbury PT, Jr. The carboxy terminus of the beta amyloid protein is critical for the seeding of amyloid formation: implications for the pathogenesis of Alzheimer's disease. Biochemistry. 1993;32(18):4693-7.

412. Mathias CJ, Bergmann SR, Green MA. Development and validation of a solvent extraction technique for determination of Cu-PTSM in blood. Nucl Med Biol. 1993;20(3):343-9.

413. Price KA, Crouch PJ, Volitakis I, Paterson BM, Lim S, Donnelly PS, et al. Mechanisms controlling the cellular accumulation of copper bis(thiosemicarbazonato) complexes. Inorg Chem. 2011;50(19):9594-605.

414. Cheng Z, Zhang J, Liu H, Li Y, Zhao Y, Yang E. Central nervous system penetration for small molecule therapeutic agents does not increase in multiple sclerosis- and Alzheimer's disease-related animal models despite reported blood-brain barrier disruption. Drug Metab Dispos. 2010;38(8):1355-61.

415. Meyer EP, Ulmann-Schuler A, Staufenbiel M, Krucker T. Altered morphology and 3D architecture of brain vasculature in a mouse model for Alzheimer's disease. Proc Natl Acad Sci U.S.A. 2008;105(9):3587-92.

416. Barnham KJ, McKinstry WJ, Multhaup G, Galatis D, Morton CJ, Curtain CC, et al. Structure of the Alzheimer's disease amyloid precursor protein copper binding domain: a regulator of neuronal copper homeostasis. J Biol Chem. 2003;278(19):17401-7.

417. Chen JJ, Rosas HD, Salat DH. Age-associated reductions in cerebral blood flow are independent from regional atrophy. Neuroimage. 2011;55(2):468-78.

418. Jiang D, Zhang L, Grant GP, Dudzik CG, Chen S, Patel S, et al. The elevated copper binding strength of amyloid-beta aggregates allows the sequestration of copper from albumin: a pathway to accumulation of copper in senile plaques. Biochemistry. 2013;52(3):547-56.

419. Sarell CJ, Syme CD, Rigby SE, Viles JH. Copper(II) binding to amyloid-beta fibrils of Alzheimer's disease reveals a picomolar affinity: stoichiometry and coordination geometry are independent of Abeta oligomeric form. Biochemistry. 2009;48(20):4388-402.

420. Syme CD, Nadal RC, Rigby SE, Viles JH. Copper binding to the amyloid-beta (Abeta) peptide associated with Alzheimer's disease: folding, coordination geometry, pH dependence, stoichiometry, and affinity of Abeta-(1-28): insights from a range of complementary spectroscopic techniques. J Biol Chem. 2004;279(18):18169-77.

421. Kaden D, Bush AI, Danzeisen R, Bayer TA, Multhaup G. Disturbed copper bioavailability in Alzheimer’s disease. Int J Alzheimers Dis. 2011;2011:5.

422. Schubert G, Vogt H, Maurer W, Riezler W. Tierexperimentelle Indikatoruntersuchungen mit radioaktivem Kupfer. Naturwissenschaften. 1943;31(49):589-90.

423. Owen CA, Hazelrig JB. Metabolism of Cu-64-labeled copper by the isolated rat liver. Am J Physiol Cell Physiol. 1966;210(5):1059-64.

424. Owen CA. Absorption and excretion of Cu-64-labeled copper by the rat. Am J Physiol. 1964;207(6):1203-6.

425. Mahoney J, Bush J, Gubler C, Moretz W, Cartwright G, Wintrobe M. Studies on copper metabolism. 15. The excretion of copper by animals. J Lab Clin Med. 1955;46:702-8.

426. Bush J, Mahoney J, Gubler C, Cartwright G, Wintrobe M. Studies on copper metabolism. 21. The transfer of radiocopper between erythrocytes and plasma. J Lab Clin Med. 1956;47:898-906.

427. Skromne-Kadlubik G, Díaz JF, Celis C. Basal ganglia scans in the human. J Nucl Med. 1975;16(8):787-8.

428. Sternlieb I, Morell AG, Tucker WD, Greene MW, Scheinberg IH. The incorporation of copper into ceruloplasmin in vivo: studies with copper-64 and copper-67. J Clin Invest. 1961;40(10):1834-40.

429. Bush JA, Mahoney JP, Markowitz H, Gubler CJ, Cart-Wright GE, Wintrobe MM. Studies on copper metabolism. XVI. Radioactive copper studies in normal subjects and in patients with hepatolenticular degeneration. J Clin Invest. 1955;34(12):1766-78.

430. Weber PM, O'Reilly S, Pollycove M, Shipley L. Gastrointestinal absorption of copper: studies with ^{64}Cu, ^{95}Zr, a whole-body counter and the scintillation camera. J Nucl Med. 1969;10:591-6.

431. Bissig KD, Honer M, Zimmermann K, Summer KH, Solioz M. Whole animal copper flux assessed by positron emission tomography in the Long-Evans cinnamon rat--a feasibility study. Biometals. 2005;18(1):83-8.

432. Squitti R, Pasqualetti P, Dal Forno G, Moffa F, Cassetta E, Lupoi D, et al. Excess of serum copper not related to ceruloplasmin in Alzheimer disease. Neurology. 2005;64(6):1040-6.

433. Paxinos G, Franklin K. Paxinos and Franklin's the mouse brain in stereotaxic coordinates. 4th ed. Amsterdam, Netherlands: Academic Press; 2013.

434. Fu X, Zhang Y, Jiang W, Monnot AD, Bates CA, Zheng W. Regulation of copper transport crossing brain barrier systems by Cu-ATPases: effect of manganese exposure. Toxicol Sci. 2014;139(2):432-51.

435. Pushkar Y, Robison G, Sullivan B, Fu SX, Kohne M, Jiang W, et al. Aging results in copper accumulations in glial fibrillary acidic protein-positive cells in the subventricular zone. Aging Cell. 2013;12(5):823-32.

436. Fu S, Jiang W, Zheng W. Age-dependent increase of brain copper levels and expressions of copper regulatory proteins in the subventricular zone and choroid plexus. Front Mol Neurosci. 2015;8:22.

437. Wang H, Wang M, Wang B, Li M, Chen H, Yu X, et al. The distribution profile and oxidation states of biometals in APP transgenic mouse brain: dyshomeostasis with age and as a function of the development of Alzheimer's disease. Metallomics. 2012;4(3):289-96.

438. Leskovjan AC, Lanzirotti A, Miller LM. Amyloid plaques in PSAPP mice bind less metal than plaques in human Alzheimer's disease. Neuroimage. 2009;47(4):1215-20.

439. Bartzokis G, Sultzer D, Cummings J, Holt LE, Hance DB, Henderson VW, et al. In vivo evaluation of brain iron in Alzheimer disease using magnetic resonance imaging. Arch Gen Psychiatry. 2000;57(1):47-53.

440. Bartzokis G, Tishler TA. MRI evaluation of basal ganglia ferritin iron and neurotoxicity in Alzheimer's and Huntingon's disease. Cell Mol Biol. 2000;46(4):821-33.

441. Grossi C, Francese S, Casini A, Rosi MC, Luccarini I, Fiorentini A, et al. Clioquinol decreases amyloid-beta burden and reduces working memory impairment in a transgenic mouse model of Alzheimer's disease. J Alzheimers Dis. 2009;17(2):423-40.

442. Zhang YH, Raymick J, Sarkar S, Lahiri DK, Ray B, Holtzman D, et al. Efficacy and toxicity of Clioquinol treatment and A-beta-42 inoculation in the APP/PS1 mouse model of Alzheimer's disease. Curr Alzheimer Res. 2013;10(5):494-506.

443. Ismail T, Mauerhofer E, Slomianka L. The hippocampal region of rats and mice after a single i.p. dose of clioquinol: loss of synaptic zinc, cell death and c-Fos induction. Neuroscience. 2008;157(3):697-707.

444. Bondiolotti G, Sala M, Pollera C, Gervasoni M, Puricelli M, Ponti W, et al. Pharmacokinetics and distribution of clioquinol in golden hamsters. J Pharm Pharmacol. 2007;59(3):387-93.

445. Love S, Bridges LR, Case CP. Neurofibrillary tangles in Niemann-Pick disease type C. Brain. 1995;118(1):119-29.

446. Auer I, Schmidt M, Lee V-Y, Curry B, Suzuki K, Shin R-W, et al. Paired helical filament tau (PHFtau) in Niemann-Pick type C disease is similar to PHFtau in Alzheimer's disease. Acta Neuropathol. 1995;90(6):547-51.

447. Neufeld EB, Wastney M, Patel S, Suresh S, Cooney AM, Dwyer NK, et al. The Niemann-Pick C1 protein resides in a vesicular compartment linked to retrograde transport of multiple lysosomal cargo. J Biol Chem. 1999;274(14):9627-35.

448. Davies JP, Chen FW, Ioannou YA. Transmembrane molecular pump activity of Niemann-Pick C1 protein. Science. 2000;290(5500):2295-8.

449. Liscum L. Niemann–Pick type C mutations cause lipid traffic jam. Traffic. 2000;1(3):218-25.

450. Sévin M, Lesca G, Baumann N, Millat G, Lyon-Caen O, Vanier MT, et al. The adult form of Niemann–Pick disease type C. Brain. 2007;130(1):120-33.

451. Patterson MC, Vecchio D, Prady H, Abel L, Wraith JE. Miglustat for treatment of Niemann-Pick C disease: a randomised controlled study. Lancet Neurol. 2007;6(9):765-72.

452. Pentchev PG, Comly ME, Kruth HS, Vanier MT, Wenger DA, Patel S, et al. A defect in cholesterol esterification in Niemann-Pick disease (type C) patients. Proc Natl Acad Sci U.S.A. 1985;82(23):8247-51.

453. Reddy JV, Ganley IG, Pfeffer SR. Clues to neuro-degeneration in Niemann-Pick type C disease from global gene expression profiling. PLoS One. 2006;1:E19.

454. Klein A, Maldonado C, Vargas LM, Gonzalez M, Robledo F, de Arce KP, et al. Oxidative stress activates the c-Abl/p73 proapoptotic pathway in Niemann-Pick type C neurons. Neurobiol Dis. 2011;41(1):209-18.

455. Smith D, Wallom KL, Williams IM, Jeyakumar M, Platt FM. Beneficial effects of anti-inflammatory therapy in a mouse model of Niemann-Pick disease type C1. Neurobiol Dis. 2009;36(2):242-51.

456. Zampieri S, Mellon SH, Butters TD, Nevyjel M, Covey DF, Bembi B, et al. Oxidative stress in NPC1 deficient cells: protective effect of allopregnanolone. J Cell Mol Med. 2009;13(9b):3786-96.

457. Zhang JR, Coleman T, Langmade SJ, Scherrer DE, Lane L, Lanier MH, et al. Niemann-Pick C1 protects against atherosclerosis in mice via regulation of macrophage intracellular cholesterol trafficking. J Clin Invest. 2008;118(6):2281-90.

458. Porter FD, Scherrer DE, Lanier MH, Langmade SJ, Molugu V, Gale SE, et al. Cholesterol oxidation products are sensitive and specific blood-based biomarkers for Niemann-Pick C1 disease. Sci Transl Med. 2010;2(56).

459. Zhang H, Wang Y, Lin N, Yang R, Qiu W, Han L, et al. Diagnosis of Niemann-Pick disease type C with 7-ketocholesterol screening followed by NPC1/NPC2 gene mutation confirmation in Chinese patients. Orphanet J Rare Dis. 2014;9:82.

460. Klinke G, Rohrbach M, Giugliani R, Burda P, Baumgartner MR, Tran C, et al. LC-MS/MS based assay and reference intervals in children and adolescents for oxysterols elevated in Niemann–Pick diseases. Clin Biochem. 2015;48(9):596-602.

461. Vázquez MC, Balboa E, Alvarez AR, Zanlungo S. Oxidative stress: a pathogenic mechanism for Niemann-Pick type C disease. Oxid Med Cell Longev. 2012;2012.

462. Christomanou H, Vanier MT, Santambrogio P, Arosio P, Kleijer WJ, Harzer K. Deficient ferritin immunoreactivity in tissues from Niemann-Pick type C patients: extension of findings to fetal tissues, H and L ferritin isoforms, but also one case of the rare Niemann–Pick C2 complementation group. Mol Gen Metab. 2000;70(3):196-202.

463. Chen C. Defective iron homeostasis in lysosomal storage diseases [Ph.D.]. University of Oxford; 2013.

464. Goez HR, Jacob FD, Fealey RD, Patterson MC, Ramaswamy V, Persad R, et al. An unusual presentation of copper metabolism disorder and a possible connection with Niemann-Pick Type C. J Child Neurol. 2011;26(4):518-21.

465. Connemann BJ, Gahr M, Schmid M, Runz H, Freudenmann RW. Low ceruloplasmin in a patient with Niemann-Pick Type C disease. J Clin Neurosci.19(4):620-1.

466. Loftus SK, Morris JA, Carstea ED, Gu JZ, Cummings C, Brown A, et al. Murine model of Niemann-Pick C disease: mutation in a cholesterol homeostasis gene. Science. 1997;277(5323):232-5.

467. Morris MD, Bhuvaneswaran C, Shio H, Fowler S. Lysosome lipid storage disorder in NCTR-BALB/c mice. I. Description of the disease and genetics. Am J Pathol. 1982;108(2):140.

468. Shio H, Fowler S, Bhuvaneswaran C, Morris M. Lysosome lipid storage disorder in NCTR-BALB/c mice. II. Morphologic and cytochemical studies. Am J Pathol. 1982;108(2):150.

469. Bhuvaneswaran C, Morris MD, Shio H, Fowler S. Lysosome lipid storage disorder in NCTR-BALB/c mice. III. Isolation and analysis of storage inclusions from liver. Am J Pathol. 1982;108(2):160-70.

470. Voikar V, Rauvala H, Ikonen E. Cognitive deficit and development of motor impairment in a mouse model of Niemann-Pick type C disease. Behav Brain Res. 2002;132(1):1-10.

471. German DC, Quintero EM, Liang CL, Ng B, Punia S, Xie C, et al. Selective neurodegeneration, without neurofibrillary tangles, in a mouse model of Niemann-Pick C disease. J Comp Neurol. 2001;433(3):415-25.

472. Amritraj A, Peake K, Kodam A, Salio C, Merighi A, Vance JE, et al. Increased activity and altered subcellular distribution of lysosomal enzymes determine neuronal vulnerability in Niemann-Pick Type C1-deficient mice. Am J Pathol. 2009;175(6):2540-56.

473. Klevay LM. Dietary cholesterol lowers liver copper in rabbits. Biol Trace Elem Res. 1988;16(1):51-7.

474. de Wolf I, Fielmich-Bouman X, Lankhorst Æ, van Oost B, Beynen A, Křen V, et al. Liver copper content of rats hypo-or hyperresponsive to dietary cholesterol. J Trace Elem Med Biol. 2003;17(3):177-82.

475. Al-Othman AA, Rosenstein F, Lei KY. Pool size and concentration of plasma cholesterol are increased and tissue copper levels are reduced during early stages of copper deficiency in rats. J Nutr. 1994;124(5):628-35.

476. Sauer SW, Merle U, Opp S, Haas D, Hoffmann GF, Stremmel W, et al. Severe dysfunction of respiratory chain and cholesterol metabolism in Atp7b−/− mice as a model for Wilson disease. Biochim Biophys Acta. 2011;1812(12):1607-15.

477. Palanimuthu D, Shinde SV, Somasundaram K, Samuelson AG. In vitro and in vivo anticancer activity of copper bis(thiosemicarbazone) complexes. J Med Chem. 2013;56(3):722-34.

478. Djoko KY, Paterson BM, Donnelly PS, McEwan AG. Antimicrobial effects of copper (II) bis (thiosemicarbazonato) complexes provide new insight into their biochemical mode of action. Metallomics. 2014;6(4):854-63.

479. Bica L, Liddell JR, Donnelly PS, Duncan C, Caragounis A, Volitakis I, et al. Neuroprotective copper bis (thiosemicarbazonato) complexes promote neurite elongation. PloS one. 2014;9(2).

480. Hueting R, Kersemans V, Cornelissen B, Tredwell M, Hussien K, Christlieb M, et al. A comparison of the behavior of (64)Cu-acetate and (64)Cu-ATSM in vitro and in vivo. J Nucl Med. 2014;55(1):128-34.

481. Handley MG, Medina RA, Nagel E, Blower PJ, Southworth R. PET imaging of cardiac hypoxia: opportunities and challenges. J Mol Cell Cardiol. 2011;51(5):640-50.

482. Lim JK, Mathias CJ, Green MA. Mixed bis(thiosemicarbazone) ligands for the preparation of copper radiopharmaceuticals: synthesis and evaluation of tetradentate ligands containing two dissimilar thiosemicarbazone functions. J Med Chem. 1997;40(1):132-6.

483. Dearling JL, Blower PJ. Redox-active metal complexes for imaging hypoxic tissues: structure–activity relationships in copper (II) bis (thiosemicarbazone) complexes. Chem Commun. 1998(22):2531-2.

484. Holland JP, Aigbirhio FI, Betts HM, Bonnitcha PD, Burke P, Christlieb M, et al. Functionalized bis(thiosemicarbazonato) complexes of zinc and copper: synthetic platforms toward site-specific radiopharmaceuticals. Inorg Chem. 2007;46(2):465-85.

485. Brown O. Novel dissymmetric copper bis(thiosemicarbazone) complexes for medical diagnostic imaging by positron emission tomography. [Ph.D.]. University of Kent; 2015.

486. Giaginis C, Tsantili-Kakoulidou A. Current state of the art in HPLC methodology for lipophilicity assessment of basic drugs. A review. J Liq Chromatogr Relat Technol. 2007;31(1):79-96.

487. Handley M. ^{64}Cu-bis(thiosemicarbazone) complexes for delineating myocardial hypoxia. [Ph.D.]. King's College London; 2012.

488. Green MA. ^{62}Cu-PTSM: a generator-based radiopharmaceutical for myocardial perfusion imaging. In: Schwaiger M, editor. Cardiac positron emission tomography. 1st ed. Boston, United States: Springer US; 1996. 161-72.

489. Tadamura E, Tamaki N, Okazawa H, Fujibayashi Y, Kudoh T, Yonekura Y, et al. Generator-produced copper-62-PTSM as a myocardial PET perfusion tracer compared with nitrogen-13-ammonia. J Nucl Med. 1996;37(5):729-35.

490. Inzelt G. Pseudo-reference electrodes. In: Inzelt G, Lewenstam A, Scholz F, Baucke F, editors. Handbook of reference electrodes. 1st ed. Berlin, Germany: Springer; 2013. 331-32.

491. Holland JP, Green JC, Dilworth JR. Probing the mechanism of hypoxia selectivity of copper bis (thiosemicarbazonato) complexes: DFT calculation of redox potentials and absolute acidities in solution. Dalton Trans. 2006(6):783-94.

492. Barbato F. The use of immobilised artificial membrane (IAM) chromatography for determination of lipophilicity. Curr Comput Aided Drug Des. 2006;2(4):341-52.

493. Bertucci C, Andrisano V, Gotti R, Cavrini V. Use of an immobilised human serum albumin HPLC column as a probe of drug-protein interactions: the reversible binding of valproate. J Chromatogr B Analyt Technol Biomed Life Sci. 2002;768(1):147-55.

494. Ayouni L, Cazorla G, Chaillou D, Herbreteau B, Rudaz S, Lantéri P, et al. Fast determination of lipophilicity by HPLC. Chromatographia. 2005;62(5-6):251-5.

495. Cater MA, Pearson HB, Wolyniec K, Klaver P, Bilandzic M, Paterson BM, et al. Increasing intracellular bioavailable copper selectively targets prostate cancer cells. ACS Chem Biol. 2013;8(7):1621-31.

496. Zheng W, Monnot AD. Regulation of brain iron and copper homeostasis by brain barrier systems: implication in neurodegenerative diseases. Pharmacol Ther. 2012;133(2):177-88.

497. AlzForum, Biomedical Research Forum, LLC. Tau P301S (Line PS19) [Internet]. Cambridge, United States: AlzForum, Biomedical Research Forum, LLC; [cited 2016 Jun 17]. Available from: http://www.alzforum.org/research-models/tau-p301s-line-ps19

498. AlzForum, Biomedical Research Forum, LLC. THY-Tau22 [Internet]. Cambridge, United States: AlzForum, Biomedical Research Forum, LLC; [cited 2016 Jun 17]. Available from: http://www.alzforum.org/research-models/thy-tau22